UDK 669+666+678+53
ISSN 1580-2949
MTAEC9, 49(2)179–309(2015)

MATER. TEHNOL.	LETNIK VOLUME 49	ŠTEV. NO. 2	STR. P. 179–309	LJUBLJANA SLOVENIJA	MAR.–APR. 2015

VSEBINA – CONTENTS

IZVIRNI ZNANSTVENI ČLANKI – ORIGINAL SCIENTIFIC ARTICLES

STROKOVNI ČLANKI – PROFESSIONAL ARTICLES

EDITOR'S PREFACE / PREDGOVOR UREDNIKA

Each issue of the journal Materiali in tehnologije/ Materials and Technology (MIT) gets larger from year to year. In Volume 48 of MIT we published 6 Issues with a total of 1030 pages. There was a total of 159 papers published: 2 as review papers, 117 as original scientific papers and 40 as professional papers. All papers were published in English (with a translation of the titles, abstracts, keywords, figure and table captions into Slovene). In total there were 581 authors from all over the world. The average number of authors per paper was 3.65. However, some of these authors appeared several times. The increasing number of authors from different countries is encouraging, as it demonstrates the quality and visibility of the journal in the international scientific community. Volume 48 contained 105 papers from the field of metallic materials, 11 papers from the field of inorganic materials, 10 papers from the field of polymers, 1 paper from the field of vacuum techniques, 6 papers from the field of chemical technology, 3 papers from the fields of nanomaterials and nanotechnologies, 6 papers from the field of building materials and 17 papers from the field of numerical methods.

In comparison with previous years, we saw an increase in the number of papers from the field of metallic materials. The interest of authors to publish in MIT is growing, which we suppose is due to the journal being involved in the system of impact factor (IF). The IF for MIT was 0.555 in the year 2014. The impact factor of the journal depends on the papers from MIT being cited in other journals. Of course, MIT is indexed in various journal databases: the Science Citation Index Expanded, the Materials Science Citation Index, and Journal Citation Reports/Science Edition. However, the papers from MIT are also indexed in numerous international secondary sources. The journal is available online at http://mit.imt.si.

In 2014 we started with our activities to include the articles published in MIT into the system of Digital Object Identifier (DOI).

We hope that the activation of the DOI system will make MIT even more interesting for authors and readers. Publication in MIT remains free of charge. However, to increase of the quality of the journal we expect from authors, papers with original scientific results, written in good English.

I would like to thank all the authors, editors, technical staff, lectors and reviewers for all their efforts that enable the regular publication of the journal Materiali in tehnologije/Materials and Technology.

Editor-in-Chief
A/Prof. Dr. Matjaž Torkar

Obseg posamezne številke revije Materiali in tehnologije/Materials and Technology (MIT) se iz leta v leto povečuje. Tako je bilo v letniku 48 natisnjenih 6 rednih številk v obsegu 1030 strani. Objavljenih je bilo 159 člankov, od tega 2 pregledna, 117 izvirnih znanstvenih in 40 strokovnih. Vseh 159 člankov je bilo objavljenih v angleškem jeziku s prevodi naslovov, povzetkov, ključnih besed in podnaslovov slik in tabel v slovenski jezik. Skupaj je bilo 581 avtorjev iz številnih držav. Povprečno število avtorjev na članek je 3,65. Nekateri avtorji se pojavljajo tudi večkrat. Rastoče število avtorjev iz različnih držav je razveseljivo, kar kaže na kakovost in odmevnost revije v mednarodnem prostoru. Po vsebini je bilo število člankov z naslednjih področij: kovinski materiali 105, anorganski materiali 11, polimeri 10, vakuumska tehnika 1, kemijske tehnologije 6, nanomateriali in nanotehnologije 3, gradbeni materiali 6 in numerične metode 17.

V primerjavi s prejšnjimi leti se povečuje predvsem število člankov s področja kovinskih materialov.

V primerjavi s prejšnjimi leti se zanimanje za objavo v MIT vsako leto povečuje, domnevno zato, ker je revija vključena v sistem dejavnika vpliva (Impact Factor), ki je bil v letu 2014 0,555. Ta dejavnik je odvisen neposredno od člankov iz MIT, ki so citirani v drugih revijah. Revija je indeksirana tudi v naslednjih bazah podatkov: Science Citation Index Expanded, Materials Science Citation Index, Journal Citation Reports/Science Edition, članki iz revije Materiali in tehnologije pa so indeksirani tudi v številnih mednarodnih sekundarnih virih. Revija je v celotnem obsegu dostopna v elektronski obliki na http://mit.imt.si.

V letu 2014 smo začeli aktivnosti za vključitev revije MIT v sistem Digital Object Identifier (DOI).

Upamo, da bo aktivacija sistema DOI napravila revijo Materiali in tehnologije/Materials and Technology še bolj zanimivo za nove avtorje. Objava v MIT ostaja brezplačna. Za povečanje kvalitete revije pričakujemo, da bodo avtorji pripravili članke z izvirnimi znanstvenimi spoznanji in v dobri angleščini.

Zahvaljujem se vsem avtorjem, urednikom, tehničnim sodelavcem, lektorjem in recenzentom, ki omogočajo redno izhajanje revije MIT.

Glavni in odgovorni urednik
doc. dr. Matjaž Torkar

UDK 669.14.018.8:620.193:620.197:621.793
Original scientific article/Izvirni znanstveni članek

ISSN 1580-2949
MTAEC9, 49(2)183(2015)

PITTING CORROSION OF TiN-COATED STAINLESS STEEL IN 3 % NaCl SOLUTION

JAMIČASTA KOROZIJA NERJAVNEGA JEKLA S PREVLEKO TiN V 3-ODSTOTNI RAZTOPINI NaCl

Israfil Kucuk, Cevat Sarioglu
Marmara University, Dept. of Metallurgical and Materials Engineering, Göztepe kampusu, 34722 Kadiköy-Istanbul, Turkey
cevat.sarioglu@marmara.edu.tr

Prejem rokopisa – received: 2013-09-30; sprejem za objavo – accepted for publication: 2014-02-12

doi:10.17222/mit.2013.176

TiN coatings deposited by arc PVD were characterized by XRD and SEM. In-situ measurements of the corrosion of the substrate and the TiN-coated substrate were made using the corrosion potential (Cor.Pot.), the polarization resistance (PR) method and electrochemical impedance spectroscopy (EIS) in a 3 % NaCl solution as a function of the immersion time. The semiconductor scale formed on the TiN was identified using a Mott-Shottky analysis as an n-type semiconductor with a flat band potential of –0.83 V vs. SCE. The TiN coating (0.5 µm thick) consisted of cubic TiN exhibiting columnar grains, pin holes, voids and porosities. The pitting corrosion of the TiN, observed visually between 1 h and 2 h, was captured by EIS and PR. The electrical circuit (EC) model used for the EIS data supported the degradation of the coating through pitting corrosion, in agreement with the visual observations. The corrosion resistance (polarization resistance) determined by the polarization resistance method (R_p) and the EIS (R_{total}) decreased suddenly during the pitting corrosion. The corrosion resistance of the TiN-coated substrate was greater than the corrosion resistance of the substrate during the approximately 24 h of exposure.

Keywords: stainless steel, TiN, coating, EIS, polarization resistance, pitting corrosion

Prevleka TiN, nanesena z obločnim PVD-postopkom, je bila pregledana z XRD in SEM. In-situ meritve korozije podlage in podlage s prevleko iz TiN so bile izvršene z metodo korozijskega potenciala (Cor.Pot.), polarizacijske upornosti (PR) in z elektrokemijsko impedančno spektroskopijo (EIS) v 3-odstotni raztopini NaCl v odvisnosti od časa namakanja. Mott-Shottkyjeva analiza je odkrila nastanek n-tipa polprevodne škaje na TiN s potencialom ravnih nivojev –0.83 V proti SCE. Prevleko TiN (debeline 0,5 µm) sestavljajo kubični TiN s stebrastimi zrni, luknjami, prazninami in poroznostjo. Vidno odkrita jamičasta korozija TiN, opažena med 1 h in 2 h, je bila posneta z EIS in PR. Model električnega tokokroga (EC), ki je bil uporabljen za EIS-podatke, podpira degradacijo prevleke z jamičasto korozijo, skladno z vizualnimi opažanji. Korozijska upornost (polarizacijska upornost), določena z metodo polarizacijske upornosti (R_p) in EIS (R_{total}) se je nenadno zmanjšala med jamičasto korozijo. Korozijska upornost podlage z nanosom TiN je bila večja kot korozijska obstojnost podlage med izpostavitvijo okrog 24 h.

Ključne besede: nerjavno jeklo, TiN, prevleka, EIS, polarizacijska upornost, jamičasta korozija

1 INTRODUCTION

Hard ceramic coatings such as TiN have been used mainly for tribological applications, such as cutting tools. The tribological properties of single-layer and multi-layer TiN coatings were extensively studied in the literature and published in a handbook.[1–8] On the other hand, the corrosion of TiN in tribological applications was often overlooked, mainly due to the shorter life time of the cutting tools. TiN, with its golden colors, has been used for decorative applications, such as watches, architectural materials and ornaments. The corrosion resistance of the TiN coating is required for these decorative applications in addition to the wear resistance.

The pitting corrosion of the TiN coating deposited on the metallic substrates AISI 304, 430 and steel was observed for different coating thicknesses, exposure times and coating techniques.[9–16] Even though the widely accepted pitting corrosion mechanism of the TiN-coated substrate in the literature was local galvanic corrosion through the galvanic coupling of the TiN coating and the substrate, there remain questions about the mechanism of pitting formation and the growth of the pitting corrosion. One of the key parameters for galvanic corrosion is defects in the coatings, such as pin holes and micro and macro porosities in the coatings. The defects in the coatings provide the electrolyte with a path to the coating/substrate interface.[9–16]

Martensitic stainless steels (EN 1.4034 was used in this work) that are generally used for the blades in kitchen appliances were coated for both decorative and wear-resistance requirements. The pitting corrosion of the TiN coating deposited by arc PVD on a stainless-steel substrate was studied in detail with the corrosion potential (Cor.Pot), the polarization resistance (PR) and electrochemical impedance spectroscopy (EIS) techniques. The mechanism of the pitting corrosion was evaluated with respect to the microstructure of the TiN coating.

2 EXPERIMENTAL PROCEDURES

The substrate material obtained from ThyssenKrupp was EN 1.4034 (X46Cr13) stainless steel. The TiN coating of the substrates was performed in an industrially sized arc PVD coating chamber (AFS ltd. Cop., Turkey). The details about the specimen preparation prior to the coating and the coating procedure are given in detail in[17]. The substrate was coated with a Ti interlayer for 1 min to improve the adhesion of the coating and later with a TiN layer for 20 min at $1.1 \cdot 10^{-3}$ mbar of nitrogen pressure and a total pressure of 10^{-2} mbar with a bias voltage of –200 V. The final deposition temperature was 250 °C.

The electrochemical corrosion units used to perform the EIS, the polarization resistance and the Mott-Shottky scan were a Gamry PC14/750 Poteniostat/Galvanostat/ZRA System. Details about the polarization resistance and the EIS techniques are given in[17]. All the tests were performed in 0.5 M (w = 3 %) NaCl aerated water solution at 25 °C using a three-electrode system (working (sample), auxiliary (graphite) and reference (standard calomel electrode (SCE)) using a Gamry paint cell unit. The Mott-Shottky analyses at a frequency of 1 Hz between +430 mV and –570 mV were performed on a TiN-coated substrate after the corrosion potential was stable.

Microstructural analyses were performed before and after the corrosion using a scanning electron microscope (SEM, Jeol, JSM-5910LV) and energy-dispersive spectroscopy (EDS). The cross-section of the coatings was observed after it was fractured in liquid nitrogen. X-ray diffraction (Rigaku, D-MAX 2200, Cu K_α radiation) was used to identify the structure of the coatings deposited on the substrate.

3 RESULTS

3.1 Microstructural characterization of the substrate and the TiN-coated substrate

An SEM micrograph of the microstructure of the substrate material is presented in **Figure 1**. The carbide phases (Cr and C-rich phase identified by EDS), etched

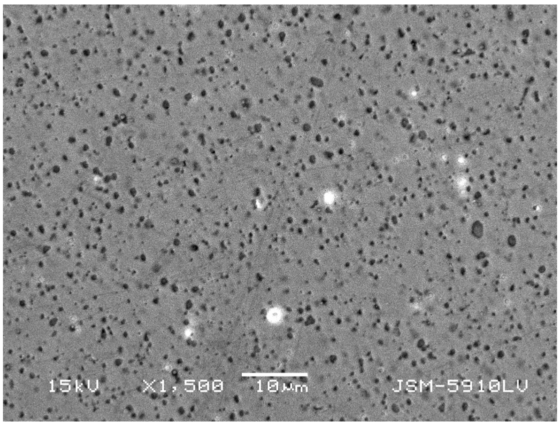

Figure 1: SEM (BEI) micrograph of EP 4034 substrate where dark-grey particles were carbides and bright phases were Fe-rich Fe-Cr particles in a grey matrix

Slika 1: SEM (BEI)-posnetek podlage iz EP 4034, kjer so temnosive pike karbidi, svetle pa faze z Fe bogati Fe-Cr-delci v sivi osnovi

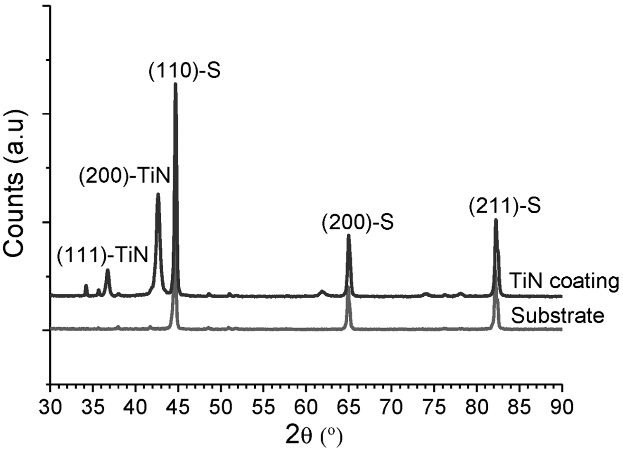

Figure 2: 2θ scan obtained from the EP 4034 steel substrate and TiN-coated substrates using the Bragg-Brentano symmetric X-ray diffraction

Slika 2: 2θ-posnetek Bragg-Brentano simetrične rentgenske difrakcije EP 4034 podlage in prevleke TiN na podlagi

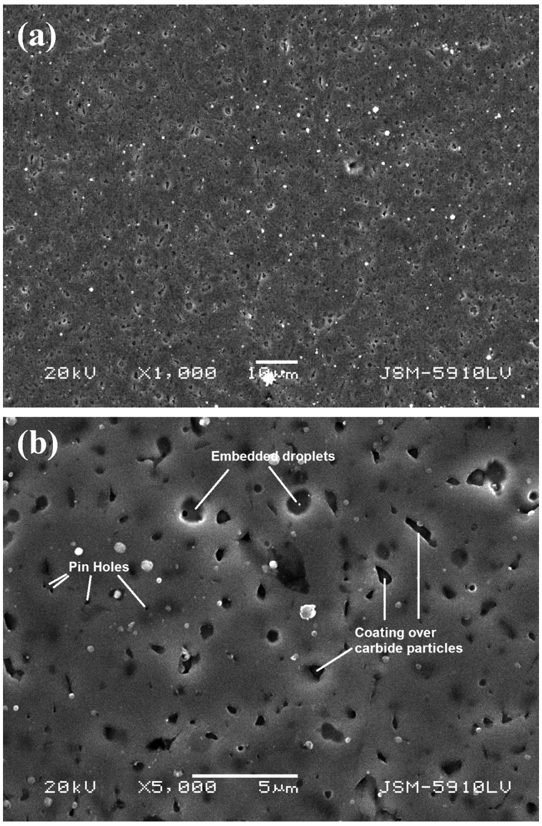

Figure 3: SEM (SEI) micrographs taken from TiN-coating surface at: a) low magnification and b) high magnification. TiN coating deposited over carbide phases (dark areas) were distinguished with depression over the surface at a) and b). Embedded droplets deposited throughout the surface were marked at b). Bright particles on coating surface were un-embedded droplets (spherical particles). Pin holes were marked on surface b).

Slika 3: SEM (SEI)-posnetka površine prevleke TiN pri: a) majhni povečavi in b) veliki povečavi. Prevleka TiN je nanesena preko karbidnih faz (temna področja), ki se razpoznajo po vdolbini na površini a) in b). Vgnezdene kapljice, nanesene na površino, so označene na b). Svetli delci na površini nanosa so nevgnezdene kapljice (sferični delci). Luknjice so označene na površini b).

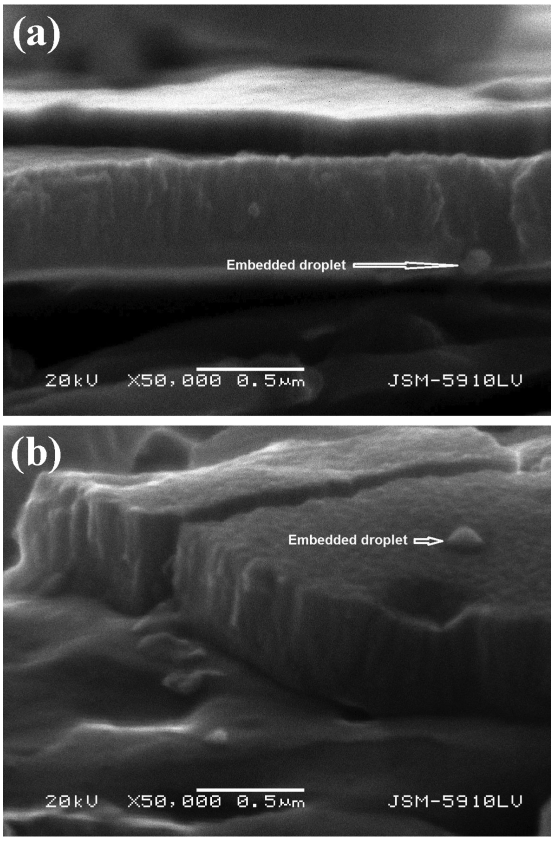

Figure 4: SEM (SEI) of micrographs of fractured surface (in liquid nitrogen) of TiN coating from different areas a) and b). Columnar grains of TiN through fractured coating seen at a) and b). Embedded droplets at surface b) and at coating/substrate interface a) were marked.

Slika 4: SEM (SEI)-posnetka površine preloma (v tekočem dušiku) prevleke TiN na različnih področjih a) in b). Stebrasta zrna TiN skozi prelom prevleke se vidijo na a) in b). Na površini b) in na stiku prevleka – podlaga a) so označene vgnezdene kapljice.

slightly more than the matrix during the electropolishing treatment, were distributed homogenously throughout the matrix. The 4034 EP stainless-steel substrate possessed a ferritic structure (α-Fe), as confirmed by the XRD (**Figure 2**).

After coating with TiN at $1.1 \cdot 10^{-3}$ mbar of N_2 partial pressure, the surface morphology of the coating reflected the morphology of the EP substrate surface, where the etched carbide phases were covered by a TiN coating (**Figure 3**). The TiN coating was identified as a cubic TiN phase (**Figure 2**). Due to the arc PVD process, the droplets formed on the surface of the TiN-coated substrates. There were two different types of droplets found on the surface of the TiN coatings (**Figures 3** and **4**). One of them was the droplets embedded to the scale, i.e., the coating. These droplets were deposited and incorporated into the coatings during the coating process (**Figures 3** and **4**). The other droplets were un-embedded macro-particles (bright, spherical particles) (**Figure 3**). They were thought to be deposited on the surface through vapour-phase precipitation after the coating was finished (when the bias was interrupted). These droplets analysed by EDS contained mainly Ti and N (Ti-rich particles). Based on a detailed surface and cross-section investigation (**Figures 3** and **4**), it was found that the TiN coating exhibited columnar grains (50 nm diameter) that were aligned perpendicular to the substrate surface (**Figure 4**) and possessed a significant amount of pin holes and porosity at the surface (**Figure 3**). The thickness of the TiN coatings, measured from the cross-section (**Figure 4**), was about 0.5 µm.

3.2 Corrosion of the substrate and the TiN-coated substrate

The corrosion of the substrate and the TiN-coated substrate was followed by corrosion potential, PR and EIS measurements during about 24 h of exposure. The visually observed state of the surface was noted during the corrosion evaluation. The corrosion potentials were plotted as a function of the exposure time in **Figure 5**. In general, the corrosion potential on the surface of the TiN decreased with time to a level close to the corrosion potential of the substrate material (**Figure 5**). At all times, the corrosion potential of the substrate was lower compared to the TiN coating during the approximately 24 h of exposure.

The polarization resistance measurements of the substrate and the TiN-coated substrate were performed for a period of 160 s (2.7 min) as a function of the exposure time (**Figures 6** and **7**). The polarization resistance values (R_p) were determined using the polarization resistance method and are plotted in **Figure 5**. The polarization resistance value (R_p) of the substrate determined from the plots in **Figure 6** increased gradually until it

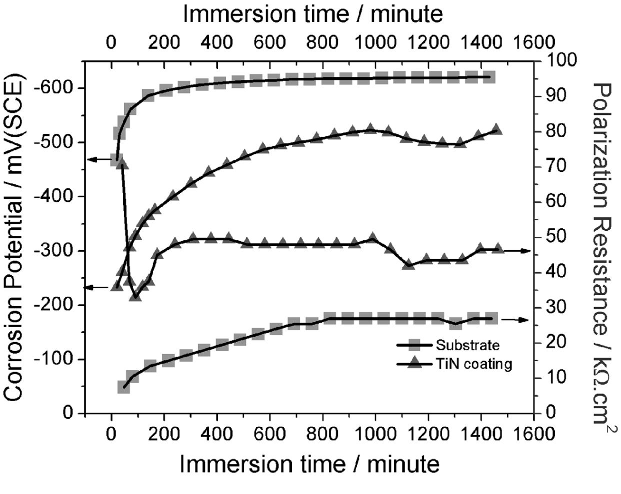

Figure 5: Corrosion potentials and polarization resistances (R_p) of the substrate and TiN-coated substrates determined from the polarization resistance scan (**Figures 6** and **7**) in 3 % NaCl solution as a function of the immersion time

Slika 5: Korozijski potencial in polarizacijska upornost (R_p) podlage in podlage s prevleko TiN so določene s posnetka polarizacijske upornosti (**sliki 6** in **7**) v 3-odstotni raztopini NaCl v odvisnosti od časa namakanja

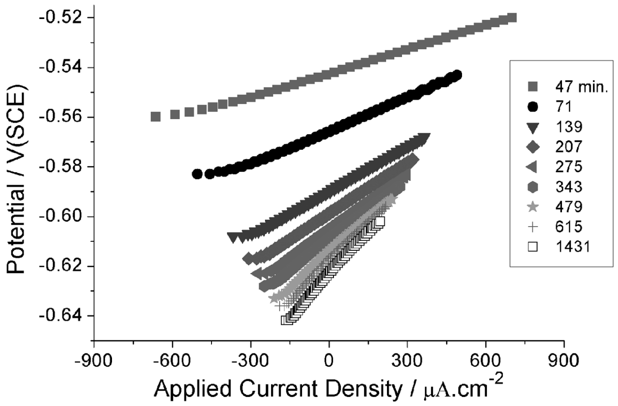

Figure 6: Polarization resistance scan of the substrate in 3 % NaCl solution as a function of immersion time

Slika 6: Zapis polarizacijske upornosti podlage v 3-odstotni raztopini NaCl v odvisnosti od časa namakanja

reached a constant value of 27 kΩ cm^2 after 819 min and remained at the same level until 1431 min of exposure, **Figure 5**. The polarization resistance (R_p) of the TiN coating (**Figure 5**) determined from the polarization resistance plots (**Figure 7**), exhibited a different evolution during the exposures 24 h. At the start, the polarization resistance (R_p) after 40 min decreased from 70.5 kΩ cm^2 to 33 kΩ cm^2 within 50 min and then gradually increased to 48 kΩ cm^2 in 300 min of exposure and stayed almost constant until 1456 min. The evolution of the polarization (R_p) is clear from the PR measurement in **Figure 7** through the expansion and contraction of the PR data. The steep drop in the polarization-resistance value during early exposure between 40 min and 90 min coincided with the visual observation of four pits formed on the surface between 80 min and 95 min of immersion time. These pits and others formed latter grew during the exposure time. During 24 hours of exposure, the corrosion resistance (polarization resistance, R_p) of the TiN-coated substrate (**Figure 5**), was greater than the corrosion resistance of the substrate.

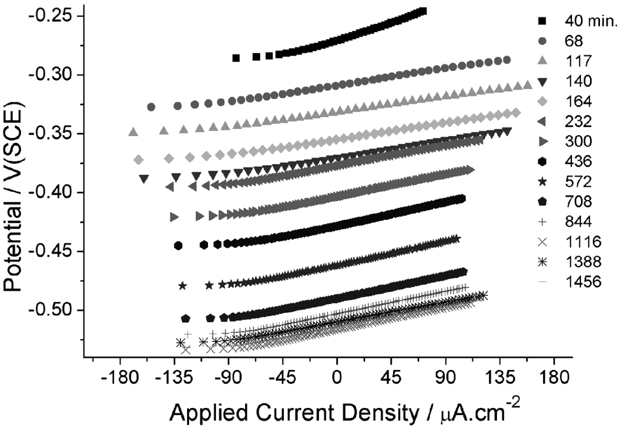

Figure 7: Polarization resistance scan of TiN coating in 3 % NaCl solution as a function of immersion time

Slika 7: Zapis polarizacijske upornosti prevleke TiN v 3-odstotni raztopini NaCl v odvisnosti od časa namakanja

The EIS measurements of the substrate and the TiN-coated substrate were also performed during about 24 h of exposure in a salt solution (**Figures 8** and **9**). The Bode and Nyquist plots for the substrate material were shown in **Figures 8a** and **8b**. In the Nyquist plots (**Figure 8a**), the real and imaginary impedance values gradually increased with the exposure time during the first 759 min and then stayed almost constant until 1439 min of exposure. The Bode plots (**Figure 8b**) exhibited a one-time constant with a minimum in the phase shift close to –80° and at a characteristic frequency of about 10 Hz. The magnitude of the impedance *Z* also increased with time, as shown for the selected exposure times in the Bode plot (**Figure 8b**).

The Bode and Nyquist plots of the TiN coatings were presented in **Figures 9a** and **9b**. The Nyquist plot (**Figure 9a**) clearly demonstrated the evolution of the real and imaginary impedance during the early exposure in the salt solution. The first measurement was performed after 40 min. In the Nyquist plot (**Figure 9a**) the impedance values dropped (shrinkage of curves) until 90 min and then started to increase up to 376 min. The evolution of the Nyquist plot took place during a visual observation of the pits (4 pits observed between 80 min and 95 min). Clearly, the pit formation and the growth of the pits at the early stage were captured by EIS measurements (particularly by the Nyquist plot, more sensitive to

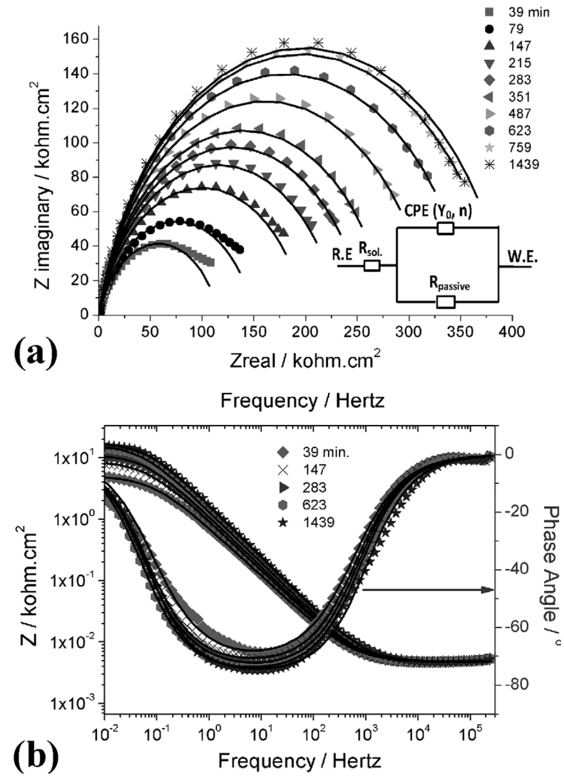

Figure 8: EIS data of the substrate for selected immersion time: a) Nyquist and b) the Bode plots

Slika 8: EIS-podatki podlage pri izbranih časih namakanja: a) Nyquistovi in b) Bodejevi diagrami

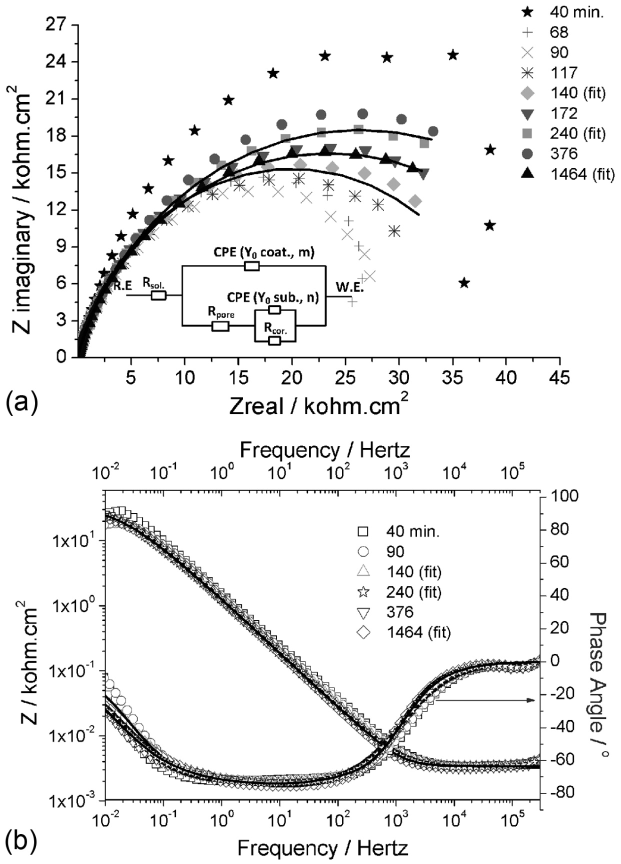

Figure 9: EIS data of TiN coating for selected immersion time: a) Nyquist plots and b) the Bode plots

Slika 9: EIS-podatki prevleke TiN pri izbranih časih namakanja: a) Nyquistovi in b) Bodejevi diagrami

evolution during pitting). After 376 min of exposure, the Bode and Nyquist plots did not vary significantly and the evolution of the impedance data (**Figure 9a**) resembled a polarization resistance scan (**Figure 7**).

3.3 Light and SEM surface examination after the corrosion

As the corrosion potentials, PR and EIS measurements were performed, the surfaces of the samples were visually observed during the exposure in the salt solution. There was no change in the colour or the pit formation on surface of the substrate. As mentioned before, at an early stage four pits were observed on the surface of the TiN-coated substrate and they grew, leaving behind circler brownish colour residues that were around these four pits. The other pits (up to 5) appeared at a later stage of the exposure and with a smaller size (lesser growth of pits). **Figure 10** shows one of the four pits formed on the surface of the TiN coating at an early stage and which grew during 1464 min of exposure. The brownish colour observed visually for the surrounding of the pits corresponded to dark-grey circles in the SEM micrograph (**Figure 10a**). A large amount of oxygen and iron elements were found in these areas by EDS analysis, indicating the dissolution of the substrate and the formation of Fe oxide on the coating surface. **Figures 10b** and **10c** showed the same pit surface at a high magnification. In some areas, the coating was spalled off and in some areas they were detached from the substrate (**Figure 10b**). At the periphery of the pit the interior of the coating was cracked and detached from the surface (**Figure 10c**). **Figure 11** presented the substrate surface for bare areas inside the pit at a high magnification. In

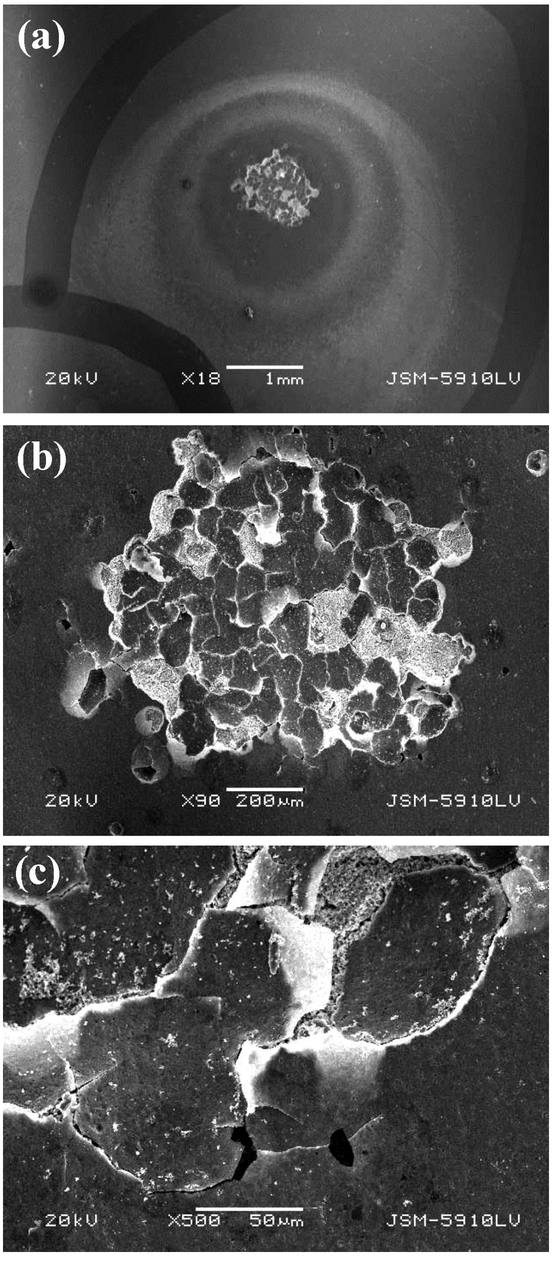

Figure 10: SEM (SEI) micrographs taken from the one of the large pits formed during early exposure: a) the micrograph of the pit marked at low magnification, b) the micrograph from the interior of the pit and c) the micrograph from the periphery of the pit interior at high magnification

Slika 10: SEM (SEI)-posnetki velike jamice, nastale v začetku namakanja: a) posnetek jamice pri majhni povečavi, b) posnetek notranjosti jamice in c) posnetek okolice jamice pri večji povečavi

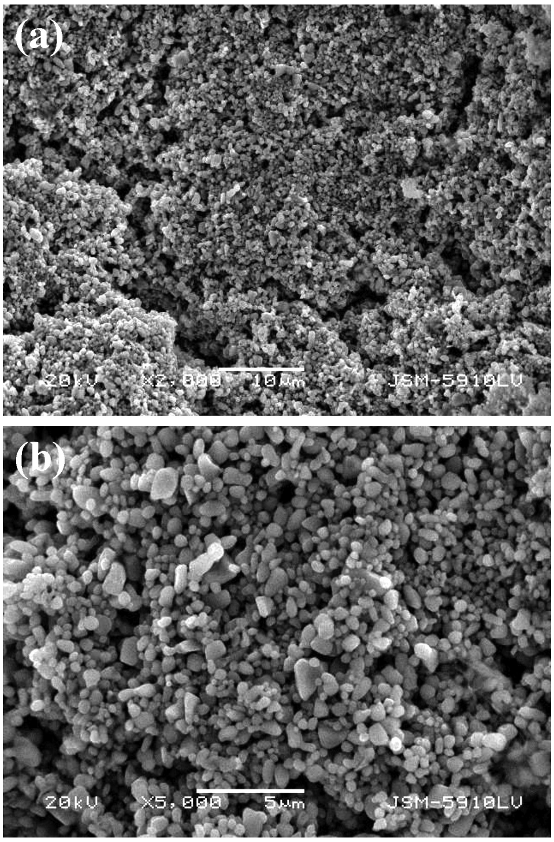

Figure 11: SEM (SEI) micrographs taken from the interior of the pit in **Figure 10** where the scale was removed: a) low magnification and b) high magnification from the same area in a). Equiaxed particles were observed on substrate surface at a) and b).

Slika 11: SEM (SEI)-posnetka okolice jamice, prikazane na **sliki 10**, kjer je bila površina odstranjena: a) majhna povečava in b) velika povečava istega področja na a). Enakoosne delce se opazi na površini podlage a) in b).

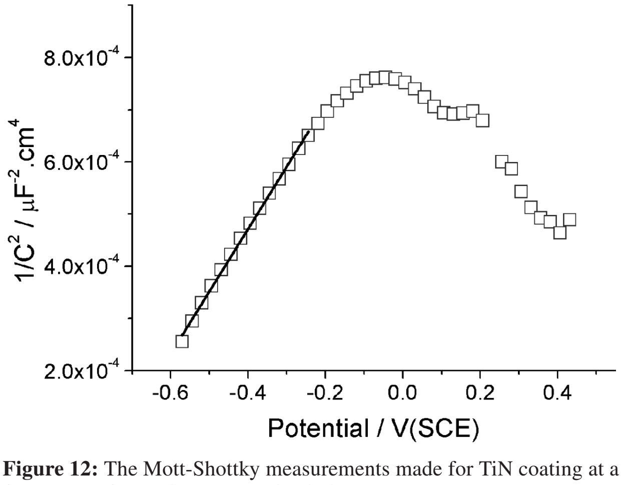

Figure 12: The Mott-Shottky measurements made for TiN coating at a frequency of 1 Hz in 3 % NaCl solution

Slika 12: Mott-Shottkyjeve meritve na prevleki TiN pri frekvenci 1 Hz v 3-odstotni raztopini NaCl

the bare areas, there were approximately diameter 1 μm round grains of pure Cr-Fe particles. These particles (**Figure 11b**), identified by EDS as Cr-rich particles containing Fe but no oxygen and Ti, were thought to be deposited on the bare, exposed substrate surface after the experiment during the drying of the surface. The same morphological observations also were made for other pits.

3.4 The Mott-Shottky measurements

The Mott-Shottky measurements were made for the TiN coatings and plotted in **Figure 12**. Before the Mott-Shottky measurement was made, there was no pit and no colour change on the surface, the corrosion potentials were stable and the EIS data indicated strong capacitive responses at an early stage of the exposure. The Mott-Shottky plot for the TiN coatings (**Figure 12**) exhibited a linear segment between –195 mV and –570 mV vs. SCE with a positive slope. The positive slope indicated an n-type semiconductor oxide layer on the TiN surface.

4 DISCUSSION

4.1 Structure of the TiN coatings

The cubic crystal structure of the TiN was identified by XRD (**Figure 2**). In the literature, the single phase of the TiN coating was generally obtained with various N_2 pressures, since TiN was stable across a wide stoichiometric range.[11–19] The grain morphology of the TiN coating was columnar (**Figure 4**). The columnar grain boundaries in the TiN coatings, aligned perpendicularly from the topmost surface down to the substrate/coating interface (**Figure 4**), were considered to be an easy path for the penetration of the electrolyte.[19] The droplets, which were considered as a preferential site for pitting in,[9] were found on the TiN coating (**Figures 3** and **4**). The TiN coatings possessed a less uniform coverage over the etched carbide phases and droplets (**Figure 3**), resulting in a large quantity of porosity and pin holes. All these defects (columnar grain boundary, droplets, pin holes and porosities) in the coating are preferential sites for the penetration of the electrolyte during the pitting corrosion of the TiN coating.

4.2 Mott-Shottky analysis of the TiN coating

In the literature, the Mott-Shottky analysis has been used to characterize the semiconductor layer formed on the surfaces of materials and coatings.[11,16–21] Based on **Figure 12**, it was concluded that the semiconductor layer formed on the TiN-coated substrate was n-type (presumably TiO_2), in agreement with the literature.[11,21]

The Mott-Shottky equation on page 127 in[20] was used to determine the flat band potential and the density of the charge (density of donors for n-type semiconductor) in the space-charge region. After taking the dielectric constant of TiO_2 as 60, cited in[21] as[20], the flat band potentials and the density of the charges were determined from the linear portion of the plot in **Figure 12** using the eq. in[20].

The density of the donors charge in the n-type TiO_2 was $2.01 \cdot 10^{25}$ cm^{-3}. Rudenja[21] found similar values for a TiN coating deposited on 304 stainless steel as $2.4 \cdot 10^{24}$ cm^{-3} in a solution of 0.1 M H_2SO_4 and 0.05 M HCl. The calculated flat band potentials from the intercept of the plots (**Figure 12**), were –0.83 V vs. SCE for the n-type TiO_2.

4.3 Corrosion of the substrate and the TiN-coated substrate and EIS modelling

The thickness of the TiN was relatively small, 0.5 µm, compared to the literature, where the thinnest coating thickness studied usually about 2 µm. For decorative applications, the coating thickness was kept as small as possible for reasons of cost (0.5 µm in this work could not be the optimum thickness). Because of this small coating thickness, a coating failure of the TiN coating (pitting) as early as about 1 h was observed. The pitting corrosion of the TiN coating at an early stage of immersion was captured by the Cor.Pot., PR and EIS measurements. In order to explain the corrosion mechanism of the TiN coating, the corrosion of the substrate and then the corrosion of the TiN coating at the early stage and later within 24 h were evaluated together with the EIS data and the EC modelling, **Figures 8** and **9** in the next section.

The EIS data of the Bode and Nyquist plots of the substrate clearly exhibited a one-time constant (particularly the phase angle vs the frequency plot in the Bode plots) during 24 h of exposure in a salt solution (**Figure 8**). It has been well known that any parallel RC circuit found in the EC represents a time constant (τ), corresponding to the characteristic frequency (ω_c).[18,19,22] Because of one time constant observation in the Bode and Nyquist plots and the absence of pitting corrosion, the EIS model (**Figure 8a**) proposed for uncoated substrates to simulate the interacting of the electrolyte with the surface consisting of a solution resistance ($R_{sol.}$) and in parallel the total resistance of the passive layer (capacitive layer), $R_{passive}$ with constant phase elements (CPE) of the passive layer. $R_{passive}$ was the resistance of the passive layer. The fit parameters, i.e., Y_0, n, $R_{sol.}$ and $R_{passive}$, were determined from the best non-linear least-square fit to the electrical circuit model with a goodness-of-fit value and they are given in **Table 1** for selected times of exposure. Also, the fitted EIS plots were given in **Figures 8a** and **8b**. The goodness of fit (χ^2) for all the samples was in the range 1–7.6 · 10^{-3} (**Table 1**). The error in the $R_{passive}$ and Y_0 was about 1 %. The value of $R_{passive}$ (**Figure 13**) calculated from the EIS data was the same as R_p calculated from the PR method (**Figure 5**) as expected.[22] Y_0, the admittance constant of the CPE, is a measure of the capacity (C).[23] Y_0 equals the capacity (C) when $n = 1$ for an ideal capacitor. The n value is related to the roughness and the inhomogeneity of the passive (capacitive) film and is less than 1 when the surface is rough.[17,18,23] The n value was about 0.84 (**Table 1**), and constant during the exposure, indicating that the surface roughness (surface area) did not change during the immersion.

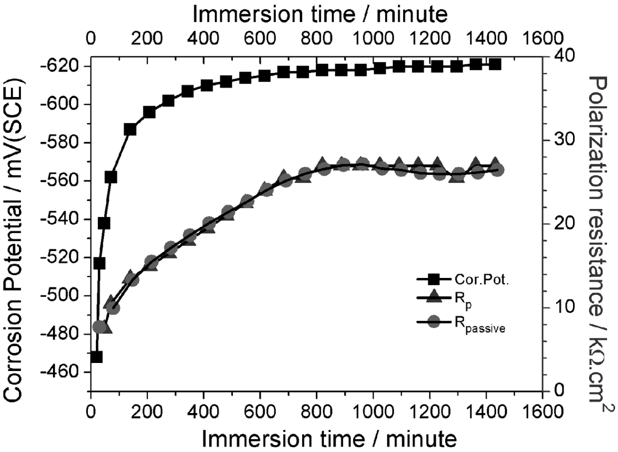

Figure 13: The corrosion potential (Cor.Pot.), polarization resistance (R_p and $R_{passive}$ calculated from EIS data) for the substrate in 3 % NaCl solution as a function of immersion time

Slika 13: Korozijski potencial (Cor.Pot.), polarizacijska upornost (R_p in $R_{passive}$ izračunani iz EIS-podatkov) za podlago v 3-odstotni raztopini NaCl v odvisnosti od časa namakanja

The polarization resistance of the EP substrate (R_p and $R_{passive}$) (**Figure 13**), indicated that the resistance of the passive layer increased from 7.5 kΩ cm^2 to 27 kΩ cm^2 with the exposure time. The Y_0 was also calculated from the EC model and plotted in **Figure 14**. The Y_0 decreased with time and the variation was logarithmic with time as R_p and $R_{passive}$. The capacity values of the passive film determined from Y_0 (presumably Cr_2O_3) (**Figure 14**) decreased logarithmically, indicating that the passive film thickened with the exposure time under assumption that the dielectric property of the passive

Table 1: The EIS fit parameters of the substrate from the electrical circuit model (EC model): Y_0, n, $R_{sol.}$ and $R_{passive}$ were determined by the best non-linear least-square fit with the goodness of the fit value (χ^2)

Tabela 1: EIS-parametri podlage, pridobljeni iz modela električnega tokokroga (EC-model): Y_0, n, $R_{sol.}$ in $R_{passive}$, so bili določeni z najboljšim ujemanjem z nelinerano metodo najmanjših kvadratov in vrednostjo ujemanja (χ^2)

Immersion time (min)	$R_{sol.}$/kΩ cm^2	$R_{passive}$/kΩ cm^2	Y_0/µcm^{-2} s^n Ω	n	Goodness of fit ($\chi^2 \cdot 10^3$)
39	7.1	7.71	213.4	0.79	2.47
147	7.1	13.32	160.7	0.81	6.883
283	7.1	17.16	132.5	0.83	0.981
623	7.2	24.09	107.3	0.84	6.423
1439	7.2	26.48	82.4	0.84	7.556

Table 2: The EIS fit parameters of the TiN coating from the electrical circuit model (EC model): Y_0 coat., Y_0 sub., n, m, $R_{\mathrm{sol.}}$, R_{pore} and $R_{\mathrm{cor.}}$ were determined by the best non-linear least-square fit with goodness of the fit value (χ^2)

Tabela 2: EIS-parametri, pridobljeni za prevleko TiN iz modela električnega tokokroga (EC model): Y_0 coat., Y_0 sub., n, m, $R_{\mathrm{sol.}}$, R_{pore}, in $R_{\mathrm{cor.}}$, so bili določeni z najboljšim ujemanjem z metodo nelineranih najmanjših kvadratov in vrednostjo ujemanja (χ^2)

Immersion time (min)	$R_{\mathrm{sol.}}/\Omega\ \mathrm{cm}^2$	$R_{\mathrm{pore}}/\mathrm{k}\Omega\ \mathrm{cm}^2$	$R_{\mathrm{cor.}}/\mathrm{k}\Omega\ \mathrm{cm}^2$	n	m	Y_0 (coat.)/ $\mu\mathrm{cm}^{-2}\mathrm{s}^n\ \Omega$	Y_0 (sub.)/ $\mu\mathrm{cm}^{-2}\mathrm{s}^n\ \Omega$	Goodness of fit ($\chi^2 \cdot 10^3$)
40	4.9	53.93	–	–	0.83	90.7	–	19.14
90	5.1	0.34	33.65	0.75	0.9	60.3	45.47	13.25
140	5.1	0.17	43.40	0.72	0.93	54.6	59.73	13.82
240	5.1	0.06	53.75	0.72	0.96	40.6	83.13	1.418
648	5.0	0.07	58.41	0.71	0.97	38.9	83.60	1.633
1124	5.2	0.05	47.78	0.73	1	30.2	84.40	1.444
1464	5.1	0.05	48.06	0.73	1	31.5	86.53	1.440

film did not change with time. The logarithmically increase in the polarization resistance (R_{p} and R_{passive}) with time verified this assumption (**Figure 13**) since (R_{p} and R_{passive}) and the current density must relate to the rate of the thickening (dx/dt).[22]

The capacitive (dielectric) layer of TiO_2 formed on TiN as implied by EIS data was identified with the Mott-Shottky analysis as n-type semiconductive layer and that was represented by Y_0. At an early stage of exposure, the transition from strong capacitive to less capacitive behaviour was observed in the EIS measurements (**Figure 9**). The transition for the TiN-coated substrate was a result of the pitting formation and growth. The transition was reproduced with three samples and took place between 1 h and 2 h of exposure for all the samples. Because of the pitting formation and growth at the substrate/TiN coating interface between 80 min and 95 min, after 40 min the EIS model used for the data in **Figure 9** was changed to the model employed in[18,19,24] for porous coatings and paints in order to include the pitting formation and the growth at the substrate/electrolyte interface. This model included two time constants (two RC) (**Figure 9a**).[19,24] The goodness of the EIS data fit was in the range 1.4–19 · 10^{-3} (**Table 2**). It was higher at an early exposure time due to the dynamic change of the corrosion state (**Table 2**). As an example, three fits are shown in **Figures 9a** and **9b**. The representative data especially during pitting were tabulated in **Table 2**. During the pitting formation and growth periods R_{total} (R_{pore} + $R_{\mathrm{cor.}}$) plotted in **Figure 15** as well as R_{pore} decreased while Y_0 sub., (admittance at substrate/electrolyte interface) increased (**Table 2**). $R_{\mathrm{cor.}}$ was the electron charge-transfer resistance at the substrate/electrolyte interface. The decrease in the pore resistance (R_{pore}) and the total resistance, and the increase in the capacity (through Y_0 sub.) at the substrate interface implied the degradation of the coating at the interface. As observed visually, these degradations took place through the pitting formation and growth. After the pits grew to some extent, the total resistance increased slightly and stayed constant for some periods up to 12 h and then fluctuated due to the new pits being formed (five new pits were observed after 24 h) (**Figures 5** and **15**). The total polarization resistance (R_{total}) and R_{p} were very similar and

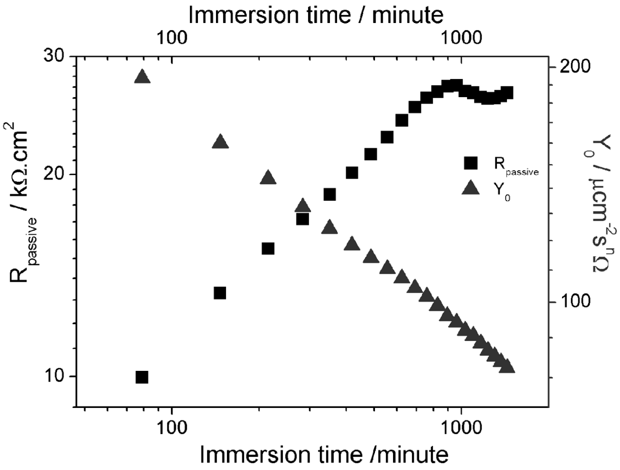

Figure 14: The admittance (Y_0) and polarization resistance (R_{passive} calculated from EIS data) for the substrate in 3 % NaCl solution as a function of immersion time

Slika 14: Admitanca (Y_0) in polarizacijska upornost (R_{passive} izračunana iz podatkov EIS) za podlago v 3-odstotni raztopini NaCl v odvisnosti od časa namakanja

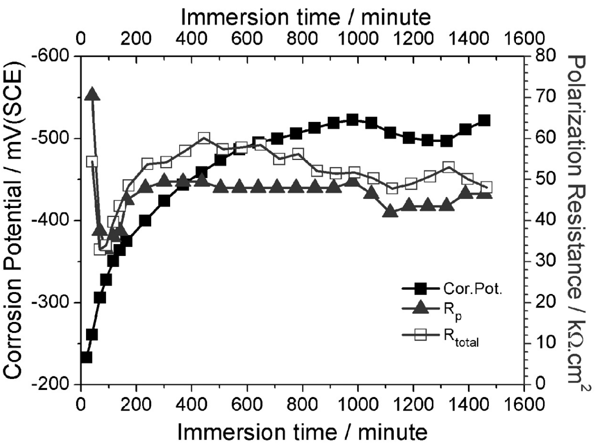

Figure 15: Corrosion potential (Cor.Pot.), polarization resistance (R_{p} and R_{total} calculated from EIS data) for the TiN coating in 3 % NaCl solution as a function of immersion time

Slika 15: Korozijski potencial (Cor.Pot.), polarizacijska upornost (R_{p} in R_{total} izračunani iz EIS podatkov) za prevleko TiN v 3-odstotni raztopini NaCl v odvisnosti od časa namakanja followed the same trend (**Figure 15**), indicating that during the EIS measurement the corrosion state did not change significantly and caused a significant error (the PR measurement took 2.7 min, shorter than the 8 min EIS measurement).

The Y_0 coat. value, (admittance constant for TiO_2 layer) decreased continuously, while the Y_0 sub., for the substrate/solution interface stayed relatively constant for longer times (**Table 2**). After the pitting corrosion, the n value for the capacitive layer at substrate/electrolyte interface remained constant at low level in the range 0.72–0.76 (**Table 2**). The value of m for the capacitive coating on TiN was always at a high level in the range 0.9–1.0 after pitting formation, while at the beginning during the pitting formation it was 0.83, indicating that surface roughness was significant during the early exposure (during pitting) and at longer exposure times the surface became smoother. Recently, He[25] studied the in-situ AFM of exposed TiN (1 μm layer) deposited by DC reactive magnetron sputtering on 304 stainless steel in a 3.5 % NaCl solution and observed decreasing in roughness with time in first exposure 60 min. They explained this result with an in-situ observation of closing the pin holes and small pores, presumably by corrosion products. Even though the χ^2 values (**Table 2**), were high for the early exposure up to 140 min, these EIS data could be used to bring about the evolution of the corrosion of the TiN during the pitting formation and growth.

Before visual observation of the pits based on their brownish colour on the surface (**Figure 10**) (formation of pitting state), the capacitive response of the surface layer (TiO_2) was believed to be degraded by the penetration of the electrolyte through the defects in the coatings, preferentially along the columnar grain boundaries, the pin holes, the large openings or the voids and droplets to the substrate/coating interface (**Figures 3** and **4**). The work of Cai[26] supported this conclusion. Cai[26] studied the effect of a post-deposition treatment of the TiN-coated steel and stainless-steel substrates with polymethyl methacrylate (PMMA) on corrosion in a 3.5 % NaCl solution. They found a significant improvement in the corrosion resistance because of effectively sealing the open voids or pores associated with the coatings. The pits were believed to form at the defect sites (columnar grain boundaries, pin holes, large openings or voids and droplets) by galvanic coupling between the substrate surface and the TiN coating surface. There was a driving force for the galvanic corrosion since the corrosion potential on the substrate surface was more active than the corrosion potential on the TiN surface (**Figure 5**) in agreement with the data reported by Mendibide,[11] who measured a more noble potential of TiN on the glass surface compared to the steel substrate.

The growth or propagation of pits is clearly documented in **Figures 10** and **11** and both were captured by the PR and EIS data (**Figures 5**, **7**, **9** and **15**). At the pit areas there was no Ti, indicating that the TiN coating during the pitting did not dissolve. The growth stage of the pit involved the growth of the pit area as a result of the detachment, cracking and spallation of the TiN coating due to the dissolution of the substrate at the TiN/substrate interface with time. Even though a number of pits formed on the TiN coated surface, the corrosion resistance after about 24 h was greater than the corrosion resistance of the substrate. This results indicated that the TiN was inherently resistant to corrosion due to the formation of the n-type semiconductor passive film (presumably TiO_2), as identified by the Mott-Shottky analysis (**Figure 12**).

5 CONCLUSIONS

1. The pitting corrosion of the TiN is directly related to the coating defects and the coating structure. The TiN coatings deposited on the substrate consisted of cubic TiN and a passive n-type oxide (presumably TiO_2) film with flat band potentials of –0.83 V vs. SCE, determined by the Mott-Shottky analysis. The coatings defects were columnar grain boundaries extending to the coating/substrate interface, the droplets, the pin holes and the porosities. These defects were preferential sites for the pitting corrosion.
2. PR and EIS measurement captured the formation and growth of the pitting corrosion. The EIS model used supported the degradation of the coating through pitting, in agreement with visual observations. The corrosion resistance (R_p and R_{total}) decreased suddenly during the pitting corrosion. The pitting corrosion was believed to take place at the defect sites by galvanic corrosion, driven by the corrosion potential differences between the TiN surface and the substrate surface.
3. The corrosion resistance of the TiN-coated substrate was greater than the corrosion resistance of the substrate for about 24 h, even though the corrosion resistance of the substrate (R_p and $R_{passive}$) increased logarithmically as the passive layer grew with time, as indicated by the decreasing Y_0. This result indicated that the TiN coating possessed a significant inherent resistance to corrosion.
4. The PR and EIS measurements used together gave similar polarization resistance results, supporting the accuracy of the EIS data and the EC model used for the substrate and the TiN-coated substrate.

Acknowledgement

Marmara University is greatly acknowledged for its financial support through the Contract No: FEN-KPS-080808-0178.

6 REFERENCES

[1] B. Warcholinski, A. Gilewicz, Surface Engineering, 27 (**2011**) 7, 491–497, doi:10.1179/026708410X12786785573355

[2] Y. H. Cheng, T. Browne, B. Heckerman, C. Bowman, V. Gorokhovsky, E. I. Meletis, Surface and Coatings Technology, 205 (**2010**) 1, 146–151, doi:10.1016/j.surfcoat.2010.06.023

[3] J. Bujak, J. Walkowicz, J. Kusinski, Surface and Coatings Technology, 180 (**2004**), 150–157, doi:10.1016/j.surfcoat.2003.10.058

[4] A. Horling, L. Hultman, M. Oden, J. Sjolen, L. Karlsson, Surface and Coatings Technology, 191 (**2005**), 384–392, doi:10.1016/j.surfcoat.2004.04.056

[5] C. Ducros, V. Benevent, F. Sanchette, Surface and Coatings Technology, 163-164 (**2003**), 681-688, doi:10.1016/S0257-8972(02)00656-4

[6] C. J. Tavares, L. Rebouta, B. Almeida, J. Bessa e Sousa, Surface and Coatings Technology, 100–101 (**1998**), 65–71, doi:10.1016/S0257-8972(97)00589-6

[7] C. J. Tavares, L. Rebouta, M. Andritschky, S. Ramos, Journal of Materials Processing Technology, 92-93 (**1999**), 177–183, doi:10.1016/S0924-0136(99)00126-0

[8] L. Hultman, J. E. Sundgren, Structure/property relationships for hard coatings, In: R. F. Bunshah (ed.), Handbook of Hard Coatings, William Andrew Publishing, New York 2001, 108–180

[9] H. A. Jehn, Surface and Coatings Technology, 125 (**2000**), 212–217, doi:10.1016/S0257-8972(99)00551-4

[10] M. Fenker, M. Balzer, H. Kappl, Thin Solid Films, 515 (**2006**) 1, 27–32, doi:10.1016/j.tsf.2005.12.020

[11] C. Mendibide, P. Steyer, J. P. Millet, Surface and Coatings Technology, 200 (**2005**), 109–112, doi:10.1016/j.surfcoat.2005.02.060

[12] M. Urgen, A. F. Cakir, Surface and Coatings Technology, 96 (**1997**), 236–244, doi:10.1016/S0257-8972(97)00123-0

[13] M. A. M. Ibrahim, S. F. Korablov, M. Yoshimura, Corrosion Science, 44 (**2002**), 815–828, doi:10.1016/S0010-938X(01)00102-0

[14] W. J. Chou, G. P. Yu, J. H. Huang, Corrosion Science, 43 (**2001**), 2023–2035, doi:10.1016/S0010-938X(01)00010-5

[15] V. K. William Grips, H. C. Barshilia, V. Ezhil Selvi, Kalavati, K. S. Rajam, Thin Solid Films, 514 (**2006**), 204–211, doi:10.1016/j.tsf.2006.03.008

[16] L. Cunha, M. Andritschky, L. Rebouta, R. Silva, Thin Solid Films, 317 (**1998**), 351–355, doi:10.1016/S0040-6090(97)00624-X

[17] I. Kucuk, C. Sarioglu, Mater. Tehnol., 49 (**2015**) 1, 19–26

[18] C. Liu, Q. Bi, A. Leyland, A. Matthews, Corrosion Science, 45 (**2003**), 1243–1256, doi:10.1016/S0010-938X(02)00213-5

[19] C. Liu, Q. Bi, A. Leyland, A. Matthews, Corrosion Science, 45 (**2003**), 1257–1273, doi:10.1016/S0010-938X(02)00214-7

[20] S. Roy Morrison, Electrochemistry at Semiconductor and Oxidized Metal Electrodes, Plenum Press, New York 1980, doi:10.1007/978-1-4613-3144-5

[21] S. Rudenja, C. Leygraf, J. Pan, P. Kulu, E. Talimets, V. Mikli, Surface and Coatings Technology, 114 (**1999**), 129–136, doi:10.1016/S0257-8972(99)00033-X

[22] D. A. Jones, Principles and Prevention of Corrosion, Prentice hall, Inc., 1992

[23] C. H. Hsu, F. Mansfeld, Corrosion, 57 (**2001**) 9, 747–748, doi:10.5006/1.3280607

[24] Y. H. Yoo, D. P. Le, J. G. Kim, S. K. Kim, P. V. Vinh, Thin Solid Films, 516 (**2008**), 3544–3548, doi:10.1016/j.tsf.2007.08.069

[25] C. He, J. Zhang, J. Wang, G. Ma, D. Zhao, Q. Cai, Applied Surface Science, 276 (**2013**), 667–671, doi:10.1016/j.apsusc.2013.03.151

[26] F. Cai, Q. Yang, X. Huang, L. R. Zhao, Corrosion Engineering, Science and Technology, 46 (**2011**) 4, 368–374, doi:10.1179/147842209X12489567719626

UDK 621.396.67:621.375.5
Original scientific article/Izvirni znanstveni članek

ISSN 1580-2949
MTAEC9, 49(2)193(2015)

DESIGN OF A WIDEBAND PLANAR ANTENNA ON AN EPOXY-RESIN-REINFORCED WOVEN-GLASS MATERIAL

ŠIROKOPASOVNA PLOSKOVNA ANTENA NA EPOKSI SMOLI, OJAČANI S STEKLENIMI VLAKNI

Rezaul Azim[1], Mohammad Tariqul Islam[2]
[1]University of Chittagong, Chittagong 4331, Bangladesh
[2]Department of Electrical, Electronic & Systems Engineering, Universiti Kebangsaan Malaysia, 43600 UKM Bangi, Malaysia
razim71@gmail.com

Prejem rokopisa – received: 2013-09-30; sprejem za objavo – accepted for publication: 2014-03-28

doi:10.17222/mit.2013.169

In this study, the design and prototyping of a compact planar antenna is presented for wideband applications. The designed transmission-line-fed antenna is composed of a rectangular radiating patch and a partial ground plane and is printed on both sides of a 1.6 mm thick, epoxy-resin-reinforced, woven-glass dielectric material. The antenna structure is planar, and its design is simple and easy to fabricate. Compared to the other substrate materials, the proposed antenna on epoxy-resin, woven-glass material could achieve a wider and less-expansive bandwidth. Experimental results show that the designed antenna could achieve an impedance bandwidth (return loss ≥ –10 dB) from 2.99 GHz to 18.31 GHz (6.12: 144.33 %). Moreover, the antenna has a good gain and exhibits stable radiation patterns within the operating band. Details of the proposed antenna are presented and discussed.

Keywords: wideband, microstrip patch, planar antenna, epoxy resin, fiberglass

V tej študiji je predstavljena zgradba in izdelava kompaktne ploskovne antene za širokopasovno uporabo. Zasnovana oddajno-sprejemna antena je sestavljena iz pravokotne sevalne in delno ozemljitvene ploskve ter natisnjena na obeh straneh 1,6 mm velike ploščice iz epoksidne smole, ojačane z dielektričnimi steklenimi vlakni. Antena je ploskovna, enostavne zgradbe in enostavna za izdelavo. V primerjavi z drugimi materiali podlage predlagana zasnova na epoksidni smoli s tkanino iz steklenih vlaken omogoča večjo pasovno širino in manjšo ekspanzivnost. Eksperimentalni rezultati kažejo, da predlagana antena lahko doseže impedančno pasovno širino (povratna izguba ≥ –10 dB) od 2,99 GHz do 18,31 GHz (6,12: 144,33 %). Poleg tega ima antena dober izkoristek in kaže stabilne vzorce sevanja v delovnem pasu. Predstavljene in obravnavane so podrobnosti o predloženem oblikovanju antene.

Ključne besede: širokopasovni, mikrotrakasta ploskev, ploskovna antena, epoksidna smola, steklena vlakna

1 INTRODUCTION

In wireless communications technology the necessity for wide and multi-band antennas is increasing rapidly due to the need to support more users and to provide information with higher data-transmission rates. Microstrip antennas are one the most suitable structures due their low profile and ease of fabrication. Compared to conventional, three-dimensional types of antennas, planar microstrip antennas printed on a piece of printed-circuit board have become very popular in modern wireless communications because they can be easily embedded into wireless devices or integrated with other RF circuitry. Usually, a planar design can be used to reduce the volumetric size of a wideband antenna by replacing the three-dimensional radiating elements with their planar versions.[1–3]

Different types of planar antennas have already been proposed for wideband applications. A variety of dielectric materials have been used for the design and prototyping of these antennas. A dielectric material used for the design of wideband antennas is required to feature a higher permittivity and lower dissipation factor.[4] Materials with a lower permittivity are good insulators for lower-frequency signals requiring high isolation in densely packed circuits, such as mobile communications.[5] On the other hand, materials with a higher dielectric constant have a greater capability to store charge and produce larger electromagnetic fields, but limited isolation between the conductors.[6] Moreover, by using a material with a higher permittivity a compact antenna can be designed that is capable of achieving a very wide operating band.[7] For example, in[8] a miniaturized, modified, circular patch antenna was designed on a ceramic-polytetrafluroethylene (PTFE) composite material. With an overall size of $0.22\,\lambda \times 0.29\,\lambda \times 0.03\,\lambda$, the proposed antenna achieved multi-band characteristics. However, the antenna failed to fulfill the requirement for a wideband antenna having triple operating bands of 5–6.3 GHz, 9.1–9.6 GHz and 10.7–11 GHz. In[9], a wideband, pentagon-shaped, planar microstrip slot antenna was designed on an epoxy-resin composite material. Combining the pentagon-shaped slot, feed line, and pentagon stub, the antenna obtained an impedance bandwidth of 124 %. However, its use in portable communication devices was limited due to its large ground plane. Ullah et al.[10] proposed a double L-shaped multi-band patch antenna on a polymer-resin substrate material. By introducing two L-shaped slots in the rectangular patch, the designed antenna could achieve a dual operating band centered at 4.85 GHz and 8.1 GHz, and thus not suitable for broadband wireless communications.

In this study, a simple planar monopole antenna that achieves a physically compact planar profile having sufficient impedance bandwidth and a stable radiation pattern is proposed for wideband applications. The antenna consists of a rectangular radiating patch and a partial ground plane. The transmission line-fed radiating patch is printed on one side of an epoxy-matrix-reinforced, woven-glass material, while the partial ground plane is printed on the other side. The epoxy-matrix-reinforced, woven-glass material is a popular and versatile high-pressure thermo set plastic laminate grade with a low dissipation factor; it is the most commonly used electrical insulator that possesses a good mechanical strength and a nearly zero water-absorption coefficient. It is observed that the radiating patch of the proposed design has a strong coupling with the ground plane and the antenna, designed on polymer-resin composite material, is capable of supporting multiple resonance modes. The overlapping of these multiple resonance modes leads to the characterization of a wideband ranging from 2.99 GHz to 18.31 GHz. The simple structure, ease of fabrication, low cost, wide operating band and stable radiation patterns make the proposed antenna suitable for use in WiMAX, WLAN, C-band, UWB and X-band applications.

2 ANTENNA DESIGN

The design layout of the proposed wideband antenna is illustrated in **Figure 1**. The antenna is designed and analysed using the method of the moment based, full-wave electromagnetic field solver IE3D. The antenna is printed on both sides of a 1.6 mm thick double-layer dielectric substrate. The dielectric material consists of an epoxy-matrix-reinforced woven glass. The fiberglass in the composition is 60 %, while the epoxy resin contributes 40 % of the composition. This composition of epoxy resin and fiberglass varies in the thickness and is direction dependent. One of the attractive characteristics of polymer-resin composites is that they can be shaped and reshaped repeatedly without losing their material characteristics.[11] Due to the ease of fabrication, design flexibility, low manufacturing costs and market availability, the epoxy-matrix-reinforced, woven-glass material has become popular in the design of communication devices.

A microstrip transmission line fed rectangular patch of 13.5 mm × 14.5 mm is printed on one side of the dielectric material, while the partial ground plane with a side length of 5.5 mm is printed on the opposite side. The value of the width and length of the transmission line is set at 2.75 mm and 6 mm, respectively, so that the input impedance of the feeding of the antenna becomes equivalent to 50 Ω. A copper cladding 35 μm is used to metalise the patch, feed line and the ground plane of the proposed antenna. The overall dimension of the designed wideband antenna is optimized to a compact size of 29 mm × 20.5 mm, which is much smaller than the antennas proposed in[9,12–14] and very suitable to be integrated into portable communication devices.

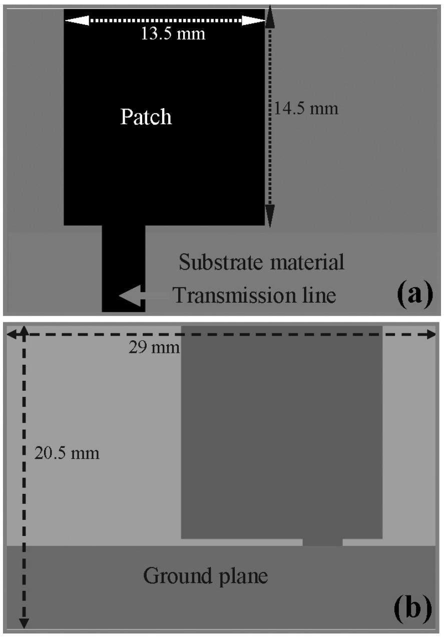

Figure 1: a) Top and b) bottom views of the proposed design
Slika 1: Videz predlagane zgradbe: a) zgoraj in b) spodaj

To investigate the effect of different dielectric materials on the performance of the proposed antenna, a parametric study was conducted. The properties of the dielectric materials are tabulated in **Table 1**, while their effect on the return-loss characteristics is depicted in **Figure 2**. It is clear from the plot that the proposed antenna with an epoxy-matrix-reinforced, woven-glass material exhibits a wider operating band than the glass and ceramic PTFE. Although the antenna with the ceramic PTFE composite material achieved a lower operating frequency because of the high dielectric constant, its bandwidth is narrower compared to glass PTFE and epoxy resin and is extremely expensive compared to the epoxy-resin dielectric material.

Table 1: Properties of the dielectric materials
Tabela 1: Lastnosti izolacijskih materialov

Dielectric material	Permittivity	Loss tangent
Glass PTFE	2.2	0.0009
Ceramic PTFE	10.2	0.002
Epoxy resin	4.6	0.02

The return-loss characteristics in **Figure 2** show that the proposed antenna with epoxy resin material exhibits six resonances across the operating band, of which the first appears at 3.4 GHz, the second at about 6.45 GHz, the third at 9.7 GHz, the fourth at 11.0 GHz, the fifth at 12.75 GHz and the final resonance is at 16.17 GHz. The figure clearly indicates that the overlapping of these

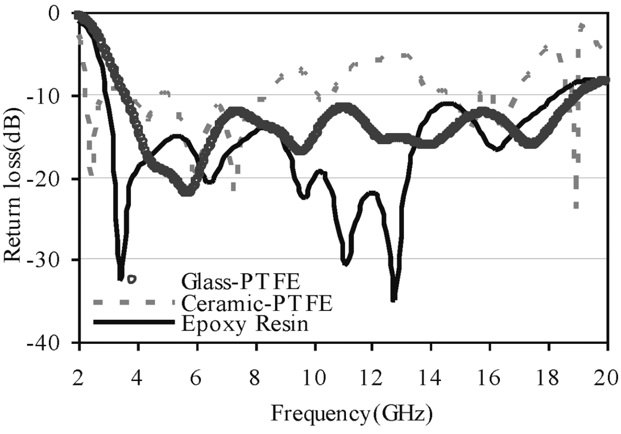

Figure 2: Return-loss characteristics for different materials
Slika 2: Značilnosti povratnih izgub za različne materiale

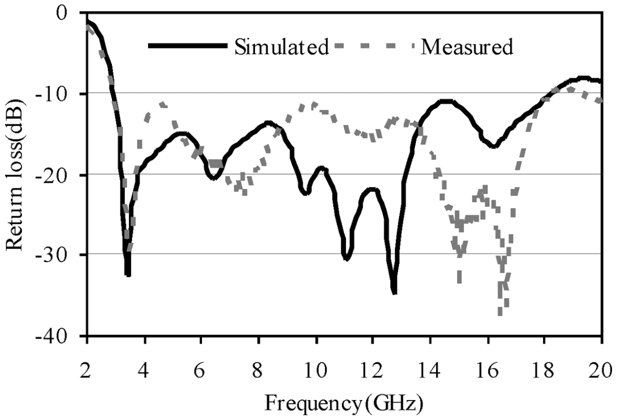

Figure 4: Measured and simulated return losses
Slika 4: Izmerjene in simulirane povratne izgube

resonances that are closely spaced across the spectrum leads to a wide operating bandwidth, ranging from 2.96 GHz to 18.31 GHz. At the first resonance frequency, when the antenna size is smaller than the corresponding wavelength, the electromagnetic signal can couple to the antenna size and can operate in the stationary wave mode. As the frequency increases, the antenna starts to operate in the mixed stationary wave and the travelling wave modes. At the higher edge frequency of the operating band, the antenna size becomes larger, corresponding to the respective wavelength, and the electromagnetic signals have to travel a long distance, resulting in a dominating travelling wave mode, as shown in **Figure 3,** which depicts the input impedance of the proposed antenna.

3 RESULTS AND DISCUSSION

The return-loss characteristic of the realised antenna was measured in an anechoic chamber using an Agilent E8362C vector network analyser. **Figure 4** plots the measured and simulated return-loss curves. The simulated –10 dB return-loss bandwidth ranges from 2.96 GHz to 18.31 GHz, equivalent to a fractional bandwidth of 144.33 %. This wideband characteristic of the proposed planar antenna is confirmed in measurements, with only a small shift of the lower edge frequency to 2.99 GHz. Despite a very small size, the proposed antenna achieved a sufficient operating band to cover the WiMAX, WLAN, C-band, UWB and X-frequency bands.

Although there is a disparity between the measured and simulated resonances that can possibly be attributed to the manufacturing tolerances and imperfect soldering effects of the SMA connector, the measured resonance frequencies are nearly identical to the simulated frequency. This mismatch may also be due to the effect of the RF feeding cable, which is used in the measurements, but not considered during the simulation. The ripples observed in the measured result may be caused by the current drain from the conducting ground plane to the outer shield of the RF feeding cable, which is not presumed during the simulation.

The peak gain of an epoxy-resin-based, wide-band antenna is illustrated in **Figure 5**. Despite a very compact dimension, the designed antenna exhibits a good gain. As the antenna would be used for short-distance wireless communication, the achieved peak gain is within the acceptable limits. The gain of the proposed

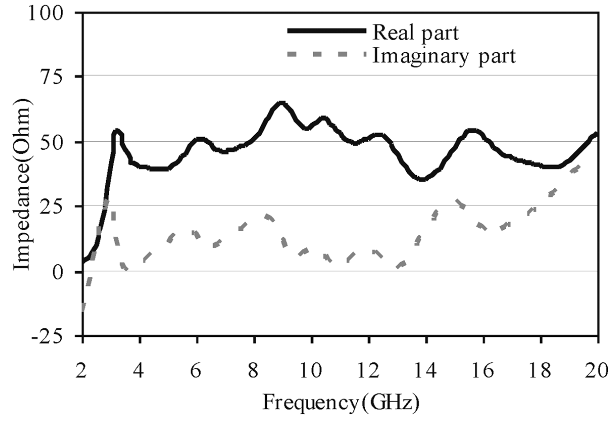

Figure 3: Real and imaginary parts of the input impedance
Slika 3: Realni in navidezni del vhodne impedance

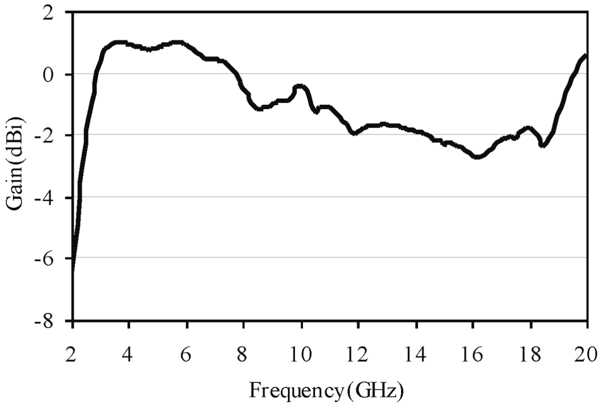

Figure 5: Gain of the proposed wideband antenna
Slika 5: Izkoristek predlagane širokopasovne antene

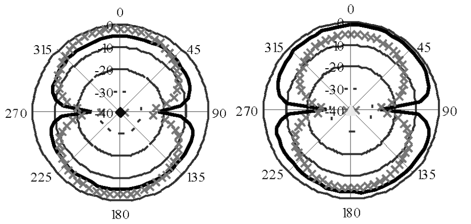

at 3.2 GHz

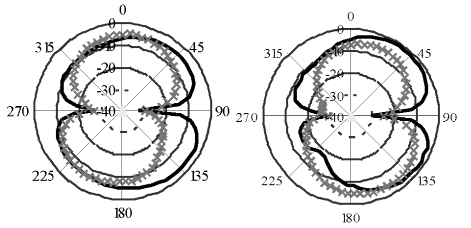

at 6.1 GHz

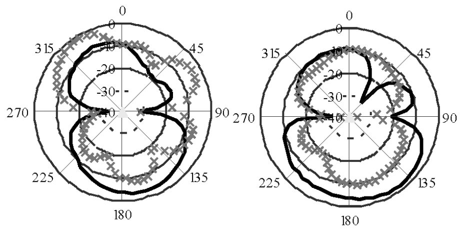

at 12.7 GHz

E-plane *H*-plane

Figure 6: Radiation patterns at different frequencies (Solid line: co-polarised field, crossed line: cross-polarised field)

Slika 6: Vzorci sevanja pri različnih frekvencah (polna črta: kopolarizirano polje, prečno: prečno polarizirano polje)

antenna could be improved using ceramic PTFE microwave substrate material rather than epoxy-resin material. However, the use of the ceramic PTFE increases the cost of the antenna and hence this option is not considered in the design.

The *E*- and *H*-plane radiation patterns of the proposed antenna at (3.2, 6.1 and 12.7) GHz are depicted in **Figure 6**. At lower frequencies, the antenna exhibits a bidirectional radiation pattern for both the *E* and *H* planes, and the patterns are approximately the same as the pattern of a typical monopole antenna. As the frequency increases, a higher-order harmonic is introduced to the patterns, and both the *H* and *E* planes become more directional, but still retain their bidirectionality. Some dips are observed, mainly at higher frequencies, and might be because the microstrip feed line is printed directly below the partial ground plane and might also be caused by the feed connector. However, the radiation patterns are remarkably stable throughout the operating band.

4 CONCLUSIONS

A compact planar microstrip antenna is designed and fabricated for a wideband application. The proposed antenna consists of a partial ground plane and a transmission-line-fed rectangular radiating element. The antenna design is analysed and optimised by the method of moment-based software IE3D and is verified by means of a prototype. The antenna is designed and fabricated on epoxy-matrix-reinforced, woven-glass material. Compared to the other dielectric materials, the proposed antenna with an epoxy matrix reinforced woven-glass material exhibits better performance in terms of bandwidth, return-loss, gain and radiation patterns. Experimental results show that the proposed antenna could achieve an impedance bandwidth from 2.99 GHz to 18.31 GHz (6.12: 1, 15.32 GHz) for a return loss of ≥ –10 dB. Moreover, the antenna achieved a good gain and stable radiation patterns. All these features of the proposed epoxy-resin-based antenna make it a worthy candidate for wideband applications in portable communication devices.

5 REFERENCES

[1] M. J. Ammann, Z. N. Chen, Wideband monopole antennas for multiband wireless systems, IEEE Antennas and Propagation Magazine, 45 (**2003**), 146–150, doi:10.1109/MAP.2003.1203133

[2] X. H. Wu, Z. N. Chen, Comparison of planar dipoles in UWB applications, IEEE Transactions on Antennas and Propagations, 53 (**2005**), 1973–1983, doi:10.1109/TAP.2005.848471

[3] M. Samsuzzaman, M. T. Islam, J. S. Mandeep, N. Misran, Printed wide-slot antenna design with bandwidth and gain enhancement on low-cost substrate, The Scientific World Journal 2014 (**2014**), Article ID 804068, 10 pages, doi:10.1155/2014/804068

[4] K. Oohira, Development of an antenna material based on rubber that has flexibility and high impact resistance, NTN Technical Review, 76 (**2008**), 58–63

[5] M. Samsuzzaman, M. T. Islam, J. S. Mandeep, Parametric analysis of a glass-micro fibre-reinforced PTFE material, multiband, patch-structure antenna for satellite applications, Optoelectronics and Advanced Materials–Rapid Communications, 7 (**2013**), 760–769

[6] A. Aguayo, Analyzing advances in antenna materials, Antenna Systems & Technology, 12 (**2010**), 14–15

[7] M. H. Ullah, M. T. Islam, A compact square loop patch antenna on high dielectric ceramic–PTFE composite material, Applied Physics A, 113 (**2013**), 185–193, doi:10.1007/s00339-012-7511-4

[8] M. H. Ullah, M. T. Islam, Miniaturized modified circular patch monopole antenna on ceramic-polytetrafluroethylene composite material substrate, Journal of Computational Electronics, 13 (**2014**), 211–216, doi:10.1007/s10825-013-0501-8

[9] S. K. Rajgopal, S. K. Sharma, Investigations on ultrawideband pentagon shape microstrip slot antenna for wireless communications, IEEE Transactions on Antennas and Propagations, 57 (**2009**), 1353–1359, doi:10.1109/TAP.2009.2016694

[10] M. H. Ullah, M. T. Islam, J. S. Mandeep, N. Misran, A new double L-shape multiband patch antenna on polymer resin material substrate, Applied Physics A: Materials Science & Processing, 110 (**2012**), 199–205, doi:10.1007/s00339-012-7114-0

[11] I. Yarovskya, E. Evansb, Computer simulation of structure and properties of crosslinked polymers: application to epoxy resins, Polymer, 43 (**2002**), 963–969, doi:10.1016/S0032-3861(01)00634-6

[12] R. Azim, M. T. Islam, N. Misran, Microstrip line-fed printed planar monopole antenna for UWB applications, Arab Journal for Science and Engineering, 38 (**2013**), 2415–2422, doi:10.1007/s13369-013-0553-x

[13] L. Liu, S. W. Cheung, R. Azim, M. T. Islam, A compact circular-ring antenna for ultra-wideband applications, Microwave and Optical Technology Letters, 53 (**2011**), 2283–2288, doi:10.1002/mop

[14] R. Azim, M. T. Islam, N. Misran, A. T. Mobashsher, Compact UWB planar antenna for broadband applications, Informacije MIDEM, 41 (**2011**), 37–40

UDK 669.35'5:620.173:548.55
Original scientific article/Izvirni znanstveni članek

ISSN 1580-2949
MTAEC9, 49(2)197(2015)

INFLUENCE OF THE STRAIN RATE ON THE PLC EFFECT AND ACOUSTIC EMISSION IN SINGLE CRYSTALS OF THE CuZn30 ALLOY COMPRESSED AT AN ELEVATED TEMPERATURE

VPLIV HITROSTI DEFORMACIJE NA POJAV PLC IN AKUSTIČNO EMISIJO MONOKRISTALOV ZLITINE CuZn30, STISKANE PRI POVIŠANI TEMPERATURI

Wojciech Ozgowicz[1], Barbara Grzegorczyk[1], Andrzej Pawełek[2], Andrzej Piątkowski[2], Zbigniew Ranachowski[3]

[1]Institute of Engineering Materials and Biomaterials of the Silesian University of Technology, Konarskiego St. 18A, 44-100 Gliwice, Poland
[2]Institute of Metallurgy and Materials Science of Polish Academy of Sciences, Reymonta St. 25, 30-059 Cracow, Poland
[3]Institute of Fundamental Technological Research of the Polish Academy of Sciences, Pawinskiego St. 5B, 02-106 Warsaw, Poland
barbara.grzegorczyk@polsl.pl

Prejem rokopisa – received: 2013-10-01; sprejem za objavo – accepted for publication: 2014-02-25

doi:10.17222/mit.2013.195

The purpose of these investigations was to determine the effect of the strain rate on the phenomenon of a heterogeneous plastic deformation of the Portevin–Le Chatelier type while testing free compression of CuZn30 single crystals with a crystallographic orientation of $[\bar{1}39]$ at 300 °C. Moreover, the relations between the work-hardening curve $\sigma - \varepsilon$ displaying the PLC effect and the characteristics of the signals of the acoustic emission generated in the uniaxial-compression test were determined. It was found that the process of plastic deformation of the tested single crystals in the analyzed range of the frequencies up to 35 kHz generates differentiated sources of acoustic-energy emission, mainly the impulsive emission generated by signal events, correlated with the oscillations of the stresses on the work-hardening curves $\sigma - \varepsilon$. The strain rate mainly causes the changes in the intensity of the oscillation typical for the PLC effect.

Keywords: plastic strain, Portevin–Le Chatelier effect (PLC), single crystals, copper alloys, compression test, acoustic emission (AE)

Namen raziskav je bil ugotoviti vpliv hitrosti deformiranja pri preizkusu stiskanja monokristalov CuZn30 s kristalografsko orientacijo $[\bar{1}39]$ pri 300 °C na pojav heterogene plastične deformacije vrste Portevin-Le Chatelier. Poleg tega so bile ugotovljene še odvisnosti med krivuljo deformacijskega utrjevanja $\sigma - \varepsilon$, ki kaže pojav PLC, in značilnostmi signalov akustične emisije pri enoosnem tlačnem preizkusu. Ugotovljeno je, da proces plastične deformacije preizkušanih kristalov v analiziranem področju frekvenc do 35 kHz proizvaja diferencirane vire emisije akustične energije, predvsem impulzivne emisije signalov, ki se skladajo z oscilacijo napetosti na krivulji deformacijskega utrjevanja $\sigma - \varepsilon$. Hitrost deformacije se kaže predvsem v spremembi intenzitete oscilacij, značilnih za PLC-pojav.

Ključne besede: plastična deformacija, Portevin-Le Chatelierov pojav (PLC), monokristali, zlitine bakra, tlačni preizkus, akustična emisija (AE)

1 INTRODUCTION

In order to determine the kinetic relations and structural changes, conditioning the mechanisms of plastic deformation it is necessary to know the process and understand the essence of various phenomena occurring in the course of plastic deformations. In many alloys a heterogeneous plastic deformation in the form of irregularities on the work-hardening curve is observed during tensile (or compression) tests. The earliest investigations concerning this phenomenon in medium-carbon steel and aluminium were published by Portevin and Le Chatelier in 1923, hence, it is called the PLC effect. Although the effect of the instability of plastic deformations of the PLC type has been known and investigated for nearly one hundred years, it is still not fully recognized and explained.[1–7] Generally, this effect was investigated on the basis of material factors, taking into account the microstructural conditions of an initiation of a localized plastic deformation and the rheological factors connected with the mechanics of plastic deformations at various thermodynamic and physico-chemical conditions.

One of the more recent methods of analyzing the phenomena occurring in the course of a plastic deformation is the acoustic emission (AE). This method consists of a detection and analysis of the acoustic signal emitted by the material while it is being mechanically loaded. The acoustic signal is a result of the propagation of elastic waves generated in the material due to a fast release of the energy accumulated in this material. The shape of an AE signal is affected by many factors such as the chemical composition and macrostructure of the tested material, the kind of the applied heat treatment,[8,9] the temperature and strain rate $(\dot{\varepsilon})$,[10] the grain size,[11] the texture and the state of precipitations.[12,13] The investigations based on AE measurements are characterized by non-invasiveness and an incomparably high sensitivity in recording physical phenomena in comparison with the other methods of investigations.

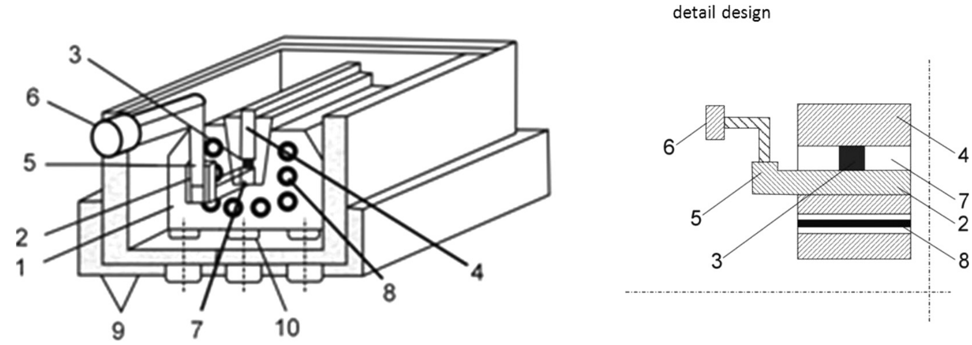

Figure 1: Duct-die block for deforming the samples at an elevated temperature with an AE probe: 1 – die-block body, 2 – guide bar, 3 – sample, 4 – punch, 5 – wave guide, 6 – AE probe, 7 – duct, 8 – heating elements, 9 – foamed polystyrene, 10 – tack bolt

Slika 1: Orodje s kanalom za deformiranje vzorcev pri povišanih temperaturah z uporabo AE-sonde: 1 – telo orodja, 2 – paličasto vodilo, 3 – vzorec, 4 – tlačilna palica, 5 – valovni vodnik, 6 – AE-sonda, 7 – vodilni kanal, 8 – grelni element, 9 – penjeni polistiren, 10 – spenjalni vijak

Table 1: Chemical composition of the monocrystalline alloy applied in the investigations

Tabela 1: Kemijska sestava monokristalne zlitine, uporabljene pri preiskavah

No.	Determination of the alloy and the kind of the applied analysis of CuZn30	Chemical composition, mass fractions, *w*/%						
		Zn	Fe	Al	Ni	Sn	Pb	Cu
1	smelting analysis of CuZn30 ingot	30.3	0.024	0.039	0.024	0.003	0.01	bal.
2	CuZn30 PN-EN 12163:2002	28.3–30.3	max 0.05	max 0.02	max 0.3	max 0.1	max 0.05	bal.

The aim of this paper is to determine the influence of the strain rate in the range of 10^{-5}–10^{-1} s^{-1} on a non-homogeneous plastic deformation, the so-called Portevin-Le Chatelier effect, in a single-crystalline CuZn30 alloy with the crystallographic orientation of $[\bar{1}39]$, compressed at a temperature of 300 °C. The additional aim is to determine the relation between the behaviour of the signals of acoustic emissions generated in the course of a plastic deformation at elevated temperature and the shape of the work-hardening curves $\sigma - \varepsilon$ in the range of the PLC effect.

2 EXPERIMENTAL PROCEDURE

The investigated material was a single-crystalline CuZn30 alloy in the form of a rod with a diameter of 3.8 mm, a length of about 200 mm and crystallographic orientation of $[\bar{1}39]$, the chemical composition of which is shown in **Table 1**. Single crystals of this alloy were obtained with the Bridgmen's method in a vertical, electrical tubular heating furnace by displacing the temperature gradient of the zone in the furnace in relation to the crucible (a quartz tube), with a charge in an atmosphere of inert gas.

In order to realize the purpose of these investigations the following procedures had to be carried out:

- mechanical tests of free compression of single crystals at 300 °C and a strain rate of 10^{-5}–10^{-1} s^{-1},
- investigations concerning the plastic deformation of single crystals by means of acoustic emission.

Compression tests of single crystals were performed at a temperature of 300 °C and at $\dot{\varepsilon}$ amounting to 10^{-5}–10^{-1} s^{-1} on a universal testing machine INSTRON 3382 equipped with a duct die including heating elements and a quartz outlet of the waveguide with an AE sensor (**Figure 1**). For the AE measurements the following setting was used: the acoustic-emission wideband sensor of type WD (PAC) provided by a company called Physical Acoustic Corp., a low-noise amplifier set to 66 dB of gain, background-noise discrimination at 0.75 V and 12-bit digital-to-analogue conversion at a rate of samples $88.2 \cdot 10^3$ s^{-1}. The settings used for the AE acquisition had been adjusted experimentally during the

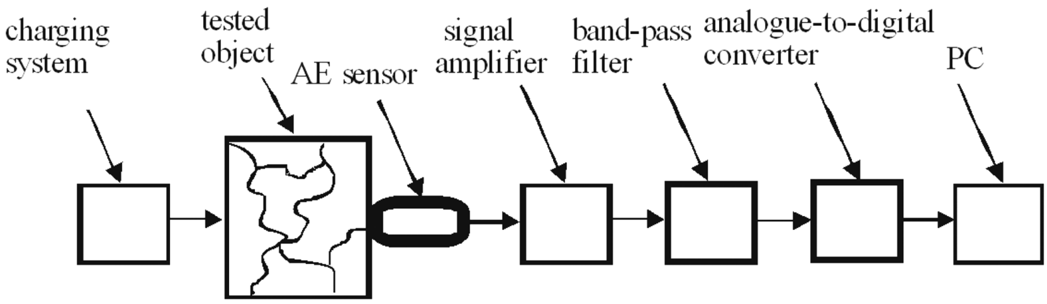

Figure 2: Simplified block diagram of the measurement and AE recording system

Slika 2: Poenostavljeni sestav merilnega in zapisovalnega sistema AE previous tests dealing with the tension and compression of metal samples.[14,15] The final deformation of the sample after the compression test amounted to about 50 %. The values of the forces within the entire range of the measurements were recorded with an accuracy of up to 0.5 %. The acoustic emission was measured during the compression tests of microcrystalline samples. In order to reduce the coefficient of friction between the butting face of the compressed sample and the steel punch, the samples were coated with a strip of Teflon.

The block diagram of the measurement, the system and the recording of AE are illustrated in **Figure 2**. The AE measurement system was connected with the recording system of the testing machine. The tests were carried out in the Accredited Laboratory of the Strength of Materials, the Polish Academy of Science, Cracow.

3 RESULTS AND DISCUSSION

The influence of the strain rate in the range of 10^{-5}–10^{-1} s^{-1} on the mechanical characteristics $\sigma - \varepsilon$ of the CuZn30 single crystals with the initial crystallographic orientation of $[\bar{1}39]$ at the constant temperature of the compression amounting to 300 °C is presented in **Figure 3** and **Table 2**. It was found that the strain rate does not cause any changes in the general shape of the work-hardening curves of the investigated single crystals, but causing a considerable effect on the level of the stresses at the yield point and intensive oscillation of the stresses on these curves. When the strain rate grows, a tendency toward decreased values of the actual stresses could be observed, particularly during the initial stage of the deformation (15–20 %). Moreover, a tendency toward decreased oscillation of the stresses on the analytical work-hardening curves was observed.

At the investigated temperature of the compression, the strain rate considerably influences the intensity of the oscillation of the stresses characterized by an occurrence of the PLC effect (**Figure 3**). The conditions of the plastic instability of the deformed single crystals are distinct in the case of low values of $\dot{\varepsilon}$ (10^{-5}–10^{-4} s^{-1}) but they fade at a medium strain rate of about 10^{-3} s^{-1} and do not occur when $\dot{\varepsilon} > 10^{-2}$–$10^{-1}$ s^{-1}. It was also found that the strain rate only slightly affects the type of the oscillation of the stress in the described conditions of deformation.

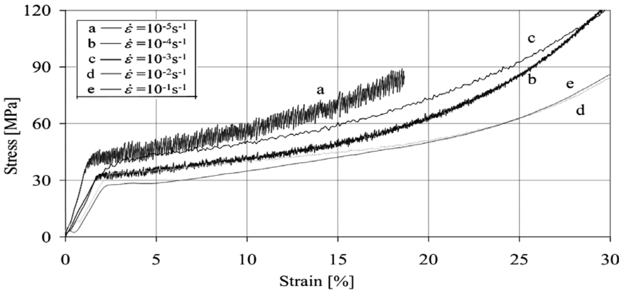

Figure 3: Influence of the strain rate on the shape of curves $\sigma - \varepsilon$ of CuZn30 single crystals with the initial orientation of $[\bar{1}39]$, compressed at 300 °C

Slika 3: Vpliv stopnje deformacije na obliko krivulje $\sigma - \varepsilon$ monokristalov CuZn30 z začetno orientacijo $[\bar{1}39]$, stisnjenih pri 300 °C

According to the classification by Brindley and Worthington[16,17] three fundamental types of the oscillation of stresses are to be distinguished. Type A occurs at a low temperature of a tensile test, characterized by an increase, followed by a sudden drop in the force, such as the oscillation of the forces occurring periodically. At elevated temperatures type-B deformation oscillations occur that are smaller and irregular. These oscillations are symmetrical in relation to the level of the work-hardening curve. Type C occurs at the highest temperature of a plastic deformation. These oscillations are characterized by a decrease of the force in relation to the level of the work-hardening curve and they are often separated from the area of homogeneous plastic deformation.

According to this system, on the compression curves ($\sigma - \varepsilon$) of the tested single crystals in the range of deformation ε (5–15 %), type-B oscillations were detected. The initiation of the PLC effect, conditioned by the critical strain (ε_c), was observed on the work-hardening curves in the range of ε (1.2–2 %). In most cases the initiation of the oscillations on the curves of the compression coincides with the yield point of the material. The value of ε_c proved to be rather independent of the strain rate. In order to quantitatively describe the serration on the stress-strain curves, the analytic parameters used in quantitative fractography were applied.[11] One of them, the so-called coefficient of development of the R_L line, was derived from the relation of $R_L = L/L'$, where L is the length of a given segment of the $\sigma - \varepsilon$ line and L' is the length of its projection. An approximately normal projection on the stress-strain curves was used.

The geometrical analysis also indicates that for the serration occurring with a particular frequency (f), R_L can be calculated with equation $R_L \cong (\bar{A}/f)^{-1}$, where $\bar{A}$ is the average amplitude of serration. The parameters calculated in compliance with the MATLAB software are gathered in **Table 2**. It was found that the higher the values of coefficient R_L (at a higher amplitude and

Table 2: Specification of the coefficients of the shape of $\sigma - \varepsilon$ curves in CuZn30 single crystals with the orientation of $[\bar{1}39]$ compressed in the range of deformations (5–15 %)

Tabela 2: Pregled koeficientov oblike krivulje $\sigma - \varepsilon$ v monokristalih CuZn30 z orientacijo $[\bar{1}39]$, stisnjenih v območju deformacij (5–15 %)

No.	Temperature of deformation (°C)	$\dot{\varepsilon}/s^{-1}$	$\varepsilon_c/\%$	Coefficient of the shape of $\sigma - \varepsilon$ curves with the PLC effect		
				R_L	A	f
1	300	10^{-2}	2.7	6.0	1.5	9.2
2		10^{-3}	2.6	4.1	2.9	12.2
3		10^{-4}	1.6	43.7	3.8	166.2
4		10^{-5}	1.2	71.6	5.5	395.2

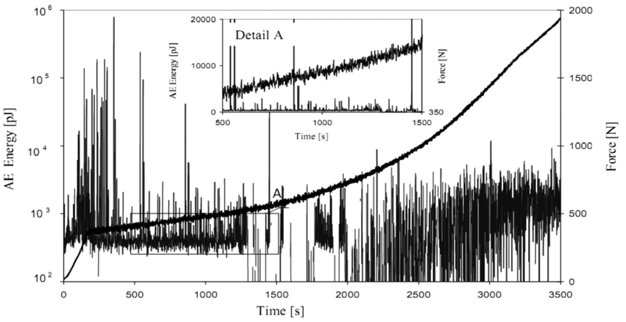

Figure 4: Dependence of the AE energy on the PLC effect recorded on the work-hardening curve during the compression testing of monocrystalline CuZn30 alloy at 300 °C and $\dot{\varepsilon}$ up to about 10^{-4} s^{-1}

Slika 4: Odvisnost energije AE od PLC-učinka, zabeleženega na krivulji preoblikovalnega utrjevanja pri tlačnem preizkusu monokristala zlitine CuZn30 pri 300 °C in $\dot{\varepsilon}$ do 10^{-4} s^{-1}

frequency of serration), the larger is the instability of the PLC plastic deformation (**Table 2**). The highest values of coefficient R_L (about 72) in the range of deformations ε (5–15 %) as well as the highest value of the amplitude of stresses (calculated as $2 \cdot A$) amounting to about 11 MPa were determined for the samples compressed at the temperature of 300 °C and with $\dot{\varepsilon}$ amounting to about 10^{-5} s^{-1}. The obtained values confirm the qualitative description of the compression curves.

The obtained results allow us to maintain that in the tested single crystals the PLC effect is a result of dynamic strain aging (DSA), which is an interaction between the sliding dislocations and free atoms. The sources of these interactions, complying with the dynamic-dislocation model of the PLC effect, are the multiplications of dislocations in the course of being affected by Frank-Read sources. The occurrence of DSA is conditioned by the rate of the migration of foreign atoms constituting the Cottrell atmosphere. The effects of the atoms of the alloy and the impurities with dislocations are responsible for retarding the dislocations, and thus also for hardening the alloy. If, therefore, a given strain rate is "imposed", we must also apply a stress that exceeds the resistance to the motion of dislocations, including the resistance resulting from the effect of the atoms of the alloy with dislocations. In order to explain, in a simple way, the qualitative model of the changes in the stress in the hardening diagram, we must assume that the break-away of a dislocation from the alloy atoms reduces the stress. This is indispensable for a further displacement of the dislocation by the value of this effect. The moment of a break-off of a dislocation from the blocking atoms involves a sudden drop in the force exciting the deformation.[18–20]

According to the dislocation-dynamic model of the PLC effect, every local drop in the loading force recorded on the $\sigma - \varepsilon$ curves is connected with unlocking the dislocation sources in a certain localized area of the sample. If there is a high concentration of internal stresses, the adjacent sources of dislocation will, successively, become unlocked due to these stresses. Therefore, the unlocked sources of dislocation operate in a state of being considerably overcharged, so that the dynamically generated dislocation increases. Consequently, this involves a formation of sliding bands, which then propagate until the time of waiting (t_w) again reaches the value of the time of aging (t_a). Then, all the sources of dislocation are effectively locked by the Cottrell atmosphere,[21] after which the process of unlocking starts again.

The results of the measurements of the acoustic emission (AE) during the compression testing of CuZn30 single crystals with the orientation of $[\bar{1}39]$ at the temperature of 300 °C and the strain rate of 10^{-5}–10^{-1} s^{-1} are gathered in **Figures 4** to **6** and **Table 3**. In the investigations of AE the descriptors of the recorded signals are usually added, such as:

- the count rate over the preset noise-discrimination level
- the signal amplitude within an AE event
- the energy of an AE event, understood as a half of the product of the AE-event duration and the squared amplitude of the AE event.

Table 3: Specification of the descriptors of the AE signals in the R_e range concerning the investigated parameters of compression

Tabela 3: Pregled opisovalcev AE-signalov v območju R_e preiskovanih parametrov pri tlačnem preizkusu

No.	Temperature of deformation (°C)	Strain rate $\dot{\varepsilon}/s^{-1}$	Sum of AE events in the R_e range	Average energy of the AE events in the R_e range (pJ)
1	300	10^{-4}	14539	20.3
2		10^{-3}	8903	42
3		10^{-2}	6714	68
4		10^{-1}	816	30

The last parameter was applied in the presented research because the squared signal amplitude combined with the event duration applied in the formula for data processing distinguishes well the signals caused by material effects from the unwanted signals caused by the drive of the loading machine and other system noises. This is because the unwanted AE sources have different spectral characteristics than the desired ones.

In most compression tests of the investigated single crystals a distinct growth of the activity of the AE energy was recorded during the initial stage of their compression and in the area of passing from the elastic to the plastic range (**Figures 4** and **5**). This growth depends on the value of $\dot{\varepsilon}$ when deformations ε amount to about 2–5 %.

An increase in AE is in both cases characterized by a more or less wide maximum change in the energy of the signal, after which AE reaches its minimum. The observed increase in the energy of the AE activity in the initial stages of the $\sigma - \varepsilon$ curves may, however, be caused, among others, by mechanical factors due to the friction and the matching of the sample to the compress-

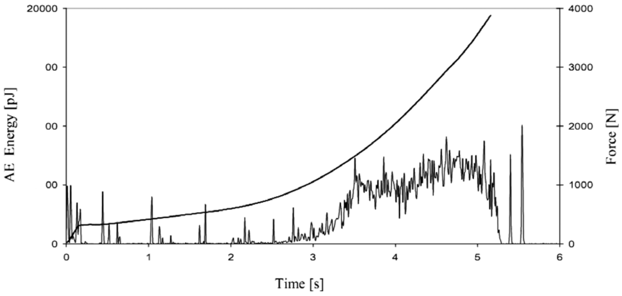

Figure 5: Dependence of the AE energy on the shape of the work-hardening curve during the compression testing of a CuZn single crystal at 300 °C and $\dot{\varepsilon}$ amounting to about 10^{-1} s^{-1}

Slika 5: Odvisnost energije AE od oblike krivulje napetostnega utrjevanja med tlačnim preizkusom monokristala CuZn pri 300 °C in vrednostjo $\dot{\varepsilon}$ do 10^{-1} s^{-1}

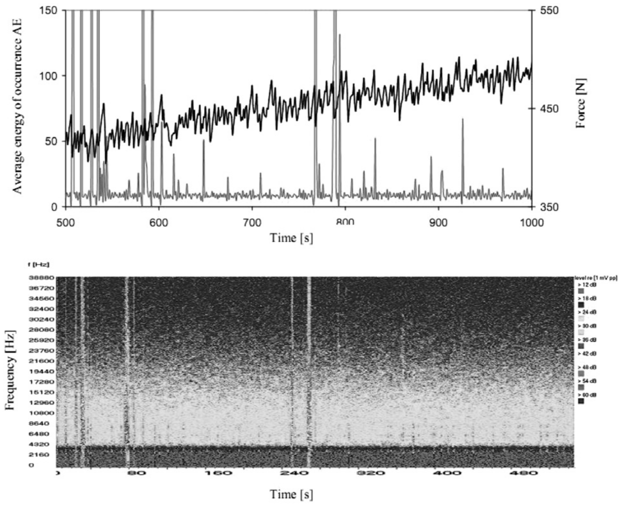

Figure 6: a) Dependence of the AE energy on the serration along the stress-strain curve (within the fragment of the diagram presented in **Figure 4**) of a CuZn30 single crystal with the orientation of [$\bar{1}39$] at 300 °C and $\dot{\varepsilon}$ up to about 10^{-4} s^{-1} and b) an acoustogram corresponding to this set of EA events

Slika 6: a) Odvisnost energije AE od nazobčanosti vzdolž krivulje napetost – deformacija (z izrezkom iz diagrama, predstavljenega na **sliki 4**) pri CuZn30-monokristalu z orientacijo [$\bar{1}39$] pri 300 °C in $\dot{\varepsilon}$ do 10^{-4} s^{-1} in b) akustogram, ki ustreza temu sklopu AE-dogodkov

ing punch of the testing machine. In the range of the yield point, however, where AE displays a merely physical aspect, the increasing AE activity is undoubtedly connected with the processes of dislocation. The AE level in this stage of the hardening of the alloy was found to be much more intensive than in the advanced stages of deformation occurring in the cases of greater drafts.

The sum and mean energy of AE depending on the strain rate during the compression test are gathered in **Table 3**. It was found that in the $\dot{\varepsilon}$ range from about 10^{-4} s^{-1} to about 10^{-2} s^{-1} the sum of events in the range of the yield point (R_e) increases with the slowing down of the strain rate. The opposite is the case when the energy of a single event reaches its mean value. A higher average value of the energy of the event, except for $\dot{\varepsilon}$ amounting to about 10^{-1} s^{-1}, corresponds to a smaller sum of events. The minimum sum of events of about 816 also corresponds to a low value (30 pJ) of the average energy of AE events. The highest sum of events occurred in the case of the single crystals deformed at the temperature of 300 °C with $\dot{\varepsilon}$ amounting to about 10^{-4} s^{-1} and the mean value of the energy of event of about 20 pJ.

It was found that in the first stage of the hardening (the stage of easy sliding) of the single crystals that do not display any PLC effect (**Figure 5**), the AE level is lower, growing with the increase in the rate of deformation, whereas in the single crystals displaying the PLC effect, the AE level is higher and its characteristics are more complex. A change in the strain rate at a given temperature does not involve any essential changes in the level of the frequency of AE. In the second stage of the hardening within the $\dot{\varepsilon}$ range of (10^{-5}–10^{-1} s^{-1}) the AE activity is greater, particularly during the initial stage. These are mostly single samples of the AE signal characterized by differentiated energy or a continuously increasing level of the AE energy, which grows with the increasing rate of deformation, independent of the occurrence of the PLC effect in the course of the compression of single crystals.

When a work-hardening curve is of a parabolic character (the third stage of hardening), AE appears in the form of strong cumulative maximum values of the energy changes in the signal in time, particularly at the beginning. Irrespective of the appearance of the PLC effect in the course of the compression testing of single crystals, it was found that in the final stage of the deformation there is also a range, in which the AE energy is intensified, although less intensive with respect to the number of pulses than in the R_e range. The observed correlations between the AE behaviour and the exerted compressive force and the evolution of the microstructure may be satisfactorily explained with the qualitative level based on the dynamic processes of dislocation connected with the motion of dislocation.[8–10,19] The processes of the formation of sliding lines in the range of the yield point were proved to be acoustically most effective. Every collective dislocation motion in the sliding systems probably leads to a release of elastic energy, generating the recorded signals.

In most compression tests of the CuZn30 single crystals displaying the PLC effect sudden reductions of the compressive forces recorded on the work-hardening curve were found to be distinctly correlated with the AE peaks (**Figure 6**). It is supposed that every increase in the oscillation of the stress on the σ – ε curves is connected with a locking of dislocations, and that every violent reduction represents a motion of a large group of dislocations (avalanches of dislocations). Similarly, it is assumed that only regular oscillations of the stresses of certain given types are connected with the generation of slip bands of the PLC effect.

4 CONCLUSIONS

The investigations dealt with in this paper lead to the following conclusions:

- The phenomenon of instability of the plastic deformation of the Portevin-Le Chatelier type occurs in the tested single crystals of alloy CuZn30 in the course of free compression at 300 °C within a limited range of the strain rate from 10^{-5} s^{-1} to 10^{-2} s^{-1}.
- In the conditions of free compression applied in the investigations, CuZn30 single crystals display characteristic oscillations of the stresses on the work-hardening curves, corresponding to the oscillations classified in the literature as the B type.
- The increasing strain rate in the compression tests leads to a distinct decrease in the stress-oscillation intensity, typical for the PLC effect.
- The plastic deformation of the investigated single crystals at elevated temperature generates in the analyzed range of frequencies (up to 35 kHz) diversified source of AE energy, mainly an impulsing emission from single events, i.e., pulsating acoustic signals with a high energy in the frequency band from 4 kHz to 8 kHz.
- The correlation between the PLC and AE effects in the tested single crystals can be explicitly explained on the basis of a dislocation-dynamic model of the PLC effect.
- In the process of plastic deformation of the tested single crystals, the applied AE method exhibits the dependence of the activity of acoustic emissions on the given stage of the hardening of the analyzed alloy.
- The intensity of AE increases mainly in the range of the yield point (R_e) on the $\sigma - \varepsilon$ curves, and also in the case of considerable deformations. When the maximum intensity of the AE signal has been reached, it fades, in most cases, to the minimum value.

5 REFERENCES

[1] A. Portevin, F. Le Chatelier, Comptes Rendus de l'Académie des Sciences Paris, 176 (**1923**), 507–510

[2] V. Scott, F. Franklin, F. Mertens, M. Marder, Physical Review E, 62 (**2000**), 8195–8206, doi:10.1103/PhysRevE.62.8195

[3] P. Hähner, E. Rizzi, Acta Materialia, 51 (**2003**), 3385–3397, doi:10.1016/S1359-6454(03)00122-8

[4] J. Balik, Materials Science and Engineering, A316 (**2001**), 102–108, doi:10.1016/S0921-5093(01)01223-0

[5] Z. Jiang, Q. Zhang, H. Jiang, Z. Chen, X. Wu, Materials Science and Engineering A, 403 (**2005**) 1, 154–164, doi:10.1016/j.msea.2005.05.059

[6] W. Ozgowicz, B. Grzegorczyk, E. Kalinowska-Ozgowicz, Journal of Achievements in Materials and Manufacturing Engineering, 29 (**2008**) 2, 123–136

[7] W. Ozgowicz, B. Grzegorczyk, Archives of Materials Science and Engineering, 39 (**2009**) 1, 5–12

[8] I. Malecki, J. Ranachowski, Acoustic emission: Sources, Methods Applications, PASCAL Publications, Warsaw 1994 (in Polish)

[9] Z. Ranachowski, Methods of measurement and analysis of acoustic emission signal, Institute of Fundamental Technological Research Polish Academy of Sciences, Warsaw, 1997 (in Polish)

[10] A. Pawelek, J. Kusnierz, Z. Ranachowski, Z. Jasienski, Archives of Acoustics, 31 (**2006**), 102–122

[11] J. Zdunek, J. Płowieć, J. Mizera, W. Spychalski, K. J. Kurzydłowski, Inżynieria Materiałowa, 3 (**2010**), 577–581

[12] J. M. Arimi, E. Duggan, M. O'Sullivan, J. G. Lyng, E. D. O'Riordan, Journal of Texture Studies, 41 (**2010**), 320–340, doi:10.1111/j.1745-4603.2010.00224.x

[13] J. S. Chen, C. Karlsson, M. Povey, Journal of Texture Studies, 36 (**2005**), 139–156, doi:10.1111/j.1745-4603.2005.00008.x

[14] S. Kudela, A. Pawełek, Z. Ranachowski, A. Piątkowski, Metallic Materials, 49 (**2011**), 271–277, doi:10.4149/km_2011_4_271

[15] A. Pawelek, J. Kusnierz, Z. Ranachowski, Z. Jasienski, J. Bogucka, Archives of Metallurgy and Materials, 54 (**2009**), 83–88

[16] B. J. Brindley, P. J. Worthington, Scripta Metallurgica, 4 (**1970**) 4, 295–297, doi:10.1016/0036-9748(70)90124-9

[17] P. Rodriguez, Material Science, 6 (**1984**), 653–663, doi:10.1007/BF02743993

[18] A. H. Cottrell, Philosophical Magazine, 44 (**1953**), 829–832, doi:10.1080/14786440808520347

[19] P. G. McCormick, Acta Metallurgica, 22 (**1974**) 4, 489–493, doi:10.1016/0001-6160(74)90102-3

[20] A. Van den Beukel, Phys. Stat. Sol. (a), 30 (**1975**) 1, 197–206, doi:10.1002/pssa.2210300120

[21] A. Pawelek, Dislocation aspects of acoustic emission in plastic deformation processes of metals, Aleksander Krupkowski Institute of Metallurgy and Materials Science, Polish Academy of Sciences, Ed. OREKOP s.c., Cracow, 2006, 1–136 (in Polish)

UDK 669.71:620.17:532.6
Original scientific article/Izvirni znanstveni članek

ISSN 1580-2949
MTAEC9, 49(2)203(2015)

DETERMINATION OF ELASTIC-PLASTIC PROPERTIES OF ALPORAS FOAM AT THE CELL-WALL LEVEL USING MICROSCALE-CANTILEVER BENDING TESTS

DOLOČANJE ELASTIČNIH IN PLASTIČNIH LASTNOSTI PENE ALPORAS NA RAVNI CELIČNE STENE Z UPOGIBNIMI PREIZKUSI Z MIKROSKOPSKO IGLO

Tomáš Doktor, Daniel Kytýř, Petr Koudelka, Petr Zlámal, Tomáš Fíla, Ondřej Jiroušek

Institute of Theoretical and Applied Mechanics, Academy of Sciences of the Czech Republic, Prosecká 76, 190 00 Prague, Czech Republic
doktor@itam.cas.cz

Prejem rokopisa – received: 2013-10-01; sprejem za objavo – accepted for publication: 2014-05-06

doi:10.17222/mit.2013.207

The presented paper is focused on determining the mechanical properties of the Alporas closed-cell aluminium foam. To utilise the favourable properties of cellular metals (e.g., high strength-weight ratio, energy absorption or insulation capabilities) a detailed description of the mechanical properties is required. Cellular metals exhibit heterogeneity at several scale levels. The contribution of the internal structure to the overall mechanical properties may not be in detail evaluated utilizing only the macroscopic testing. On the other hand, the compact material of cell walls is influenced by its composition (titanium- and calcium-rich regions are present in aluminium). Therefore, localised testing techniques with a small region of interest (e.g., indentation methods) may neglect the inhomogeneity along the cell walls. Hence, a testing of isolated cell walls was performed. A custom-developed modular loading device (based on precise linear bearing stages) was assembled to enable cantilever bending tests. The load was applied with a stepper motor and the loading force was measured with a micro-scale load cell with a loading capacity of 2.25 N. Displacements of the samples were measured optically. Several points along the longitudinal axis of a sample were tracked using the Lucas-Kanade tracking algorithm and the obtained displacements were compared to the analytically prescribed deflection curve. Based on the obtained deflections and measured forces, a stress-strain diagram was constructed and the constants of the elastic-plastic material model were evaluated.

Keywords: aluminium foam, cantilever bending, micromechanics, optical strain measurement

Članek obravnava določanje mehanskih lastnosti aluminijaste pene Alporas z zaprtimi porami. Za uporabo ugodnih lastnosti celičnih kovinskih materialov (npr. visoko razmerje med trdnostjo in maso, absorpcija energije ali izolacijske zmožnosti), je potrebeno poznati mehanske lastnosti. Celični materiali kažejo heterogenost, če jih opazujemo pri različnih merilih velikosti. Podrobna ocena notranje zgradbe in njen prispevek k mehanskim lastnostim ni mogoč zgolj z uporabo makroskopskega preizkušanja. Po drugi strani pa zgradba vpliva na kompakten material celičnih sten (v aluminiju je mogoče najti področja, ki so bogata s titanom in kalcijem). Zato je mogoče, da preveč lokalizirano preizkušanje (npr. metoda za določanje trdote) zanemari nehomogena področja na stenah celic. Zato je bilo izvršeno preizkušanje posamezne celične stene. Sestavljena je bila modularna obremenitvena naprava, ki omogoča natančne stopnje linearne obremenitve, da so mogoči upogibni preizkusi z mikroskopsko iglo. Vzorec je bil obremenjen s koračnim motorjem, pri čemer je bila sila obremenitve izmerjena z mikroskopsko merilno celico z nosilnostjo 2,25 N. Premik vzorcev je bil izmerjen optično. Nekaj točk ob vzdolžni osi vzorca je bilo spremljano s sledilnim algoritmom Lucas-Kanade, ugotovljeni premiki pa so bili primerjani z analitično določeno krivuljo deformacije. Na podlagi ugotovljenih deformacij in izmerjenih sil je bil postavljen diagram odvisnosti med obremenitvijo in deformacijo. Ocenjene so bile konstante elastično-plastičnega modela materiala.

Ključne besede: aluminijska pena, upogibanje igle, mikromehanika, optično merjenje deformacije

1 INTRODUCTION

Aluminum foams are lightweight materials with a favourable combination of mechanical properties, e. g., a high strength-to-weight ratio. This material, widely used in damping applications as an impact-energy absorbent and as a thermal or acoustic insulation, was studied in detail at the macroscopic level[1,2]. Moreover, models for predicting the macroscopic deformation behaviour were developed[3].

To enable the exploitation of the favourable properties of aluminium foams for structural applications, a detailed description of their deformation behaviour is required. Due to complex inner structures of closed-cell foams, exhibiting a significant inhomogeneity at the cellular level[4] (in terms of the size and shape of the cells as well as the thickness of cell walls), an analysis of the deformation response of a cellular structure requires a complex mathematical description and modelling. The numerical models of metal foams have to reflect both the geometry of the cellular structure and the mechanical properties of the base material.

Since the cell-wall material contains residuals of the foaming agents (calcium and titanium) and micropores are present after the foaming process, the mechanical properties should not be measured solely with direct localized measurement techniques (e.g., the nanoindentation where the measured properties have to be processed with a homogenization procedure[5]).

To provide a more complex description of the foam's deformation response a microstructural numerical model of a representative volume element was developed in our recent study based on X-ray imaging and tomographic reconstruction[6]. However, the parameters of the constitutive material model that was necessary in the finite-element simulation have to take into consideration also the material properties at the level of cell walls.

In this study, a micromechanical testing methodology was employed to determine the mechanical properties of the base material of the Alporas aluminium foam. A cantilever arrangement of the loading test was used to ensure a simple description of the boundary conditions for both analytical and numerical evaluations of the experiments.

2 MATERIALS AND METHODS

2.1 Specimen preparation

The specimens were prepared from the Alporas closed-cell aluminium foam (Shinko Wire, Inc, Japan). Flat cell walls were identified in the cellular structure. The cells containing such walls were carefully extracted using a hand-operated micro-lathe (Dremel FortiFlex, Bosch GmbH, Germany). To protect the base cell-wall material against a plastic deformation the specimens were embedded into rosin (with a high purity and transparency and a melting point not exceeding 80 °C) during every distinct step of the preparation procedure. A specimen's shape was finalized by precise grinding and polishing using an oscillation grinding machine, TegraPol (Struers, A/S, Denmark).

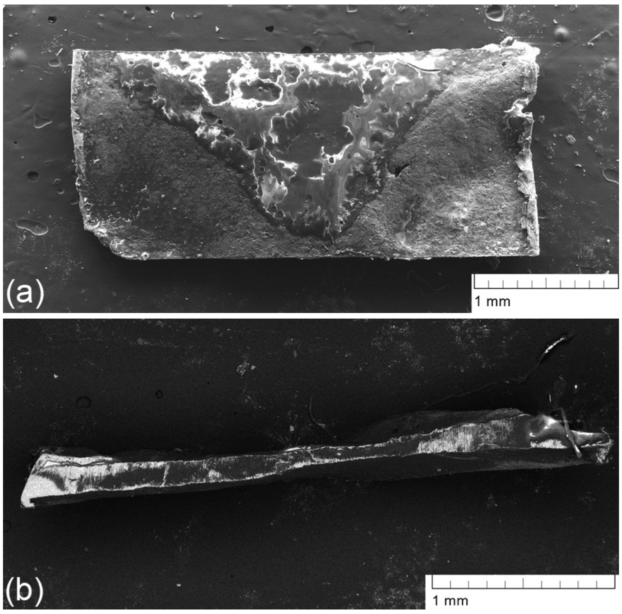

Figure 1: a) Specimen extracted from the cellular structure of Alporas aluminium foam, b) cross-section (SEM)

Slika 1: a) Vzorec, izrezan iz celične stene aluminijske pene Alporas, b) prečni prerez (SEM)

2.2 Sample-volume description

To determine the geometrical characteristics required for evaluating the bending tests (i.e., the distance between the clamp and the loading point and the cross-sectional characteristics) a set of projections of each specimen was acquired with a scanning electron microscope (SEM) (Mira II, Tescan, s. r. o., Czech Republic). Since the specimens had a metallic nature, the secondary electron probe was employed for the scanning. The obtained projections provided a resolution of 2 μm per pixel. For each specimen three projections were acquired, a floor plan (normal to the loading direction, **Figure 1a**) and two longitudinal faces (parallel to the in-plane loading, **Figure 1b**). A volumetric model of each specimen was developed using a custom-assembled image-processing procedure developed in the language of computational environment MatLab (Mathworks, Inc., USA).

2.3 Experimental set-up

For the loading test an in-house loading set-up was designed and assembled. The set-up was based on linear bearing stages (Standa Ltd, Lithuania) with a resolution of 1 μm and a travel range of up to 50 mm. The motion of the loading point was provided with a precise linear bearing stage, UMR 9.0 (Newport, Ltd, USA) with a resolution of 0.1 μm and a travel range of 5 mm, which was driven by a stepper motor (Microcon, s. r. o., Czech Republic). The reaction force at the loading point was measured with a miniature load cell in the cantilever arrangement (FPB350, Futek Inc., USA) with a loading capacity of 2.25 N and a read-out unit, OM911 (Orbit Merret, s. r. o., Czech Republic) with a sampling rate of

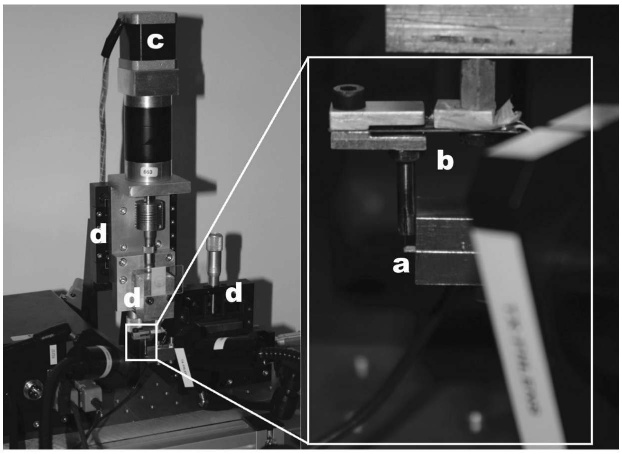

Figure 2: Experimental set-up for micro-scale loading tests: a) specimen, b) load cell, c) stepper motor, d) linear bearing stages

Slika 2: Eksperimentalni sestav za preizkuse obremenitve na mikroskopski ravni: a) vzorec, b) merilna celica, c) koračni motor, d) nastavljanje linearnih obremenitev

100 Hz. A detailed description of the loading set-up is depicted in **Figure 2**.

2.4 Loading procedure

The loading was performed in the cantilever arrangement in order to overcome the issues of low stiffness of the supports and the eccentricity of the loading point that occurred during our previous studies where the three-point bending arrangement was used. The clamp was implemented by placing a specimen between two prisms connected together with a pair of screws (**Figure 2**).

The loading tests were displacement controlled. The synchronization of the loading and force logs was ensured with the custom software based on an open-source LinuxCNC project and real-time Linux kernel. The loading rate was set to 1 μm s^{-1}.

2.5 Strain measurement

Due to a high compliance of the load cell (even higher than the deflection of the loaded point of a specimen) the strain could not be determined directly from the displacement prescribed by the linear bearing stage. Instead, the displacements were measured optically from a set of projections of the loading scene captured with a CCD camera (Manta G504B, Allied Vision Technologies, GmbH, Germany) with a resolution of 2452 px × 2056 px attached to a light microscope (Navitar Imaging, Inc., USA) that provided a magnification of up to 24×. The acquisition of the projections was controlled by in-house-built software based on the OpenCV[7] (Open Source Computer Vision) library and Python programming language. The acquisition rate of the camera was 2 fps, which enabled an identification of a sufficient number of points on the force-displacement curve. A selected loading scene is depicted in **Figure 3**.

2.6 Strain-stress curve evaluation

From the sets of projections, displacements were determined using a digital-image-correlation (DIC) software tool[8] based on the Lucas-Kanade tracking algorithm[9]. The points on the specimens' surfaces were selected along their longitudinal axes and the displacements of each point were tracked by searching for the highest correlation coefficient between the two consequent projections.

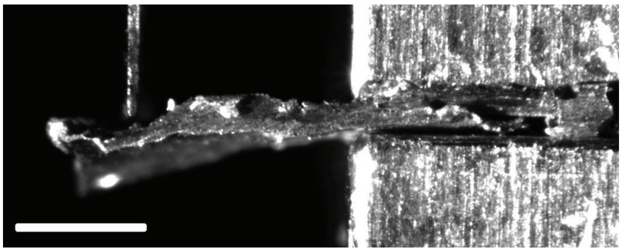

Figure 3: Loading scene of a clamped specimen (image acquired with a CCD camera and light microscope, the bar corresponds to 1 mm)
Slika 3: Obremenjen vzorec (posnetek narejen s CCD-kamero, dolžina traku ustreza 1 mm)

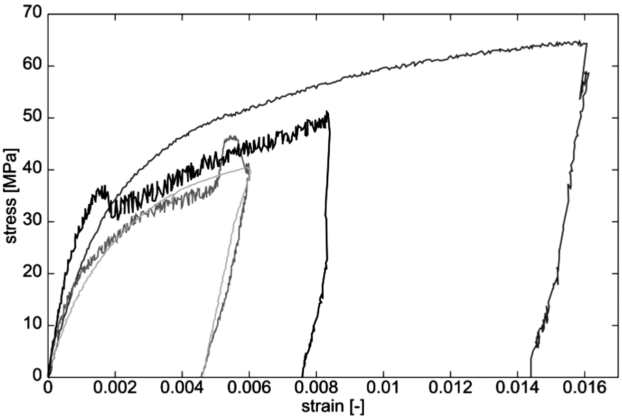

Figure 4: Stress-strain curves of the tested specimens
Slika 4: Krivulje napetost – raztezek preizkušanih vzorcev

The engineering stress (σ) and strain (ε) values were determined from the geometrical properties of a tested specimen and optically measured displacements of the loading point using Equations (1) and (2):

$$\varepsilon = \frac{3uh}{2l^2} \tag{1}$$

$$\sigma = \frac{Flh}{2I_Z} \tag{2}$$

Here u denotes the displacement of the loading tip, h is the height of a specimen, F is the loading force, l is the distance between the clamp and the loading point and I_Z is the axial quadratic moment of inertia of the loaded cross-section. From the slope of the unloading phase, the Young's modulus was determined and the yield point was estimated using the offset method at a 0.2 % strain level.

3 RESULTS AND DISCUSSION

Deformation behaviour of the isolated cell walls was described using micro-scale cantilever measurements. The obtained stress-strain curves are presented in **Figure 4** (selected curves only). The curves exhibit similar slopes in their initial parts as well as in their unloading phases. Different portions of the plastic strain are caused by the non-uniformity in the specimens' dimensions due to a highly irregular geometrical arrangement of the cellular structure. The obtained values of the Young's modulus are (36.7 ± 5.23) GPa, the yield stress reached (39.0 ± 9.7) MPa and the yield strain reached (0.279 ± 0.044) %.

4 CONCLUSIONS

Based on a series of the cantilever bending tests of the isolated cell walls of the Alporas aluminium foam elastic and plastic mechanical properties were determined. The obtained results scatter slightly among the measured sets, which might be caused by a highly irregular nature of the tested material in terms of its geometrical arrangement. This issue may be overcome using an inverse numerical evaluation of the measured results in conjunction with the precise geometrical models obtained with the X-ray tomography.

The obtained results may serve as the parameters for the constitutive material models for microstructural numerical models. The conjunction of the material properties of the foam's base material and the microstructural models (e. g., developed by X-ray computed micro-tomography) will provide a more detailed description of the mechanical behaviour of the metal foam.

Acknowledgements

The authors would like to express their gratitude to the Czech Science Foundation (research project No. P105/12/0824). The institutional support of RVO: 68378297 is also gratefully acknowledged for the financial support of this research. We were delighted to cooperate with MDDr. Eva Kamenická, an excellent operator of the micro-lathe.

5 REFERENCES

[1] R. Pippan, Deformation behaviour of closed-cell aluminium foams in tension, Acta Materialia, 49 (**2001**), 2463–2470, doi:10.1016/S1359-6454(01)00152-5

[2] M. I. Idris, T. Vodenitcharova, M. Hoffman, Mechanical behaviour and energy absorption of closed-cell aluminium foam panels in uniaxial compression, Materials Science and Engineering A, 517 (**2009**) 1–2, 37–45, doi:10.1016/j.msea.2009.03.067

[3] Y. Mu, G. Yao, L. Liang, H. Luo, G. Zu, Scripta Materialia, 63 (**2010**), 629–632, doi:10.1016/j.scriptamat.2010.05.041

[4] V. Králík, J. Němeček, Two-scale model for prediction of macroscopic elastic properties of aluminium foam, Chemicke Listy, 106 (**2012**) 3, 458–461

[5] J. Němeček, P. Zlámal, V. Králík, J. Němečková, Modeling Inelastic Properties of Metal Foam Based on Results from Nanoindentation, 14th Int. Conf. on Civil, Struct. & Env. Eng. Comp., Cagliari, 2013, 103

[6] O. Jiroušek, T. Doktor, D. Kytýř, P. Zlámal, T. Fíla, P. Koudelka, I. Jandejsek, D. Vavřík, X-ray and finite element analysis of deformation response of closed-cell metal foam subjected to compressive loading, Journal of Instrumentation, 8 (**2013**), C02012, doi:10.1088/1748-0221/8/02/C02012

[7] G. Bradski, The OpenCV Library, Dr. Dobb's Journal of Software Tools [online] (**2000**), article id 2236121, [posted 2008-01-15 19:21:54], Available from World Wide Web: http://www.drdobbs.com/open-source/the-opencv-library/184404319

[8] I. Jandejsek, J. Valach, D. Vavrik, Optimization and Calibration of Digital Image Correlation Method, Proceedings of Experimental Stress Analysis 2010, Velke Losiny, Czech Republic, 2010, 121–126

[9] B. D. Lucas, T. Kanade, An Iterative Image Registration Technique with an Application to Stereo Vision, Proceedings of Imaging Understanding Workshop, Vancouver, 1981, 121–130

UDK 544.6:57:669.295
Original scientific article/Izvirni znanstveni članek

ISSN 1580-2949
MTAEC9, 49(2)207(2015)

ELECTROCHEMICAL BEHAVIOR OF BIOCOMPATIBLE ALLOYS

ELEKTROKEMIJSKO VEDENJE BIOKOMPATIBILNIH ZLITIN

Ivana Petrášová, Monika Losertová
VŠB-Technical University of Ostrava, Faculty of Metallurgy and Materials Engineering, Department of Non-Ferrous Metals, Rafining and Recycling, 17. listopadu 15/2172, 70833 Ostrava, Czech Republic
ivana.petrasova@vsb.cz

Prejem rokopisa – received: 2013-10-02; sprejem za objavo – accepted for publication: 2014-05-09

doi:10.17222/mit.2013.218

The electrochemical behavior of Ti6Al4V and Ti22Nb alloys was studied in a 0.15 M (0.9 %) physiological sodium chloride solution at room temperature (22 ± 1) °C. The experimental samples of the Ti6Al4V alloy were in different states of the thermomechanical treatment: as-received and hot rolled. The samples of Ti22Nb were studied in the as-cast, heat-treated and aged stages. The microstructural features of the Ti6Al4V alloy in three different states influenced not only the passivation but also the rate of corrosion that was (0.12, 0.07 and 0.10) mm per year for the equiaxed ($\alpha + \beta$), acicular α in the transformed β grains and coarse lamellar ($\alpha + \beta$) phases, respectively. The as-cast TiNb sample with a dendritic microstructure and very fine martensite showed the lowest corrosion rate of 0.26 mm per year unlike the specimens after the heat treatment and aging with the rate of 0.34 mm and 0.33 mm per year, respectively.

Keywords: Ti6Al4V, Ti22Nb, electrochemical behavior

Preučevano je bilo elektrokemijsko vedenje zlitin Ti6Al4V in Ti22Nb v fiziološki raztopini natrijevega klorida 0,15 M (0,9 %) pri sobni temperaturi (22 ± 1) °C. Vzorci zlitine Ti6Al4V za preizkuse so bili v različnih termomehanskih stanjih: v dobavljenem stanju in vroče valjani. Vzorci Ti22Nb so bili v litem stanju, toplotno obdelani in starani. Razlike v mikrostrukturi zlitine Ti6Al4V v treh različnih stanjih vplivajo na pasivacijo in na hitrost korozije, ki je bila (0,12, 0,07 in 0,10) mm na leto pri enakoosnih ($\alpha + \beta$), igličastih α- in transformiranih β-zrnih ter grobo lamelarnih fazah ($\alpha + \beta$). Vzorci TiNb z dendritno mikrostrukturo in drobnim martenzitom so pokazali najmanjšo hitrost korozije 0,26 mm na leto, v primerjavi z vzorci po toplotni obdelavi in staranju pa z 0,34 mm in 0,33 mm na leto.

Ključne besede: Ti6Al4V, Ti22Nb, elektrokemijsko vedenje

1 INTRODUCTION

The 316L stainless steel, cobalt-chromium alloys and Ti-alloys are three important classes of the most used metallic biomaterials, especially for orthopedic implants, even in highly loaded areas such as artificial joints[1,2]. Nowadays, titanium and its alloys are the most attractive biomaterials for orthopedic implants and other devices for dental applications due to their relatively good fatigue resistance, excellent biocompatibility, better corrosion resistance in body fluids and lower elasticity modulus compared to the other metallic biomaterials[1,3]. Pure titanium and ($\alpha + \beta$) Ti-alloys were originally used as structural materials, especially for aerospace structures, and only afterwards they were adopted for biomedical applications. In the recent decades, many titanium alloys have been developed. The Ti6Al4V became the standard alloy and it was the first titanium alloy used as a biomaterial[1].

Recently, the development of β titanium alloys has drawn considerable attention in the biomedical area for their much lower Young's modulus compared to the α (105 GPa for pure Ti)[4] or ($\alpha + \beta$) Ti alloys (110 GPa for Ti6Al4V)[4], thus exhibiting a better biomechanical compatibility. A large modulus mismatch between a metallic implant and the adjacent bone (the Young's modulus of the human bone is 10–30 GPa) will cause the stress-shielding effect, leading to an excessive bone resorption and implant loosening[4].

Recently developed β alloys based on TiNb showing superelasticity[5] have a high potential to serve as alternatives for the NiTi shape-memory alloys in biomedical applications. The reason for the substitution of Ni with Nb is a very good cytocompatibility of Nb as indicated in the studies in vitro and in vivo[6]. The corrosion resistance of the TiNb alloys has also been shown to be similar or superior to that of Ti alone. Despite the potential benefits of the TiNb alloys, their development for biomedical applications is still at the beginning[7].

The aim of the presented work is to compare the microstructure effects on the electrochemical behavior of two titanium alloys with different thermal and mechanical treatments. The electrochemical experiments were performed on Ti6Al4V and TiNb with amount fraction x = 22 % Nb (Ti22Nb) in the NaCl solution.

Most of the recent works focused on the biocompatible titanium alloys in different stages of the microstructure deal with the mechanical behavior[8]. The effects of the microstructure on the corrosion properties of titanium alloys have not been studied extensively[9].

2 EXPERIMENTAL

The study of electrochemical behavior was performed on two titanium alloys in various states of the thermal and thermomechanical processing.

The Ti6Al4V alloy with the composition given in **Table 1** was studied in three microstructure stages: in the as-received stage and after being rolled above the β transus at two diverse temperatures of 900 °C or 1100 °C. The Ti22Nb alloy was tested in following states: in the as-cast state, after being solution annealed at 900 °C for 1 h and water quenched or after being solution annealed at 900 °C for 1 h, aged at 400 °C for 1 h and water quenched[10]. The denotation of the specimens in relation to the treatment is listed in **Table 2**.

Table 1: Chemical composition of the studied Ti6Al4V alloy in mass fractions, *w*/%

Tabela 1: Kemijska sestava uporabljene zlitine Ti6Al4V v masnih deležih, *w*/%

Al	V	C	Fe	H	O	N	Y	O + N
5.50–6.75	3.50–4.50	max. 0.08	max. 0.30	max. 0.0125	max. 0.20	max. 0.05	max. 0.005	max. 0.25

Table 2: Denotation of experimental specimens

Tabela 2: Oznake vzorcev

Stage/alloy	as-recived	rolled at 900 °C	rolled at 1100 °C
Ti6Al4V	A	B	C
Stage/alloy	as-cast	solution annealed	aged
Ti22Nb	D	E	F

For light microscopy the specimen were prepared with the standard metallographic techniques involving grinding, mechanical polishing and etching in Kroll's reagent containing HF, HNO_3 and distilled water (8 : 15 : 77). The microstructures were observed in the etched state using a light microscope GX51.

Electrochemical studies were carried out using linear polarization at room temperature (22 ± 1) °C. The corrosion tests were performed using an Autolab PGSTAT 128n apparatus and a personal computer with software Nova 1.7. The electrochemical measurements were performed using a three-electrode cell containing a working electrode (a specimen) with the exposed area of $\approx$ 16 mm^2 or $\approx$ 10 mm^2, an Ag/AgCl (SSC) electrode in saturated KCl as the reference electrode and a platinum mesh as the counter electrode. A solution of 0.15 M (0.9 %) NaCl was used as the electrolyte. The specimens were grinded before the tests with the wheel paper of up to 1000 mesh and then polarized from –2 V to +1.5 V with a scan rate of 2 mV/s. The scan rate was selected according to[11].

3 RESULTS AND DISCUSSION

The microstructures of the electrochemically tested specimens are shown on the micrographs in **Figures 1** and **2**. The fine-grained microstructure of the Ti6Al4V alloy presented in **Figure 1a** consisted of equiaxed α grains (light) in the transformed β matrix (dark) containing coarse acicular α. After the hot rolling at 900 °C, the coarse β grains transformed into fine acicular α, as shown in **Figure 1b**. **Figure 1c** shows coarse lamellar α at the prior β-grain boundaries, β grains with fine α precipitates in the centre of the specimen and coarse plate-like α at the surface of the specimen after the hot rolling at 1100 °C.

The as-cast dendritic microstructure of the Ti22Nb alloy was formed of (α + β) and very fine martensite needles, as presented in **Figure 2a**. In spite of the annealing at 900 °C for one hour in argon, the dendritic structure remained conserved and the water quenching from 900 °C (above the β transus) retained the β phase

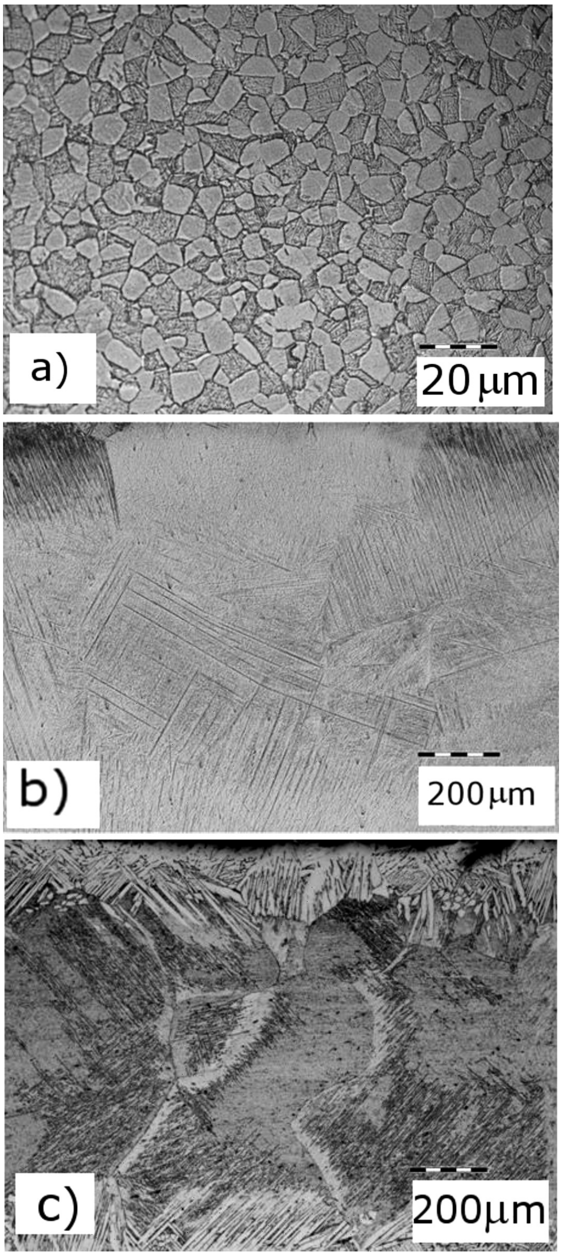

Figure 1: Light micrographs of Ti6Al4V: a) as-received (A), b) after hot rolling at 900 °C (B), c) after hot rolling at 1100 °C (C)

Slika 1: Mikrostruktura Ti6Al4V: a) dobavljeno stanje (A), b) po vročem valjanju na 900 °C (B), c) po vročem valjanju na 1100 °C (C)

Table 3: Values of the corrosion parameters determined with the Tafel plot analysis for Ti6Al4V and Ti22Nb alloys in 0.15 M NaCl solution
Tabela 3: Korozijski parametri, določeni s Taflovo analizo za zlitini Ti6Al4V in Ti22Nb v 0,15 M raztopini NaCl

Alloy State of treatment	Ti6Al4V A	Ti6Al4V B	Ti6Al4V C	Ti22Nb D	Ti22Nb E	Ti22Nb F
$j_{\mathrm{corr}}/(\mu\mathrm{A/cm^2})$	7.23	4.03	6.19	14.86	20.53	20.35
$E_{\mathrm{corr}}/\mathrm{V}$	–0.467	–0.444	–0.361	–0.330	–0.536	–0.545
$R_{\mathrm{p}}/\mathrm{k\Omega}$	11.03	27.32	23.80	9.80	14.60	13.60

that transformed into martensite at lower temperatures[10]. Indeed, very fine martensite needles were observed in the annealed and quenched microstructure at a high magnification of light microscopy, as shown in **Figure 2b**. After the aging at 400 °C and water quenching the dendritic microstructure was formed of the (α + β) phases (**Figure 2c**). No martensite was observed.

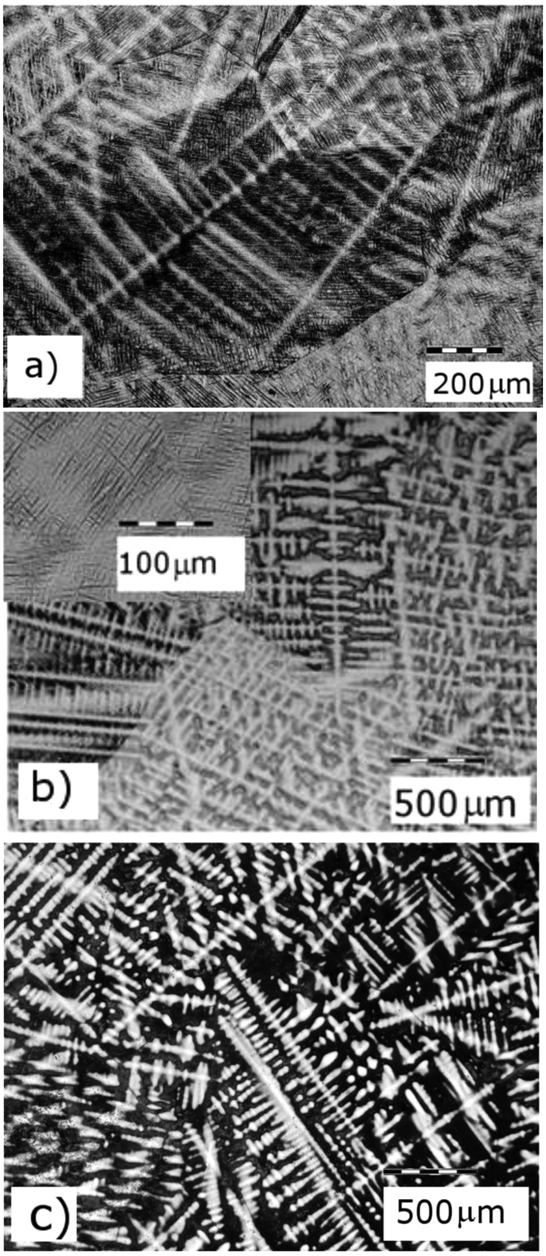

Figure 2: Light micrographs of Ti22Nb: a) as-cast (D), b) after solution annealing (E), c) after solution annealing and aging (F)
Slika 2: Mikrostruktura Ti22Nb: a) lito stanje (D), b) po raztopnem žarjenju (E), c) po raztopnem žarjenju in staranju (F)

The linear-polarization results for the Ti6Al4V and Ti22Nb alloys in the 0.15 M NaCl solution are shown in **Figures 3** and **4**. The polarization parameters, including the corrosion potential (E_{corr}), the corrosion current density (j_{corr}) and the polarization resistence (R_{p}) obtained using the Tafel extrapolation method, are listed in **Table 3**.

Comparing the linear polarization curves of the three specimens of the Ti6Al4V alloy shown in **Figure 3**, it can be seen that there are no significant diferences between the cathodic polarization curves. The nature of the anodic polarization curve for specimen C (**Figure 3**, curve C) indicates an almost stable passive behavior over the entire potential range. The corrosion potential (E_{corr}) estimated from the Tafel region is –0.361 V (SSC). The passive current first continuously increases with the potential, but at around 0 V a slight decrease is observed; then, from about 0.5 V the passive current slightly increases with the higher potentials. The E_{corr} of samples

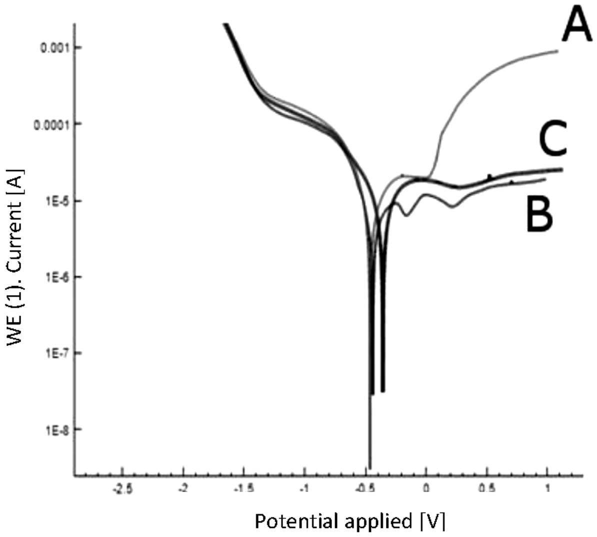

Figure 3: Linear polarization curves obtained in the 0.15 M NaCl solution at room temperature for different Ti6Al4V stages: A – as-received, B – after hot rolling at 900 °C, C – after hot rolling at 1100 °C
Slika 3: Linearne polarizacijske krivulje, dobljene v 0,15 M raztopini NaCl pri sobni temperaturi za Ti6Al4V, za stanja: A – dobavljeno stanje, B – po vročem valjanju na 900 °C, C – po vročem valjanju na 1100 °C

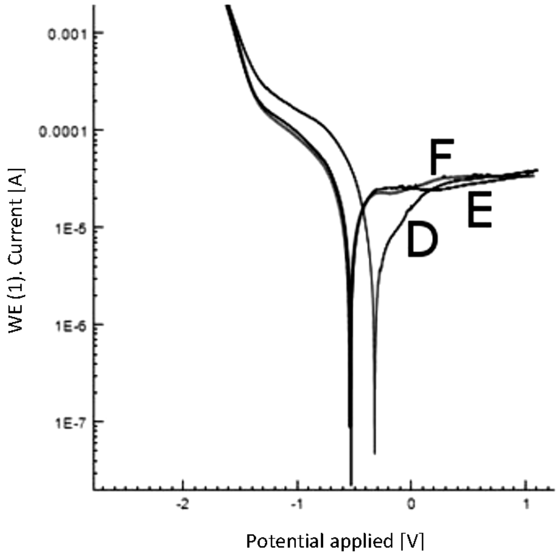

Figure 4: Linear polarization curves obtained in the 0.15 M NaCl solution at room temperature for different Ti22Nb stages: D – as-cast, E – after solution annealing at 900 °C, F – after aging at 400 °C

Slika 4: Linearne polarizacijske krivulje, dobljene v 0,15 M raztopini NaCl pri sobni temperaturi za Ti22Nb, za stanja: D – lito stanje, E – po raztopnem žarjenju na 900 °C, F – po staranju na 400 °C

A and B (curves A, B, **Figure 3**) shifts to more negative values than in the case of specimen C. For specimen A, the passive film is broken down at more positive potentials than for sample B and then the current sharply increases (**Figure 3**, curve A). Specimen B (**Figure 3**, curve B) shows several active-passive transitions followed by the passivation domain at the higher potentials. This behavior may be related to the effect of the presence of the fine acicular α phase in the microstructure that can act as effective galvanic couples leading to a higher rate of corrosion[12]. Indeed, the microstructural features of all three states influenced not only the passivation but also the rate of corrosion that was (0.12, 0.07 and 0.10) mm per year for the equiaxed (α + β) (A), acicular α in the transformed β grains (B) and coarse lamellar (α + β) (C), respectively.

The samples of the Ti22Nb alloy showed quite similar polarization behaviors with the increasing potential. The as-cast specimen of Ti22Nb (**Figure 4**, curve D) exhibited a corrosion potential E_{corr} of –0.324 V (SSC), which was slightly more noble than the corrosion potentials observed for samples E (–0.499 V (SSC)) and F (–0.537 V (SSC)). The polarization behavior can be regarded as stable passivity. Comparing the microstructural features of the three specimens, it can be concluded that the more β is retained, the higher stability of the passivation region can be expected. Sample D having a dendritic microstructure with very fine martensite had the lowest corrosion rate (0.26 mm per year), unlike specimens E and F after the heat treatment (0.34 mm and 0.33 mm per year, respectively).

The electrochemical behaviors of both alloys in the 0.15 M NaCl solution are dissimilar, as seen in **Figures 3** and **4**. For the Ti6Al4V alloy, a passive region followed by a breakdown and repassivation was observed on the anodic polarization diagrams in all three cases. On the contrary, the Ti22Nb alloy showed a relatively stable passivation region over the entire potential range. However, the corrosion rate for Ti22Nb was about three times higher. No visible surface changes were observed on any specimens after the anodic polarization.

4 CONCLUSION

Based on the experimental results it can be concluded that the corrosion resistance of titanium alloys is determined not only by the alloy composition but also by the microstructure formed after different thermal or thermomechanical treatments.

The electrochemical behavior of the Ti6Al4V and Ti22Nb alloys was studied in the 0.15 M (0.9 %) physiological NaCl solution at room temperature. The experimental samples of the Ti6Al4V alloy were tested in different states of the thermomechanical treatment: the as-received state with the (α + β) microstructure and after being hot rolled at 900 °C and 1100 °C with a fine acicular α phase and a coarse lamellar (α + β) phase, respectively. The samples of Ti22Nb were studied in the following stages: the as-cast stage with very fine martensite needles in the dendritic (α + β) microstructure, the stage after being heat treated at 900 °C or quenched, having martensite needles in the retained β phase and after being aged at 400 °C, having a dendritic (α + β) microstructure. With respect to the corrosion related to the microstructural features, Ti6Al4V in all three investigated stages displayed lower values of the corrosion rate than measured for the Ti22Nb alloys.

Nevertheless, the samples of the Ti22Nb alloys showed a more stable passivation behavior than the Ti6Al4V alloy. No visible surface changes were observed on any specimens after the anodic polarization.

Acknowledgments

The experimental work was performed with the support of projects No. TA03010804 financed by the Technology Agency of the Czech Republic, No. CZ.1.05/2.1.00/01.0040 "Regional Materials Science and Technology Centre" within the frame of the operational program "Research and Development for Innovations" financed by the Structural Funds and from the state budget of the Czech Republic, and the Grant of SGS, No. SP2013/64 – "Specific research in metallurgy, material and processing engineering" financed by VŠB – Technical University of Ostrava, Czech Republic.

5 REFERENCES

[1] T. C. Niemeyer, C. R. Grandini, L. M. C. Pinto, A. C. D. Angelo, S. G. Schneider, Journal of Alloys and Compounds, 476 (**2009**) 1–2, 172–175, doi:10.1016/j.jallcom.2008.09.026

[2] H. Zohdi, H. R. Shahverdi, S. M. M. Hadavi, Electrochemistry Communications, 13 (**2011**) 8, 840–843, doi:10.1016/j.elecom.2011.05.017

[3] Y. J. Bai, Y. B. Wang, Y. Cheng, F. Deng, Y. F. Zheng, S. C. Wei, Materials Science and Engineering C, 31 (**2011**) 3, 702–711, doi:10.1016/j.msec.2010.12.010

[4] F. X. Xie, X. B. He, S. L. Cao, X. Lu, X. H. Qu, Corrosion Science, 67 (**2013**), 217–224, doi:10.1016/j.corsci.2012.10.036

[5] H. Y. Kim, Y. Ikehara, J. I. Kim, H. Hosoda, S. Miyazaki, Acta Materialia, 54 (**2006**) 9, 2419–2429, doi:10.1016/j.actamat.2006.01.019

[6] H. Matsuno, A. Yokoyama, F. Watari, M. Uo, T. Kawasaki, Biomaterials, 22 (**2001**) 11, 1253–1262, doi:10.1016/S0142-9612(00)00275-1

[7] R. E. McMahon, J. Ma, S. V. Verkhoturov, D. Munoz-Pinto, I. Karaman, F. Rubitschek, H. J. Maier, M. S. Hahn, Acta Biomaterialia, 8 (**2012**) 7, 2863–2870, doi:10.1016/j.actbio.2012.03.034

[8] M. Niinomi, M. Nakai, J. Hieda, Acta Biomaterialia, 8 (**2012**) 11, 3888–3903, doi:10.1016/j.actbio.2012.06.037

[9] M. Atapour, A. Pilchak, G. S. Frankel, J. C. Williams, M. H. Fathi, M. Shamanian, Corrosion, 66 (**2010**) 6, 065004-1–065004-9, doi:10.5006/1.3452400

[10] P. Štěpán, M. Losertová, Proc. of the 21st International Conference on Metallurgy and Materials, Metal 2012, Brno, 2012, 1581

[11] S. Barril, S. Mischler, D. Landolt, Wear, 259 (**2005**) 1–6, 282–291, doi:10.1016/j.wear.2004.12.012

[12] F. Karimzadeh, M. Heidarbeigy, A. Saatchi, Journal of Materials Processing Technology, 206 (**2008**) 1–3, 388–394, doi:10.1016/j.jmatprotec.2007.12.065

UDK 621.777:669.295
Original scientific article/Izvirni znanstveni članek

ISSN 1580-2949
MTAEC9, 49(2)213(2015)

PREPARATION AND THERMAL STABILITY OF ULTRA-FINE AND NANO-GRAINED COMMERCIALLY PURE TITANIUM WIRES USING CONFORM EQUIPMENT

PRIPRAVA KOMERCIALNE ULTRADROBNE IN NANOZRNATE Ti-ŽICE Z OPREMO CONFORM IN NJENA TERMIČNA STABILNOST

Tomáš Kubina[1], Jaromír Dlouhý[1], Michal Köver[1], Mária Dománková[2], Josef Hodek[1]
[1]COMTES FHT, Prumyslova 995, 334 41 Dobrany, Czech Republic
[2]Institute of Materials Science, Faculty of Materials Science and Technology in Trnava, STU in Bratislava, Bottova 25, 917 24 Trnava, Slovakia
tomas.kubina@comtesfht.cz

Prejem rokopisa – received: 2013-10-03; sprejem za objavo – accepted for publication: 2014-04-01

doi:10.17222/mit.2013.226

Processes based on severe plastic deformation (SPD) capable of producing microstructures with sizes of the order of nanometres are gaining increasing importance. One of the available ways to make production more efficient is to combine the CONFORM continuous extrusion process with the ECAP method. This paper describes our initial experience with this combined process in a CONFORM 315i machine, equipped with a specially designed die chamber. Trials were performed to explore the impact of the CONFORM equipment's settings on the microstructure of the Ti wire. The feedstock consisted of CP-Ti grade 2 bar with a diameter of 10 mm. The decisive parameter for the entire process, i.e., the die-chamber temperature, was varied and controlled. Specimens with grain sizes of 1.4 µm and 420 nm were obtained. Using these specimens, the temperatures at which the recovery processes began to take effect were determined by thermal analysis.

Keywords: CONFORM-ECAP, titanium wire, ultrafine microstructure, nanostructure, thermal stability

Postopki, ki temeljijo na veliki plastični deformaciji (SPD), pri katerih nastaja mikrostruktura z nanometrskimi dimenzijami, pridobivajo na pomenu. Ena od mogočih poti za bolj učinkovito proizvodnjo je kombinacija kontinuirnega postopka ekstruzije CONFORM in metode ECAP. Ta članek opisuje začetne izkušnje s tem kombiniranim postopkom z napravo CONFORM 315i, opremljeno s posebno oblikovano komoro. Preizkusi so bili opravljeni zato, da bi ugotovili vpliv nastavitve naprave CONFORM na mikrostrukturo Ti-žice. Vložek je bila palica CP-Titan 2 premera 10 mm. Spreminjana in kontrolirana je bila temperatura komore kot ključni parameter celotnega postopka. Dobljeni so bili vzorci z velikostjo zrn 1,4 µm in 420 nm. Pri teh vzorcih je bila s termično analizo določena temperatura, pri kateri se začne proces poprave.

Ključne besede: CONFORM-ECAP, žica iz titana, ultradrobna mikrostruktura, nanostruktura, termična stabilnost

1 INTRODUCTION

In the past 15 years, numerous SPD processes (Severe Plastic Deformation) have been developed. These processes are used for achieving grain refinement in materials, typically to a grain size between 100 nm and 400 nm. Their efficiency in processing a large volume of material is, however, still insufficient for industrial-scale applications. This drawback has now been overcome by the CONFORM method, which is known for a long time and is used for the continuous, industrial-scale production of sections, mostly from aluminium. By merging two processes, where the feedstock is forced through a die by the friction force of a wheel, ECAP becomes a continuous process[1,2]. The first results of limited-scope process experiments conducted by COMTES FHT were presented in[3]. The ultrafine titanium obtained was annealed isothermally to explore the growth of the mean grain size. In this case, the grain-growth kinetics can be described as grain coarsening from the very beginning of the annealing process. The isothermal grain coarsening is described with the equation:

$$d^{1/n} - d_0^{1/n} = tK_0 \exp\left(-\frac{Q}{RT}\right) \qquad (1)$$

where d is the mean grain size at the annealing time t, T is the temperature, n is the time exponent, d_0 is the initial grain size, K_0 is a constant, R is the universal gas constant and Q is the grain-growth activation energy. Equation (1) was used for expressing the distorted grain-growth rate in CP-Ti in terms of the time exponent (n) and the activation energy (Q). The scatter in the measured mean grain size also caused problems in finding the activation energy Q. Its value was determined using graphical methods: 248 kJ mol^{-1} (at the mean $n = 0.19$)[4]. This value is substantially higher than the activation energy of Ti self-diffusion (169.1 kJ mol^{-1})[5] and the grain-growth activation energy in CP-Ti after eight ECAP passes (176 kJ mol^{-1})[6].

This paper expands the knowledge of the production of nanostructured titanium and describes its thermal stability by thermo-physical tests with a contrast to the stability of an ultrafine-grained variant.

2 EXPERIMENTAL

The feedstock consisted of CP-Ti grade 2 bar with a diameter of 10 mm. The chemical composition of the feedstock is shown in **Table 1**. It was measured using a Bruker Q4 Tasman optical emission spectrometer and a Bruker G8 Galileo gas analyser.

Table 1: Chemical composition of feedstock in mass fractions, *w*/%
Tabela 1: Kemijska sestava uporabljenega materiala v masnih deležih, *w*/%

Fe	O	C	H	N	Ti
0.046	0.12	0.023	0.0026	0.0076	99.822

Titanium bars were converted into an "endless" bar of the same diameter as the feedstock using the CONFORM 315i machine. The material's mechanical properties at room temperature were determined with cylindrical tensile test specimens with a gauge length of 25 mm and a diameter of 5 mm. In addition, V-notch impact tests were conducted using specimens with a 3 mm × 4 mm cross-section. Two processing experiments were conducted with different sets of extrusion parameters.

The microstructures of the specimens were observed in a JEOL JSM 7400 FEG scanning electron microscope with a field-emission gun and with a Nordlys (Oxford Instruments) EBSD (Electron Backscatter Diffraction) detector. The specimens for the EBSD analysis were prepared by ion polishing in a JEOL SM-09010 Cross Section Polisher. The EBSD observation conditions were as follows: 25 kV voltage, working distance of 15.5 mm, 500 point × 500 point lattice and a step size of 0.1 μm. The EBSD maps were displayed and edited using HKL Channel 5 software. The intercept grain size was assessed by measuring the lengths between points of intersection between grain boundaries and a square grid, according to the Czech Standard ČSN EN ISO 643.

For the purposes of observation in the transmission electron microscope (TEM), thin foils were prepared with final electrolytic thinning in a Tenupol 5 device, using a solution of 300 mL CH_3OH + 175 mL 2-butanol + 30 mL $HClO_4$ at –10 °C and a voltage of 40 V. The TEM analysis was performed in a JEOL 200CX instrument with an acceleration voltage of 200 kV. Selective electron diffraction was used for the determination of the phases.

The effect of deformation on the thermal expansion of titanium and the temperature range for recovery were explored using a Linseis L75 Platinum horizontal dilatometer with an Al_2O_3 specimen chamber and a pull bar. The temperature changes were monitored with a thermocouple on specimens of diameter 5 mm and lengths of approximately 20 mm. Nitrogen (N_2) was used as the protective gas. After heating to 950 °C at a rate of 3 K/min the specimen was cooled at 20 K/min to 600 °C. Then the specimen was left to cool in air to the ambient temperature. The recovery processes were monitored in a Linseis PT-1600 heat-flux calorimeter equipped with an S-type thermocouple. The measurement was conducted in Ar at a flow rate of 600 mL/min on specimens with a mass of approximately 41 mg, cut off from diameter bars 5 mm and placed in Al_2O_3 crucibles with lids.

3 MICROSTRUCTURE AFTER EXPERIMENTAL PROCESSING

The feedstock microstructure contained equiaxed grains with scarce twins (**Figure 1**). After the deformation it consisted of two types: recrystallized equiaxed grains and a small proportion (less than 15 %) of distorted grains divided into sub-grains by low-angle boundaries. The as-received and distorted microstructures exhibited an identical pronounced texture with (1000) planes aligned with the specimen axis. The experimental extrusion was based on varying the key parameters: the speed of the wheel, the die-chamber temperatures and the cooling downstream of the die chamber. The process-controlling parameter was the die-chamber temperature, and it was varied from an initial 500 °C to a final 350 °C. The specimens represent runs at various die-chamber temperatures. The microstructure of the specimen processed in the die chamber at a temperature of 500 °C consisted of recrystallized equiaxed grains with a bimodal size with an average size of 1.9 μm. Neither the small nor the large grains exhibit distorted structures. The die-chamber temperature of 450 °C is sufficient for the microstructure to recover/recrystallize. No effects of the cooling were detected. The recovery/recrystallization and potential grain growth finished before the specimen was cooled. The specimen pro-

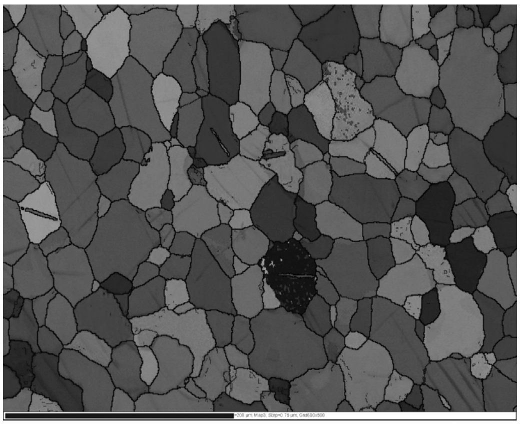

Figure 1: Microstructural state of the feedstock material (length of scale 200 μm)
Slika 1: Stanje mikrostrukture izhodnega materiala (dolžina skale je 200 μm)

Table 2: Mechanical properties and average grain size for various states of CP-Ti
Tabela 2: Mehanske lastnosti in povprečna velikost zrn pri različnih stanjih CP-Ti

	Proof stress $R_{p0.2}$/MPa	UTS R_m/MPa	A_g/%	A_5/%	Z/%	KCV/(J cm^{-2})	d/μm
Feedstock	354	470	9.3	32.3	64.2	64.2	5.39
Single pass (350 °C)	620	694	12.0	26.3	55.7	27.5	1.4
Three passes (200 °C)	637	698	1.77	17.8	66.2	––	0.42

cessed at the die chamber temperature of 400 °C began to show changes as it contained a small amount (10–15 %) of deformed, un-recrystallized grains. Distorted grains with a size of no more than 5 μm × 10 μm were divided by low-angle boundaries into sub-grains. The average grain size was 1.9 μm.

Figure 2 shows the microstructure upon water cooling after the processing at a chamber temperature of 350 °C, consisting of slightly elongated, deformed grains. The EBSD analysis was focused on the centre of the circular cross-section of the extruded product. The analysed surface is in a plane that is parallel to the bending plane/flow plane in the CONFORM chamber. On the EBSD maps the axis of the extruded section is vertical and the specimen grain size was 1.4 μm. The titanium wire processed in this way was then used for the annealing experiment. The mechanical properties of the feedstock and of the Ti wire after a single pass at the die chamber temperature of 350 °C are listed in **Table 2**. As expected, the yield stress and the ultimate strength of the product are higher than those of the feedstock. On the other hand, its contraction, elongation and the impact toughness upon the first pass are lower than those of the feedstock.

In the second processing experiment, the feedstock preheating device of the CONFORM machine was turned off, the chamber temperature was set to 200 °C and the wheel speed was 0.5 m s^{-1}. In this experiment, three CONFORM passes of Ti wire were used. As the amount of strain introduced into the material was substantial, the EBSD examination did not give any result. All three specimens were also examined using the TEM.

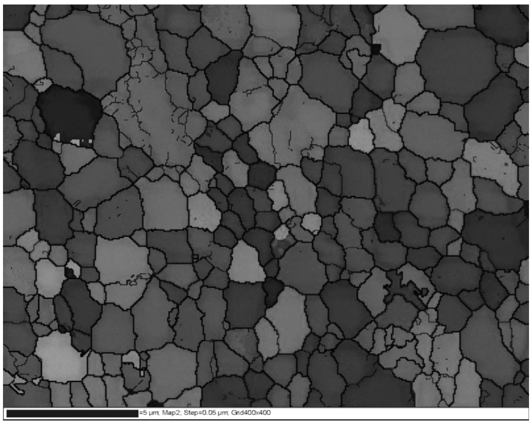

Figure 2: Microstructural state of CP-Ti subjected to one pass through the CONFORM machine at 350 °C (length of scale 200 μm)
Slika 2: Stanje mikrostrukture CP-Ti po 1 prehodu skozi napravo CONFORM pri 350 °C (dolžina skale je 200 μm)

3.1 TEM analysis of the microstructure

From samples of Ti wire upon each pass, foils for the transmission electron microscopy observations, oriented in longitudinal and transverse directions, were prepared and in this work the results of the examination of the longitudinal cross-sections are presented. In this direction, the change in grain size with the introduced strain was critically assessed.

Upon the first CONFORM pass with a chamber temperature of 200 °C, the microstructure on the longitudinal section consisted of polyhedral grains with an elevated dislocation density, distorted grains and even disc-shaped grains, as shown in **Figure 3**.

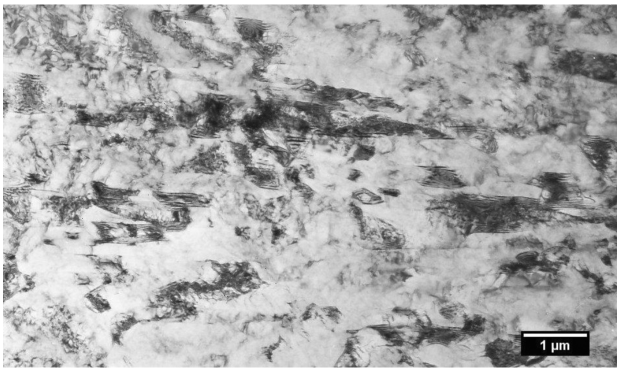

Figure 3: Region with grains with deformation texture within Ti wire after the first pass at 200 °C
Slika 3: Področje z zrni z deformacijsko teksturo v Ti-žici po prvem prehodu pri 200 °C

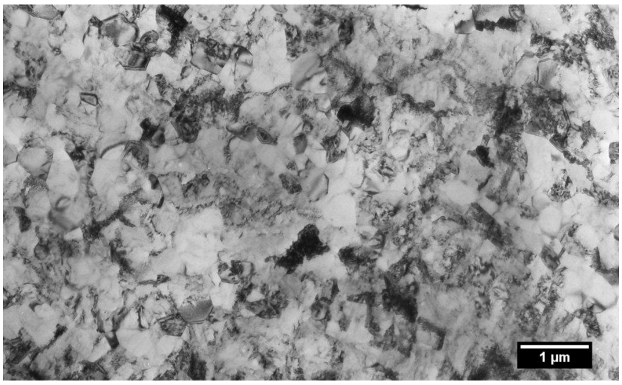

Figure 4: General view of Ti wire substructure after second pass at 200 °C
Slika 4: Videz podstrukture v Ti-žici po drugem prehodu pri 200 °C

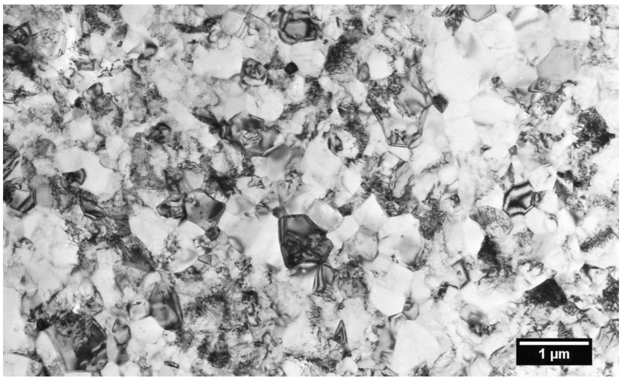

Figure 5: General view of Ti wire substructure after third pass at 200 °C

Slika 5: Videz podstrukture v Ti-žici po tretjem prehodu pri 200 °C

The nature of the substructure of the samples taken upon the second pass is similar to the condition seen on the transverse cross-section and the very fine-grained polyhedral microstructure is shown in **Figure 4**. The grain size measured was $d_{str} \approx (310 \pm 30)$ nm, with a difference compared to the previous specimen. On the longitudinal section there were areas of distorted grains or grains with a disc morphology, while the previous specimen contained no such grains.

Figure 5 characterizes the substructure of the specimens on the longitudinal section through the wire upon three CONFORM passes. The nature of the substructure is very similar to that on the transverse cross-section. The grains are polygonal, with a mean size of $d_{str} \approx (420 \pm 30)$ nm. On this section too, areas can be found where the dislocation density is low, but locations with a higher dislocation density are present as well.

4 RESULTS OF THE THERMAL ANALYSIS

The results of the dilatometer measurement were processed with Linseis Data Evaluation software (**Figure 6**). The specimen after one pass through the CONFORM machine at 350 °C showed a reduced elongation, which can be explained by the annihilation of dislocations and the elimination of the lattice stress. This was not observed in the annealed feedstock, which received no deformation and so eventual effects of the phase transformation can be ruled out. The calculated difference between the changes in the lengths of the feedstock and the processed specimen suggest that in the temperature range 432–576 °C the recovery caused a substantial change in the length.

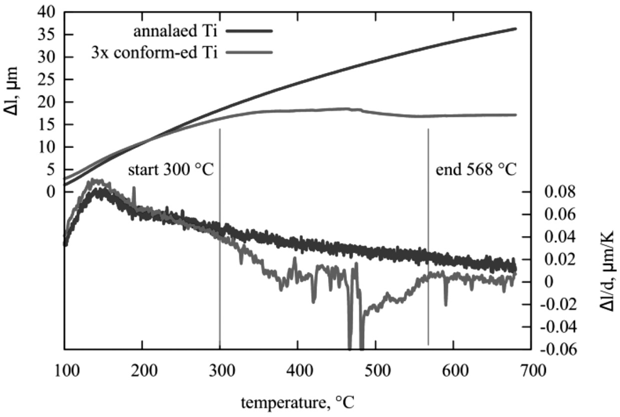

Figure 7: Dependence of the change of length on the temperature for different states of CP-Ti processed at 200 °C

Slika 7: Odvisnost spremembe dolžine od temperature za različna stanja CP-Ti, predelanega pri 200 °C

The same method was used for measuring the variation in the thermal expansion for the specimen upon three passes at 200 °C. The lower limit of the interval of the initial recovery of deformed Ti wire is shifted towards notably lower temperatures, to 300–560 °C, according to **Figure 7**.

The results of the differential scanning calorimeter (DSC) measurement on a specimen after a single pass at 350 °C are shown in **Figure 8**. Above 300 °C, the temperature increase in both specimens is in accordance with the thermal schedule (constant heating rate of

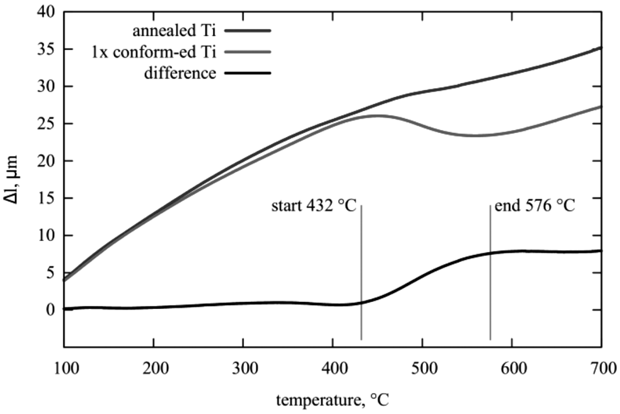

Figure 6: Dependence of the change in length on the temperature for different states of CP-Ti processed at 350 °C

Slika 6: Odvisnost spremembe dolžine od temperature za različna stanja CP-Ti, predelanega pri 350 °C

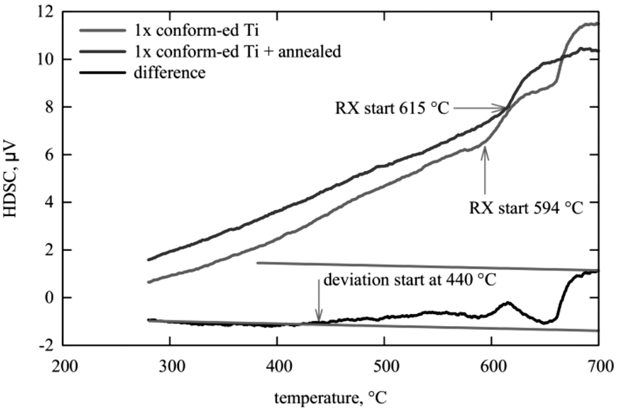

Figure 8: Heat flux vs. temperature dependence in a specimen after a single pass at 350 °C

Slika 8: Odvisnost toplotnega toka od temperature v vzorcu po enem prehodu pri 350 °C

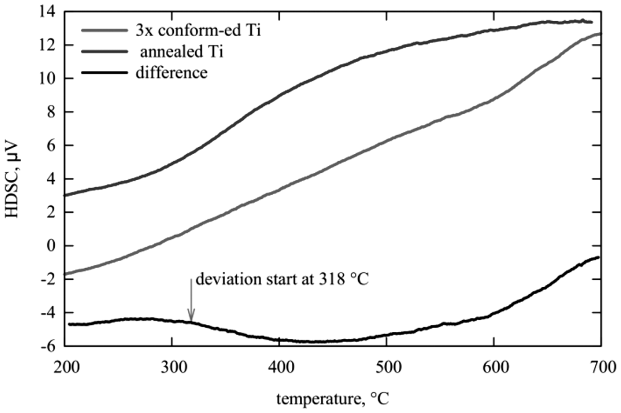

Figure 9: Heat flux vs. temperature dependence in a specimen after three passes at 200 °C

Slika 9: Odvisnost toplotnega toka od temperature v vzorcu po treh prehodih pri 200 °C

10 K/min). Despite that, the curves for both specimens (the processed one and the one annealed in the DSC) show differences. As the calculation shows, there is a steeper increase in the stress in the processed specimen at temperatures above 440 °C (**Figure 8**). Apparently, an exothermic reaction, generating heat, takes place. This region matches the recovery zone identified in the dilatometric measurement. (The higher onset temperature found in the DSC may be due to the higher heating rate, the larger specimen, and the resulting response). It may be attributed to the release of heat by recovery stress relaxation. In the processed specimens, the recrystallization peak was detected at lower temperatures, in accordance with the theoretical and empirical knowledge of the dependence of recrystallization on the temperature and the strain. In the specimen processed with three passes through the CONFORM machine at 200 °C, the DSC method showed a more notable decrease in the temperature for the onset of the exothermic reaction, being approximately 320 °C, as shown in **Figure 9**.

The recrystallization temperature in the undeformed specimen was T_{rx} = 615 °C, and 594 °C for a single-pass "conformed" specimen. The decrease in the recrystallization temperature down to 527 °C in a CP-Ti specimen after eight ECAP passes has been reported in[7].

5 CONCLUSION

The effect of CONFORM straining on the microstructure of a Ti wire was investigated. It was found that the die-chamber temperature had the strongest influence. The smallest mean grain size found by EBSD was 1.4 µm, which was achieved at a die-chamber temperature of 350 °C. The microstructure of the processed material after three passes at a die chamber temperature of 200 °C was examined. After the first pass, the microstructure contained a notable number of slip bands, and after the second and third passes, the character of microstructure was identical, with fine polyhedral grains with low and high dislocation densities. After the third CONFORM pass, the mean grain size of $d_{str} \approx (420 \pm 30)$ nm was obtained. The thermal analysis showed that the increasing amount of strain introduced temperatures for the onset of the recovery decrease. In the Ti wire with the mean grain size of 1.4 µm, the recovery began at approximately 440 °C, and for the Ti wire with the grain size of 420 nm, this temperature is even lower, i.e., 310 °C. As polyhedral grains with varying dislocation densities are present, is becomes clear that the recovery phenomena take place even during the forming process. It also suggests that the forming temperature is lower than the recorded die-chamber temperature.

6 REFERENCES

[1] G. J. Raab, R. Z. Valiev, T. C. Lowe, Y. T. Zhu, Continuous processing of ultrafine grained Al by ECAP-Conform, Materials Science and Engineering: A, 382 (**2004**) 1/2, 30–34, doi:10.1016/j.msea.2004.04.021

[2] G. Raab et al., Long-Length Ultrafine-Grained Titanium Rods Produced by ECAP-Conform, Materials Science Forum, 584–586 (**2008**), 80–85, doi:10.4028/www.scientific.net/MSF.584-586.80

[3] M. Duchek, T. Kubina, J. Hodek, J. Dlouhy, Development of the production of ultrafine-grained titanium with the conform equipment, Mater. Tehnol., 47 (**2013**) 4, 515–518

[4] T. Kubina, J. Dlouhy, M. Köver, J. Hodek, Preparation and thermal stability of ultra fine-grained commercially pure titanium wire, Proc. of Recent trends in structural materials COMAT 2012, Pilsen, 2012, [cited 2013-09-30]. Available from world Wide Web: http://www.comat.cz/files/proceedings/11/reports/1301.pdf

[5] E. A. Brandes, G. B. Brook, Smithels Metals Reference Book, 7th ed., Butterworth-Hernemann, Oxford 1992

[6] M. Hoseini et al., Thermal stability and annealing behaviour of ultrafine grained commercially pure titanium, Materials Science and Engineering A, 532 (**2012**), 58–63, doi:10.1016/j.msea.2011.10.062

[7] J. Gubicza et al., Microstructure of severely deformed metals determined by X-ray peak profile analysis, Journal of Alloys and Compounds, 378 (**2004**) 1/2, 248–252, doi:10.1016/j.jallcom.2003.11.162

UDK 536.21:536.28
Original scientific article/Izvirni znanstveni članek

ISSN 1580-2949
MTAEC9, 49(2)219(2015)

ESTIMATION OF THE THERMAL CONTACT CONDUCTANCE FROM UNSTEADY TEMPERATURE MEASUREMENTS

DOLOČANJE KONTAKTNE TOPLOTNE PREVODNOSTI IZ NERAVNOTEŽNEGA MERJENJA TEMPERATURE

Jiří Kvapil, Michal Pohanka, Jaroslav Horský

Heat Transfer and Fluid Flow Laboratory, Faculty of Mechanical Engineering, Brno University of Technology, Technická 2, 616 69 Brno, Czech Republic
kvapil@fme.vutbr.cz

Prejem rokopisa – received: 2013-10-08; sprejem za objavo – accepted for publication: 2014-03-28

doi:10.17222/mit.2013.238

Thermal contact conductance is an important parameter for describing the heat transfer between two bodies. When two solids are put in contact and heat transfer occurs, a temperature drop is observed at the interface between the solids. This is caused by an imperfect joint, which occurs because the real surfaces are not perfectly smooth and flat. This paper describes an experimental device for the evaluation of the thermal contact conductance, which was designed and fabricated in the Heat Transfer and Fluid Flow Laboratory. This device was built mainly for simulating metal-forming conditions, which include high pressures (up to 360 MPa) and high temperatures (up to 1200 °C) in the contact of two solids. The principle of this investigation is the unsteady measurement of the temperatures of two solids that are put in contact under different conditions. The surface temperature and thermal contact conductance can be calculated from the measured temperatures by an inverse heat-transfer task. The measured temperature history and the calculated values of the thermal contact conductance for pilot tests are presented in this paper.

Keywords: thermal contact conductance, inverse heat conduction problem, heat-transfer coefficient

Kontaktna toplotna prevodnost je pomemben parameter za opisovanje prehoda toplote med dvema telesoma. Ko sta dve trdni snovi v stiku, se pri prenosu toplote opazi znižanje temperature na stiku med dvema trdnima snovema. To nastane zaradi nepopolnega stika, ker realne površine niso popolnoma gladke in ravne. Ta članek opisuje eksperimentalno napravo za oceno kontaktnega prevajanja toplote, konstruirane v laboratoriju za prenos toplote in toka tekočin. Naprava je bila zgrajena predvsem za simulacijo razmer pri preoblikovanju materialov, ki vključujejo velik tlak (do 360 MPa) in visoke temperature (do 1200 °C) na stiku med dvema trdnima materialoma. Princip teh raziskav je neravnotežno merjenje temperature dveh trdnih snovi, ki sta v kontaktu v različnih razmerah. Temperatura površine in kontaktna prevodnost toplote se lahko izračunata iz izmerjenih temperatur z upoštevanjem inverznega prenosa toplote. V tem članku sta predstavljeni zgodovina merjenja temperature in izračunane vrednosti kontaktne toplotne prevodnosti pri opravljenih preizkusih.

Ključne besede: toplotna prevodnost kontakta, problem inverznega prenosa toplote, koeficient toplotne prevodnosti

1 INTRODUCTION

Heat transfer over an interface has been the subject of research for decades, as it plays an important role in applications such as nuclear-reactor cooling, the aerodynamic heating of supersonic aircraft and missiles, satellite thermal control, the packaging of electronics, turbine and internal combustion engine design, etc.

When two solids with different temperatures come into contact, heat transfer occurs. A temperature drop is observed at the interface between the solids because of the surface imperfections. No truly smooth surface really exists. In reality, the contact is created at only a few discrete points. The contact point size and the density depend on the surface roughness, the physical properties of asperities and the contact pressure. The real contact-area fraction is only 0.01–0.1 % without pressure. Pressure is one of the most important parameters that can affect the real contact area. Nevertheless, for metals the direct contact takes an area of around 1–2 % for several tens of MPa in the contact.[1] The heat transfer is decreased due to the (air) layer partially filling the voids between the surfaces, although heat flows or radiates through these voids. Many models and empirical and semi-empirical correlations to predict the thermal contact conductance have been published.[2] However, these models have restrictions in terms of the maximum contact pressure (up to 7 MPa) and temperature and are not convenient for an estimation of the thermal contact conductance in conditions simulating metal forming and hot rolling.

2 METHODS OF MEASUREMENT

Usually, thermal contact conductance is measured using steady-state experiments (**Figure 1**).[3] The two bodies are in contact and their ends are cooled and heated. The temperature distribution is measured using thermocouples inside the bodies. After a couple of hours, the constant heat flux q is obtained and the temperature drop ΔT at the interface is estimated by extrapolation. From this, the thermal contact conductance h_c can be calculated:

$$h_c = \frac{q}{\Delta T} \tag{1}$$

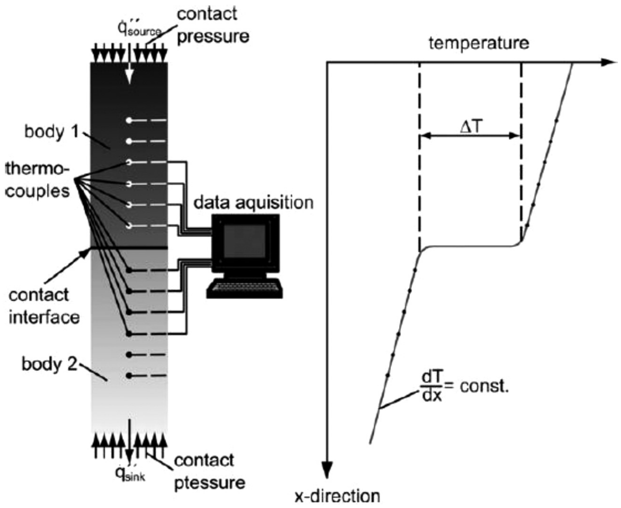

Figure 1: Experimental device for steady-state measurement of the thermal contact conductance[3]

Slika 1: Eksperimentalna naprava za ravnotežne meritve kontaktne toplotne prevodnosti[3]

The next procedure to estimate the thermal contact conductance is an unsteady measurement. This procedure is described here. Two thermocouples are embedded close to the surface of the bodies in contact. The measured temperature history is used for an inverse calculation and the thermal contact conductance is derived. This method is much faster but more difficult to calculate in comparison with steady-state experiments.

3 EXPERIMENTAL PROCESS

An experimental device (**Figure 2**) for estimating the thermal contact conductance in various conditions was built in the Heat Transfer and Fluid Flow Laboratory. The main part of the device is a steel body in the shape of a hollow cylinder. Two smaller cylinders, top and bottom, and a spring are located inside the hollow cylinder (**Figure 3**). A temperature sensor is embedded in the bottom cylinder and has a diameter of 12 mm. The top cylinder is used for compressing the spring to the required force, which is measured by a force sensor. The trigger mechanism is used to prevent the bottom cylinder and the sensor from moving. The first thermocouple (type K, diameter of 0.5 mm) is built in the temperature sensor at a depth of 0.9 mm from the surface and the second thermocouple (type K, diameter of 1.5 mm) is in the test plate at a depth of 2 mm from the surface.

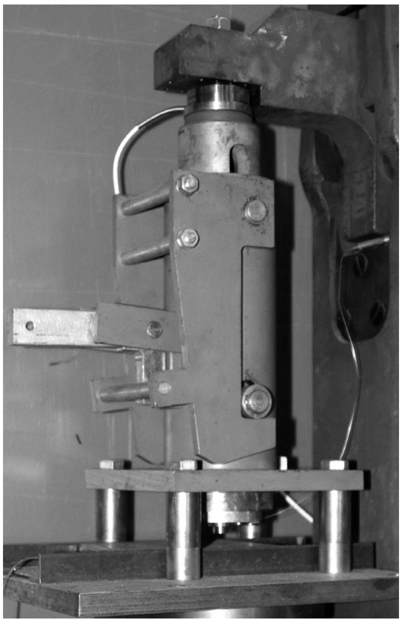

Figure 2: Experimental device

Slika 2: Naprava za preizkuse

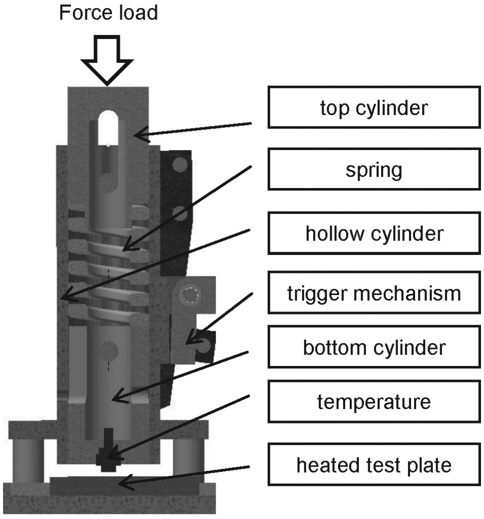

Figure 3: Cross-section of the experimental device

Slika 3: Prerez naprave za preizkuse

This device can be used for measuring a variety of initial conditions, like contact pressure (up to 360 MPa), temperature (up to 1200 °C), different types of materials in contact, surface roughness and scales on the surface.

3.1 Experimental procedure

The experiment begins by heating the test plate to the required temperature. Independent of the heating, the

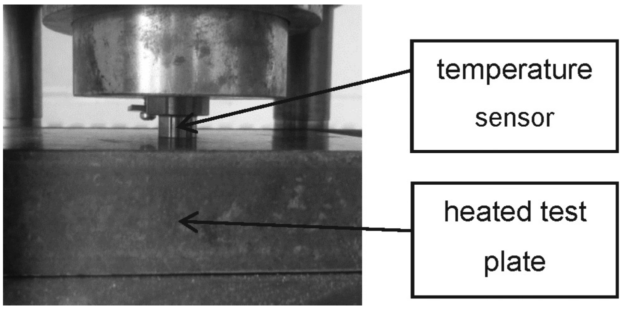

Figure 4: Contact of the temperature sensor and the heated test plate in detail

Slika 4: Detajl stika senzorja temperature in ogrevane preizkusne plošče spring is pressed to the required load. Then the test plate is inserted into the experimental device and the trigger mechanism is released. When the surfaces of the sensor and the test plate are in contact (see the detail in **Figure 4**), heat transfer occurs because of the different temperatures of the bodies in contact. The temperatures are measured and stored in the data logger.

Three experiments (**Table 1**) with different initial parameters were performed and the measured temperature history from Exp2 is shown in **Figure 5**. The time 0 s marks the time of contact.

Table 1: List of experiments
Tabela 1: Seznam preizkusov

Test name	Contact pressure	Test plate	
		Initial temperature	Surface (roughness)
Exp1	25 MPa	330 °C	grinded (R_a 0.8)
Exp2	25 MPa	530 °C	grinded (R_a 0.8)
Exp3	70 MPa	820 °C	grinded (R_a 0.8)

The heat flux and the surface temperatures of the temperature sensor and the test plate during the experiment are calculated by the inverse heat-conduction task.

4 INVERSE HEAT-CONDUCTION TASK

Two 2D models, one for the temperature sensor and the second for the test plate, were used for the numerical computation. The models also include the thermocouples inside because the homogeneity of the material is disrupted by the inserted thermocouples, and thus the temperature profile is also disrupted. A one-dimensional sequential Beck's approach[4–6] is used to compute the heat fluxes and the surface temperatures of the temperature sensor. The main feature of this method is the sequential estimation of the time-varying heat fluxes and surface temperatures and using future time-step data to stabilize the ill-posed problem. The measured temperature history from the temperature sensor is used as the input T^* in the minimizing equation:

$$SSE=\sum_{i=m+1}^{m+f}(T_i^*-T_i)^2 \tag{2}$$

where m is the current time, f is the number of future time steps and T_i is the computed temperatures from the forward solver[7]. The SSE denotes the sum of square errors. The value of the surface heat flux q at time m is:

$$q^m=q^{m-1}+\frac{\sum\limits_{i=m+1}^{m+f}(T_i^*-T_i\big|_{q^m=0})\cdot\zeta_i}{\sum\limits_{i=m+1}^{m+f}(\zeta_i)^2} \tag{3}$$

$$\zeta_i=\frac{\partial T_i}{\partial q_m} \tag{4}$$

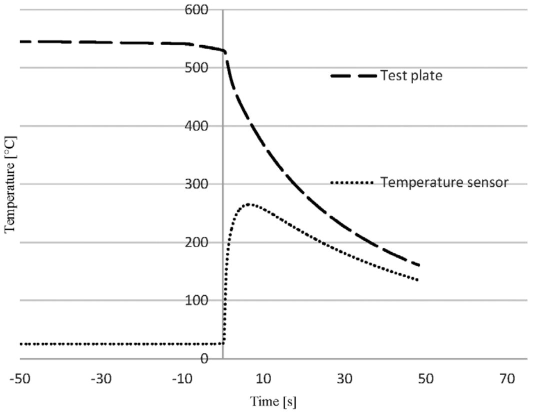

Figure 5: Temperature history of Exp2
Slika 5: Potek temperature pri Exp2

where ζ_i is a sensitivity coefficient at time index i to the heat-flux pulse at time m. The temperatures $T_i\big|_{q^m=0}$ at the thermocouple location of the temperature sensor computed from the forward solver use all the previously computed heat fluxes without the current one q^m. When the heat flux is found for time m, the corresponding surface temperatures of the temperature sensor T_{surf1}^m and the test plate T_{surf2}^m are computed from the forward solver using q^m as the boundary condition in the contact area for the temperature sensor and the test plate. Using this procedure, the whole heat-flux history and the surface-temperature history are computed. When the surface heat flux q^m and the surface temperatures T_{surf1}^m and T_{surf2}^m are known, the thermal contact conductance h_c is computed from:

$$h_c^m=\frac{q^m}{\dfrac{\left(T_{surf2}^m+T_{surf2}^{m-1}\right)}{2}-\dfrac{\left(T_{surf1}^m+T_{surf1}^{m-1}\right)}{2}} \tag{5}$$

5 RESULTS

The computed heat-flux history and surface-temperature histories of the bodies in contact from Exp2 are shown in **Figures 6** and **7**.

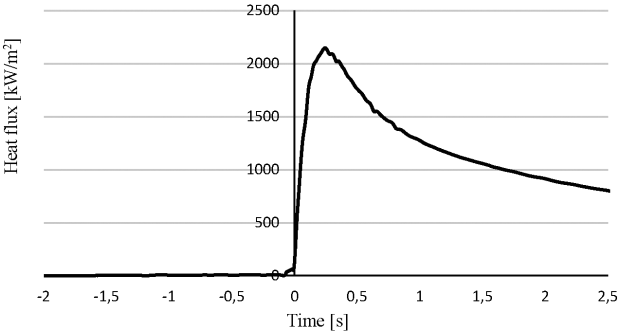

Figure 6: Computed heat-flux distribution of Exp2
Slika 6: Izračunana razporeditev toka toplote po Exp2

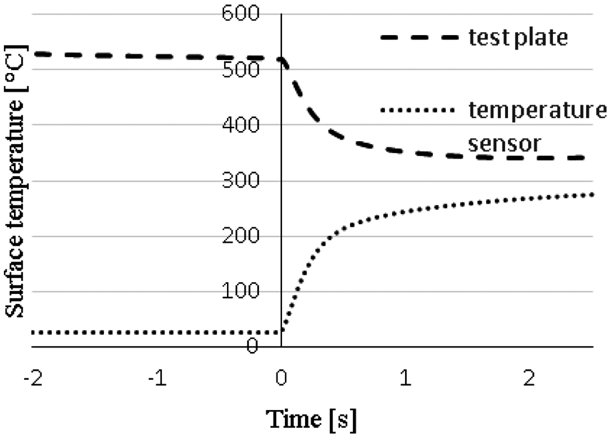

Figure 7: Computed surface temperatures of Exp2
Slika 7: Izračunane temperature površine pri Exp2

The inverse calculations, made for all the experiments and results in the form of thermal contact conductance, are shown in **Figure 8**.

Fieberg[3] dealt with the unsteady measurement of thermal contact conductance using a method where the temperature is measured using a high-speed infrared camera. During the experiments, he focused on conditions similar to those in a combustion engine, where the contact pressure can be up to 250 MPa and the temperature can be up to 630 °C. He mainly tested steel-aluminium alloys, but he also published an experiment with steel. His distribution of the thermal contact conductance with steel bodies for 34 MPa in the contact and a starting temperature at 270 °C is shown in **Figure 8**.

Theoretically, the distribution of the thermal contact conductance with time should be constant. This corresponds quite well with our experiments, and also with Fieberg[3], but in our case, directly after the contact, it takes some time (around 0.3–0.5 s) to stabilize the level of thermal contact conductance. This is caused by vibrations after the sudden contact of the temperature sensor and the heated test plate. It is obvious that an important influence on the thermal contact conductance comes from the contact pressure and the initial temperature of the test plate.

6 CONCLUSION

In this paper, an experimental device for the unsteady measurement of the temperatures of two solids that are put in contact has been described. New numerical models for computing the thermal contact conductance from the temperature history were developed, three pilot experiments were made and the results were presented. The computed distributions of the thermal contact conductance show a strong dependence on the contact pressure and the initial temperature. The estimated thermal contact conductance for a contact pressure of 25 MPa and an initial temperature of 330 °C is 9100 $W/(m^2 K)$, while for 25 MPa and 530 °C it is 12200 $W/(m^2 K)$ and for 70 MPa and 820 °C it is 35500 $W/(m^2 K)$. These results could be used in numerical simulations of metal forming and hot rolling where the values of thermal contact conductance in the interface between two solids are still missing. Additionally, there is a need for similar experiments focusing on the influence of the thermal contact conductance by surface roughness, type of material and thickness of the scales.

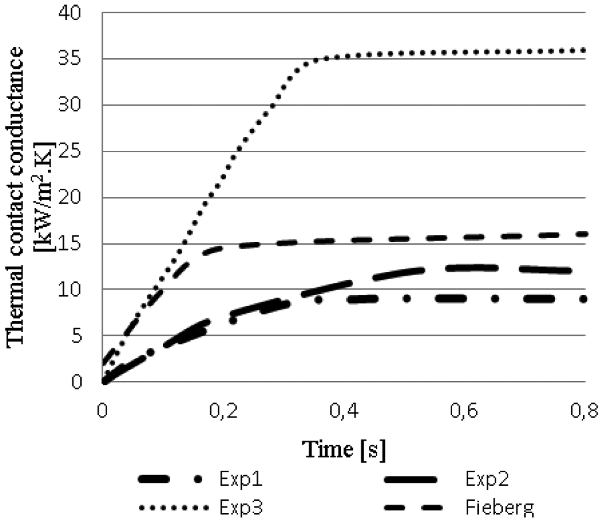

Figure 8: Distributions of thermal heat conduction for various initial conditions
Slika 8: Razporeditev toplotne prevodnosti za različne začetne razmere

Acknowledgement

The research in the presented paper has been supported within the project No. CZ.1.07/2.3.00/ 20.0188, HEATEAM – Multidisciplinary Team for Research and Development of Heat Proceeding.

7 REFERENCES

[1] F. P. Bowden, D. Tabor, The friction and lubrication of solids, Oxford University Press, London 1950, 391 p.

[2] A. Wang, J. Zhao, Review of prediction for thermal contact resistance, Science China Technological Sciences, 53 (**2010**) 7, 1798–1808, doi:10.1007/s11431-009-3190-6

[3] C. Fieberg, R. Kneer, Determination of thermal contact resistance from transient temperature measurements, International Journal of Heat and Mass Transfer, 51 (**2008**) 5–6, 1017–1023, doi:10.1016/j.ijheatmasstransfer.2007.05.004

[4] J. Beck, B. Blackwell, C. R. Clair, Inverse heat conduction: ill-posed problems, Wiley, New York 1985, 308 p.

[5] M. Pohanka, K. A. Woodbury, A Downhill Simplex method for computation of interfacial heat transfer coefficients in alloy casting, Inverse Problems in Engineering, 11 (**2003**), 409–424, doi:10.1080/1068276031000109899

[6] M. Raudensky, Heat Transfer Coefficient Estimation by Inverse Conduction Algorithm, International Journal of Numerical Methods for Heat and Fluid Flow, 3 (**1993**) 3, 257–266, doi:10.1108/eb017530

[7] W. J. Minkowycz, E. M. Sparrow, J. Y. Murthy, Handbook of Numerical Heat Transfer, 2nd edition, John Willey & Sons, New Jersey 2006, 968 p.

UDK 669.14:620.193:620.197.2:577
Original scientific article/Izvirni znanstveni članek

ISSN 1580-2949
MTAEC9, 49(2)223(2015)

POTENTIODYNAMIC AND XPS STUDIES OF X10CrNi18-8 STEEL AFTER ETHYLENE OXIDE STERILIZATION

POTENCIODINAMIČNE IN XPS ANALIZE JEKLA X10CrNi18-8 PO STERILIZACIJI Z ETILEN OKSIDOM

Witold Walke[1], Joanna Przondziono[2]

[1]Silesian University of Technology, Faculty of Biomedical Engineering, Ch. de Gaulle'a 66, 41-800 Zabrze, Poland
[2]Silesian University of Technology, Faculty of Materials Engineering and Metallurgy, Krasińskiego 8, 40-019 Katowice, Poland
witold.walke@polsl.pl

Prejem rokopisa – received: 2013-11-14; sprejem za objavo – accepted for publication: 2014-05-09

doi:10.17222/mit.2013.281

An innovative development in the treatment of heart, blood and vascular-system diseases using low-invasive techniques led to a development of new forms of tools (among other devices: cardiologic guide wires) made of the X10CrNi18-8 steel. The authors of this study made an attempt to evaluate the impact of one of the medical sterilisation methods, i.e., the ethylene oxide sterilisation of a wire made of the X10CrNi18-8 steel after electrochemical polishing and chemical passivation. One of the basic criteria for deciding about the suitability of a specific material for a vascular tool is the proper corrosion resistance in a blood environment. It is directly connected with the chemical composition of the surface layer. Therefore, an evaluation was made on the basis of pitting-corrosion tests and the tests of the chemical compositions of the surface layers by means of the XPS method. The samples were subjected to the tests before and after the ethylene oxide sterilisation. The obtained results explicitly prove that the chemical-passivation process of the X10CrNi18-8 steel improves its resistance to corrosion in a blood environment. The resistance is higher due to the creation of a thin passive layer, mainly built of Fe_2O_3 and Cr_2O_3 on the surface, which was proved during the XPS tests. Next, the sterilisation in ethylene oxide had a favourable influence on the electrochemical properties of the X10CrNi18-8 steel, irrespective of the way of surface preparation. The presence of the alloying elements in the oxidised form was also detected in the surface layer, contributing to the improvement of the corrosion resistance in contact with the blood.

Keywords: X10CrNi18-8 steel, EO sterilization, XPS, pitting corrosion

Razvoj inovativnih metod pri zdravljenju srca, kot tudi krvno-žilnih bolezni, z uporabo malo invazivnih tehnik je pripeljal do novih oblik orodij (med drugim tudi kardioloških uvajalnih žic), izdelanih iz jekla X10CrNi18-8. Avtorji te študije si prizadevajo oceniti vpliv ene od sterilizacijskih metod, to je sterilizacija žice, izdelane iz jekla X10CrNi18-8 z etilen oksidom, po elektrokemijskem poliranju in po kemijski pasivaciji. Eden od osnovnih meril, ki odločajo o primernosti določenega materiala za orodja za ožilja, je primerna korozijska obstojnost v krvi. Ta je neposredno povezana s kemijsko sestavo površinske plasti. Zato je bila izdelana ocena na podlagi preizkusov jamičaste korozije in analize sestave površine z XPS-metodo. Vzorci so bili preizkušeni pred sterilizacijo z etilen oksidom in po njej. Dobljeni rezultati so neposredno dokazali, da proces kemijske pasivacije jekla X10CrNi18-8 izboljša njegovo odpornost proti koroziji v okolju s krvjo. To je povezano z nastankom tanke pasivne plasti iz Fe_2O_3 in Cr_2O_3 na površini, kar je bilo dokazano z XPS-analizami. Sterilizacija in etilen oksid imata ugoden vpliv na elektrokemijske lastnosti jekla X10CrNi18-8, ne glede na način priprave površine. Na površini je bila odkrita prisotnost oksidiranih legirnih elementov, ki prispevajo k izboljšanju korozijske odpornosti pri stiku s krvjo.

Ključne besede: jeklo X10CrNi18-8, EO-sterilizacija, XPS, jamičasta korozija

1 INTRODUCTION

Cardiologic guide wires have an extremely important role in the success of a coronary intervention. It is believed that the success of such a treatment depends on the type and quality of a guide wire. The guide wire is the first to reach the area of atherosclerotic lesion and it passes through a narrowing, previously passing along a complicated route inside the vessels, e.g., coronary arteries. Quite frequently, it also has to pass through a lesion that is totally closed. Guide wires differ as far as their profile, flexibility and tip configuration are concerned. The market offers guide wires with a J-shaped tip or a straight tip for individual forming. The diameter of modern guide wires is within the range of 0.35–0.45 mm, and their length is within the range of 180–300 mm. These wires, due to their direct contact with the blood, must feature a proper set of electrochemical properties also determined by the conditions of medical sterilisation.[1,2] An important issue in the process of forming guide-wire functional characteristics is the selection of the characteristics of the metallic material they are made of.[3–5] Mechanical characteristics of the material are selected on the ground of biomechanical characteristics determined for individual forms of instruments, taking the anatomical load for each type of the system into consideration. A crucial issue for the cardiologic guide-wire functional characteristics is the proper method of the surface preparation. The restrictions arising from implementing a tool made of a metallic material in the blood and vascular system have made numerous researchers look for the ways of efficiently diminishing the influences of the body fluids on the metal corrosion. It results from the analysis of the subject-matter data that one of the main factors influencing the efficiency of a treatment is the guide-wire surface roughness. The significance of the surface-layer chemical composition cannot be neglected either.[6,7] One of the basic treatments increasing the corrosion resistance of steel in the environment of human blood is the chemical-passivation process. Therefore, the authors of this study attempted to make an evaluation of the influence of the surface treatment (electrochemical polishing and chemical passivation) of steel X10CrNi18-8 on the biotolerance in the environment of human blood under the conditions of sterilisation with ethylene oxide.

2 EXPERIMENTAL WORK

Samples made of steel X10CrNi18-8 in the form of a wire with a diameter of 1 mm were selected for the tests. The chemical composition of the steel is presented in **Table 1**.

Table 1: Chemical composition of X10CrNi18-8 steel in mass fractions, *w*/%
Tabela 1: Kemijska sestava jekla X10CrNi18-8 v masnih deležih, *w*/%

Steel	C	Mn	Si	P	S	Cr
X10CrNi18-8	0.08	0.91	0.68	0.028	0.001	17.96

The differentiation of the surface roughness was achieved by means of mechanical treatment – grinding (R_a = 0.60 μm) and mechanical polishing (R_a = 0.14 μm). Chemical passivation was made in HNO_3 40 %. Next, the samples were subjected to sterilisation with ethylene oxide. The sterilisation was performed at the temperature of 55 °C in a Steri-Vac 5 XL steriliser. Before the tests, all the samples were cleaned in ethanol 96 % in an ultrasonic disintegrator. Next, the samples corresponding to the consecutive stages of the surface preparation were tested for the resistance to pitting corrosion. The tests were carried out in accordance with ASTM.[8,9] Polarisation curves were registered by means of potentiostat PGP-201 by Radiometer. A saturated calomel electrode (SCE) of the KP-113 type was used as the reference electrode. A platinum electrode of the PtP-201 type served as the auxiliary electrode. The change in the potential in the anodic direction took place at the rate of 1 mV/s. Once the current density reached the value of 1 mA/cm^2, the polarisation direction was changed and, at the same time, a return curve was registered. The tests were made in an alternative solution simulating a human-blood environment – in an artificial-blood plasma. The chemical composition of the artificial-blood plasma is presented in **Table 2**. The temperature of the artificial-blood plasma during the tests was (37 ± 1) °C and pH = 7.2.[10,11] The Stern method was applied for determining the parameters typical of the corrosion resistance of the tested alloys.

Table 2: Chemical composition of artificial plasma
Tabela 2: Kemijska sestava umetne plazme

Component	Amount in distilled water g/L
NaCl	6.8
$CaCl_2$	0.2
KCl	0.4
$MgSO_4$	0.1
$NaHCO_3$	2.2
Na_2HPO_4	0.126
NaH_2PO_4	0.026

XPS (X-ray photoelectron spectroscopy) was applied for identifying the chemical composition of the sample surface layer before and after the chemical-passivation process and sterilization in ethylene oxide. A photoelectron spectrometer made by Prevac with an analyser and monochromatic X-ray source by VG Scienta were used. Photoelectrons were activated with an X-ray tube with an aluminium anode and a quartz monochromator that ensured the Al K_α radiation with an energy of 1486.6 eV. The spectra in a wide range of electron bond energy as well as detailed spectra with high resolution made as in-depth profiles were tested. Ion etching was performed with Ar^+ ions with an energy of 4 keV. The analysed area was rectangular with the following dimensions: 260 μm × 1000 μm, with the longer side parallel to the axis of the samples. The ion-etching area was 2000 μm × 2000 μm, which ensured a safe distance from the edge of the crater created as a result of the argon-ion bombardment of the surface. The chemical composition was determined by integrating the respective photoemission lines with the application of programme MULTIPAK by Physical Electronics.

Table 3: Potentiodynamic-test results for X10CrNi18-8 steel
Tabela 3: Rezultati potenciodinamičnih preizkusov na jeklu X10CrNi18-8

Surface type	Corrosion potential E_{corr}/mV	Breakdown potential E_b/mV	Polarisation resistance (average) R_p/(kΩ cm^2)	Corrosion current density (average) $i_{corr.}$/(μA/cm^2)
Before EO				
Polished	–63 to –55	+377 to +383	229	0.114
Passivated	+15 to +25	+690 to +700	1070	0.024
After EO				
Polished	–81 to –71	+520 to +560	1060	0.025
Passivated	–72 to –63	+790 to +830	2470	0.010

3 RESULTS AND DISCUSSION

The performed potentiodynamic tests in the artificial-blood plasma supplied the information regarding the corrosion resistance of austenitic steel X10CrNi18-8 with its surface prepared in different ways and subjected to the sterilisation process. Potentiodynamic-test results are presented in **Table 3**. Anodic-polarisation curves are shown in **Figure 1**.

It was determined that the average corrosion-potential value for the wire subjected to electrochemical polishing was lower (E_{corr} = –59 mV) than that obtained for the wire subjected to chemical passivation (E_{corr} = +20 mV). The mean values of the perforation potential and possible repassivation, determined on the ground of the registered polarisation curves, were also lower for the wire subjected to polishing. It was also proved that there were significant differences between the determined values of corrosion-current density i_{corr} and polarisation resistance R_p (**Figure 1** and **Table 3**).

In order to identify the chemical composition of the surface layer created as the result of the electrochemical treatment and sterilisation process, XPS tests were performed. An analysis of the spectral lines for the respective elements enabled us to draw the conclusions regarding their chemical states and their changes depending on the depth of the analysed layer (**Figure 2**). The bond energy of electron states depends on the chemical compound, in which an element is present. A favourable decrease in the main alloying elements of Fe, Cr and Ni in relation to the substrate, as well as an increase in the participation of oxide compounds of those

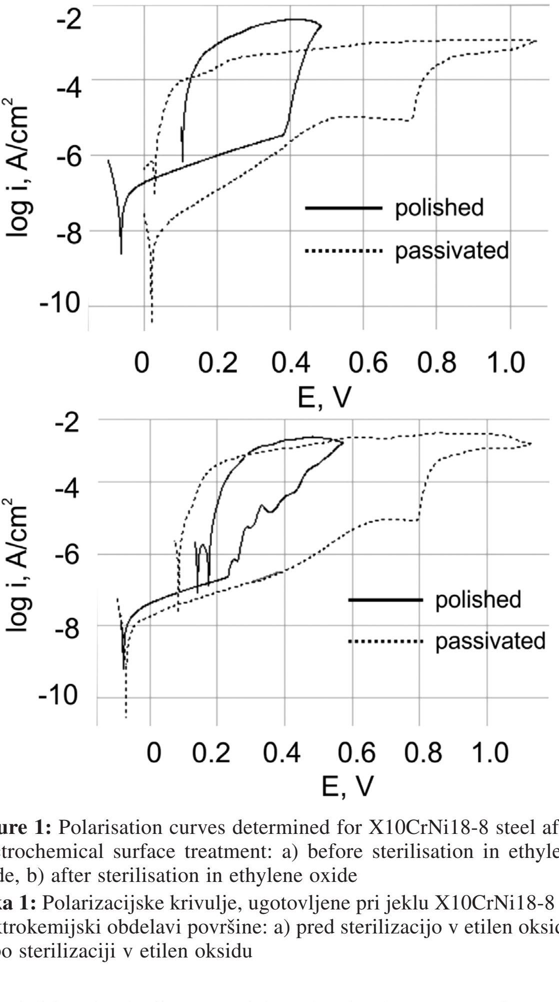

Figure 1: Polarisation curves determined for X10CrNi18-8 steel after electrochemical surface treatment: a) before sterilisation in ethylene oxide, b) after sterilisation in ethylene oxide

Slika 1: Polarizacijske krivulje, ugotovljene pri jeklu X10CrNi18-8 po elektrokemijski obdelavi površine: a) pred sterilizacijo v etilen oksidu, b) po sterilizaciji v etilen oksidu

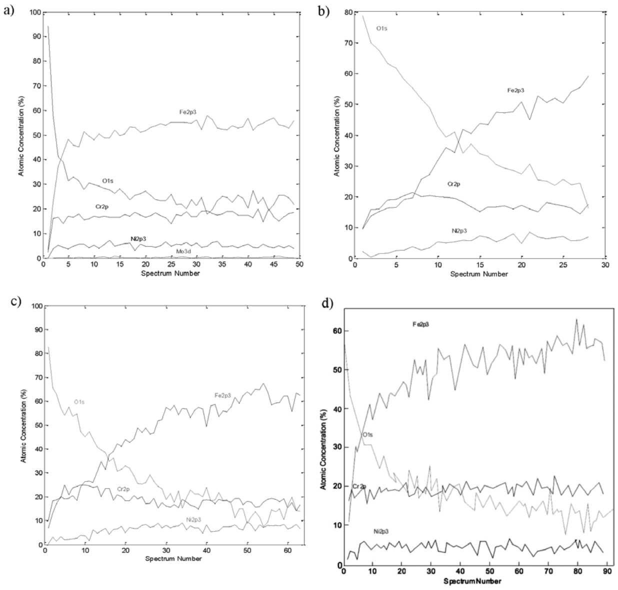

Figure 2: In-depth profiles registered for X10CrNi18-8 steel after the processes of: a) electrochemical polishing, b) electrochemical polishing and sterilisation in ethylene oxide, c) chemical passivation, d) chemical passivation and sterilisation in ethylene oxide

Slika 2: Profil koncentracije v globino pri jeklu X10CrNi18-8 po: a) elektrokemijskem poliranju, b) elektrokemijskem poliranju in sterilizaciji z etilen oksidom, c) kemijski pasivaciji, d) kemijski pasivaciji in sterilizaciji z etilen oksidom

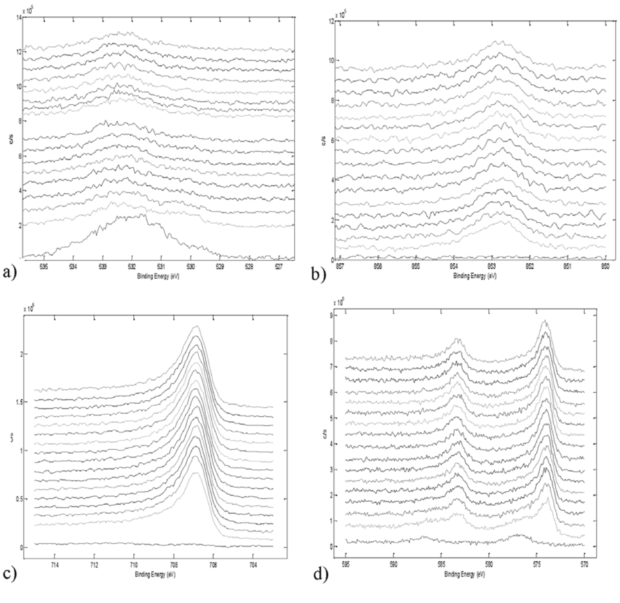

Figure 3: XPS spectra of X10CrNi18-8 steel for lines (electrochemical polishing): a) O1s, b) Ni2p3/2, c) Fe2p3/2, d) Cr2p

Slika 3: XPS-spektri za jeklo X10CrNi18-8 za linije (elektrokemijsko poliranje): a) O1s, b) Ni2p3/2, c) Fe2p3/2, d) Cr2p

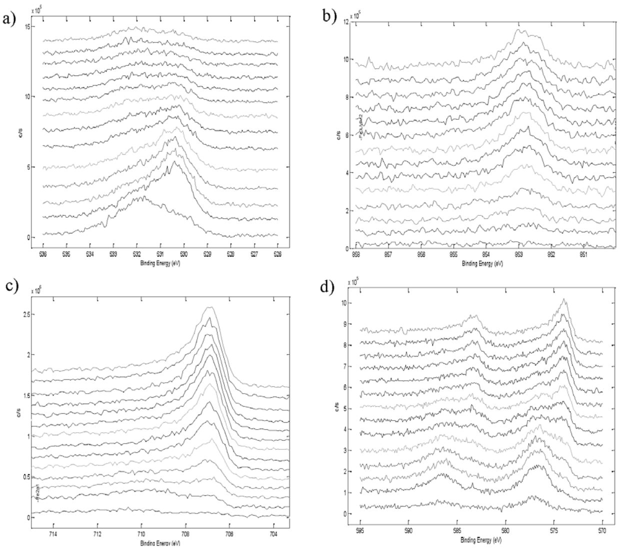

Figure 4: XPS spectra of X10CrNi18-8 steel for lines (electrochemical polishing and sterilisation in ethylene oxide): a) O1s, b) Ni2p3/2, c) Fe2p3/2, d) Cr2p

Slika 4: XPS-spektri za jeklo X10CrNi18-8 za linije (elektrokemijsko poliranje in sterilizacija z etilen oksidom): a) O1s, b) Ni2p3/2, c) Fe2p3/2, d) Cr2p

elements were detected in the composition of the passive layer obtained after the electrochemical treatment and sterilisation in ethylene oxide (**Figures 3** to **6**). Oxide compounds feature better haemocompatibility. Measured line O1s may be subordinate to several chemical states. The main line with the energy of 285.29 eV could be assigned to hydrocarbons, ever present on the surface. A weak line with the maximum energy of 283.50 eV that came from carbides, e.g., Cr_3C_2, was also visible. Other weak lines at their maximum levels, with their energy slightly higher than 285.30 eV could be attributed to the organic compounds containing oxygen or the carbonates created during the surface treatment of the sample. With respect to analysing the Fe spectrum, two chemical states are visible: metallic Fe (707 eV) and the form of oxide, Fe_2O_3 (711 eV), which may be determined through a comparison with the spectra of the respective iron oxides and an analysis of the satellites, e.g., 719 eV – the typical position of Fe_2O_3.[12] For chromium, the oxidized condition was dominant; line $Cr2p_{3/2}$ with an energy of 577.0 eV was emitted by Cr_2O_3, whereas the weak line with an energy of 574.4 eV was emitted by metallic chromium. The line of oxygen included various chemical states. The line with an energy of about 531.6 eV, which could be attributed to Cr_2O_3, was dominant.[13] For the transition metals, such as chromium or nickel, the effect of the reduction due to the ion bombardment was taken into consideration. This effect is particularly important when interpreting the nickel spectra. Nickel oxides are largely reduced due to the ions with an energy of 4 keV. The absence of nickel oxides in the spectra may just partially result from this effect (**Table 4**).

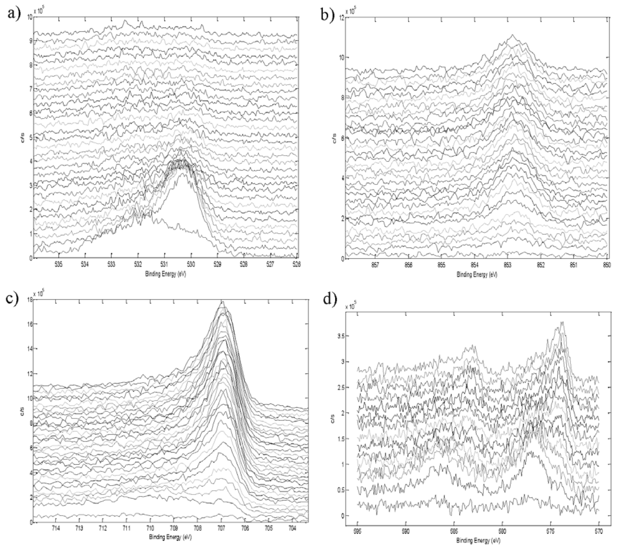

Figure 5: XPS spectra of X10CrNi18-8 steel for lines (chemical passivation): a) O1s, b) Ni2p3/2, c) Fe2p3/2, d) Cr2p

Slika 5: XPS-spektri za jeklo X10CrNi18-8 za linije (kemijska pasivacija): a) O1s, b) Ni2p3/2, c) Fe2p3/2, d) Cr2p

Table 4: Results of XPS analyses

Tabela 4: Rezultati XPS-analiz

Surface type	Elements in amount fractions, *x*/%				
	O	C	Fe	Cr	Ni
Before EO					
Polished	35.16	52.05	7.61	5.17	-
Passivated	55.11	41.21	2.23	1.03	0.41
After EO					
Polished	34.55	50.23	9.29	5.92	-
Passivated	60.76	33.25	3.25	3.52	0.21

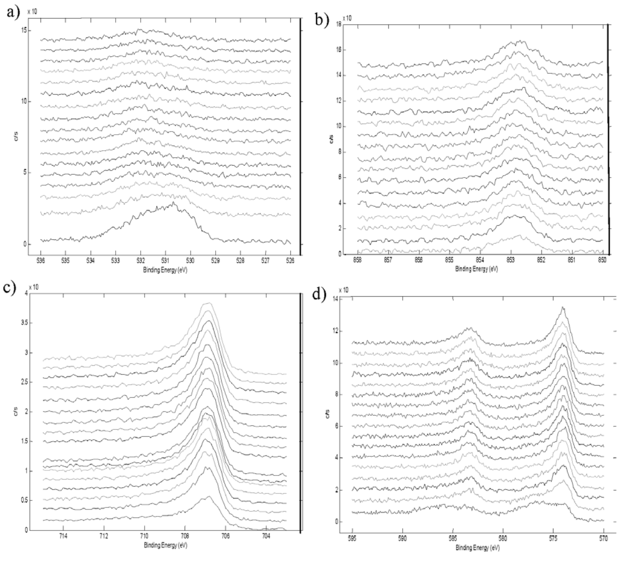

Figure 6: XPS spectra of X10CrNi18-8 steel for lines (chemical passivation and sterilisation in ethylene oxide): a) O1s, b) Ni2p3/2, c) Fe2p3/2, d) Cr2p

Slika 6: XPS-spektri za jeklo X10CrNi18-8 za linije (kemijska pasivacija in sterilizacija z etilen oksidom): a) O1s, b) Ni2p3/2, c) Fe2p3/2, d) Cr2p

4 CONCLUSIONS

An innovative progress in treating cardiovascular-system diseases using low-invasive methods led to the production of new forms of tools, such as guide wires. Those tools, introduced as the first ones to a narrowed section of a blood vessel, many times increase its cross-section in a situation of its total closure. Some limitations, observed in the clinical practice, resulting from the introduction of the tools made of metallic materials to blood vessels, are mainly connected with the blood coagulation on their surfaces.[14] Therefore, the study contains an evaluation of the impact of the surface treatment that enables us to increase the biotolerance of the X10CrNi18-8 steel in a blood environment under the conditions of sterilisation with ethylene oxide.

The analysis of the results of the electrochemical-corrosion tests proved differentiated corrosion resistance of the wires made of the X10CrNi18-8 steel. Less favourable values of the determined parameters that characterise the corrosion resistance result from restricting their surface treatment only to polishing (**Table 3**).

Next, the in-depth profiles obtained for individual variants of the surface treatment showed that electrochemical polishing, chemical passivation and sterilisation in ethylene oxide caused an increase in the oxygen in the surface layer in relation to the substrate, mainly resulting in the oxides such as: Cr_2O_3 and Fe_2O_3. Consequently, the concentrations of individual alloying elements (Fe, Cr, Ni) in relation to the chemical composition of the substrate were substantially decreased, which is found to be extremely favourable for the haemocompatibility of guide wires. All the elements occurred mainly in the oxidised condition.

To sum up, it must be stated that the chemical-passivation process performed after electrochemical polishing of the X10CrNi18-8 steel has a favourable impact on the physical and chemical characteristics, improving the haemocompatibility of the cardiologic guide wires made of this type of steel.

Acknowledgements

This project was financed from the funds of the National Science Centre in Cracow.

5 REFERENCES

[1] M. Kaczmarek, W. Walke, W. Kajzer, Arch. Mater. Sci. Eng., 28 (**2007**) 5, 273–276

[2] J. Marciniak, J. Tyrlik-Held, W. Walke, Z. Paszenda, Eng. of Biomat., X (**2007**) 69–72, 90–93

[3] D. Baim, W. Grossman, Angiography and Intervention, 6th edition, LWW, Philadelphia 2000

[4] D. Baim, W. Grossman, Angiography and Intervention, 7th edition, LWW, Philadelphia 2006

[5] M. Dewey, F. Teige, D. Schnapauff, Ann. of Int. Med., 145 (**2006**) 6, 407–415, doi:10.7326/0003-4819-145-6-200609190-00004

[6] W. Walke, J. Przondziono, Metalurgija, 50 (**2011**) 3, 201–204

[7] W. Walke, J. Przondziono, Arch. of Metall. and Mat., 58 (**2013**) 2, 625–630, doi:10.2478/amm-2013-0048

[8] ASTM F2129-08 Standard Practice for Selecting Generic Biological Test Methods for Materials and Devices, 2008

[9] ASTM F746-04(2009): Standard Test Method for Pitting or Crevice Corrosion of Metallic Surgical Implant Materials, 2009

[10] J. Marciniak, J. Tyrlik-Held, W. Walke, Z. Paszenda, Arch. Mater. Sci. Eng., 28 (**2007**) 5, 289–292

[11] W. Kajzer, A. Krauze, W. Walke, J. Marciniak, J. Achiev. Mat. Manuf. Eng., 18 (**2006**), 115–118

[12] C. R. Clayton, Y. C. Lu, J. Electrochem. Soc., 133 (**1986**) 12, 2465–2473, doi:10.1149/1.2108451

[13] J. M. Grimal, P. Marcus, Corr. Sci., 5 (**1992**), 805–814, doi:10.1016/0010-938X(92)90113-H

[14] A. Tortoriello, G. Pedrizzetti, J. of Biomech., 37 (**2004**), 1–11, doi:10.1016/S0021-9290(03)00259-8

UDK 666.3/.7:620.187
Original scientific article/Izvirni znanstveni članek

ISSN 1580-2949
MTAEC9, 49(2)229(2015)

TEM REPLICA OF A FLUORIDE-MISERITE GLASS-CERAMIC GLAZE MICROSTRUCTURE

TEM-REPLIKE MIKROSTRUKTURE STEKLOKERAMIČNE FLUOR-MIZERITNE GLAZURE

Jesus Ma. Rincón, Raquel Casasola
Vitreous and Ceramics Lab/Group, Instituto CC Construcción E. Torroja, CSIC, Madrid
jrincon@ietcc.csic.es

Prejem rokopisa – received: 2014-01-27; sprejem za objavo – accepted for publication: 2014-04-10

doi:10.17222/mit.2014.020

Several glazes were obtained for an application onto the surface of clay-based ceramic tiles that are usually produced by fast firing. Original glasses within the F-K_2O-CaO-SiO_2 system were obtained and during the sinter- crystallization of glass ceramic, fluoride-miserite ($KCa_5Si_8O_{22}F_2$) nanocrystals with an amount of 4.5 % F_2 were precipitated in the glassy matrix. These glassy tiles can be used for floor and wall coverings in buildings, for certain decorations in civil engineering and for pavements exhibiting good wear and anti-slip properties. The TEM-replica and extraction-replica methods were revisited for observing the microstructures of these glasses under the conventional TEM to elucidate clearly the phase separation that gives rise to the opalescence of these glasses and is strongly dependent on the fluorine included in the structures of these glasses.

Keywords: TEM-replica method, glass ceramics, glazes, tiles, miserite

Pridobljenih je bilo več glazur za uporabo na površini keramičnih ploščic na osnovi gline, ki se navadno proizvajajo s hitrim žganjem. V originalnem steklu iz sistema F-K_2O-CaO-SiO_2 so bili s postopkom sintranja in kristalizacije steklokeramike izločeni nanokristali fluor-mizerita ($KCa_5Si_8O_{22}F_2$) z vsebnostjo 4,5 % F_2. Te steklaste ploščice se lahko uporabijo na tleh ali stenah poslopij, ali kot dekoracija v gradbeništvu in za pločnike, ker izkazujejo dobre obrabne in protizdrsne lastnosti. Uporabljena je bila metoda TEM-replik in ekstrakcijskih replik za opazovanje mikrostrukture teh stekel v konvencionalnem TEM za pojasnitev ločevanja faz, ki povzročijo opalescenco teh stekel, kar je močno odvisno od fluora, ki je vključen v strukturi teh stekel.

Ključne besede: metoda TEM-replik, steklokeramike, glazura, ploščice, mizerit

1 INTRODUCTION

Glass ceramics developed widely in the previous century and found new applications in the first decade of the 21st century[1]. These applications include the use of the glass-ceramic processing (nucleation + crystal growth) in the production of improved glazes for ceramic-tile coverings[2]. These new glazes produced from frits give rise to a wide range of crystallites precipitated in the vitreous matrix of a glaze and are compatible with the fast-firing process and, even more importantly, with the traditional clay-ceramic and/or porcelainized substrates. The liquid-liquid phase separation or immiscibility in the glazes susceptible to a transformation in microcrystalline coatings has not yet been well described for ceramic tiles. With respect to the above, the glass ceramics, in which the fluoride phases are crystallized, are of great interest for the production of the materials with high toughness and flexural-strength values.

The aim of this work is to show the microstructures obtained in several original K_2O-CaO-SiO_2 glasses with different fluorine amounts, close to the composition of the crystalline phase called miserite $K(Ca,Ce)_6Si_8O_{22}(OH,F)_2$.[3] Though TEM/EDS allow us to carry out a microstructure determination of ceramics[4], due to the difficulties of the ion-thinning preparation, it was the objective of this research to apply the old traditional extraction carbon-triafol replica method to demonstrate the capability of observing the glass-in-glass or liquid-liquid phase separation[5,6], which additionally allowed us to simultaneously perform an analysis of the particle extraction, thus saving the time and cost required for the thinning methods.

2 MATERIALS AND METHODS

The original or starting glasses were obtained from some batch compositions with a miserite stoichiometric composition, $K(Ca,Ce)_6Si_8O_{22}(OH,F)_2$, without cerium, where the hydroxyl ions were first substituted with fluorine and later, in the second series, corrected with the consecutive additions of mass fractions (5, 8, 9 and 10) % fluorine added as a pure chemical CaF_2 powder. Potassium and calcium were added as carbonates and alumina, as well as silica, as pure oxides. The melting was carried out in a super-kanthal furnace at 1450 °C for one hour using alumina-silica crucibles from Lomba SL, Galicia, Spain. **Table 1** shows the initial, basic compositions and **Table 2** shows the corrected and final compositions determined with SEM/EDS for the M-4, M-8 and M-10 glasses. The M-5 composition is the closest to the stoichiometric miserite, being similar to M-10 but including Na_2O to facilitate the melting and the pouring operation after the melting. The M-4 glass includes some alumina stabilizing this glass and a higher amount of K_2O, while M-8 and M-9 allow a comparison of the increased calcium additions. As can be seen in the original composition, the basicity or the CaO/SiO_2 ratio, which is well known, is a factor controlling the viscosity variation at high temperatures in the 0.29–0.58 range.

Table 1: Initial or theoretical compositions of the "miserite glasses", studied with TEM, in mass fractions, *w*/%

Tabela 1: Začetna ali teoretična sestava "mizeritnih stekel", preiskovanih s TEM, v masnih deležih, *w*/%

Oxide (*w*/%)	M-4	M-5	M-8	M-9	M-10
Na_2O	–	–	–	–	5.00
K_2O	7.35	5.56	6.66	6.24	5.29
CaO	26.64	33.14	20.00	25.00	31.48
Al_2O_3	8.00	–	–	–	–
SiO_2	55.00	56.81	67.97	63.72	53.97
F (expressed as F_2)	3.00	4.49	5.37	5.04	4.27
Basicity (CaO/SiO_2)	0.48	0.58	0.29	0.39	0.58

After the melting of these original glasses, it was necessary to prepare new glasses with the increasing and sequential fluorine additions in order to determine the corrosion of the crucibles and the volatilization of fluorine in this type of glasses. **Figure 1** shows that fluorine volatilization growths linearly when the fluorine amount in the miserite glasses is increased. In the same way **Figure 2** shows the alumina amounts in the final glasses prepared with the increasing fluorine amount. It can be seen that the alumina amount added to these glasses on the basis of the corrosion of the alumina-silica crucibles also grows linearly, with the silica being in the same range for all the glasses considered, as can be seen in **Table 2,** affecting the actual compositions of the glasses analysed with SEM/EDS.

Table 2: Compositions, obtained with SEM/EDS, of the glass samples corrected with the increasing fluorine amount (fluorine and alumina are deduced from the crucible corrosion and the volatilization curves for M-5 and M-9 glasses)

Tabela 2: SEM/EDS-sestava v popravljenih vzorcih stekla s povečano vsebnostjo fluora (fluor in glinica izvirata iz korozije lonca in krivulje izhlapevanja za stekla M-5 in M-9)

Oxide (*w*/%)	M-E	M-5	M-8	M-9	M-10
K_2O	4.79	4.61	4.56	4.52	4.48
CaO	34.02	33.85	31.37	31.73	32.21
Al_2O_3	4.63	4.98	7.66	7.70	7.87
SiO_2	54.05	53.58	52.13	51.37	50.82
F (expressed as F_2)	2.51	2.80	4.27	4.90	5.63
Basicity (CaO/SiO_2)	0.62	0.63	0.60	0.60	0.63

Then, the final compositions of the sequential fluoride-miserite glasses show that the potassium amount is stable in different compositions, being volatile to the same extent in all the glasses studied. Calcium is also stable in all the glasses and close to the stoichiometric miserite composition. Even the basicities of these glasses are very similar, with the increasing fluorine amount being in a very narrow range of 0.60–0.63. However, the alumina based on the crucible corrosion grows with the increasing fluorine amount.

In order to investigate the microstructures of the original or starting glasses formulated around the miserite composition, the TEM-replica method was used to avoid the expensive and time-consuming preparations of the ion-thinning methods. Thus, the double triafolcarbon replica method used for years for observing very

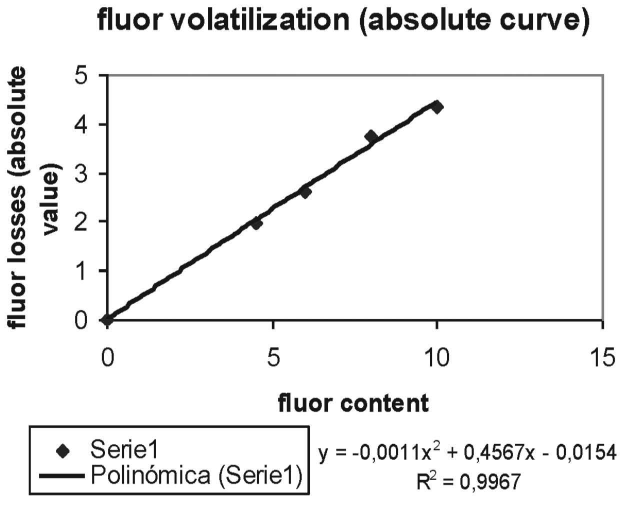

Figure 1: Absolute values of fluorine losses depending on the fluorine added to the original glasses

Slika 1: Absolutna vrednost izgub fluora v odvisnosti od dodanega fluora originalnim steklom

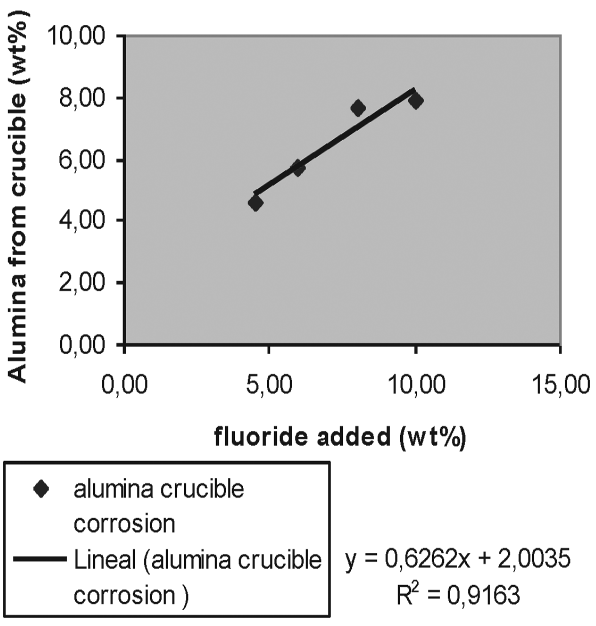

Figure 2: Alumina amounts determined with SEM/EDS versus the fluoride added to the sequential original glasses

Slika 2: Vsebnost glinice, ugotovljene s SEM/EDS, v odvisnosti od dodajanja fluorida zaporednim steklom

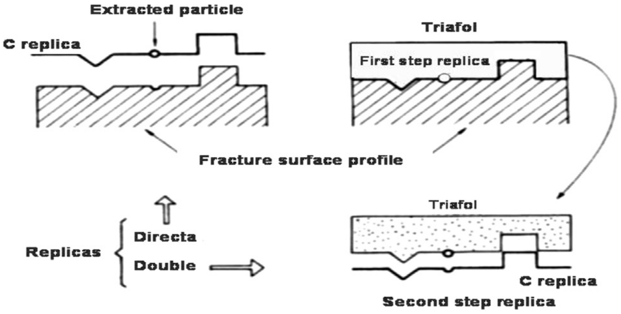

Figure 3: Succesive steps for the preparation of direct and double triafol-carbon replicas[7]

Slika 3: Zaporedje stopenj priprave neposrednih in dvojnih replik triafol – ogljik[7]

fragile samples with TEM was revisited as shown by Rincón et al.[7] **Figure 3** shows a simple drawing of the method steps from a fresh fracture and HF 2 %, 10 s, to the etched glass surfaces. The final carbon-replica skins were deposited on 3 mm Cu grids after transfering, smooth drying in an acetone bath and dissolving the first triafol plastic replica. The TEM equiment for the final observation of the replicas was a Philips CM-10 instrument working at 100 kV.

3 RESULTS AND DISCUSSION

Figures 4 and **5** show a summary of the main observations of the microstructures of the fluoride-miserite composition glasses. In the M-4 glass (**Figure 4**) a clear liquid-liquid phase separation of dispersed droplets with some networks in some areas can be seen.

In the case of glass M-5, the glass-in-glass phase separation is not present due to the crystallization of very small crystallites with an elongated shape in some cases. According to the binary CaO–SiO_2 phase diagram these crystals in the M-5 glass must be of wollastonite, coexisting with the liquid phase.

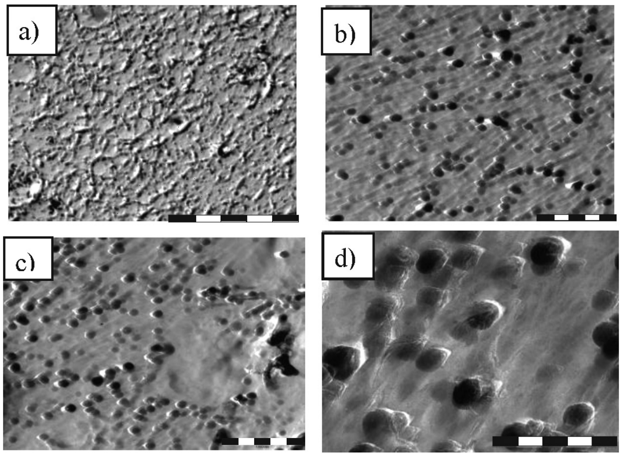

Figure 4: TEM micrographs of double replicas of M-4 glass: the inserted bars correspond to these magnifications: a) 5000 nm, b) 1000 nm, c) 1000 nm and d) 500 nm

Slika 4: TEM-posnetki dvojnih replik iz stekla M-4: prikazano merilo ustreza naslednjim povečavam: a) 5000 nm, b) 1000 nm, c) 1000 nm in d) 500 nm

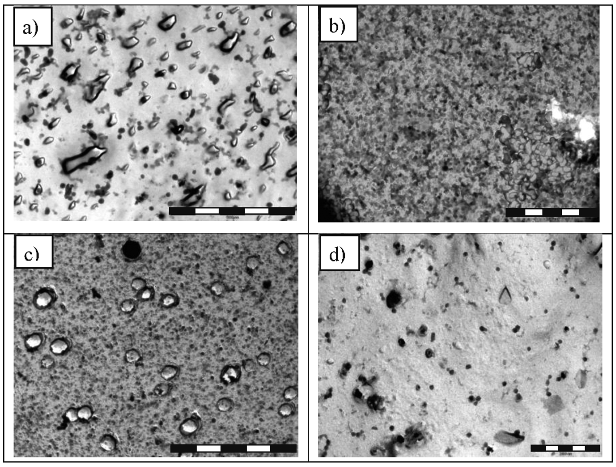

Figure 5: TEM double-replica micrographs for: a) M-5, b) M-8, c) M-9 and d) M-10 glasses: the inserted bars correspond to these magnifications: a) 5000 nm, b) 2000 nm, c) 5000 nm and d) 2000 nm

Slika 5: Mikroposnetki TEM dvojne replike iz stekel: a) M-5, b) M-8, c) M-9 in d) M-10; vrisano merilo pomeni ustrezno povečavo: a) 5000 nm, b) 2000 nm, c) 5000 nm in d) 2000 nm

Table 3: Quantitative evaluation of the glass-in-glass phase separation and the crystallites precipitated in the miserite glasses from the TEM replica observations

Tabela 3: Kvantitativna ocena izločanja stekla v steklu in izločkov kristalitov v mizeritnih steklih iz opazovanj TEM-replik

Original glasses	V_f (estimated)/%	Droplet average diameter (nm ± 10 nm)	Crystal average diameter (nm ± 20 nm)
M-4	50	120	No crystallites
M-5	30	No droplets	800–1000
M-8	80	130 (interconnected)	clusters = 1800
M-9	80	100	830
M-10	10	100 (very few droplets)	480

For the other glasses investigated with TEM, the representative micrographs obtained with the replica observations are shown in **Figures 5a** to **5d**. It can be seen that the M-8, M-9 and M-10 glasses show different microstructures. Thus, in the M-8 glass, there are clusters of crystals coexisting with opaque nanocrystals, possibly of cuspidine and/or miserite. The microstructure of glasses M-9 and M-10 is completely different, there are rounded and pseudo-polyonal habit crystallites that must be undissolved Ca_2F in the glassy matrix. Droplets are shown at higher magnifications. In these glasses the Ca_2F crystals coexist with very small nanodroplets of the residual phase separation or, more probably, the nanocrystals of miserite (dark nanocrystals) and cuspidine (white nanocrystals). **Table 3** shows volume fraction of immiscibility and size of droplets and nanocrystals.

When the compositions of these miserite glasses are located in the binary $CaSiO_3$–SiO_2 diagram taken from[8] (**Figure 6**), showing the over-liquidus glass-in-glass

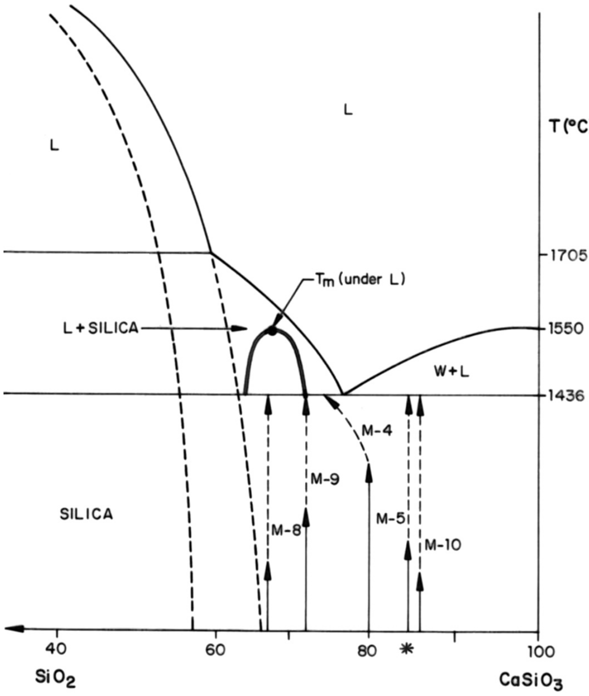

Figure 6: $CaSiO_3$–SiO_2 binary system with the liquid-liquid phase-separation zone (a phase-separation dome below the liquidus and near the eutectic and/or an extension to the third component are proposed) (modification of the figure from[8])

Slika 6: Binarni sistem $CaSiO_3$–SiO_2 z ločenim področjem izločanja talina-talina (predlagano je izločanje kupolaste faze pod likvidusom blizu evtektika in/ali razširitev do tretje komponente; prirejeno po viru[8])

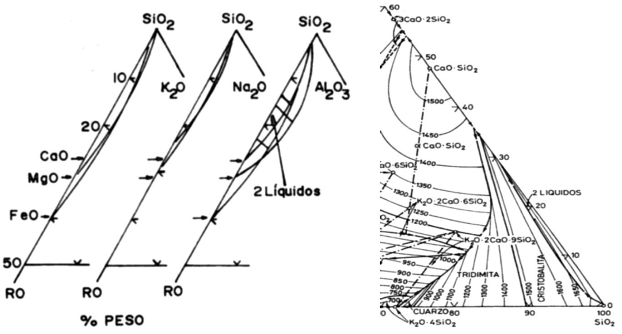

Figure 8: Ternary compositions of glasses showing the narrow glass-in-glass and/or liquid-phase separation zones for the ternary systems: RO–K_2O–SiO_2, RO–Na_2O–SiO_2, RO–Al_2O_3–SiO_2 and K_2O–CaO–SiO_2 [6]

Slika 8: Ternarna sestava stekel, ki prikazuje ozko področje steklo v steklu in/ali področje izločanja taline v ternarnih sistemih: RO–K_2O–SiO_2, RO–Na_2O–SiO_2 , RO–Al_2O_3–SiO_2 in K_2O–CaO–SiO_2 [6]

phase separation, it can be seen that all the considered compositions are far from this zone and that droplets of the phase separation are present in the M-4, M-8 and M-9 glasses. The M-8 and M-9 compositions are located in the two phases of silica + liquid area below the liquidus. The M-4 composition is very close to the eutectic, between the above-mentioned area and the wollastonite + liquid area below the liquidus. The M-5 and M-10 glasses with very similar compositions are located in the wollastonite + liquid area. Therefore, these glasses were produced during the cooling as a precipitation of very small crystals of wollastonite (CaO–SiO_2) with no glass-in-glass phase separation. Conversely, the compositions of M-8 and M-9 show a phase separation during the TEM replica observations of the droplets that must be enriched with SiO_2 according to the theory of the phase separation in glasses[5,6]. This fact made us think that there is a dome below the liquidus in this zone, consisting of silica + liquid zone and that this is the only explanation for the immiscibility in these glasses, considering the simplification of this composition system.

This proposed cupula or dome of immiscibility is congruent with the inclusion of the third modifier cations in these glasses (**Tables 1** and **2**) and the relative location of immiscibility in the binary systems, as can be seen in **Figure 6**, where an extension of the immiscibility in this area and/or, as proposed, the second immiscibility dome occurring below the liquidus can be found in this area of the simplified phase diagram. Even more, if we consider the ternary systems of Na_2O–CaO–SiO_2, K_2O–CaO–SiO_2 and Al_2O_3–CaO–SiO_2 the phase-separation areas are very

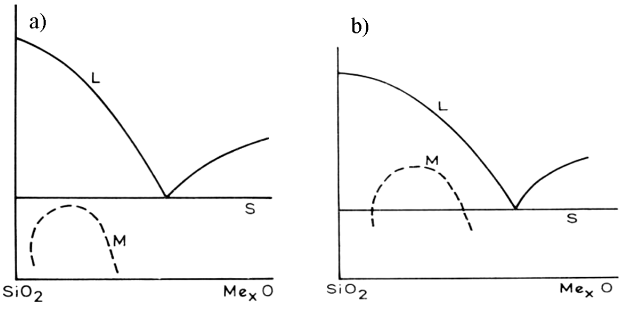

Figure 7: a) Liquid-phase separation below the solidus line in a binary system and b) liquid-phase separation below the liquidus in a binary system[9]

Slika 7: a) Izločanje staljene faze pod solidusno linijo v binarnem sistemu in b) izločanje staljene faze pod likvidusno linijo v binarnem sistemu[9]

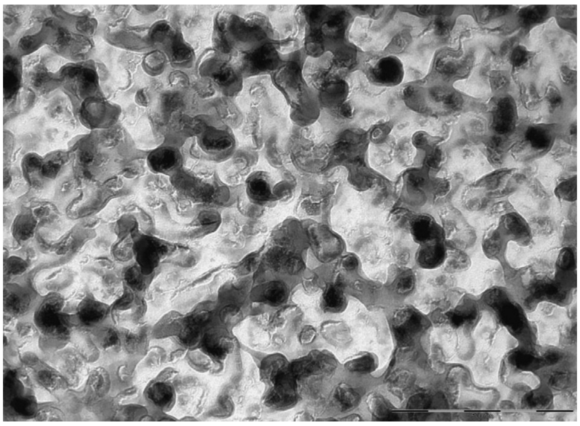

Figure 9: Microstructure of the M-8 miserite glass showing a spinodal-like decomposition

Slika 9: Mikrostruktura mizeritnega stekla M-8, ki kaže razgradnjo, podobno spinodalni reakciji narrow being the miserite glasses within the limits of these immiscibility zones.

Therefore, the presence of liquid immiscibility in these glasses is very critical but, in any case, favored by the presence of fluorine ions in a glass network structure. As shown in **Figure 6**, this area of the metastable immiscibility in miserite glasses can be produced at the 1436 °C solidus limit and extended below such a solidus line in the metastable conditions, which are the usual liquid-freezing conditions for obtaining glasses. Another possible hypothesis is that the known area of the metastable miscibility at the solidus where the eutectic and the liquidus line of the monotectic reaction (1705 °C) are located can be extended or widened to the lower silica amount in this diagram. This situation is well-known in the binary $R_2O–SiO_2$ systems as shown in **Figure 7**[9] and even in the corresponding ternary diagrams (**Figure 8**)[5,6].

The miserite M-8 glass shows, in some zones, an interconnected-droplet microstructure, while this type of immiscibility microstructure was not observed in the other miserite glasses (**Figure 9**). In principle, this may correspond to the spinodal decomposition as demonstrated by the Cahn theory for the compositions in the center of the phase-separation cupolas[5,6]. In this case, while observing the relative location of the M-8 glass in a simplified pseudobinary system involving CaO (**Figure 6**) it can be seen that this composition is close to the centre of the proposed second dome, close to T_c, the temperature of the maximum immiscibility for the binary domes. Therefore, in spite of the very narrow areas of the phase separation in the basic composition of the $K_2O–CaO–Al_2O_3–SiO_2$ glasses and the similarly that was demonstrated by Chiang and Kingery[10] it is possible to obtain the glasses with a liquid-liquid immiscibility according to the several microstructures of the phase-separation phenomena.

Finally, it is evident that this immiscibility can be observed with scanning electron microscopy (SEM). However, our experience in observing this effect in glasses showed that a clear definition of immiscibility is only possible when revisiting the traditional TEM replica method, as was the case in this investigation. More research is now in progress involving different compositions of mica glass-ceramics such as fluorphlogopite and others[11].

4 CONCLUSIONS

The TEM replica method was revisited to study the microstructures of the original fluoride-miserite glasses, using the conventional TEM, and to elucidate the phase separation inherent to these opalescent glasses. These liquid-liquid and/or glass-in-glass phase separations strongly depend on the fluorine level in a vitreous structure, reaching the maximum values with the lowest fluorine amounts. At higher fluorine concentrations there are precipitations of Ca_2F and the nanocrystals of wollastonite, cuspidine and/or miserite, depending on the glass composition.

Acknowledgement

The authors wish to thank for the facilities provided by the Polytechnic University of Valencia (UPV), Servei de Microscopia Electronica, and the valuable help from Manuel Planes when using the TEM equipment. They also thank Eduardo Cabrero, IETcc, CSIC, for helping them draw the original figures and Dr. M. Romero from the IETcc-CSIC for giving valuable advice to R. Casasola regarding her Ph. D. Thesis.

5 REFERENCES

[1] A. G. Guy, Essentials of Materials Science, McGraw-Hill, 1976, 97

[2] J. Ma. Rincón, Principles of nucleation and controlled crystallization of glasses, Polym. Plast. Technol. Engineering, 31 (**1992**) 3–4, 309–357, doi:10.1080/03602559208017751

[3] R. Casasola, J. M. Pérez, J. Ma. Rincón, M. Romero, 50th Congress of the Spanish Glass and Ceramics Society VI-P-01, Bol. Soc. Esp. Ceram. Vidr., 49 (**2010**) 5, 35

[4] J. Ma. Rincón, Microstructural characterization by electron microscopy of ceramics and glasses, Microscopy and Analysis, (**1996**), 23–25

[5] J. Ma. Rincón, Separación de fases en el vidrio, Bol. Soc. Esp. Ceram. Vidr., 11 (**1972**) 1, 111–125

[6] J. Ma. Rincón, A. Durán, Separación de fases en Vidrios, El Sistema $Na_2O-B_2O_3-SiO_2$, Edited by the Spanish Glass and Ceramic Society, SECV, Arganda del Rey, Madrid, 1982

[7] J. Ma. Rincón, P. Callejas, F. Capel, Fractografía de vidrios y materiales vitrocristalinos, Bol. Soc. Esp. Ceram. Vidr., 28 (**1989**) 4, 257–267

[8] J. R. Taylor, A. T. Dinsdale, Thermodynamic and phase diagram data for the $CaO-SiO_2$ system, Calphad, 14 (**1990**) 1, 71–88, doi:10.1016/0364-5916(90)90041-W

[9] E. Plumat, La formation de systèmes pseudo-vitreux et pseudo-cristallines, Silicates Industriels, 1 (**1967**), 5–13

[10] Y. M. Chiang, W. D. Kingery, Spinodal decomposition in a $K_2O–Al_2O_3–CaO–SiO_2$ glass, Journal of the Amer. Ceram. Soc., 66 (**1983**) 9, c171–c172, doi:10.1111/j.1151-2916.1983.tb10632.x

[11] R. Casasola, Ph. D. Thesis, Autonoma University of Madrid, 2013

UDK 519.61/.64:620.174:620.173
Original scientific article/Izvirni znanstveni članek

ISSN 1580-2949
MTAEC9, 49(2)235(2015)

EXPERIMENTAL ANALYSIS AND MODELING OF THE BUCKLING OF A LOADED HONEYCOMB SANDWICH COMPOSITE

EKSPERIMENTALNA ANALIZA IN MODELIRANJE UPOGIBANJA OBREMENJENEGA SATASTEGA SENDVIČNEGA KOMPOZITA

Abderrahmane Bentouhami, Boualem Keskes
Laboratoire de mécanique de précision appliquée, Institut d'Optique et Mécanique de Précision, Université Ferhat Abbas de Sétif, Algérie
bentouhamidahman@yahoo.fr, bkeskes2012@gmail.com

Prejem rokopisa – received: 2014-02-22; sprejem za objavo – accepted for publication: 2014-03-28

doi:10.17222/mit.2014.039

Sandwich panels have the best stiffness-to-lightness ratio, which is what makes them very useful in industrial applications. This paper is focused on a study of the buckling capacities of the core components under uniaxial compression. The critical buckling loads for various core densities and materials of honeycomb panels were experimentally and numerically investigated. The specimens under lateral loading showed three zones: zone 1 is the initial elastic state, followed by the plateau region in zone 2, while zone 3 shows a monotonically stiffening region, associated with the densification of the material. The effect of the core density and its materials on the behavior and the damage was highlighted. From the experiment it is clear that the buckling load of the specimens increases as the core density is increasing. In terms of stiffness and load at failure, the honeycomb sandwich panel had better mechanical characteristics than its components. The study also calculated the numerical buckling loads of the panels using the ABAQUS finite-element analysis program. The achieved experimental and numerical results were compared with each other. In conclusion, a good correlation between theory and experiment was found.

Keywords: honeycomb sandwich panel, buckling analysis, compression, finite-element method, collapse

Sendvični paneli imajo najboljše razmerje med togostjo in maso. To jih dela primerne za industrijsko uporabo. Ta članek je usmerjen v študij zdržljivosti za upogibanje ključnih komponent pri enoosni tlačni obremenitvi. Eksperimentalno in numerično so bile preiskane kritične upogibne obremenitve za različne ključne gostote in material satastih plošč. Vzorci, stransko obremenjeni, so pokazali tri področja: področje 1 je začetno elastično stanje, ki mu sledi področje platoja, tj. področje 2. Področje 3 prikazuje monotono upogibanje, povezano z zgoščevanjem materiala. Ocenjen je bil vpliv ključne gostote in materialov glede vedenja in poškodb. Iz preizkusov je razvidno, da z naraščanjem ključne gostote narašča tudi odpornost proti upogibni obremenitvi vzorcev. Glede na upogibanje in obremenitev pri porušitvi ima satasta sendvična plošča boljše mehanske lastnosti v primerjavi z njenimi komponentami. V študiji je tudi izračunana numerična upogibna obremenitev panelov z analizo končnih elementov s programom ABAQUS. Primerjani so dobljeni eksperimentalni in numerični rezultati. Dobljena je bila dobra korelacija med teorijo in eksperimentalnimi rezultati.

Ključne besede: satasta sendvična plošča, analiza upogibanja, tlačenje, metoda končnih elementov, porušitev

1 INTRODUCTION

Honeycomb sandwich panels are increasingly used in engineering applications (aviation, astronautics and navigation, automotive, etc.), where a high rigidity as well as lightness is important. A number of core materials and core configurations have been proposed recently. The most commonly used core materials are honeycombs and foams. Honeycomb sandwich panels are obtained by covering the upper and lower surfaces of the honeycomb with sheets. Metal or non-metal materials can be used as the lower and upper surface face sheet materials of honeycomb sandwich panels. The widespread use of honeycomb in practice generated a need to establish their mechanical properties. Previous studies on the crushing behavior of honeycomb structures included the early work reported by McFarland,[1] who developed a semi-empirical model to predict the crushing stress of hexagonal cell structures subjected to axial loading. This model as later improved to incorporate both the bending and extensional deformation of such cellular structures.[2]

Meanwhile, the mechanical properties of honeycomb structures in the lateral directions were investigated both analytically and experimentally by Gibson and Ashby,[3] and Gibson et al.[4] In their works, phenomenological models were proposed. More detailed analyses of the buckling of tubes with various geometries have been reported, and some of these results correlated well with the experimental data.[5–9] A more complete description of the buckling mechanisms for thin-walled tubular structures subjected to quasi-static and dynamic loading can be found in[10,11]. On the other hand, the mechanical behavior of sandwich composite panels made of honeycomb cellular structures has been studied extensively. For example, the force-indentation relationship for beams and plates made of sandwich polymer composites was investigated by Wu and Sun.[12] This relationship was later adopted by Lee and Tsotsis[13] to develop an impact model to predict the transient responses of sandwich composite parcels. As for sandwich plates and shells whose faces were made of metal, experimental results have been reported by Goldsmith and Sackman.[14] A plasticity model has been reported by Jamjian et al.[15] for metallic sandwich panels subjected to impact, in which the honeycomb was treated as a continuum with a discontinuous density.

Kaman et al.[16] have experimentally and numerically investigated the behavior and failure mechanisms of honeycomb core panels. They have determined that the critical buckling load of Nomex is higher than that of aluminum comb composite panels for all cell sizes. Castanié et al.[17] showed that the compression load is essentially taken by the vertical edges of the hexagonal cell. From the axial compression collapse tests on the aluminum honeycomb sandwich panel specimen, various potential influential parameters, i.e., the core height, core-cell thickness and panel aspect ratio, it was observed that the core height would be a crucial parameter affecting the sandwich panel's ultimate compressive strength.[18] Tsang and Lagace[19] reported the different failure mechanisms in impact-damaged sandwich panels subjected to uniaxial compressive loads. They observed that the damage propagation and final failure modes were dependent on the relative extents of the core and face-sheet damage. They reported dimple propagation across the width of the panel, which occurred in the presence of core damage, with the final failure mode being a face-sheet fracture. Zhou and Mayer[20] studied the shear, tearing, and compression tests over honeycomb aluminum, which showed different failure modes involved in a general crash accident. Mohr and Doyoyo,[21,22] Hong et al.[23] performed multi-axial loading tests of honeycomb materials and derived the macroscopic yield functions for the honeycomb materials. Wilbert et al.[24] proved that following an initial linear response, the cell walls buckle elastically. The post-buckling response is initially stiff and stable, but the inelastic action progressively softens it, leading to a limit load instability. The deformation localizes first at mid-height in the form of a sharp buckle, which with the load continuing to drop more into folding. When the walls of the fold come into contact, the local collapse is arrested, the load begins to recover, and a second fold develops on one side of the first one. The second fold in turn collapses, forming a new load peak and a second trough. This progressive folding keeps repeating until the whole panel is consumed and the structure returns to a stiff response.

The present study is concerned with the more traditional problem of transverse compression. In particular, we aim to establish all aspects of the compressive response and explain the buckling phenomena of honeycomb sandwich structures. The critical buckling loads for various core densities and the materials of honeycomb panels are experimentally and numerically investigated. The different specimens exhibited similar load/displacement curves and the differences observed were only due to the behavior of the different materials. The study also calculates the numeric buckling loads of the panels using the ABAQUS finite-element analysis program. The achieved experimental and numerical results are compared with each other and the results are presented in curves. In conclusion, a good correlation between theory and experiment was found.

2 EXPERIMENTAL PROCEDURES

The critical buckling loads and crushing behavior of the honeycomb sandwich panels were determined by running through compression tests using a computerized universal testing machine Zwick/Roell (100 kN) (**Figure 1**). The test procedure for the compressive properties was

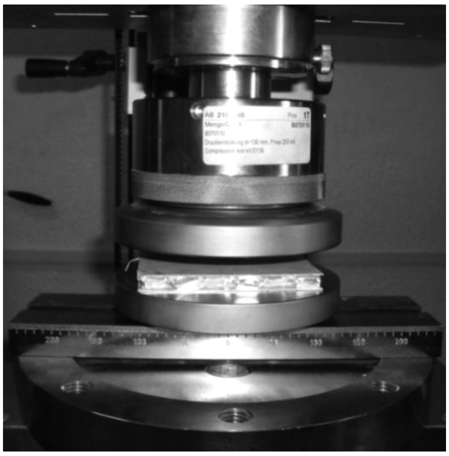

Figure 1: Experimental set-up of the compressive test
Slika 1: Eksperimentalni sestav za tlačni preizkus

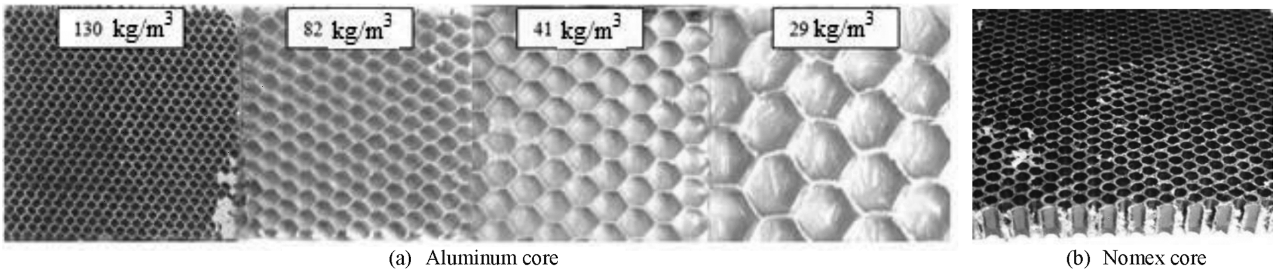

(a) Aluminum core

(b) Nomex core

Figure 2: Typologies of investigated honeycomb sandwich: a) aluminum core, b) Nomex core
Slika 2: Vrste preiskovanih satastih sendvičnih plošč: a) jedro iz aluminija, b) jedro nomex

as per the ASTM C 365 standards. Aluminum honeycomb with cell sizes of (3.2, 6.4, 9.6 and 19.2) mm and densities of (29, 41, 82 and 130) kg/m^3, Nomex honeycomb with a cell size of 3.2 mm and densities of (48, 80, 128 and 144) kg/m^3 were used to complete the tests series (**Figure 2**). The dimension of the compressive specimen was 50 mm × 50 mm × 10 mm. The tests were performed at a constant cross-head speed of 0.5 mm/min.

2.1 Modeling of the cell walls of honeycomb composites

When the honeycomb composite was loaded in compressive mode, it was assumed that a uniform compression was achieved on the two edges parallel to the compressive loading direction of each wall, as shown in **Figure 3**. It was also assumed that the cell walls of the honeycomb composite were rigidly constrained by the neighboring cell walls and that all the cell walls were deformed to the same strain. Therefore, the compressive stress of the honeycomb composite is the sum of the stresses carried by the individual cell walls. The assumptions, due to its geometrical symmetry of the cross-section, are as follows:[25]

When the thickness h_c of a honeycomb core is not large compared with the length of side a, the buckling mode of a cell shell is based on a cell wall, every wall has a similar buckling mode, and the phases among the cell walls are the same or reversed. At the same time, every prismatic edge remains a straight line, and each cell wall looks like a rectangular thin-walled plate simply supported on all four edges.

If a sandwich panel with a hexagonal cell core is thick, the buckling mode of the cell shell is a deflection of the axial centerline, and the deformation of every prismatic edge is similar to that of he axial centerline. According to Equation (1), every wall becomes a rectangular, thin-walled, nd simply supported on all four edges, as described in **Figure 3**. The buckling investigation on a ell wall can be substituted for that of the entire cell shell. The governing differential equation of the cell wall can be expressed as follows:

$$D\left(\frac{\partial^4 W}{\partial x^4}+2\frac{\partial^4 W}{\partial x^2 \partial y^2}+\frac{\partial^4 W}{\partial y^4}\right)+F_x\ \frac{\partial^2 W}{\partial x^2} \tag{1}$$

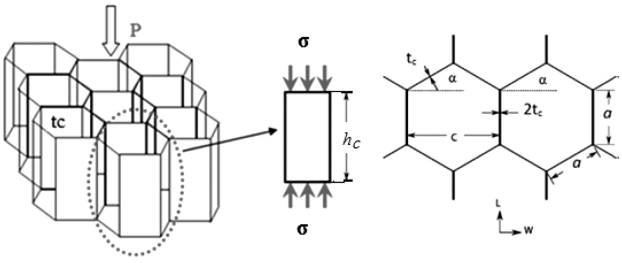

Figure 3: Modeling of honeycomb core with hexagonal cell under uniform compression loading

Slika 3: Modeliranje satastega jedra s heksagonalnimi celicami pri enakomerni tlačni obremenitvi

The boundary conditions are often written as:

$$W=0,\ \frac{\partial^2 W}{\partial y^2}=0 \text{ when } y=0,\ a \tag{2}$$

$$W=0,\ \frac{\partial^2 W}{\partial x^2}=0 \text{ when } x=0,\ h_c \tag{3}$$

Under the restriction of boundary conditions, the solution (local buckling) of Equation (1) can be written as:

$$W(x,y)=\sum_{m=1}^{\infty}\sum_{n=1}^{\infty} A_{mn}\ \sin\frac{m\pi x}{h_c}\sin\frac{n\pi y}{a} \tag{4}$$

The formula for a rectangular cell wall under equal uniform compression on two opposite edges, h_c, was shown as in Equation (5). The theoretical compressive stress on a cell wall used in this study was based on Zhang and Ashby's model and can be expressed as follows:

$$F=K_C\ \frac{E}{1-v^2}\left(\frac{t_c^3}{h_c}\right) \tag{5}$$

where K_C is the end constraint factor in the compression mode and its value[26,27] is 5.73, E is the elastic modulus of the cell walls, v is the Poisson's ratio of the cell walls, t_c is the thickness of the cell wall and h_c is the length of the free wall.

Equation (1) is expressed as the load F on a cell wall. The compressive load of the individual hexagonal cell of the honeycomb core is the sum of the loads carried by the individual cell walls. The total compressive load is $10F$, which is the sum of the compressive load, $2F$, carried out by the free walls with single thickness and the compressive load, $8F$, and carried by the ribbon with double thickness because the load is proportional to the cube of the thickness, as shown in Equation (5). The area, A_{hex}, of the individual hexagonal cell in a honeycomb core is calculated as $2h_c \cos\alpha \times h_c \sin\alpha + 2h_c \cos\alpha \times h_c$, where α is the angle of the inclined cell wall. The compressive strength, σ_C, carried by the unit hexagonal cell, is expressed as in Equation (2):

$$\sigma_c=\frac{10F}{A_{hex}}=\frac{5K_C E}{(1-v^2)\cos(1+\sin\alpha)}\frac{t^3}{hc^3} \tag{6}$$

3 RESULTS AND DISCUSSION

Figure 4 shows a typical stress-strain curve obtained from a compressive test of the honeycomb composite.

The compressive deformation process can be categorized into three regions (1, 2 and 3) based on the compressive stress-strain behavior.

The figure shows that the stress-strain relationship is linear in Region 1 up to the bare compressive strength. The honeycomb cell walls are in the elastic buckling condition in Region 1 (**Figure 5**).

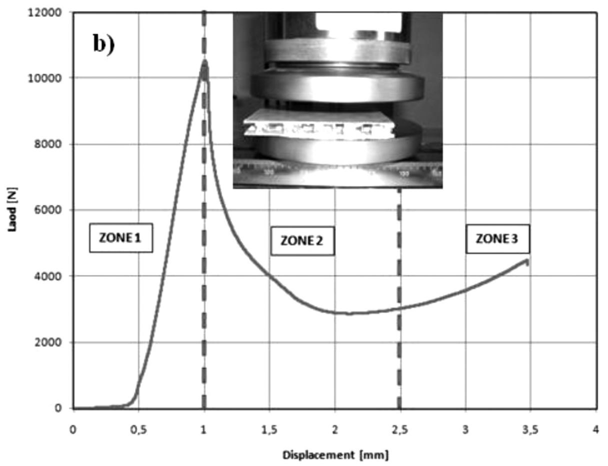

Figure 4: Load-displacement curve for an aluminum honeycomb sandwich

Slika 4: Krivulja obremenitev – raztezek satasto sendvične plošče iz aluminija

Later, a sudden decrease in the compressive stress occurs in Region 2. In this region, the core walls are in the plastic buckling condition and, as a result, wall folding occurs (**Figure 5**).

The compressive stress remains approximately stable in Region 3 until the densification of the folds in the honeycomb core. This stable stress value is defined as the crushing strength. In this region the crushing and fracture of the cores start (**Figure 5**). Depending on the core densification at the end of Region 3, an increase in the compressive stress is observed, as was reported in[16–24].

Initial collapse occurs at a load that is about twice that of the average steady load causing progressive crushing. The amplitudes of the little peaks, which signify progressive folding collapse, are higher initially and gradually decrease, as shown in **Figure 4**. Plastic collapse always occurred at one (usually the top) end and the deformation front gradually progressed with continued crushing until the plastic folding deformation approached the lower end of the specimen. Then the load increased very rapidly, indicating the densification of the specimen. The load-displacement graphics of the aluminum and Nomex honeycomb sandwich panels for different densities, resulting from the experiment, are given in

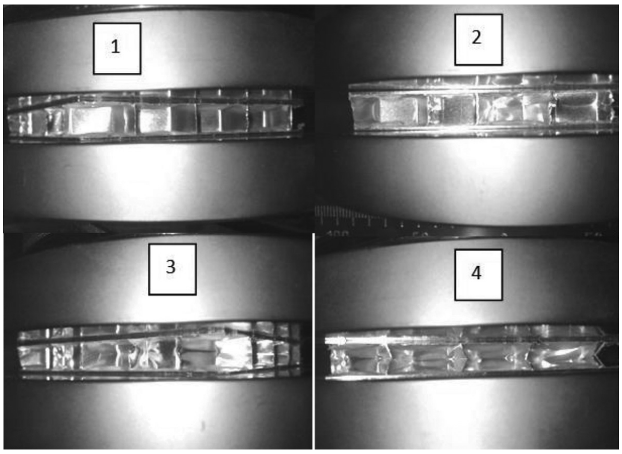

Figure 5: Stages of quasi-static compression test of aluminum honeycomb: (1) initial state, (2) buckling initiation, (3) progressive folding and (4) densification

Slika 5: Stopnje kvazistatičnega tlačnega preizkusa satja iz aluminija: (1) začetno stanje, (2) začetek upogibanja, (3) napredovanje zlaganja, (4) zgoščevanje

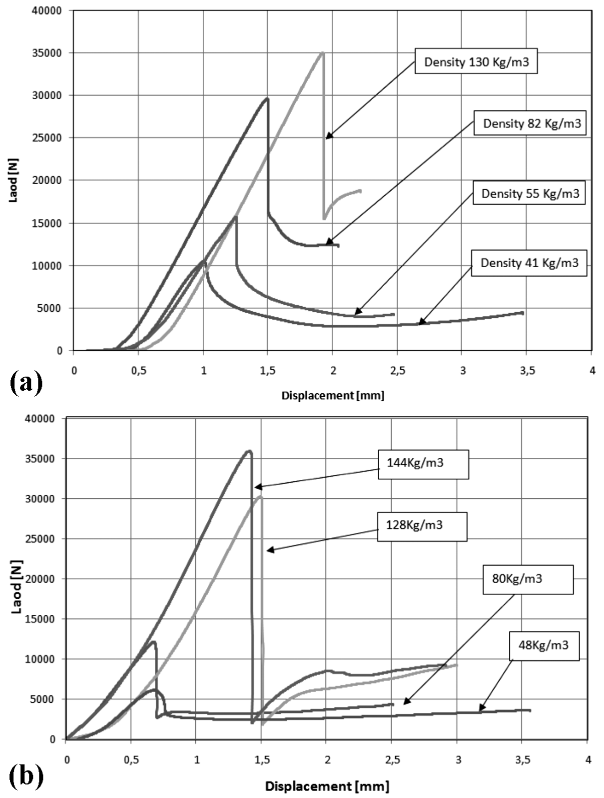

Figure 6: Load-displacement curves for honeycomb sandwich panels for different core densities: a) aluminium and b) Nomex

Slika 6: Krivulje obremenitev – raztezek za sataste sendvične panelne plošče z različno gostoto jedra: a) aluminij, b) nomex

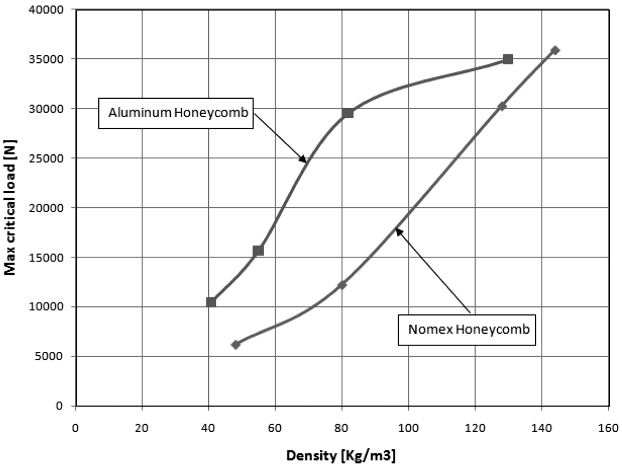

Figure 7: Evolution of the critical maximum load with the core density

Slika 7: Odvisnost kritične maksimalne obremenitve od gostote jedra

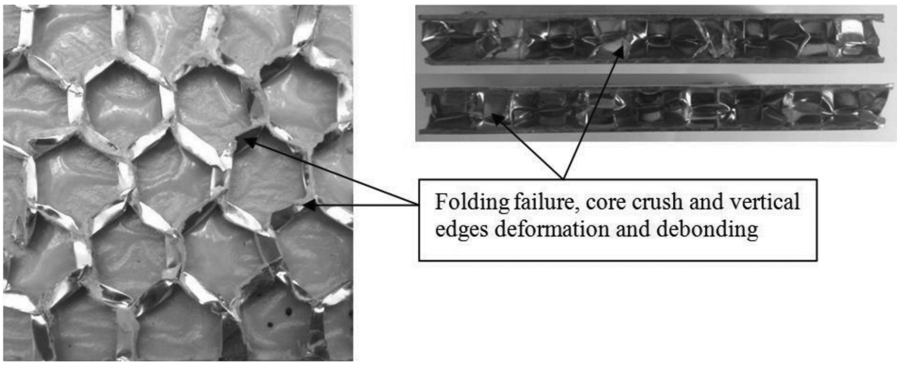

Figure 8: Failure mode of aluminum honeycomb sandwich
Slika 8: Način porušitve satastega sendviča iz aluminija

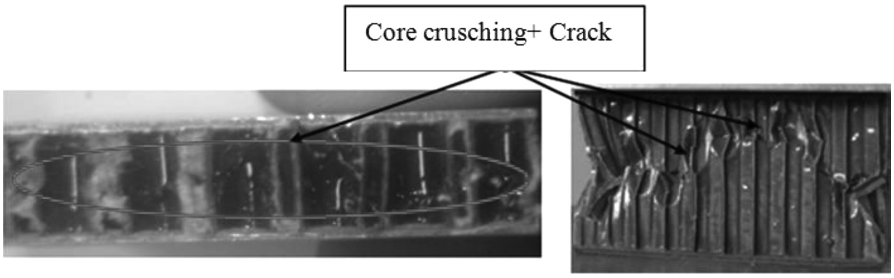

Figure 9: Failure modes of Nomex honeycomb panels for a cell size of 3.2 mm
Slika 9: Način porušitve sataste plošče nomex z velikostjo celice 3,2 mm

Figure 6. It is clear that the maximum critical buckling load values of the aluminum core panels are higher than those of the Nomex core panels (**Figure 7**). Also, as the density increased, the compressive strength of both the Nomex and aluminum honeycomb panels increased.

The honeycomb compressive behavior intrinsically relates to the cell-wall buckling behavior under compression, because in reality the vertical cell walls can never be compressed along the length direction until a pure compressive failure due to the instability of the thin structure occurs. Therefore, the dominant mode of damage in these structures is the buckling of the cells' walls.

Besides the compressive strength, the establishment of the incurred failure modes during the experiment is also important. As the load increased, the initial honeycomb wall buckling and the later regional cell wall folding and core crushing were observed in the aluminum core sandwich panels (**Figure 8**). The failure modes of the Nomex panels under compression load show a similar behavior to that of the aluminum honeycomb. But for the Nomex core panels, which are more than aluminum, prior to the core crushing failure, crack generation occurred (**Figure 9**). The failure, which started as a cell-wall buckling, caused cracks under greater compression loads (**Figures 8** and **9**) than were reported in[16,21–24]. For the honeycomb core compressed in the axial direction, the localization occurs in the well-defined plastic collapse bands at the interface between the crushed and uncrushed structural regions.

Figure 10 shows the evolution of the load for two different cell-wall thicknesses. From the obtained results, we see that the stiffness of the honeycomb sandwich panels increases with the cell-wall thickness.

To account for the influence of the thickness of the cell wall, the compression test has been made and the results of the variation of the load for two different wall thicknesses of the honeycomb core for a 6.4 mm cell size, the obtained results are given in the figure. According to the results of the experiment, we find that the wall thickness of the cell also has a significant impact on the

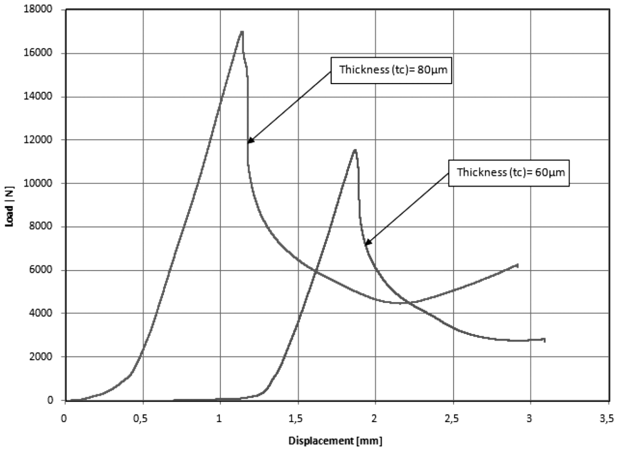

Figure 10: Effect of the cell-wall thickness on the buckling load for an aluminum honeycomb core
Slika 10: Vpliv debeline sten celic na obremenitev pri upogibu za satasto celico iz aluminija

critical buckling load. It is clear that the critical buckling load increased with an increase of the cell-wall thickness.

4 NUMERICAL STUDY

The ABAQUS package program, based on the finite-element method, is used as the solution method to numerically establish the critical buckling loads and the complex compressive response and crushing of honeycomb sandwich panels after the buckling observed in the experiments. The shell elements are appropriate because the thickness is the smallest planar dimension (**Figures 11** and **12**). The finite-element mesh uses the fully integrated S4R shell element as a regular mesh with nearly square elements, while the number of elements used was selected from convergence studies. The panels, for which the compression test was performed, are three-dimensional and the mechanical properties of the utilized materials are given in **Table 1**.

Table 1: Sizes cell and mechanical properties of used core materials for modeling
Tabela 1: Velikost celic in mehanske lastnosti uporabljenih materialov za jedra za modeliranje

Density (kg/cm^3)	h_c/mm	S/mm	t_c/mm	E_c/MPa	ν_c
29	8.8	19.2	0.080	69000	0.3

To study the sensitivity of the critical buckling load with various parameters, such as the cell's number, the cell's size and the thickness of the cell wall, we con-

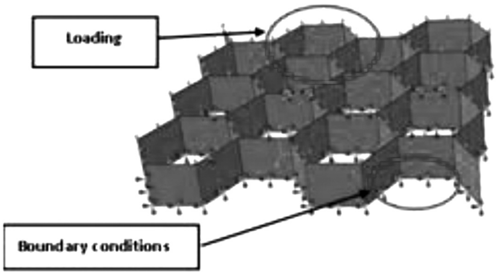

Figure 11: Finite-element model and boundary conditions of honeycomb sandwich panels
Slika 11: Model končnih elementov in robni pogoji za satasto sendvično ploščo

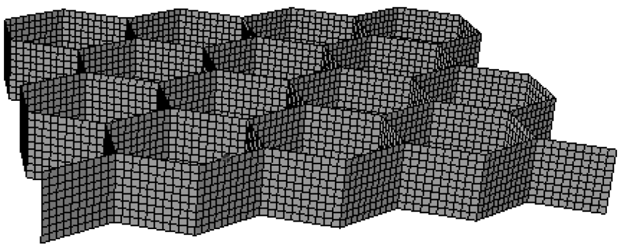

Figure 12: Finite-element mesh (S4R) model for buckling simulation of honeycomb sandwich panel
Slika 12: Model mreže končnih elementov (S4R) za simulacijo upogibanja sataste sendvične plošče

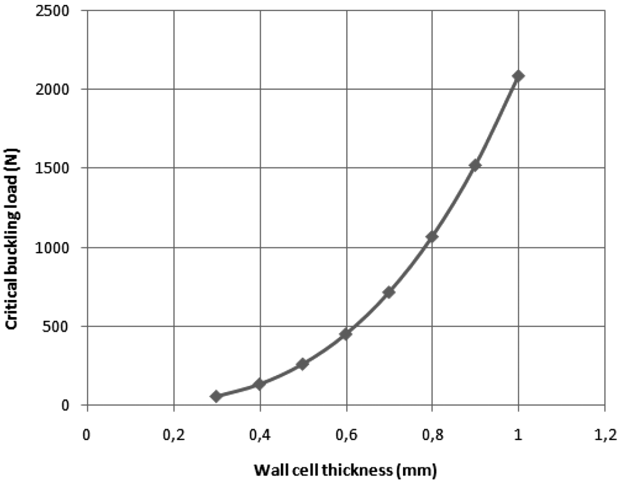

Figure 13: Variation of buckling load with cell-wall thickness for different honeycomb core materials for a cell size 19.2 mm
Slika 13: Spreminjanje obremenitve pri upogibanju v odvisnosti od debeline stene celice za različne materiale satastega jedra pri velikosti celice 19,2 mm

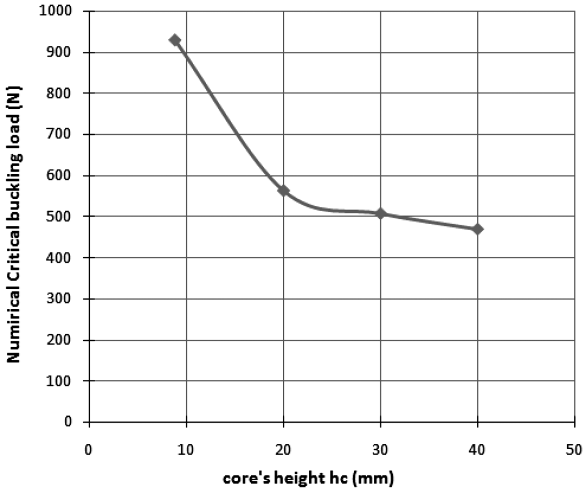

Figure 14: Variation of the numerical critical buckling load (F_{cn}) with the core thickness (h_c)
Slika 14: Spreminjanje numerične kritične obremenitve (F_{cn}) pri upogibu z debelino jedra (h_c)

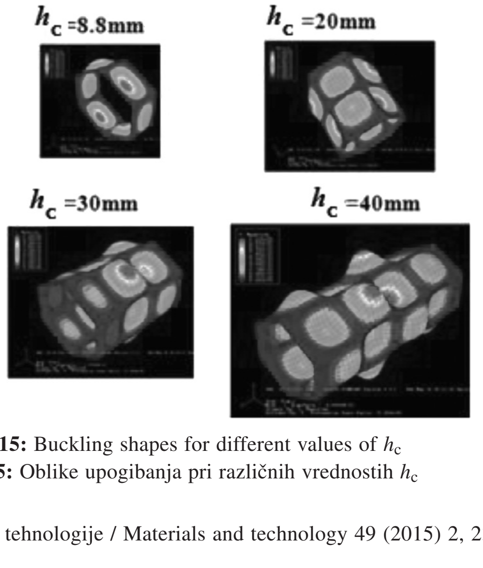

Figure 15: Buckling shapes for different values of h_c
Slika 15: Oblike upogibanja pri različnih vrednostih h_c

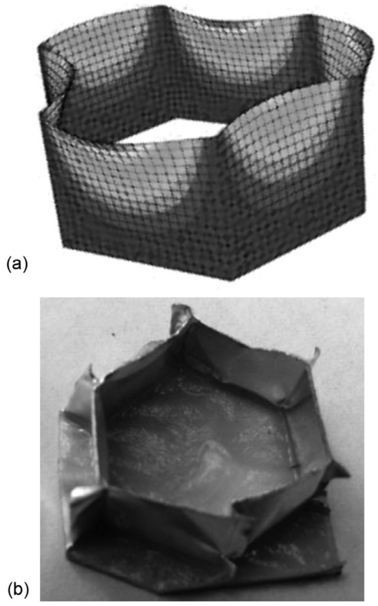

Figure 16: a) Experimental and b) numerical deformation of aluminum honeycomb for a cell size of 19.2 mm
Slika 16: a) Eksperimentalna in b) numerična deformacija satja iz aluminija za velikost celice 19,2 mm

ducted the following simulation runs on the finite-element code ABAQUS.

To account for the influence of the cell-wall thickness, simulations using the finite element code were made and the results of the variation of the numerical critical buckling load and the cell-wall thickness of the honeycomb sandwich panels for 19.2 mm cell sizes obtained are given in **Figure 13**. According to the results of the simulation, we find that the wall thicknesses of the cell have a significant impact on the critical buckling load and the resistance of the honeycomb sandwich panels. It is established that the critical buckling load increased with an increase of the cell-wall thickness.

To explain the effect of the core's thickness (h_c) on the numerical critical buckling (F_{cn}), the differences applications on the finite-elements code ABAQUS are realized. We can simply understand from **Figure 14** that by increasing the height of the core (h_c), the value of the numerical critical buckling load (F_{cn}) decreases.

The different values of (h_c), (F_{cn}) and the corresponding analytical buckling equations are summarized in **Table 2**. The buckling modes obtained for each (h_c) are shown in **Figure 15**. **Figure 16** represents a comparison between failure modes of one cell obtained from experiment and numerical results for aluminum honeycomb core with cell's size of 19.2 mm.

Figure 17 shows the evolution of the critical buckling load with the cell number of the honeycomb core for a 19.2 mm cell size. From the obtained results it is clear that the stiffness of the honeycomb sandwich panels increases with the number of cells. It is seen that the experimental and numerical deformation conditions are relatively coherent.

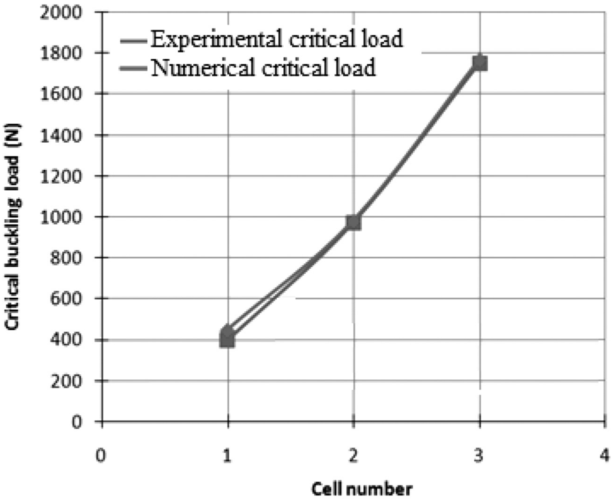

Figure 17: Variation of buckling load with the cell number for honeycomb core materials for a 19.2 mm cell size
Slika 17: Spreminjanje upogibne obremenitve s številom celic za material s satastim jedrom pri velikosti celice 19,2 mm

Table 2: Different height of core (h_c) with correspondent buckling load (F_{cn}) and analytical equations of buckling
Tabela 2: Različne višine jeder (h_c) s pripadajočo obremenitvijo pri upogibu (F_{cn}) in analitsko enačbo upogibanja

h_c	$R = h_c/a$	F_{cn}/N	analytical equations of buckling
8.8	$\sqrt{2} \geq R$	928.8	$W(x,y)= A_{11} \sin\frac{\pi x}{h_c} \sin\frac{\pi y}{a}$
20	$\sqrt{2} \leq R \leq \sqrt{6}$	562.67	$W(x,y)= A_{21} \sin\frac{2\pi x}{h_c} \sin\frac{\pi y}{a}$
30	$\sqrt{6} \leq R \leq \sqrt{12}$	507	$W(x,y)= A_{31} \sin\frac{3\pi x}{h_c} \sin\frac{\pi y}{a}$
40	$\sqrt{12} \leq R \leq 2\sqrt{5}$	469	$W(x,y)= A_{41} \sin\frac{4\pi x}{h_c} \sin\frac{\pi y}{a}$

5 CONCLUSIONS

The buckling load of sandwich plates with a honeycomb core subjected to compression damage has been investigated experimentally and numerically. The cell size and the wall thickness, and the materials, are parameters that have to be determined with respect to the usage area of the honeycomb sandwich structures optimally. The honeycomb compressive behavior intrinsically relates to the cell-wall buckling behavior under in-plane compression, because in reality the vertical cell walls can never be compressed along the length direction until a pure compressive failure due to the instability of the thin structure occurs. The following are the obtained results of the study:

- The critical buckling load of aluminum panels is determined to be higher than that of the Nomex honeycomb panels.
- The failure modes of the Nomex honeycomb sandwich panels under compression load show similar

behavior as that of the aluminum honeycombs. However, for the Nomex core panels, which are much more brittle than aluminum, prior to the core crushing failure, crack generation incurred.

- As the core's density increased, the maximum critical buckling load increased, both for the Nomex and the aluminum comb panels.
- It was observed that the core's height is a crucial parameter affecting the ultimate compressive strength of the sandwich panel.
- Besides the core's densities and the core height, the core-wall thickness also has an important effect on the critical buckling load. The critical buckling load increased as the cell-wall thickness increased.

6 REFERENCES

[1] R. K. McFarland Jr, Hexagonal cell structures under post-buckling axial load, AIAA Journal, 1 (**1963**) 6, 1380–1385, doi:10.2514/3.1798

[2] T. Wierzbicki, Crushing analysis of metal honeycombs, International Journal of lmpact Engineering, 1 (**1983**) 2, 157–174, doi:10.1016/0734-743X(83)90004-0

[3] L. J. Gibson, M. F. Ashby, Cellular Solids, Structure and Properties, Pergamon Press, Oxford 1988

[4] L. J. Gibson, M. F. Ashby, G. S. Schajer, C. I. Robertson, The mechanics of twodimensional cellular materials, Proc. R. Soc. Lond. A, 382 (**1982**), 43–59, doi:10.1098/rspa.1982.0087

[5] D. Mohr, T. Wierzbicki, Crushing of soft-core sandwich profiles: experiments and analysis, International Journal of Mechanical Sciences, 45 (**2003**) 2, 253–271, doi:10.1016/S0020-7403(03)00053-5

[6] W. Abramowicz, T. Wierzbicki, Axial crushing of multicorner sheet metal columns, Journal of Applied Mechanics, 56 (**1989**) 1, 113–120, doi:10.1115/1.3176030

[7] S. Li, S. R. Reid, Relationship between the elastic buckling of square tubes and rectangular plates, Journal of Applied Mechanics, 57 (**1990**) 4, 969–973, doi:10.1115/1.2897669

[8] W. Abramowicz, N. Jones, Dynamic axial crushing of square tubes, International Journal of lmpact Engineering, 2 (**1984**) 2, 179–208, doi:10.1016/0734-743X(84)90005-8

[9] W. Abramowicz, N. Jones, Dynamic axial crushing of circular tubes, International Journal of Impact Engineering, 2 (**1984**) 3, 263–281, doi:10.1016/0734-743X(84)90010-1

[10] N. Jones, Structural Impact, Cambridge University Press, Cambridge 1989

[11] W. Johnson, S. R. Reid, Metallic energy dissipating systems, and the update, Applied Mechanics Reviews, 31 (**1978**), 277–288, Updated in: 39 (**1986**), 315-319

[12] C. L. Wu, C. T. Sun, Low velocity impact damage in composite sandwich beams, Composite Structures, 34 (**1996**) 1, 21-27, doi:10.1016/0263-8223(95)00127-1

[13] S. M. Lee, T. K. Tsotsis, Indentation failure behaviour of honeycomb sandwich panels, Composites Science and Technology, 60 (**2000**) 8, 1147–1159, doi:10.106/S0266-3538(00)00023-3

[14] W. Goldsmith, J. L. Sackman, An experimental study of energy absorption in impact on sandwich plates, International Journal of Impact Engineering, 12 (**1992**) 2, 241–262, doi:10.1016/0734-743X(92)90447-2

[15] M. Jamjian, J. L. Sackman, W. Goldsmith, Response of an infinite plate on a honeycomb foundation to a rigid cylindrical impactor, International Journal of Impact Engineering, 15 (**1994**) 3, 183–200, doi:10.1016/S 0734-743X(05)80012-0

[16] M. O. Kaman, M. Y. Solmaz, K. Turan, Experimental and Numerical analysis of Critical Buckling Load of Honeycomb Sandwich panels, Journal of Composite Materials, 44 (**2010**) 24, 2819-2831, doi:10.1177/0021998310371541

[17] B. Castanié, C. Bouvet, Y. Aminanda, J. J. Barrau, P. Thevenet, Modelling of low-energy/low-velocity impact on Nomex honeycomb sandwich structures with metallic skins, International Journal of Impact Engineering, 35 (**2008**) 7, 620–634, doi:10.1016/j.ijimpeng.2007.02.008

[18] M. Giglio, A. Manes, A. Gilioli, Investigations on sandwich core properties through an experimental – numerical approach, Composites: Part B: Engineering, 43 (**2012**) 2, 361–374, doi:10.1016/j.compositesb.2011.08.016

[19] P. H. W. Tsang, P. A. Lagace, Failure Mechanisms of Impact-damaged Sandwich Panels Under Axial Compression, AIAA, (**1994**) 1396, 745–754, doi:10.2514/6.1994-1396

[20] Q. Zhou, R. R. Mayer, Characterization of Aluminum Honeycomb Material Failure in Large Deformation Compression, Shear and Tearing, Journal of Engineering Materials and Technology, 124 (**2002**) 4, 412-420, doi:101115/1.1491575

[21] D. Mohr, M. Doyoyo, Large plastic deformation of metallic honeycomb: orthotropic rate-independent constitutive model, International Journal of Solids and Structures, 41 (**2004**) 16-17, 4435–4456, doi:10.1016/j.ijsolstr.2004.02.062

[22] D. Mohr, M. Doyoyo, Deformation-induced folding systems in thin-walled monolithic hexagonal metallic honeycomb, Int. J. Solids Struct., 41 (**2004**) 41, 3353–3377, doi:10.1016/j.ijsolstr.2004.01.014

[23] S. T. Hong, J. Pan, T. Tyan, P. Prasad, Quasi-static Crush Behaviors of Aluminum Honeycomb Specimens under Compression Dominant Combined Loads, International Journal of Plasticity, 22 (**2006**) 1, 73–109, doi:10.1016/j.ijplas.2005.02.002

[24] A. Wilbert, W. J. Jang, S. Kyriakides, J. F. Floccari, Buckling and progressive crushing of laterally loaded honeycomb, International Journal of Solids and Structures, 48 (**2011**) 5, 803–816, doi:10.1016/j.ijsolstr.2010.11.014

[25] S. Liang, H. L. Chen, Investigation on the square cell honeycomb structures under axial loading, Composite Structures, 72 (**2006**) 4, 446–454, doi:10.1016/j.compstruct.2005.01.022

[26] H. S. Lee, S. H. Hong, J. R. Lee, Y. K. Kim, Mechanical behavior and failure process during compressive and shear deformation of honeycomb composite at elevated temperatures, Journal of Materials Science, 37 (**2002**) 6, 1265-1272, doi:10.1023/A:1014344228141

[27] X. Fan, I. Verpoest, D. Vandepitte, Finite Element Analysis of Out-of-plane Compressive Properties of Thermoplastic Honeycomb, Journal of Sandwich Structures and Materials, 8 (**2006**) 5, 437-458, doi:10.1177/1099636206065862

UDK 620.178.3
Original scientific article/Izvirni znanstveni članek

ISSN 1580-2949
MTAEC9, 49(2)243(2015)

FATIGUE BEHAVIOUR OF X70 STEEL IN CRUDE OIL

VEDENJE JEKLA X70 PRI UTRUJANJU V SUROVI NAFTI

Ľubomír Gajdoš[1], Martin Šperl[1], Jaroslav Bystrianský[2]
[1]Institute of Theoretical & Applied Mechanics, Academy of Sciences of the Czech Republic, v.v.i., Department of Thin-Walled Structures,
Prosecká 25, Prague 9, 190 00, Czech Republic
[2]Institute of Chemical Technology, Technická 5, Prague 6, 166 28, Czech Republic
gajdos@itam.cas.cz

Prejem rokopisa – received: 2014-02-25; sprejem za objavo – accepted for publication: 2014-04-10

doi:10.17222/mit.2014.041

The fatigue properties of the X70 steel in crude oil and in the water separated from the crude-oil phase were tested, the stress-cycle-asymmetry ratio being $R = 0$. As a reference, fatigue tests in air were also carried out. The fatigue specimens used were prepared from the Vohburg an der Donau – Nelahozeves (IKL) crude-oil pipeline after 13 years of exploitation. The tests were aimed at assessing the degree of degradation of the fatigue properties of this steel due to the environmental impacts typical for the crude-oil processing and transport. For added value, fatigue tests were also carried out in an alkaline solution on specimens prepared from a new pipe. The results of the tests showed that the fatigue properties of the steel in crude oil were slightly better than in air, but much poorer in the water separated from the crude-oil phase.

Keywords: corrosion fatigue, S-N curve, X70 steel, crude oil, separated water

Preizkušeno je bilo vedenje jekla X70 pri utrujanju v surovi nafti in v vodi, izločeni iz surove nafte, pri čemer je bilo razmerje asimetrije napetostnih ciklov $R = 0$. Za primerjavo so bili izvršeni tudi preizkusi utrujanja na zraku. Uporabljeni vzorci za utrujanje so bili izrezani iz naftovoda Vohburg an der Donau – Nelahozeves (IKL) za surovo nafto po 13 letih obratovanja. Namen preizkusov je bila ocena stopnje degradacije zaradi vpliva okolja, značilnega za pridobivanje in transport surove nafte. Kot zanimivost so bili izvršeni tudi preizkusi utrujanja v alkalni raztopini pri vzorcih iz novih cevi. Rezultati preizkusov so pokazali, da je vedenje jekla pri utrujanju v nafti nekaj boljše kot na zraku, vendar občutno slabše v vodi, izločeni iz surove nafte.

Ključne besede: korozijsko utrujanje, S-N-krivulja, jeklo X70, surova nafta, izločena voda

1 INTRODUCTION

The transportation of crude oil from a production site to a refinery and from the refinery to the oil consumers needs to be very safe because, in the event of an accident, an oil-spillage disaster endangers the natural environment and causes financial losses. Crude oil is transported by sea in tankers and on land by trucks, trains and pipelines. Tankers are generally subjected to the corrosive action of seawater, and studies of the effect of seawater on the fatigue properties of the steels used in ship structures are therefore very important[1]. No less important is the transportation of crude oil on land through the pipelines. In comparison with the trucks and trains used for transporting oil, in recent decades the pipelines have proved to be highly economical and very safe. A number of pipelines are currently under construction all over the world.

The crude-oil flow rate is not constant as it varies according to the demand for crude oil. The crude-oil pressure increases when the flow volume increases and vice versa. Based on the records obtained, the pressure fluctuation is about 7 bar. On average, there are ten pressure changes in the month. The pressure fluctuation may result in the corrosion fatigue of a pipeline wall and some of its parts become corrosive[2]. It is therefore useful and has become a matter of interest to examine the fatigue behaviour of the steel in contact with the transported crude oil. Naturally, it would be desirable to conduct the fatigue tests with the frequency of the stress changes of the same order as the frequency of the crude-oil pressure changes encountered in practice (10^{-4} Hz), but this would require tests of unrealistic duration. It is more convenient to carry out ordinary resonant-frequency fatigue tests which, of course, cannot represent the actual corrosion-fatigue resistance of a crude-oil pipeline. Nevertheless, the results can be taken as informative data indicating relative fatigue-resistance values of the pipelines for various crude oils.

2 FATIGUE TESTS

The material used in the tests (X70) was taken from a real IKL oil pipeline, with an outside diameter of 711 mm and a wall thickness of 8.5 mm, after the pipeline had been in operation for about 13 years. The steel contained mass fractions (w/%) C 0.18, Mn 1.3, Si 0.23, P 0.009, S 0.021, Ni 0.03, and V 0.01 and its structure was bainitic with the bandings in the longitudinal direction. The static tensile properties in the hoop direction were as follows: the ultimate tensile strength $R_m = 610$ MPa, the yield stress $R_{p0.2} = 495$ MPa, and the elongation at failure $A_5 = 31$ %. This steel is designated as X70-A.

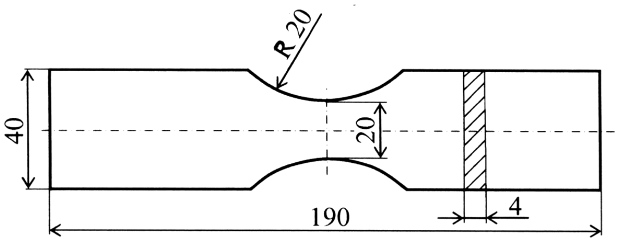

Figure 1: Fatigue specimen of varying width
Slika 1: Vzorec za utrujanje z različno širino

For added value, fatigue tests were also carried out in an alkaline solution. They were performed on another steel sample of the same grade (X70), taken from a new pipe with a diameter of 508 mm and a wall thickness of 10 mm. The static mechanical properties of this steel were as follows: R_m = 625 MPa, $R_{p0.2}$ = 500 MPa, and A_5 = 24 %. In order to distinguish it from the steel taken from the pipeline, this steel was designated as X70-B.

The fatigue tests were performed in zero-to-tension loading with the resonance frequency of 130–133 Hz, using an Instron electromagnetic resonance fatigue machine, model 1603, with an automatic system for the mean-load control and with the maximum force level F = 100 kN. Flat specimens of a varying width and a constant thickness were used in the tests (**Figure 1**).

The reference fatigue tests of X70-A were made in air, while the main fatigue tests were made in liquid environments: in crude oil and in the water separated from the crude-oil phase. The fatigue tests of the X70-B steel were made in a 1 N water alkaline solution of Na_2CO_3 and $NaHCO_3$ in the ratio of 1 : 1 with pH = 9.325.[3]

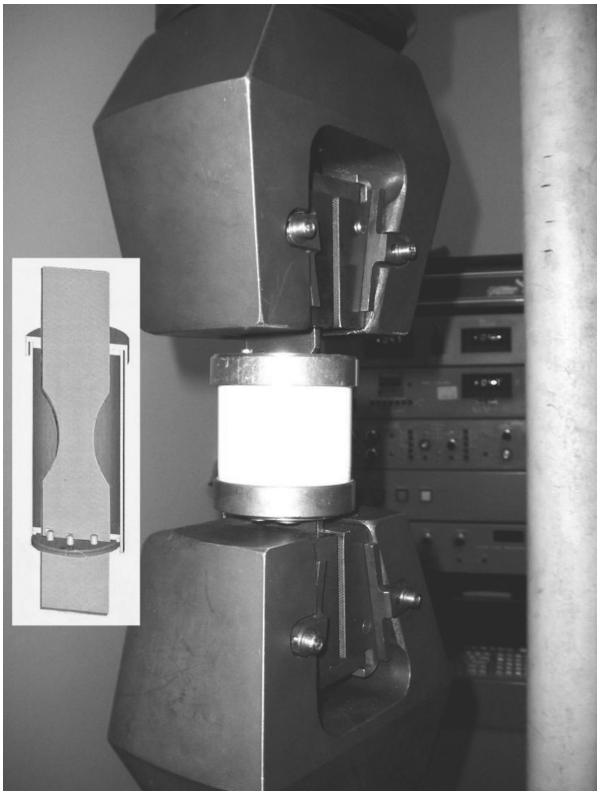

Figure 2: View of a specimen in a sealing cell, in the grips of the fatigue machine
Slika 2: Vzorec v zatesnjeni celici, vpet v čeljusti naprave za utrujanje

In cooperation with the RCP Prague, a special sealing cell was developed for the fatigue tests in a liquid medium (**Figure 2**). The number of cycles to fracture N_f was determined as the number of the stress cycles that the resonance machine was able to exert without changing the set-up parameters. The relative sizes of the cracks at the instant when the machine was automatically stopped were approximately 0.25–0.4 of the minimum width of a specimen.

The fatigue tests in the water phase separated from the crude oil (Vohburg–Nelahozeves) were, to some extent, specific since this environment is, in fact, a residue of the deposit water that is present, in small amounts, in the transmitted crude oil, either in an emulsified form or a dissolved form (in very small amounts)[4]. The chemical composition of separated water is shown in **Table 1**.

Table 1: Results of an analysis of the water phase
Tabela 1: Rezultati analize vodne faze

pH	–	7.0
specific conductivity	mS m^{-1}	2000
dissolved substances	g dm^{-3}	14
neutralization capacity (KNK$_{4.5}$)	mmol dm^{-3}	11
Σ (Ca + Mg)	mmol dm^{-3}	22
chlorides (Cl^-)	g dm^{-3}	8.1
sulphates (SO_4^{2-})	mg dm^{-3}	31
oxygen (15–25 °C)	mg dm^{-3}	9.5–8.5

Before the actual fatigue tests, the water was left in contact with the air in order to saturate with oxygen (carbon dioxide). The oxygen amount corresponded to the saturation at the temperatures between 18 °C and 23 °C.

3 RESULTS OF THE FATIGUE TESTS

All the results of the fatigue tests are presented in **Figure 3**. In addition to the curves pertaining to the X70-A steel specimens there is also an S-N curve obtained for the specimens from the X70-B steel. The level of the fatigue limit in zero-to-tension loading of the X70-A steel specimens is represented by a horizontal dashed line. It is taken as 0.6 R_m [5] which, in this case, yields a magnitude of 366 MPa.

The figure shows that at the upper margin of the family of all the experimental points (indicating the best fatigue properties) there are triangles corresponding to crude oil and dark diamonds corresponding to the alkaline solution applied to the X70-B steel. In the bottom part of the family of the experimental points there are, with a big downward shift, light diamonds that relate to separated water. Slightly below the triangles

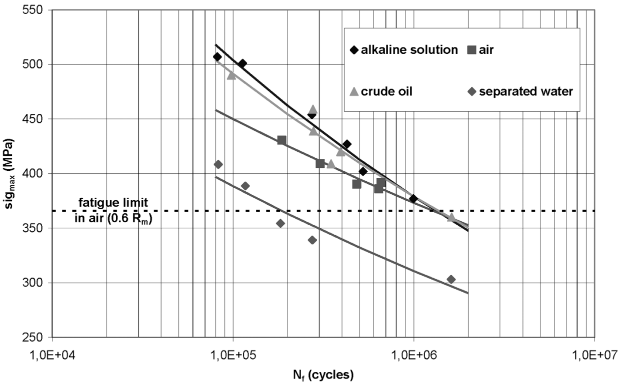

Figure 3: Aggregate presentation of the fatigue-test results
Slika 3: Skupna predstavitev rezultatov preizkusov utrujanja

there are squares representing the results obtained in air. This shows that, in relation to the fatigue properties of the X70-A steel in air, the influence of crude oil appears to be non-aggressive, and it also follows that the effect of the alkaline solution on the X70-B steel appears to be very similar to the effect of crude oil on the X70-A steel. However, separated water has a very negative influence on the corrosion-fatigue properties of X70-A. Some of the results obtained for the X70-A steel are presented in[6].

If the S-N curve obtained in air is considered as a reference curve, then, according to this diagram, the crude-oil environment does not worsen the fatigue-corrosion resistance of the steel up to the fatigue limit region, i.e., up to a life of $2 \cdot 10^6$ cycles. The decrease in the maximum stress in a cycle with the number of cycles to fracture is, however, more rapid in crude oil than in air. As indicated by the position of the S-N curve for separated water in the diagram, the presence of separated water in crude oil leads to a considerable deterioration of the fatigue properties of the tested steel.

If we express the S-N curves in the following form:

$$\sigma_{\max} = \frac{A}{(N_{\mathrm{f}})^{\mathrm{b}}} \tag{1}$$

constants *A* and *b* take the magnitudes shown in **Table 2**.

Table 2: Constants of the S-N curves for X70-A and X70-B steels
Tabela 2: Konstanti krivulje S-N za jekli X70-A in X70-B

environment	steel	*A*	*b*
air	X70-A	1147.4	0.0813
crude oil	X70-A	1803.1	0.1129
separated water	X70-A	1188.3	0.0971
alkaline solution	X70-B	2098.3	0.1239

As already specified, by identifying the fatigue limit with the maximum stress in a cycle for a life of $N_{\mathrm{f}} = 2 \cdot 10^6$ cycles, we can obtain probable fatigue limits in zero-to-tension loading. For the X70-A steel, these are: $\sigma_{\mathrm{f}} = 353$ MPa in air, $\sigma_{\mathrm{f}} = 350$ MPa in crude oil, and $\sigma_{\mathrm{f}} = 290$ MPa in separated water; and for the X70-B steel $\sigma_{\mathrm{f}} = 348$ MPa in the alkaline solution.

4 DISCUSSION

It was experimentally proved that crude oil has no negative effect on the fatigue properties of the X70-A steel. This contrasts with the effect of separated water, which exhibited corrosion aggressivity towards this steel. The corrosion aggressivity of separated water occurs due to its saturation with oxygen and a high amount of chlorides[7]; however, the presence of acid carbonates in high concentrations reduces its aggressivity[8]. Under the conditions of a crude-oil pipeline, separated water can contain only a limited amount of oxygen, but under the conditions of long-term storage separated water can become saturated with air[9]. This environment can then be considered as the most aggressive possible environment[10,11]. In other words, due to a low pH value and a high $[c(\mathrm{Cl}) + c(\mathrm{SO_4})]/c(\mathrm{HCO_3})$ ratio, separated water is an environment characterized by the highest chemical corrosion activity.

The effect of a crude-oil environment on the fatigue properties of steel is comparable to that of an inert environment since it manifests itself by preventing the surface from having contact with the oxygen in the air (fatigue tests in air).

The composition of the alkaline solution (its alkalinity and the presence of the $\mathrm{HCO_3^-}$ / $\mathrm{CO_3^{2-}}$ system) leads to a passivation of the steel that, subsequently, results in a lower aggressivity of the solution.

5 CONCLUSIONS

1. A comparison of the fatigue properties of the X70 steel in air and in crude oil has shown that crude oil had no aggressive effect on the steel in the sense of reducing its fatigue characteristics. The S-N curve for crude oil was above the reference S-N curve for air. A similar fatigue behaviour of the steel was exhibited when an alkaline solution was used, i.e., the corresponding S-N curves were very close to each other. However, quite a different situation was observed in the fatigue tests performed in separated water, which had an aggressive effect on the steel. The corresponding S-N curve was below the other curves, the decrease in terms of the cyclic load being 15–20 % with regard to the reference S-N curve.

2. It can be stated that a crude-oil environment improves the fatigue properties of the steel up to the region of the fatigue limit, i.e., up to a life of $N_{\mathrm{f}} = 2 \cdot 10^6$ cycles. The decrease in the maximum stress in a cycle with the increasing fatigue life is much more rapid in crude oil than in air. By contrast, separated water markedly worsens the fatigue properties. Thus, for example, when the specimens are cycled in crude oil with $\sigma_{\max} = 380$ MPa, their mean life is $N_{\mathrm{f}} = 976500$ cycles; however, their life is reduced to $N_{\mathrm{f}} = 125700$ cycles when they are cycled in separated water, i.e., their life is reduced by a factor of

approximately 7.8. In this case the slope of the decrease in the cyclic stress is roughly the same as in air.

3. If the fatigue limit is considered as the maximum stress in a zero-to-tension cycle (the stress range) corresponding to a life of $N_f = 2 \cdot 10^6$ cycles, the fatigue limit for crude oil (350 MPa) is practically the same as those for air (353 MPa) and alkaline solution (348 MPa). The smallest magnitude of the fatigue limit (290 MPa) is found for separated water.

Acknowledgements

This work was supported by RVO: 68378297 and by the projects P105/10/2052 of the Grant Agency of the Czech Republic, and TE 02000162 of the Technological Agency of the Czech Republic.

6 REFERENCES

[1] V. Kasemi, A. Haxhiraj, Mater. Tehnol., 42 (**2008**) 6, 169–170

[2] Ľ. Gajdoš et al., Structural Integrity of Pressure Pipelines, Transgas, a.s., Prague 2004, 137–160

[3] M. Šperl, Vliv korozního poškození na provozní spolehlivost plynovodních potrubí, (The Effect of Corrosion Damage on Operation Reliability of Gas Linepipes), Ph.D. Dissertation, Czech Technical University, Faculty of Transportation Sciences, Prague, 2008

[4] Z. A. Foroulis, Werkstoffe und Korrosion (Materials and Corrosion), 33 (**1982**) 3, 121–131, doi:10.1002/maco.19820330302

[5] P. Hopkins, Defect Assessment in Pipelines, APA Course, Prague, Czech Republic, 2001

[6] Ľ. Gajdoš, M. Šperl, J. Bystrianský, J. Pressure Vessel Technol., 137 (**2015**) 5, 051401, doi:10.1115/1.4029659

[7] L. Garverick, Corrosion in the Petrochemical Industry, ASM International, 1994

[8] H. H. Uhlig, R. W. Revie, Corrosion and Corrosion Control, 3rd ed., Wiley-Interscience, New York, USA 1985, 415–441

[9] DIN 50 930 (1993): Korrosion Metallischer Werkstoffe im Innern von Rohrleitungen, Behältern und Apparaten bei Korrosionsbelastung durch Wässer, Teile 1 bis 5, (Corrosion of Metallic Materials inside Pipelines, Vessels and Apparatuses Caused by Water, Parts 1–5), 1993

[10] R. Martínez-Palou et al., Journal of Petroleum Science and Engineering, 75 (**2011**) 3–4, 274–282, doi:10.1016/j.petrol.2010.11.020

[11] N. H. Abdurahman, Y. M. Rosli, N. H. Azhari, B. A. Hyder, Journal of Petroleum Science and Engineering, 90–91 (**2012**), 139–144, doi:10.1016/j.petrol.2012.04.025

UDK 621.791/.792:669.24
Original scientific article/Izvirni znanstveni članek

ISSN 1580-2949
MTAEC9, 49(2)247(2015)

USE OF LARSON-MILLER PARAMETER FOR MODELING THE PROGRESS OF ISOTHERMAL SOLIDIFICATION DURING TRANSIENT-LIQUID-PHASE BONDING OF IN718 SUPERALLOY

UPORABA LARSON-MILLERJEVEGA PARAMETRA ZA MODELIRANJE IZOTERMNEGA STRJEVANJA PRI SPAJANJU Z VMESNO TEKOČO FAZO SUPERZLITINE IN718

Majid Pouranvari[1], **Seyed Mostafa Mousavizadeh**[2]

[1]Materials and Metallurgical Engineering Department, Dezful Branch, Islamic Azad University, Dezful, Iran
[2]Department of Materials Engineering, Faculty of Engineering, Hakim Sabzevari University, Sabzevar, Iran
mpouranvari@yahoo.com

Prejem rokopisa – received: 2014-03-10; sprejem za objavo – accepted for publication: 2014-05-09

doi:10.17222/mit.2014.048

The progress of diffusion-induced isothermal solidification, which is a vital issue in transient-liquid-phase bonding, is modeled using the Larson-Miller parameter (*LMP*). The solidification mechanisms of the liquid phase during the TLP bonding of a wrought IN718 nickel-based superalloy with different bonding times/temperatures and the data were analyzed using the Larson-Miller parameter. Based on the Larson-Miller parameter (*LMP*), the TLP bonding parameter was defined in the form of $LMP = T_B[70 + \ln(t_B)]$ to explore the effects of the bonding temperature (T_B) and the bonding time (t_B) on the isothermal solidification progress. It was found that there is a direct linear relationship between the *LMP* and the isothermal-solidification-zone size.

Keywords: transient-liquid-phase bonding, isothermal solidification, superalloy, Larson-Miller parameter

Napredovanje z difuzijo spodbujenega izotermnega strjevanja, ki je vitalen del spajanja z vmesno tekočo fazo, je modelirano z uporabo Larson-Millerjevega parametra (*LMP*). Mehanizem strjevanja tekoče faze med TLP-spajanjem superzlitine IN718 na osnovi niklja pri različnih časih/temperaturah ter podatki so bili analizirani z uporabo Larson-Millerjevega parametra. Na tej podlagi je bil določen parameter TLP-spajanja v obliki $LMP = T_B[70 + \ln(t_B)]$, da bi ugotovili vpliv temperature spajanja (T_B) in časa spajanja (t_B) na napredovanje izotermnega strjevanja. Ugotovljeno je bilo, da obstaja neposredna linearna odvisnost med *LMP* in velikostjo področja izotermnega strjevanja.

Ključne besede: spajanje s prehodno tekočo fazo, izotermno strjevanje, superzlitina, Larson-Millerjev parameter

1 INTRODUCTION

Nickel-based superalloys are extensively used in the modern industry due to their excellent high-temperature tensile strength, stress rupture and creep properties, fatigue strength, oxidation and corrosion resistance and microstructural stability at elevated temperatures[1–3].

Transient-liquid-phase (TLP) bonding is considered as an interesting repairing/joining process for nickel-based superalloys due to its ability to produce near-ideal joints[4]. In the TLP bonding, by placing a thin filler alloy (i.e., interlayer) of an alloying metal containing a melting-point-depressant (MPD) element between the two pieces of the base metal to be joined and heating the entire assembly, a liquid phase is formed[5]. The diffusion of the melting-point depressants (MPD) from the molten interlayer into the base metal causes significant compositional changes in the liquid phase and increases the liquidus temperature of the liquid phase. Once the liquidus temperature reaches the bonding temperature, isothermal solidification starts. As a result of the absence of a solute rejection at the solid/liquid interface during the isothermal solidification, the formation of the second phase is basically prevented and a single-phase microstructure is formed in the ISZ. If a sample is cooled down before the completion of isothermal solidification, the residual liquid will be solidified during the cooling. A non-equilibrium segregation of the MPD elements results in a formation of eutectic-type solidification products consisting of hard and brittle intermetallic phases[6–9]. Therefore, there is a critical bonding time (t_{IS}) beyond which the formation of a eutectic-type microstructure in the joint centerline is precluded (i.e., the entire liquid phase is solidified isothermally).

In their studies of the effects of the stress and temperature on the creep-rupture time of gas-turbine alloys, Larson and Miller[10] showed that their results could be collapsed onto a common curve using a normalization of the following form: $LMP = T[C + Ln(t)]$. This normalization has been widely used since as a phenomenological method to relate the effects of the time and temperature on various thermally activated processes (for example[11,12]). Since the isothermal solidification process is the key stage of the TLP bonding, this paper aims at investigating the application of the Larson-Miller parameter to modeling the progress of isothermal solidifi-

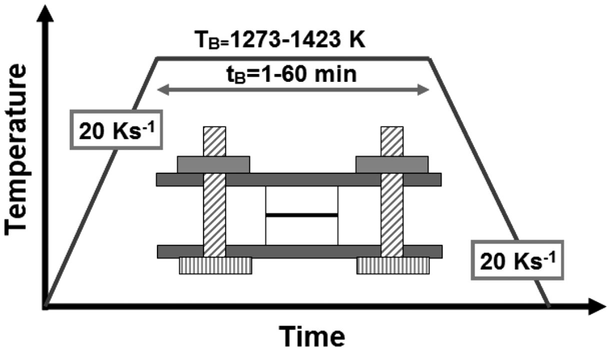

Figure 1: Temperature-time history during the TLP bonding of the IN718 alloy. The fixture used to hold the samples during the bonding is also superimposed in the figure.

Slika 1: Temperaturna in časovna odvisnost med TLP-spajanjem zlitine IN718. Prikazano je tudi uporabljeno držalo vzorcev med spajanjem.

cation during the transient-liquid-phase bonding of a superalloy.

2 EXPERIMENTAL PROCEDURE

The wrought IN718 nickel-based superalloy (Ni-20.26Fe-18.23Cr-4.85Nb-3.10Mo-0.93Ti-0.61 Al-0.19Si (*w*/%)) was TLP bonded using a 50 μm thick BNi-2 (Ni-7Cr-4.5Si-3.2B-3Fe). 10 mm × 5 mm × 5 mm coupons were sectioned from the base metal using an electro-discharge machine. Thereafter, in order to remove the oxide layer, the contacting surfaces were ground using 600-grade SiC paper and then ultrasonically cleaned in an acetone bath. The interlayer was then inserted between the two base-metal coupons. A Cr-Mo steel fixture (**Figure 1**) was used to fix the coupons in order to hold this sandwich assembly and reduce the metal flow during the TLP operation. **Figure 1** shows the thermal history during the bonding of the samples. The bonding was carried out in a furnace at the temperatures of (1273, 1323, 1373 and 1423) K under a vacuum of approximately 1.33 · 10^{-5} mbar. The bonding time was varied from 1–60 min.

The bonded specimens were sectioned perpendicular to the bond and then microstructural observations of the cross-sections of the specimens were carried out using a light microscope and a field-emission scanning electron microscope (FESEM). For the microstructural examinations, the specimens were etched using a solution containing 10 mL of HNO_3, 10 mL of $C_2H_4O_2$ and 15 mL of HCl. Semi-quantitative chemical analyses of the phases formed in the centerline of the bond region and adjacent to the base metal were conducted with a JEOL 5900 FESEM equipped with an ultra-thin-window Oxford energy-dispersive X-ray spectrometer (EDS).

3 RESULTS AND DISCUSSION

3.1 Microstructure evolution during isothermal solidification

Figure 2a depicts a typical microstructure of TLP bonded IN718 using a Ni-7Cr-4.5Si-3.2B-3Fe filler alloy

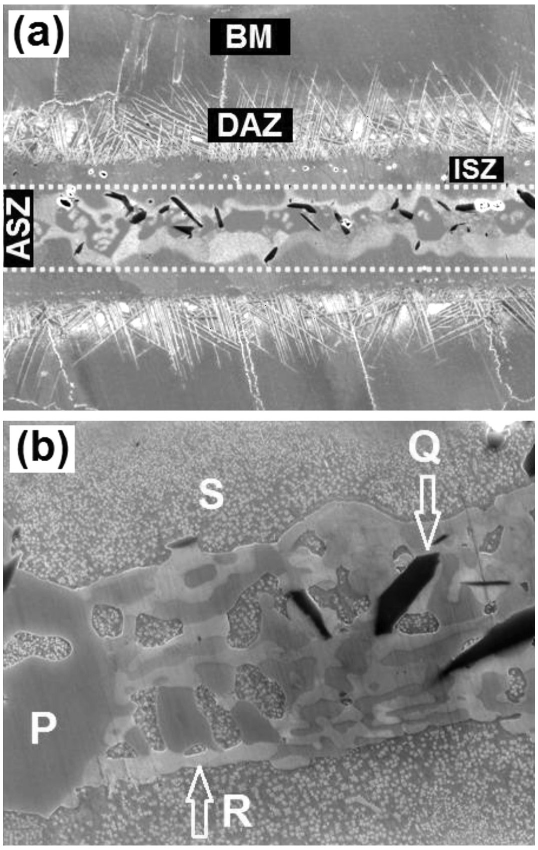

Figure 2: a) Typical overview of TLP bonded wrought IN718 with the partial-isothermal-solidification joint region, b) detailed view of ASZ: the microconstituents marked as P, Q and R are Ni-rich boride, Cr-rich boride and Ni-rich silicide. The zone marked as S is the eutectic gamma solid solution containing fine Ni_3Si precipitates.

Slika 2: a) Značilen videz spojenih TLP-vzorcev IN718 s področjem delnega izotermnega strjevanja, b) detajl videza ASZ: mikrogradniki, označeni s P, Q in R so z Ni bogati borid, s Cr bogati borid in z Ni bogati silicid. Področje, označeno s S, je evtektična gama-raztopina, ki vsebuje drobne izločke Ni_3Si.

Table 1: Chemical compositions (amount fraction, *x*/%) of different metallic constituents for various phases observed in the athermal solidification zone

Tabela 1: Kemijska sestava (množinski delež, *x*/%) različnih kovinskih gradnikov v različnih fazah, opaženih v območju neizotermnega strjevanja

Microconstituent/Element	Ni	Cr	Fe	Si	Mo	Nb	Al	Ti
P	84.05	6.53	3.53	0.95	–	3.55	1.38	–
Q	13.42	79.32	1.40	0.10	2.63	3.00	0.13	–
R	79.10	3.15	2.23	15.05	0.12	0.12	0.2	0.04
S	77.04	7.61	4.64	9.62	0.21	0.52	0.14	0.22

at 1050 °C for 10 min indicating a steep microstructural gradient in the joint area. Three distinct microstructural zones can be distinguished in the affected bonding area, namely:

- the isothermal solidification zone (ISZ),
- the athermal solidification zone (ASZ),
- the diffusion-affected zone (DAZ).

The ISZ is composed of a thin layer of the γ solid solution formed at the solid/liquid interface towards the joint centerline due to isothermal solidification. As can be seen in **Figure 2b**, the ASZ is composed of four distinct phases marked with P, Q, R and S. **Table 1** shows the EDS-SEM analysis of the phases formed in the ASZ. According to **Table 1**:

- P is a Ni-rich boride intermetallic formed during the cooling of the residual liquid.
- Q is a Cr-rich boride intermetallic formed during the cooling of the residual liquid.
- R represents Ni-rich the silicide eutectic microconstituents formed during the cooling of the residual liquid.
- S is the eutectic-γ formed during the non-isothermal solidification of the residual liquid as part of the eutectic solidification product. This region contains extensive fine Ni_3Si precipitates formed during the solid-state precipitation reaction during the cooling, not directly from the solidification of the remaining liquid.

According to the morphology of the phases in the ASZ, it can be concluded that they are formed during the eutectic-type reaction during the cooling of the liquid phase. Considering the brittleness of the intermetallic phases in the bonding condition when the isothermal solidification is not accomplished completely, the stress concentration associated with the eutectic microconstituents plays the key role in determining the joint strength. It was shown that the size of the athermal solidification zone (ASZ) is the controlling factor for the shear strength of the partially isothermally solidified TLP bonded IN718[6].

3.2 *Effect of process parameters on isothermal solidification progress*

The time required to obtain a eutectic-free joint centerline is the key parameter in designing a TLP bonding cycle. Studying the effects of the bonding parameters on the time required to ensure the completion of isothermal solidification can serve as the first step toward the optimization of the process parameters to obtain an isothermally solidified joint free of deleterious intermetallic formations in the joint centerline. Therefore, to investigate the effects of the bonding parameters on the isothermal solidification progress, bonding was carried out at the temperatures of (1273, 1323, 1373 and 1423) K with various durations. Taking the γ-solid solution/eutectic boundary as the solid/residual liquid interface at the end of each holding time, the average ASZ size was measured. **Figure 3a** shows the variation in the ASZ size with respect to the bonding time at various bonding temperatures. **Figure 3b** shows a contour plot of the ASZ versus the bonding time and temperature. As can be seen, the ASZ size decreases with the increasing bonding temperature and bonding time due to a larger diffusion of the melting-point-depressant

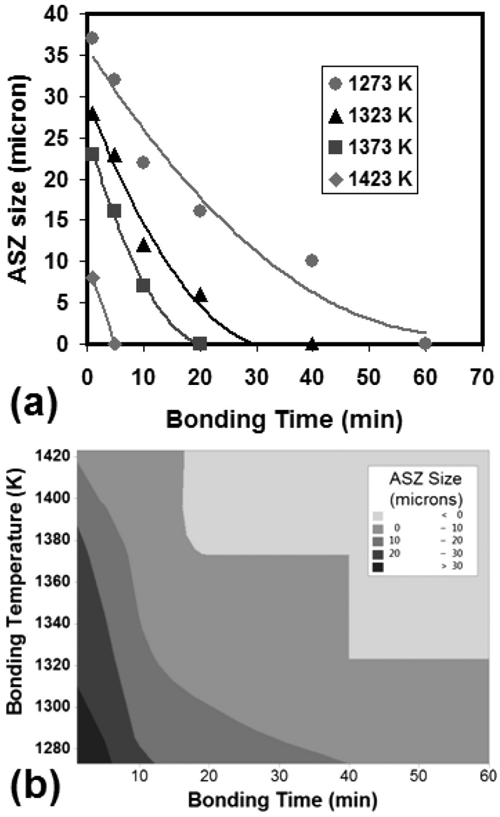

Figure 3: a) Effect of the bonding time and temperature on the ASZ size, b) contour plot of the ASZ size versus the bonding time and temperature

Slika 3: a) Vpliv časa in temperature spajanja na velikost ASZ, b) prikaz obrisa velikosti ASZ, glede na čas in temperaturo spajanja

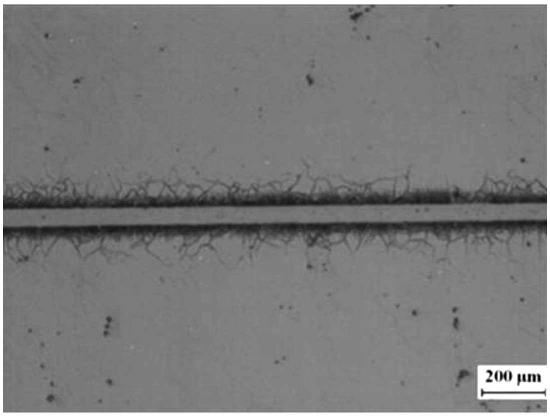

Figure 4: Typical eutectic-free joint indicating the completion of isothermal solidification

Slika 4: Značilen spoj brez evtektika, ki prikazuje dokončanje izotermnega strjevanja

(MPD) elements into the base metal. When the bonding time was sufficient for the completion of isothermal solidification, a eutectic-free joint centerline was obtained (**Figure 4**). According to **Figure 3**, the time required to ensure the completion of isothermal solidification decreases as the bonding temperature increases.

In this section the progress of isothermal solidification is analyzed using the Larson-Miller normalization. The development of the Larson-Miller normalization starts by expressing the rate for a thermally activated process, *r*, as an Arrhenius-type equation[10]. The rate of isothermal solidification is equal to the rate of the solid/liquid movement during the bonding process that can be expressed as follows[13]:

$$r = \frac{\mathrm{d}X(t)}{\mathrm{d}t} = \frac{D}{(C_\mathrm{L} - C_\mathrm{S})}\left(\frac{\partial C}{\partial t}\right)_{x=X(t)} \qquad (1)$$

where D is the diffusivity of the MPD element in the BM, C_L and C_S are the equilibrium liquidus and solidus, respectively, $(\partial C / \partial t)_{x=X(t)}$ is the gradient of the MPD element at the solid/liquid interface and $X(t)$ is the liquid/solid interface position.

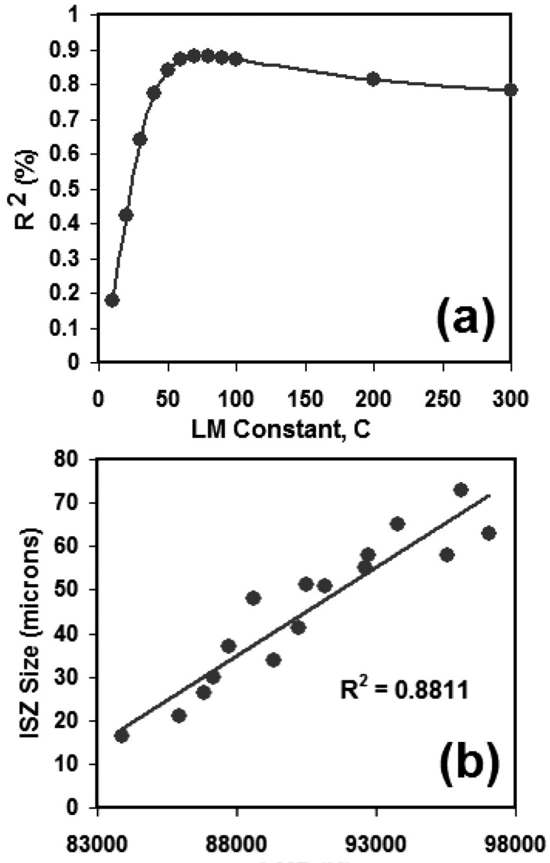

Figure 5: a) Coefficient of determination for fitting versus the Larson-Miller constant, *C*, b) ISZ size versus *LMP* [*T*(70 + ln (*t*))] in TLP bonding of IN718/Ni-Cr-Fe-Si-B/IN718

Slika 5: a) Koeficient ujemanja z Larson-Millerjevo konstanto *C*, b) velikost ISZ v odvisnosti od *LMP* [*T*(70 + ln (*t*))] in pri TLP-spajanju IN718/Ni-Cr-Fe-Si-B/ IN718

Since the diffusion coefficient is related to the temperature using an Arrhenius-type equation, the rate of isothermal solidification in a given time can be expressed as an Arrhenius-type equation:

$$r = A\exp\left(-\frac{Q}{RT}\right) \qquad (2)$$

where A is the pre-exponential factor, Q is the activation energy, R is the universal gas constant and T is the temperature. Rearranging Equation (2) leads to the following equation:

$$\frac{Q}{R} = T\left[\ln(A) - \ln(r)\right] \qquad (3)$$

Since the rate r is inversely proportional to time t, Equation (3) can be further written as:

$$\frac{Q}{R} = T\left[\ln(A) + \ln(t)\right] \qquad (4)$$

Equation (4) serves as the basis for the Larson-Miller parameter, the *LMP*:

$$LMP = \frac{Q}{R} = T\left[C + \ln(t)\right] \qquad (5)$$

with the Larson-Miller constant defined as $C = \ln A$.

The width of the ISZ was measured for each bonding time and temperature and the variation in the ISZ size versus the *LMP* with various Larson-Miller constants (*C*) was plotted. A linear trend line was used to fit the data to the *LMP*. The coefficient of determination (R^2) was determined at each LM constant (*C*). **Figure 5a** shows the variation in the coefficient of determination (R^2) versus the LM constant. According to **Figure 5a** the best fitting was obtained when *C* was 70. **Figure 5b** shows the variation in the ISZ size versus *LMP* = *T*[70 + ln(*t*)] confirming the following linear relationship between the ISZ size and the *LMP*:

$$\text{Size ISZ/µm} = 0.0041\ T_\mathrm{B}[70 + \ln(t_\mathrm{B})] - 324.07 \qquad (6)$$

where T_B (*K*) is the bonding temperature and t_B (h) is the bonding time.

Therefore, this normalization allowed the progress of isothermal solidification for different bonding times and at different bonding temperatures to be described with a common curve.

4 CONCLUSIONS

The understanding of isothermal solidification is of key importance in determining the mechanical performance of a transient-liquid-phase bonded joint. In this paper, the isothermal solidification during the TLP bonding of a wrought IN718 superalloy is studied and the results are analyzed using the Larson-Miller parameter. The following conclusions can be drawn from this study:

1) When the bonding time in not sufficient for the isothermal solidification completion, the joint centerline contains a eutectic-type microconstituent that can degrade the mechanical properties of the joint.
2) The isothermal solidification time required to obtain a eutectic-free joint centerline is reduced as the bonding temperature increases from 1273 K to 1423 K.
3) Based on the Larson-Miller parameters (*LMP*), the TLP bonding parameter is defined as $T_B\,[70 + Ln(t_B)]$ to explore the effects of the bonding temperature (T_B) and the bonding time (t_B) on the isothermal solidification progress. It was found that there is a direct linear relationship between the *LMP* and the isothermal-solidification-zone size.

Acknowledgement

The authors would like to thank the Dezful Branch, Islamic Azad University for providing the financial support of this work under the research project entitled: "Investigation on the effect of chemical composition of filler metal on the phase transformations and mechanical properties of diffusion brazed IN718 nickel based superalloy".

5 REFERENCES

[1] A. Milosavljevic, S. Petronic, S. Polic-Radovanovic, J. Babic, D. Bajic, Mater. Tehnol., 46 (**2012**) 4, 411–417

[2] R. Sunulahpašić, M. Oruč, M. Hadžalić, M. Rimac, Mater. Tehnol., 46 (**2012**) 3, 263–267

[3] A. Semenov, S. Semenov, A. Nazarenko, L. Getsov, Mater. Tehnol., 46 (**2012**) 3, 197–203

[4] W. F. Gale, D. A. Butts, Sci. Technol. Weld. Joining, 9 (**2004**), 283–300, doi:10.1179/136217104225021724

[5] I. Tuah-Poku, M. Dollar, T. B. Massalski, Metall. Trans. A, 9 (**1988**), 675–686, doi:10.1007/bf02649282

[6] M. Pouranvari, A. Ekrami, A. H. Kokabi, Mater. Sci. Eng. A, 568 (**2013**), 76–82, doi:10.1016/j.msea.2013.01.029

[7] D. S. Duvall, W. A. Owczarski, D. F. Paulonis, Weld. J., 53 (**1974**), 203–214

[8] M. Pouranvari, A. Ekrami, A. H. Kokabi, Mater. Tehnol., 47 (**2013**) 5, 593–599

[9] M. Pouranvari, Mater. Tehnol., 48 (**2014**) 1, 113–118

[10] F. R. Larson, J. A. Miller, Trans. ASME, 74 (**1952**), 765–775

[11] S. Venkadesan, A. K. Bhaduri, P. Rodriguez, K. A. Padmanabhan, J. Nucl. Mater., 186 (**1992**), 177–184, doi:10.1016/0022-3115(92)90332-f

[12] A. M. Limarga, J. Iveland, M. Gentleman, D. M. Lipkin, D. R. Clarke, Acta Mater., 59 (**2011**), 1162–1167, doi:10.1016/j.actamat.2010.10.049

[13] Y. Zhou, W. F. Gale, T. H. North, Int. Mater. Rev., 40 (**1995**), 181–196, doi:10.1179/imr.1995.40.5.181

UDK 669.295:539.538:621.793/.795
Original scientific article/Izvirni znanstveni članek

ISSN 1580-2949
MTAEC9, 49(2)253(2015)

EFFECT OF SEVERE AIR-BLAST SHOT PEENING ON THE WEAR CHARACTERISTICS OF CP TITANIUM

VPLIV INTENZIVNEGA POVRŠINSKEGA KOVANJA S PESKANJEM Z ZRAKOM NA OBRABNE LASTNOSTI CP-TITANA

Abdullah Cahit Karaoglanli
Department of Metallurgical and Materials Engineering, Bartin University, 74100 Bartin, Turkey
karaoglanli@bartin.edu.tr, cahitkaraoglanli@gmail.com

Prejem rokopisa – received: 2014-03-24; sprejem za objavo – accepted for publication: 2014-06-05

doi:10.17222/mit.2014.055

In this study, air-blast shot peening was applied to analyze the wear characteristics of CP titanium (Grade II). The specimens were exposed to different plastic-deformation rates via different severe shot-peening conditions in order to determine the wear behaviour of CP titanium. A free-ball micro-abrasion test was performed on the specimens shot peened with different Almen intensities. Nanohardness measurements were also performed to investigate the work-hardened layer – the coarse-grained-structure transition zone. Light microscopy and scanning electron microscopy (SEM) were used to analyze both the wear tracks and the severely deformed layer. As a result, the plastically deformed layer thickness reaches approximately 100 μm beneath the surface. Moreover, the hardness and wear durability after severe shot peening is increased.

Keywords: air-blast shot peening, wear, nanoindentation, plastic deformation, ultra-fine-grain durability

V tej študiji je bilo uporabljeno peskanje z zrakom za študij lastnosti pri obrabi CP-titana (Grade II). Vzorci so bili izpostavljeni različnim stopnjam deformacije v različnih razmerah peskanja, da bi ugotovili vedenje CP-titana pri obrabi. Izvršen je bil abrazijski preizkus z mikrokroglicami na vzorcih po peskanju z različno Almen-intenziteto. Izvršene so bile meritve nanotrdote za preiskavo utrjenega sloja in grobozrnate strukture prehodne cone. Za analizo sledov obrabe in močno deformiranih slojev sta bili uporabljeni svetlobna in vrstična elektronska mikroskopija (SEM). Debelina plastično deformiranega sloja doseže globino okrog 100 μm pod površino. Trdota in odpornost proti obrabi se po močnem peskanju povečata.

Ključne besede: hladno kovanje površine s peskanjem z zrakom, obraba, nanoodtisek, plastična deformacija, odpornost ultra drobnih zrn

1 INTRODUCTION

Surface treatments are generally applied to metallic materials, particularly machine parts before service conditions to increase service life and efficiency.[1] Mechanical properties such as wear, fatigue, fretting fatigue and corrosion are influenced by surface treatments.[2,3] To analyze these mechanical and physical effects on the surface-treated materials, nanoindentation, scratch, hardness and thermal tests are performed.[4–9] Surface treatments are investigated within the branch of mechanical and thermal surface treatments. Mechanical surface treatments cover a wide variety of processes and shot peening, laser peening, deep drawing, burnishing, sand blasting, brush cleaning are given as example processes.[10,11] Nitriding, carburising, nitrocarburising, plasma nitriding and boriding processes are beneath the thermal-surface treatments.[12]

Shot peening has been widely used as a mechanical surface treatment to improve the fatigue resistance of critical machine parts.[13] Also, the shot-peening effect on the oxidation, corrosion and fretting-fatigue properties of materials has been studied.[13–15]

Oxidation and the above mentioned properties are also important for coatings and other surface treatments.[16,17]

With respect to enhancing the mechanical properties without altering the chemical compositions of materials, severe plastic deformations attract a lot of attention.[18] Severe plastic deformation, just as ECAP (equal-channel angular pressing), HPT (high-pressure torsion) or ARB (accumulative roll bonding) is performed to increase mechanical properties by decreasing the grain size of the whole bulk materials.[18,19] Nevertheless, these methods are applied restrictedly due to the high-pressure requirements. Shot peening may be more influential if performed as a severe plastic deformation.[19] It applies a high plastic deformation only to the material surfaces made of a wide variety of materials due to the easiness of the application.[13,20] By raising the conditions of the conventional shot peening, severe shot peening which applies a very high plastic deformation to a material surface was conceived.[20] In recent years, studies depicted that severe shot peening made positive contributions to the increased wear characteristics, creating fine-grained-surface bulk materials.[21] Severe shot peening is applied in the ways of high-energy shot peening, ultrasonic shot peening, etc.[22–24] Most of the severe-plastic-deformation studies show a highly deformed layer with ultra-fine grains that has superior mechanical properties in comparison with the interior parts.[25] From this point of view, obtaining a highly deformed surface with better properties is a way of improving the wear properties of metallic materials.[26–28] Several techniques are used for determining the wear behaviour of materials.[29] Micro-abrasion is one of these test techniques due to its simplicity with respect to the abrasive-wear behaviour of materials.[30]

In this study, attention is focused on the mechanical properties and the wear characteristics of the bulk CP titanium materials with severely deformed surfaces. The specimens are subjected to a free-ball micro-abrasion test subsequent to a severe shot-peening process. The distinction between the severe shot-peened and as-received titanium specimens are performed via mechanical and physical investigations.

2 EXPERIMENTAL STUDIES

Commercially pure titanium (Grade II) material with the dimensions of 20 mm × 20 mm × 8 mm was machined and a normalizing heat treatment was performed to release the machining and manufacturing effects. The surfaces of the specimens were ground with 200, 400, 800 and 1200 grade emery papers and then mechanically polished with 6 µm and 1 µm pastes. The specimens were subjected to the air-blast severe shot peening with different Almen intensities (**Table 1**). In addition, the air pressures were (750, 800 and 870) kPa for 31A, 35A and 9C, respectively. The Almen intensities were selected due to the high-plastic-deformation exposure.[20] The intensities were 31A, 35A and 9C. The C Almen strip is used as the highest plastic deformation in comparison to the A and N strips.[31]

Table 1: Severe-shot-peening conditions for CP-titanium (Grade II) specimens

Tabela 1: Razmere pri močnem peskanju vzorca CP-titan (Grade II)

Specimen No.	Almen intensity	Shot type	Shot size	Coverage (%)
1	31A	SAE-J2175	S230	200
2	35A	SAE-J2175	S230	200
3	9C	SAE-J2175	S230	200

The specimens were etched with a 3 % Nital solution following the severe shot-peening process. Afterwards light and SEM (Vega Tescan) microstructure images were obtained on the cross-sections and the peened surfaces. A Schimadzu DUH-W201S ultra-micro-hardness tester was used to determine the hardness alteration from the surface to the interior. The experimental load applied was 50 mN and the duration was 10 s.

The fixed-ball micro-abrasion test method was used for determining the wear performance of the shot-peened surfaces with different Almen intensities. The diameter, the material and the hardness of the ball were 25.4 mm, AISI 52100 steel and 65 Rc, respectively. The wear volume was calculated using Equation (1):[32]

$$V \approx \frac{\pi b^4}{64R} \text{ for } b << R \tag{1}$$

where V is the volume of the material removed by wear, b is the diameter of the wear crater, and R is the radius of the ball.

The fixed-ball micro-abrasion tests were performed on the peened surfaces of the CP-titanium (Grade II) specimens for 2 min, at 120 r/min, under the normal loads of (0.5, 1 and 1.5) N to determine the wear-volume loss on the peened-specimen surfaces. 800-mesh SiC particles were used as the abrasive and distilled water including 25 % SiC particles was used as the abrasive solution.

3 RESULTS AND DISCUSSION

The specimens peened with the 31A, 35A and 9C Almen intensities are shown in **Figure 1**. The images show the cross-sections of the peened specimens. A severe plastic deformation with a severe shot-peening

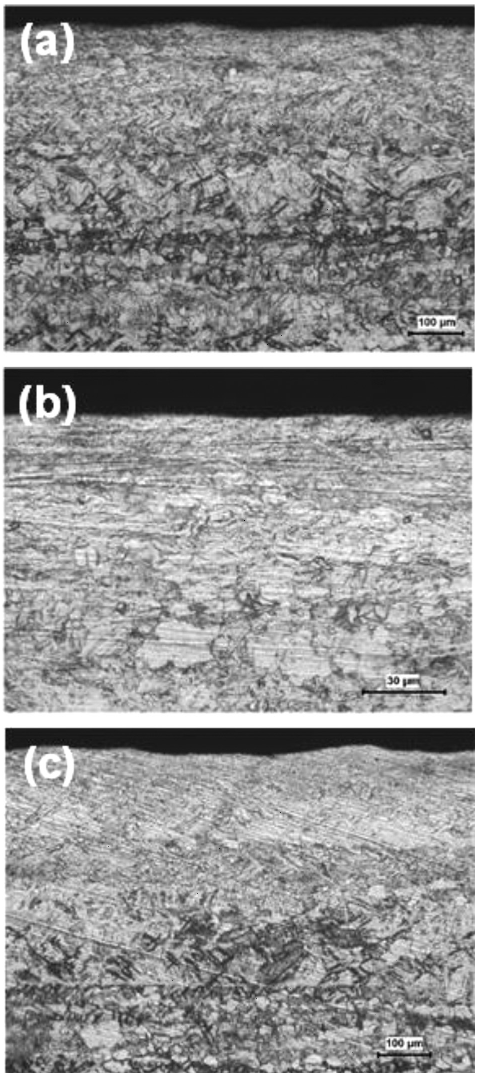

Figure 1: Light-microscope images of severely shot-peened titanium specimens peened with: a) 31A, b) 35A, c) 9C Almen intensities

Slika 1: Mikrostruktura močno peskanega vzorca iz titana z različno Almen-intenziteto: a) 31A, b) 35A, c) 9C exposure just below the surface is observed. Approximately 100 µm beneath the surface, grain boundaries become dense and lose their homogeneity and visibility. With the increasing Almen intensity, especially at the intensity of 9C, a very dense, severely deformed surface can be noticed; it is separated from the interior structure because fine grains appear due to a high plastic deformation. Also, shot tracks and waves on the surface peened with 9C are denser compared with 31A and 35A. In the literature the reported surface roughness also increases with the increasing plastic deformation.[20]

The severely deformed structure of the surface was investigated using a SEM analysis (**Figure 2**). In line with the studies made before, the images of the specimens peened with 31A, 35A and 9C show that a high plastic deformation ruined the homogenous microstructure and created quite a dense and heterogenous ultra-fine-grained structure.[22,33–35] Although the magnifications are high, the grain boundaries cannot be seen. Due to a dislocation-density increase and piling up around the grains, the boundaries are invisible just like reported in[36,37].

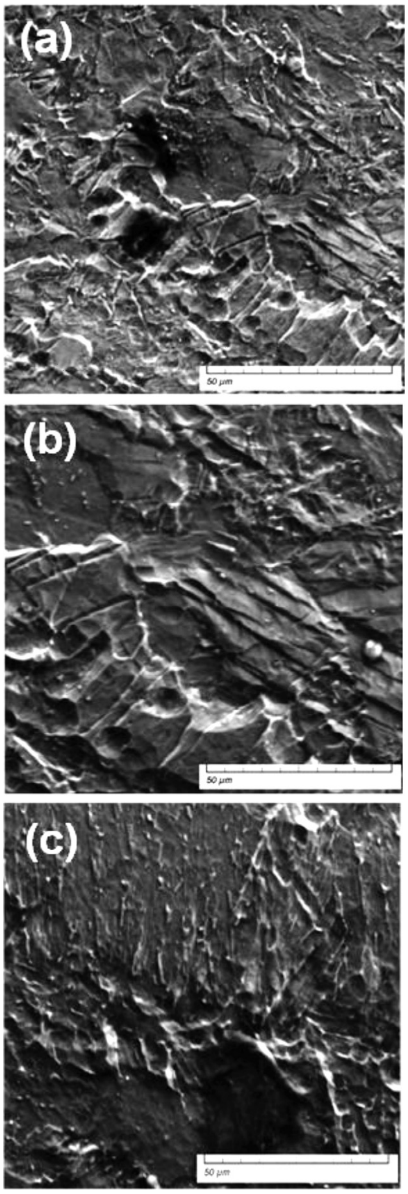

Figure 2: SEM images of severely shot-peened titanium specimens peened with: a) 31A, b) 35A, c) 9C Almen intensities

Slika 2: SEM-posnetki močno peskanega vzorca iz titana z različno Almen-intenziteto: a) 31A, b) 35A, c) 9C

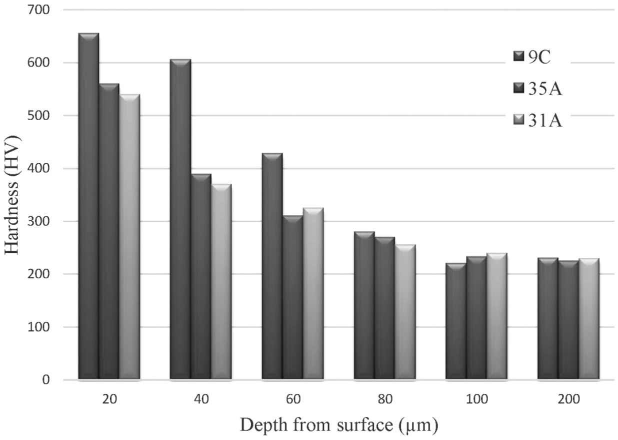

Figure 3: Hardness variation versus depth according to the Almen intensities

Slika 3: Spreminjanje trdote z globino glede na različno Almen-intenziteto

Nanohardness measurements were performed to determine the effect of the plastic deformation on the surface and the effect release to the interior. **Figure 3** depicts the hardness variation from the surface to the bulk interior. As seen on the figure, after approximately 150 µm a large part of the plastic-deformation impact was released, being very similar to the ones presented in[21,38]. The hardness increase is the highest on the surfaces of the specimens. Nevertheless, for the specimen peened with the 9C Almen intensity, the hardness decrease does not occur as abruptly as in the cases of 31A and 35A. As seen from **Figure 1**, an ultra-fine-grain, highly deformed layer provides a higher and more stabilized hardness down to 50 µm.

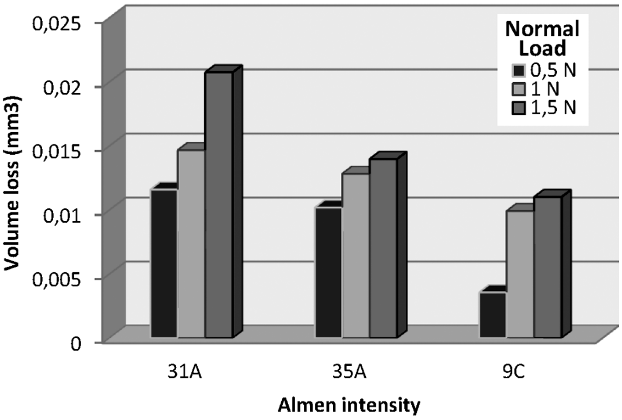

Figure 4: Volume loss versus Almen intensity for the normal load

Slika 4: Izguba volumna v odvisnosti od Almen-intenzitete pri normalni obremenitvi

The volume loss is evaluated on the basis of the crater dimensions from the light and SEM images. The mathematical approach taken from the literature was used in this study.[21] The volume loss decreases with the increasing Almen intensity. The Almen intensity causes an exposure to a severe plastic deformation, increasing the hardness of the contact surfaces of the materials. The hardness increase induces a reduction in the wear-volume loss.

Figure 4 shows the graphs indicating the volume loss of the specimens, subjected to the wear process using the 800-mesh SiC abrasives under the (0.5, 1 and 1.5) N loads and shot peened at different Almen intensities. As seen in **Figure 4**, the volume loss of the specimens increased in parallel with the increasing load. This is due to the fact that the force applied on the particles, stuck between the subsurface and the ball, increases resulting in a higher shear force with a deeper plunge of the abrasive particles into the specimen.

The lowest volume losses are observed on the specimen shot peened at the 9C Almen intensity, followed by the specimens shot-peened with the 35A and 31A Almen intensities, respectively. This can be primarily attributed to the surface hardness of the specimens. It would be appropriate to correlate the surface hardness of a specimen with the plastic deformation occurring on the surface area of the specimen depending on the increasing Almen intensity, since the stresses generated on the surface result in an increased dislocation density, hence, an increased hardness in this area of the specimen. Additionally, the density of the compressive stresses generated in this area varies depending on the Almen intensity and has a positive effect on the wear resistance.

Figure 5 shows a SEM image of a crater formed as a result of the micro-abrasion wear test made on a specimen that was shot-peened at the 9C Almen intensity. The wear tracks, obtained as a result of the tests carried out in compliance with the ASTM G77 standard using different Almen values, exhibited a circular geometry as expected.

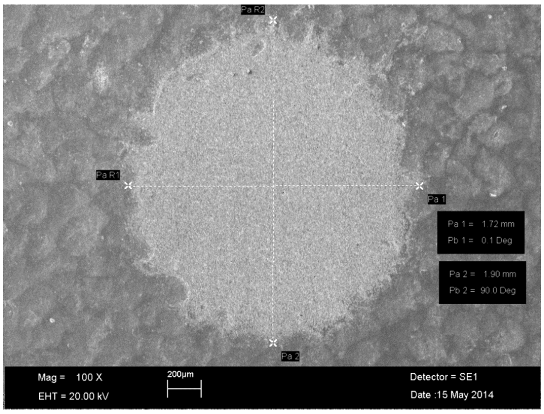

Figure 5: SEM image of a wear crater obtained on the titanium alloy shot peened with the 9C Almen intensity

Slika 5: SEM-posnetek kraterja na titanovi zlitini, peskani z 9C Almen-intenziteto

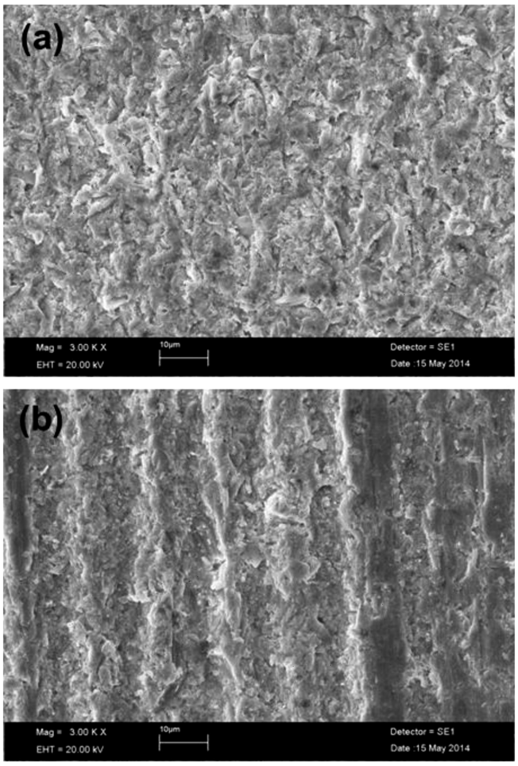

Figure 6: SEM images of the worn surfaces obtained with the 31A Almen intensity at the normal loads of: a) 0.5 N and b) 1.5 N

Slika 6: SEM-posnetka obrabljene površine, obdelane z Almen-intenziteto 31A pri obtežbi: a) 0,5 N in b) 1,5 N

Figures 6a and **6b** show the wear-surface images of the specimens subjected to the micro-scale abrasion process under the loads of 0.5 N and 1.5 N and shot-peened at the 31A Almen intensity. A three-body wear-abrasion mechanism was encountered on the specimens that were subjected to the wear process under 0.5 N. This is due to the rolling abrasion of the abrasive particles on the surface. A two-body abrasion-wear mechanism, thereby, a groove formation was observed on the specimens, subjected to the wear process under 1.5 N. This is a consequence of the plunging of the abrasive SiC particles into the ball surface with the increasing load, which results in a cut-off titanium alloy.

The wear-surface images of the specimens shot peened at the 35A Almen intensity under the 0.5 N and 1.5 N loads are given in **Figures 7a** and **7b**. Here, the wear mechanisms occurring at the 31A Almen intensity are observed as well; however, the groove depths, obtained under the load of 1.5 N, happened to be lower due to a higher material hardness.

The wear-surface images of the specimens shot peened at the 9C Almen intensity are shown in **Figure 8**. The wear mechanism obtained under the 1.5 N load differs from that of the other two specimens. The plunging of the abrasive particles into the material surface was obstructed due to an increased surface hardness and a three-body abrasion mechanism was observed due to the rolling of these particles.

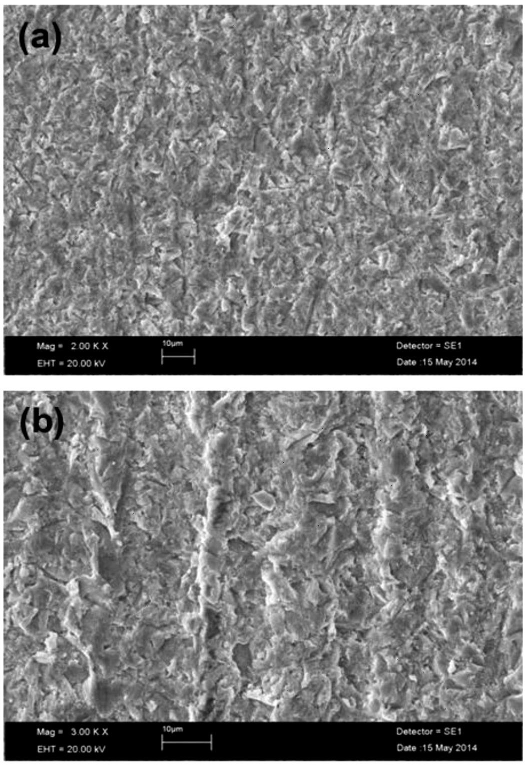

Figure 7: SEM images of the worn surfaces obtained with the 35A Almen intensity at the normal loads of: a) 0.5 N and b) 1.5 N
Slika 7: SEM-posnetka obrabljene površine, obdelane z Almen-intenziteto 35A pri obtežbi: a) 0,5 N in b) 1,5 N

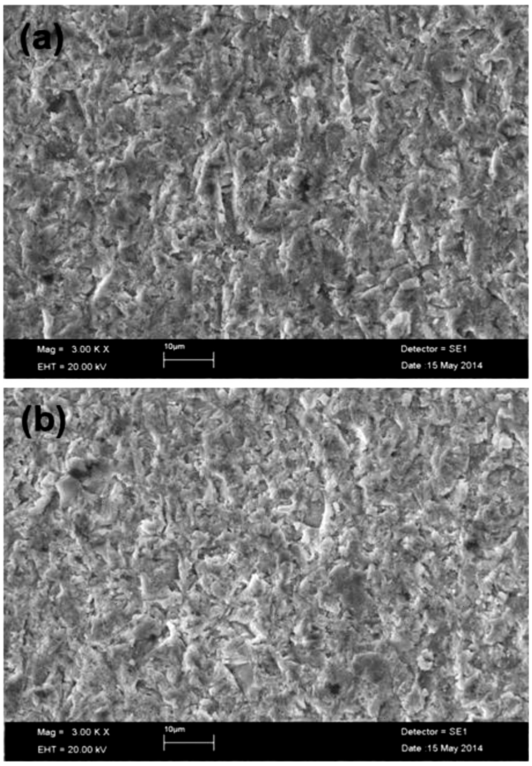

Figure 8: SEM images of the worn surfaces obtained with the 9C Almen intensity at the normal loads of: a) 0.5 N and b) 1.5 N
Slika 8: SEM-posnetka obrabljene površine, obdelane z Almen-intenziteto 9C pri obtežbi: a) 0,5 N in b) 1,5 N

4 CONCLUSIONS

In this study, commercially pure titanium (Grade II) specimens were subjected to severe air-blast shot peening with different Almen intensities. Different Almen intensities exposed the specimen surfaces to different plastic-deformation rates. Severe plastic-deformation rates caused a microstructural and mechanical behaviour alteration. With the increasing Almen intensity a finer and deeper grain structure occurred and this structure become more complex. However, according to the SEM images, although the magnifications were so high, the grain boundaries cannot be seen and the structure has a very dense layer and a plastically deformed surface. The hardness variation is also compatible with the optical and SEM images. With the decreasing Almen intensity the hardness was reduced and after approximately 100 µm a large part of the plastic deformation was released. The wear-volume loss was reduced with the increasing Almen intensity. The highest wear resistance was obtained with the specimens shot peened at the 9C Almen intensity, followed by the 35A and 31A Almen intensities. On the specimens shot peened at the 9C Almen intensity a three-body abrasion-wear mechanism was observed at all normal loads. However, on the specimens shot peened at the 35A and 31A Almen intensities, three-body abrasion was observed at the low load (0.5 N) and two-body abrasion was observed at the high load (1.5 N). These results show that the Almen intensity and, thereby, the surface hardness are the key parameters for the control of the wear behaviour of a Ti alloy.

Acknowledgments

The author gratefully acknowledges the Turkish Air Force Air Supply and Maintenance Command for the shot-peening applications.

5 REFERENCES

[1] K. Z. Shepelyakovskiil, Bulk-surface hardening as a method for increasing strength, reliability, and service life of machine parts, Metal Science and Heat Treatment, 37 (**1995**) 11, 433–440, doi: 10.1007/BF01154216

[2] G. Q. Wu, Z. Li, W. Sha, H. H. Li, L. J. Huang, Effect of fretting on fatigue performance of Ti-1023 titanium alloy, Wear, 309 (**2014**) 1–2, 74–81, doi:10.1016/j.wear.2013.10.010

[3] W. Brostow, K. Czechowski, W. Polowski, P. Rusek, D. Toboła, I. Wronska, Slide diamond burnishing of tool steels with adhesive coatings and diffusion layers, Materials Research Innovations, 17 (**2013**) 4, 269–277, doi:10.1179/1433075X12Y.0000000060

[4] W. M. Ke, F. C. Zhang, Z. N. Yang, M. Zhang, Micro-characterization of macro-sliding wear for steel, Materials Characterization, 82 (**2013**), 120–129, doi:10.1016/j.matchar.2013.05.009

[5] A. Khellouki, J. Rech, H. Zahouani, Micro-scale investigation on belt finishing cutting mechanisms by scratch tests, Wear, 308 (**2013**), 17–28, doi:10.1016/j.wear.2013.09.016

[6] B. D. Beakea, T. W. Liskiewicz, Comparison of nano-fretting and nano-scratch tests on biomedical materials, Tribology International, 63 (**2013**), 123–131, doi:10.1016/j.triboint.2012.08.007

[7] L. Jiangliang, X. Dangsheng, W. Hongyan, H. Zhongjia, D. Jihui, T. Rajnesh, Tribological Properties of Laser Surface Texturing and Molybdenizing Duplex-Treated Ni-Base Alloy, Tribology Transactions, 53 (**2010**), 195–202, doi:10.1080/10402000903097478

[8] A. C. Karaoglanli, G. Erdogan, A. Turk, I. Ozdemir, F. Ustel, Study of the microstructural and oxidation behavior of YSZ and YSZ/Al2O3 TBCs with HVOF bond coatings, Mater. Tehnol., 46 (**2012**) 5, 439–444

[9] C. Edoardo, G. Luca, P. Barbara, Modelling of the transient thermal field in laser surface treatment test, The International Journal of Advanced Manufacturing Technology, 40 (**2009**), 307–315, doi:10.1007/s00170-007-1350-z

[10] A. Igor, K. N. Ravi, S. Yuji, W. Lothar, O. R. Robert, On the effect of deep-rolling and laser-peening on the stress-controlled low- and high-cycle fatigue behavior of Ti–6Al–4V at elevated temperatures up to 550 °C, International Journal of Fatigue, 44 (**2012**), 292–302, doi:10.1016/j.ijfatigue.2012.03.008

[11] S. Anand Kumar, R. Sundar, S. Ganesh Sundara Raman, H. Kumar, R. Gnanamoorthy, R. Kaul, K. Ranganathan, S. M. Oak, L. M. Kukreja, Fretting Wear Behavior of Laser Peened Ti-6Al-4V, Tribology Transactions, 55 (**2012**), 615–623, doi:10.1080/10402004.2012.686087

[12] B. Edenhofer, W. Grafen, J. Müller-Ziller, Plasma-carburising a surface heat treatment process for the new century, Surface and Coatings Technology, 142–144 (**2001**), 225–234, doi:10.1016/S0257-8972(01)01136-7

[13] M. A. S. Torres, H. J. C. Voorwald, An evaluation of shot peening, residual stress and stress relaxation on the fatigue life of AISI 4340 steel, International Journal of Fatigue, 24 (**2002**), 877–886, doi:10.1016/S0142-1123(01)00205-5

[14] V. Azar, B. Hashemi, Y. M. Rezaee, The effect of shot peening on fatigue and corrosion behavior of 316L stainless steel in Ringer's solution, Surface and Coatings Technology, 204 (**2010**), 3546–3551, doi:10.1016/j.surfcoat.2010.04.015

[15] X. H. Zhang, D. X. Liu, H. B. Tan, X. F. Wang, Effect of TiN/Ti composite coating and shot peening on fretting fatigue behavior of TC17 alloy at 350 °C, Surface and Coatings Technology, 203 (**2009**), 2315–2321, doi:10.1016/j.surfcoat.2009.02.058

[16] A. C. Karaoglanli, E. Altuncu, I. Ozdemir, A. Turk, F. Ustel, Structure and durability evaluation of YSZ + Al2O3 composite TBCs with APS and HVOF bond coats under thermal cycling conditions, Surface and Coatings Technology, 205 (**2011**) 2, 369–373, doi:10.1016/j.surfcoat.2011.04.081

[17] A. C. Karaoglanli, H. Dikici, Y. Kucuk, Effects of Heat Treatment on Adhesion Strength of Thermal Barrier Coating Systems, Engineering Failure Analysis, 32 (**2013**), 16–22, doi:10.1016/j.engfailanal.2013.02.029

[18] K. Kyungjin, Y. Jonghun, Evolution of the microstructure and mechanical properties of AZ61 alloy processed by half channel angular extrusion (HCAE), a novel severe plastic deformation process, Materials Science and Engineering A, 578 (**2013**), 160–166, doi:10.1016/j.msea.2013.04.073

[19] E. Kaveh, I. Kazutaka, K. Takanobu, H. Zenji, Equal-Channel Angular Pressing and High-Pressure Torsion of Pure Copper: Evolution of Electrical Conductivity and Hardness with Strain, Materials Transactions, 53 (**2012**) 1, 123–127, doi:10.2320/matertrans.MD201109

[20] O. Unal, R. Varol, Almen intensity effect on microstructure and mechanical properties of low carbon steel subjected to severe shot peening, Applied Surface Science, 290 (**2014**), 40–47, doi:10.1016/j.apsusc.2013.10.184

[21] O. Unal, R. Varol, A. Erdogan, M. S. Gok, Wear behaviour of low carbon steel after severe shot peening, Materials Research Innovations, 17 (**2013**), 519–523, doi:10.1179/1433075X13Y.0000000106

[22] S. Bagherifard, P. I. Fernández, R. Ghelichi, M. Guagliano, Fatigue properties of nanocrystallized surfaces obtained by high energy shot peening, Procedia Engineering, 2 (**2010**), 1683–1690, doi:10.1016/j.proeng.2010.03.181

[23] Y. K. Gao, Improvement of fatigue property in 7050–T7451 aluminum alloy by laser peening and shot peening, Materials Science and Engineering A, 528 (**2011**), 3823–3828, doi:10.1016/j.msea.2011.01.077

[24] T. Chaise, J. Li, D. Nélias, R. Kubler, S. Taheri, G. Douchet, V. Robin, P. Gilles, Modelling of multiple impacts for the prediction of distortions and residual stresses induced by ultrasonic shot peening (USP), Journal of Materials Processing Technology, 212 (**2012**), 2080–2090, doi:10.1016/j.jmatprotec.2012.05.005

[25] N. A. Prakash, R. Gnanamoorthy, M. Kamaraj, Surface nanocrystallization of aluminium alloy by controlled ball impact technique, Surface and Coatings Technology, 210 (**2012**), 78–89, doi:10.1016/j.surfcoat.2012.08.069

[26] K. S. Anand, R. S. Ganesh Sundara, T. S. N. Sankara Narayanan, R. Gnanamoorthy, Fretting wear behaviour of surface mechanical attrition treated alloy 718, Surface and Coatings Technology, 206 (**2012**), 4425–4432, doi:10.1016/j.surfcoat.2012.04.085

[27] T. Fu, Z. F. Zhou, Y. M. Zhou, X. D. Zhu, Q. F. Zeng, C. P. Wang, K. Y. Li, J. Lu, Mechanical properties of DLC coating sputter deposited on surface nanocrystallized 304 stainless steel, Surface and Coatings Technology, 207 (**2012**), 555–564, doi:10.1016/j.surfcoat.2012.07.076

[28] M. Mubarak Ali, S. Ganesh Sundara Raman, S. D. Pathak, R. Gnanamoorthy, Influence of plasma nitriding on fretting wear behaviour of Ti–6Al–4V, Tribology International, 43 (**2010**), 152–160, doi:10.1016/j.triboint.2009.05.020

[29] H. Caliskan, A. Erdogan, P. Panjan, M. S. Gök, A. C. Karaoglanli, Micro-abrasion wear testing of multilayer nanocomposite TiAlSiN/TiSiN/TiAlN hard coatings deposited on the AISI H11 steel, Mater. Tehnol., 47 (**2013**) 5, 563–568

[30] A. C. Karaoglanli, H. Caliskan, M. Gok, A. Erdogan, A. Turk, A comparative study of the microabrasion wear behavior of CoNiCrAlY coatings fabricated by APS, HVOF and CGDS techniques, Tribology Transactions, 57 (**2014**) 1, 11–17, doi:10.1080/10402004.2013.820372

[31] S. Bagherifard, M. Guagliano, Influence of mesh parameters on FE simulation of severe shot peening (SSP) aimed at generating nanocrystallized surface layer, Procedia Engineering, 10 (**2011**), 2923–2930, doi:10.1016/j.proeng.2011.04.485

[32] D. Sun, J. A. Wharton, R. J. K. Wood, Micro-abrasion mechanisms of cast CoCrMo in simulated body fluids, Wear, 26 (**2009**), 1845–1855, doi:10.1016/j.wear.2009.03.005

[33] S. Bagherifard, M. Guagliano, Fatigue behavior of a low-alloy steel with nanostructured surface obtained by severe shot peening, Engineering Fracture Mechanics, 81 (**2012**), 56–68, doi:10.1016/j.engfracmech.2011.06.011

[34] K. Dai, L. Shaw, Comparison between shot peening and surface nanocrystallization and hardening processes, Materials Science and Engineering A, 463 (**2007**), 46–53, doi:10.1016/j.msea.2006.07.159

[35] G. Liu, J. Lu, K. Lu, Surface nanocrystallization of 316L stainless steel induced by ultrasonic shot peening, Materials Science and Engineering A, 286 (**2000**), 91–95, doi:10.1016/S0921-5093(00)00686-9

[36] M. A. Terres, N. Laalai, H. Sidhom, Effect of nitriding and shot-peening on the fatigue behavior of 42CrMo4 steel: Experimental analysis and predictive approach, Materials & Design, 35 (**2012**), 741–748, doi:10.1016/j.matdes.2011.09.055

[37] K. Farokhzadeh, J. Qian, A. Edrisy, Effect of SPD surface layer on plasma nitriding of Ti–6Al–4V alloy, Materials Science and Engineering A, 589 (**2014**), 199–208, doi:10.1016/j.msea.2013.09.077

[38] G. Li, J. Chen, D. Guan, Friction and wear behaviors of nanocrystalline surface layer of medium carbon steel, Tribology International, 43 (**2010**), 2216–2221, doi:10.1016/j.triboint.2010.07.004

UDK 519.61/.64:621.791/.792
Professional article/Strokovni članek

ISSN 1580-2949
MTAEC9, 49(2)259(2015)

FINITE-ELEMENT MINIMIZATION OF THE WELDING DISTORTION OF DISSIMILAR JOINTS OF CARBON STEEL AND STAINLESS STEEL

UPORABA KONČNIH ELEMENTOV ZA ZMANJŠANJE POPAČENJA OBLIKE PRI VARJENJU OGLJIKOVEGA IN NERJAVNEGA JEKLA

Eslam Ranjbarnodeh[1], **Majid Pouranvari**[2], **Mehdi Farajpour**[3]
[1]Mining and Metallurgical Engineering Department, Amirkabir University of Technology, Tehran, Iran
[2]Young Researchers Club, Dezful Branch, Islamic Azad University, Dezful, Iran
[3]Department of Mechanical Engineering, Islamic Azad University, East Tehran Branch, Tehran, Iran
islam_ranjbar@yahoo.com, islam_ranjbar@aut.ac.ir

Prejem rokopisa – received: 2012-08-07; sprejem za objavo – accepted for publication: 2014-05-27

doi:10.17222/mit.2012.057

In the present study, on the basis of a verified model, the effects of geometrical and operational variables on the welding distortion of dissimilar joints were investigated. Then, considering the welding current, the fixing time and the sequence of the welding operation, the magnitude of the welding deformation was minimized. The results showed that in the studied dissimilar joint between carbon steel and stainless steel, the minimum distortion occurred when the welding current was about 95 A, the fixing time was 120 s and the symmetric layout was used.

Keywords: minimization, welding distortion, dissimilar joint, welding variables

V tej študiji je bil preiskovan s preizkušenim modelom vpliv geometrijskih in procesnih spremenljivk na popačenje oblike pri varjenju različnih materialov. Obseg deformacije pri varjenju je bil zmanjšan z upoštevanjem varilnega toka, določitvi časa in zaporedja varilskih operacij. Rezultati pri študiju varjenja ogljikovega in nerjavnega jekla so pokazali, da je najmanjše popačenje oblike doseženo pri varilnem toku okrog 95 A, času 120 s in simetrični izvedbi varjenja.

Ključne besede: zmanjšanje, popačenje oblike pri varjenju, spajanje različnih materialov, spremenljivke pri varjenju

1 INTRODUCTION

Dissimilar joints are made of two materials that are considerably different in mechanical and/or chemical senses. Alloying between the base metals and filler metals is of great importance when dissimilar joints are made using fusion-welding processes. The resulting weld metal can show completely different mechanical properties as well as the distribution of the residual stress and the distortion within the weldment compared to the applied base metal(s) and filler metal. In this respect, proper designing of the welding procedure for these welds is of importance to engineers and scientists[1]. In welding operations, residual stresses and distortions are formed in the welded structures due to severe temperature gradients, as they can cause brittle fractures reducing the fatigue life as well as stress corrosion cracking. There are many published studies about the effect of welding residual stresses on the performance of welded structures. For example, Francis et al.[2] studied the influence of the residual stress in the vicinity of a weld on the structural integrity. They found that the martensite start temperature of the weld filler metal can be adjusted to mitigate the residual-stress distributions in ferritic steel welds.

Klobčar et al.[3] developed a finite-element model to predict the deformation and residual stresses and detect the areas critical to cracking during the repair welding of complex-geometry tooling.

Francis et al.[4] reviewed the metallurgical issues that arise in ferritic steel welds, relating them to the difficulties of calculating residual stresses and highlighting some stimulating areas for future research. It should be mentioned that welding residual stresses and distortions are affected by many factors: the thermo-physical and mechanical properties of base metal(s), the geometry of the weldment, the heat input, the welding sequence, etc.[5] So far, a few studies about the residual stresses in similar as well as dissimilar arc-welding operations have been published. For instance, Sahin et al.[6] used a two-dimensional finite-element model to predict the residual stresses in a brazed joint between 1.0402 and brass (BS CZ107). They found higher residual stresses in the steel part of the joint with the higher yield strength. Katsareas et al.[7] developed two-dimensional and three-dimensional models to predict the residual-stress distribution in a dissimilar joint between A508 and 1.4301. They used the element-death-and-birth technique to simulate an addition of the filler metal to the weld pool. Ranjbarnodeh et al.[8] simulated the heat transfer in dissimilar arc welding of stainless steel to carbon steel. They used the finite-element software ANSYS to investigate the effects of process parameters on the temperature distribution and residual stresses of a dissimilar joint. According to the literature, there are several studies on the effects of welding parameters on the magnitude and distribution of welding residual stresses. Teng et al.[9] developed a model to evaluate the effects of welding speed, specimen size, mechanical constraint and preheating on residual stresses. In another study, Teng et al.[10] evaluated the residual stresses with various types of welding sequences in the single-pass welding. But, few researches examined the finite-element simulation of the effect of the welding parameters on the residual distortion. Tsirkas et al.[11] developed a model to study the effect of the welding speed on the residual stresses and distortion in butt welds of similar butt joints, in which the AH36 steel was used as the base metal. Their results showed that increasing the welding speed greatly affected the welding residual distortion.

Considering the published works on dissimilar joints, further studies are necessary to investigate the welding residual distortions of dissimilar welds, particularly under different welding conditions, as well as the welding sequences and the fixing time in a fixture. Moreover, to the best knowledge of the authors, there is no comprehensive research on the minimization of the welding distortion of dissimilar joints. Therefore, in the present study, a thermo-mechanical model was utilized to evaluate the effects of the welding current, the welding sequence, the fixing time, the similarity and the joint geometry on the residual distortions of dissimilar butt joints of carbon and stainless steels made with the TIG welding process. A finite-element software, ANSYS, was used to solve the governing equations of the heat transfer and elastic-plastic distortion. Finally, considering the fixing time, the welding current and the sequence, the magnitude of the welding distortion was minimized.

2 MATHEMATICAL MODEL AND EXPERIMENTAL PROCEDURES

In this work, the finite-element method is employed to solve the heat-conduction problem during and after dissimilar welding. Equation (1) can be employed to describe the temperature variations inside the parts being welded:

$$\frac{\partial}{\partial x}\left(k\frac{\partial T}{\partial x}\right)+\frac{\partial}{\partial y}\left(k\frac{\partial T}{\partial y}\right)+\frac{\partial}{\partial z}\left(k\frac{\partial T}{\partial z}\right)=\rho C\frac{\partial T}{\partial t} \tag{1}$$

where T denotes the temperature, k is the thermal conductivity, C is the specific heat, ρ is the density, t represents the welding time, z represents the welding direction, x is the transverse direction and y is the thickness direction. In addition, convection-conduction boundary conditions presented in Equation (2) are assumed, except for the region affected by the welding arc where the Gaussian heat source is employed as the boundary condition as illustrated in Equation (3):

$$-k\frac{\partial T}{\partial n}=h(T-T_{\mathrm{a}}) \tag{2}$$

$$k\frac{\partial T}{\partial y}=q(r)=\frac{\eta VI}{2\pi r^{2}}\exp\left[-\frac{1}{2}\left(\frac{r}{\sigma}\right)^{2}\right] \tag{3}$$

Here, n denotes the normal direction to the surface boundary, T_{a} is the ambient temperature, $q(r)$ is the welding input energy, r is the distance from the center of the heat source and σ is the Gaussian distribution parameter, which is assumed as the radius of the area to which 95 % of the energy is entered[8], while r is assumed to be 1.5 mm and $\eta = 0.6$.[8]

It should be mentioned that the finite-element software, ANYSYS, is employed to solve the above heat-conduction problem. Regarding the thermal response of the material being welded, it is expected to produce a severe temperature gradient close to the welding arc and, therefore, very fine elements are required in the region of the weld pool to archive accurate results. Thus, the mesh is generated in such a way that the size of the elements increases exponentially in the transverse direction, i.e., the x-axis. The mesh system used in the model is illustrated in **Figure 1**. At the same time, the mechanical response of the weldment should be determined by solving the equilibrium problems as shown in Equations (4) and (5):

$$\sigma_{ij,j}+b_{j}=0 \tag{4}$$

$$\sigma_{ij}=\sigma_{ji} \tag{5}$$

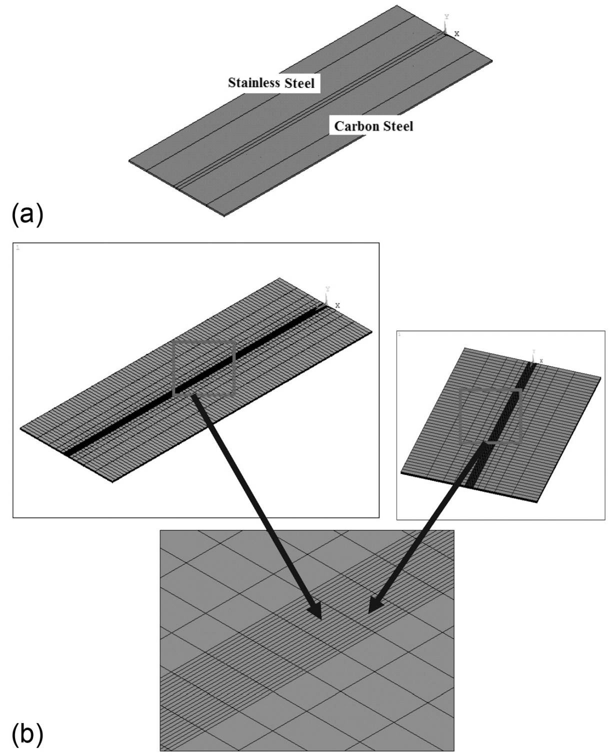

Figure 1: a) Model geometry and b) the used finite-element mesh
Slika 1: a) Geometrija modela in b) uporabljena mreža končnih elementov

where σ_{ij} is the Cauchy stress tensor and b_i is the body force vector, while the thermo-elastic-plastic behavior, based on the Von Mises yield criterion and the isotropic strain-hardening rule, is considered in the model. Accordingly, the constitutive equations can be written as follows:[6]

$$[d\sigma]=[D^{ep}][d\varepsilon]-[C^{th}]dT \tag{6}$$

where D^{ep} is the elastic-plastic matrix, C^{th} is the thermal strain matrix, $d\sigma$ is the stress increment, $d\varepsilon$ is the strain increment and dT is the temperature increment. Since the thermal elastic-plastic analysis is a non-linear and path-dependent problem, the incremental calculations, together with the iterative solution techniques, are employed in the model.

It is worth noting that, in the finite-element analysis, for the short samples a total of 5670 elements and 7130 nodes were employed, while for the long samples a total of 11340 elements and 14105 nodes were used in the analysis. The temperature-dependent material properties are assumed for both the stainless-steel and low-carbon-steel parts. The convection heat-transfer coefficient was taken as 25 W/(m^2 K) for the surfaces in contact. The total duration of the joining process consisted of two main parts in the model. The first part was used to complete the welding stage and the remaining time was used to perform the cooling in and out of the fixture. During and after the welding stage the model was constrained in order to prevent a rigid body motion. It should be noted that for the mechanical part of the simulation the results of the thermal part were applied as the body force and thermal stresses were calculated at each step, in other words, the thermo-mechanical problem was handled as a sequentially coupled one.[8] Using the validated model[8], the simulations were repeated for different lengths, thicknesses, welding currents, welding sequences and holding times of the fixture and similar joint. **Table 1** shows the chemical compositions of the steels used in the welding experiments. The dimensions of the samples were $L \times 80 \times t$ (mm^3) where L is the sample length and t is the sample thickness, but the filler was not used. The welding parameters used for preparing the experimental samples are shown in **Table 2**. The welding speed was 3.56 mm/s for all the samples. After the completion of the joints, the maximum magnitude of the welding distortion of all the samples was measured using a height gauge in the *Y*-direction as shown in **Figure 2** and the resulting distortions were compared with the computed results.

Figure 2: Measurement setup for the welding-induced distortion
Slika 2: Merjenje popačenja oblike zaradi varjenja

Table 1: Chemical compositions of the applied base metals in mass fractions, *w*/%
Tabela 1: Kemijska sestava uporabljenih jekel v masnih deležih, *w*/%

Material	C	Si	Mn	Ni	Cr	Ti
Stainless steel (AISI409)	0.015	0.59	0.27	0.13	11.28	0.17
Carbon steel (CK4)	0.025	0.013	0.19	0.04	0.01	–

Table 2: Applied welding parameters
Tabela 2: Uporabljeni parametri varjenja

Joint type	Welding sequence	Welding current (A)	Thick-ness (mm)	Length (mm)	Sample
dissimilar	progressive	120	2	450	120LPD
dissimilar	progressive	120	2	225	120SPD
dissimilar	progressive	150	3	225	150Thick
dissimilar	progressive	150	2	225	150Thin
dissimilar	progressive	105	2	450	105LPD
dissimilar	progressive	135	2	450	135LPD
dissimilar	progressive	95	2	450	95LPD
dissimilar	symmetric	95	2	450	95LSD
similar	progressive	120	2	225	120SS-SS
similar	progressive	120	2	225	120CS-CS
dissimilar	back step	120	2	225	120SBD
dissimilar	symmetric	120	2	225	120SSD

3 RESULTS AND DISCUSSION

The comparison of the experimental and simulation results of the distortion measurements are presented in **Table 3**. As can be seen, there is a logical consistency between the experimental and simulated data. The effect of the sample length on the welding residual distortion was investigated using the samples with two different

Table 3: Comparison between experimental and simulated distortion data
Tabela 3: Primerjava med eksperimentalnimi in simuliranimi podatki o popačenju oblike

Simulated distortion (mm)	Experimental distortion (mm)	Sample
5.47	8.1	70SPD
16.4	22.1	70LPD
17.6	18.5	105LPD
4.43	6.1	120SPD
21.9	24.3	120LPD
18.2	23.1	105LPS
19.4	24.2	120LPS
19.7	25.5	135LPS
10.2	9.8	120LPDS

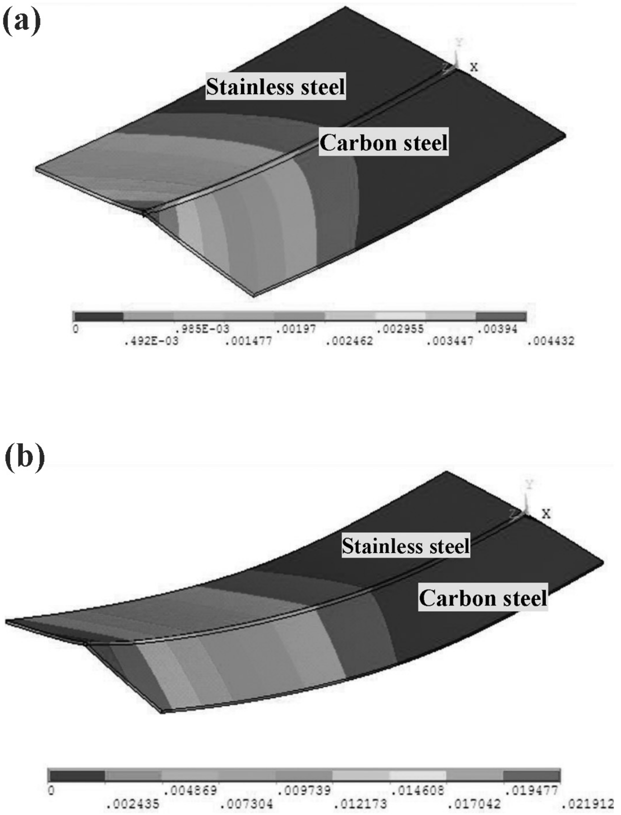

Figure 3: Effect of the length on the welding distortion: a) longer sample, b) shorter sample

Slika 3: Vpliv dolžine na popačenje oblike pri varjenju: a) daljši vzorec, b) krajši vzorec

lengths, 120SPD and 120LPD. The distortion of the longer sample, with twice the length, is over five times larger than that of the shorter sample as shown in **Figure 3**. This can be related to the lower stiffness of the longer sample (120LPD). Stiffness is the resistance of a body to distortion due to an applied force. Contrary to elastic modulus, stiffness is not an intrinsic material property. In other words, it depends on the geometry and material property (elastic modulus). For an element in tension or compression, the axial stiffness is defined with Equation (7):

$$K=\frac{A\times E}{L}=\frac{W\times t\times E}{L} \tag{7}$$

where L denotes the sample length, A is the cross-sectional area, E is the Young's modulus, W is the width of the specimen and t shows the thickness. The double length of the longer sample causes the half stiffness, i.e., a lower resistance to distortion and, accordingly, a higher welding distortion. The next point is the effect of the thickness on the welding distortion. **Figure 4** compares the distortions for two different thicknesses. Again, according to Equation (7), a higher thickness means a higher stiffness. Therefore, the thicker structure is more resistant to distortion. Increasing the thickness from 2 mm to 3 mm decreased the maximum magnitude of distortion from 6.7 mm to 0.3 mm.

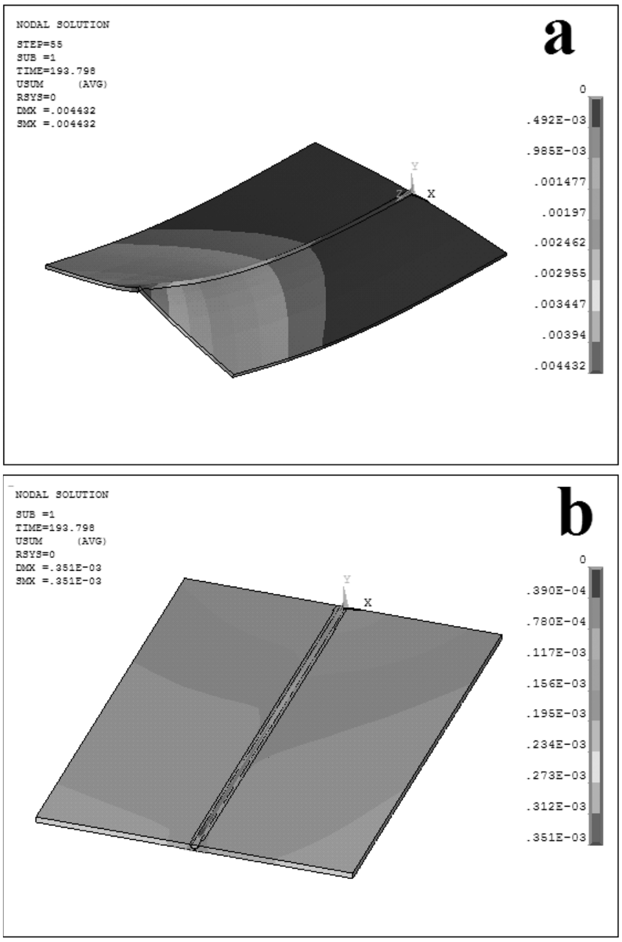

Figure 4: Effect of the thickness on the welding distortion: a) thicker sample (3 mm), b) thinner sample (2 mm)

Slika 4: Vpliv debeline na popačenje oblike pri varjenju: a) debelejši vzorec (3 mm), b) tanjši vzorec (2 mm)

The maximum distortions for different welding currents are compared in **Table 4**. As expected, a higher welding current induced a higher welding distortion due

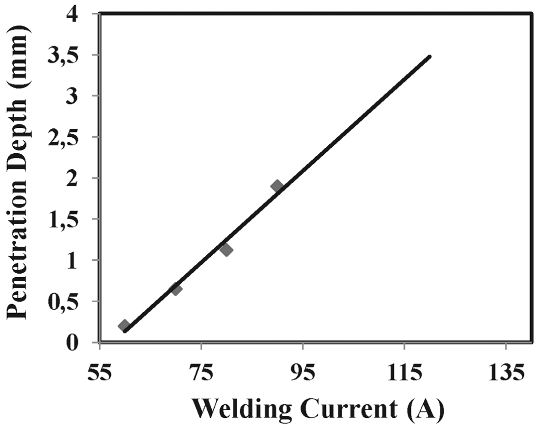

Figure 5: Effect of the welding current on the joint penetration

Slika 5: Vpliv varilnega toka na penetracijo v spoju

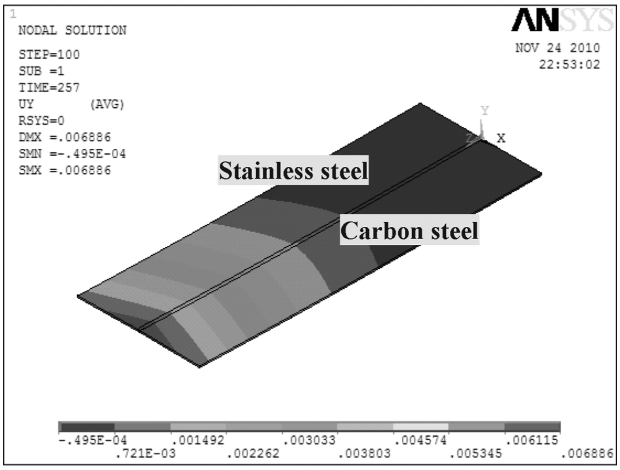

Figure 6: Distortion of sample 95LPD
Slika 6: Popačenje oblike pri vzorcu 95LPD

to a higher welding-heat input. Therefore, it can be concluded that the minimum distortion would be attained for the minimum applicable welding heat input keeping a full penetration. Using the simulation results, the minimum welding current to reach a full penetration was found to be about 95 A, as illustrated in **Figure 5**. Using this welding current, the simulation was repeated and the result showed that the minimum possible distortion for a progressive layout was about 6.8 mm (**Figure 6**).

Table 4: Maximum distortions for different welding currents
Tabela 4: Maksimalna popačenja pri različnih tokovih varjenja

135LPD	120LPD	105LPD	Sample
135	120	105	Welding current (A)
23.7	21.9	17.6	Distortion (mm)

The effect of the welding sequence on the welding distortion was investigated for three different sequences. **Figure 7** shows a schematic illustration of the used welding sequences and **Figure 8** indicates the effects of the used welding sequences on distortion. As it is demonstrated, the symmetric layout causes the minimum residual distortion. This can be due to the movement of the welding heat source from the middle of the plate with the minimum degree of freedom to the endpoint with the highest degree of freedom. It should be noted that this result is in agreement with the other researchers.[9,12] According to the authors' knowledge there is no detailed numerical study on the effect of the holding time in a

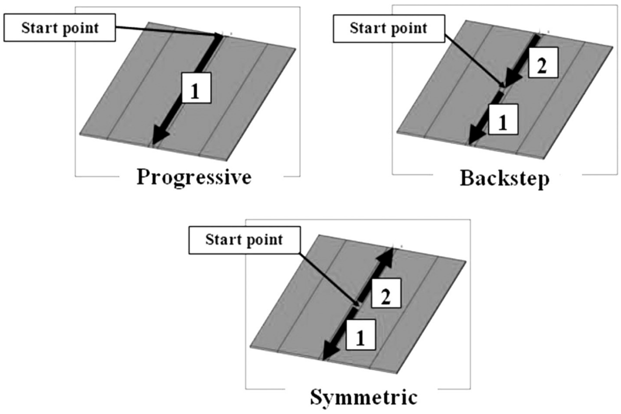

Figure 7: Schematic illustration of the used welding sequences
Slika 7: Shematski prikaz uporabljenih sekvenc varjenja

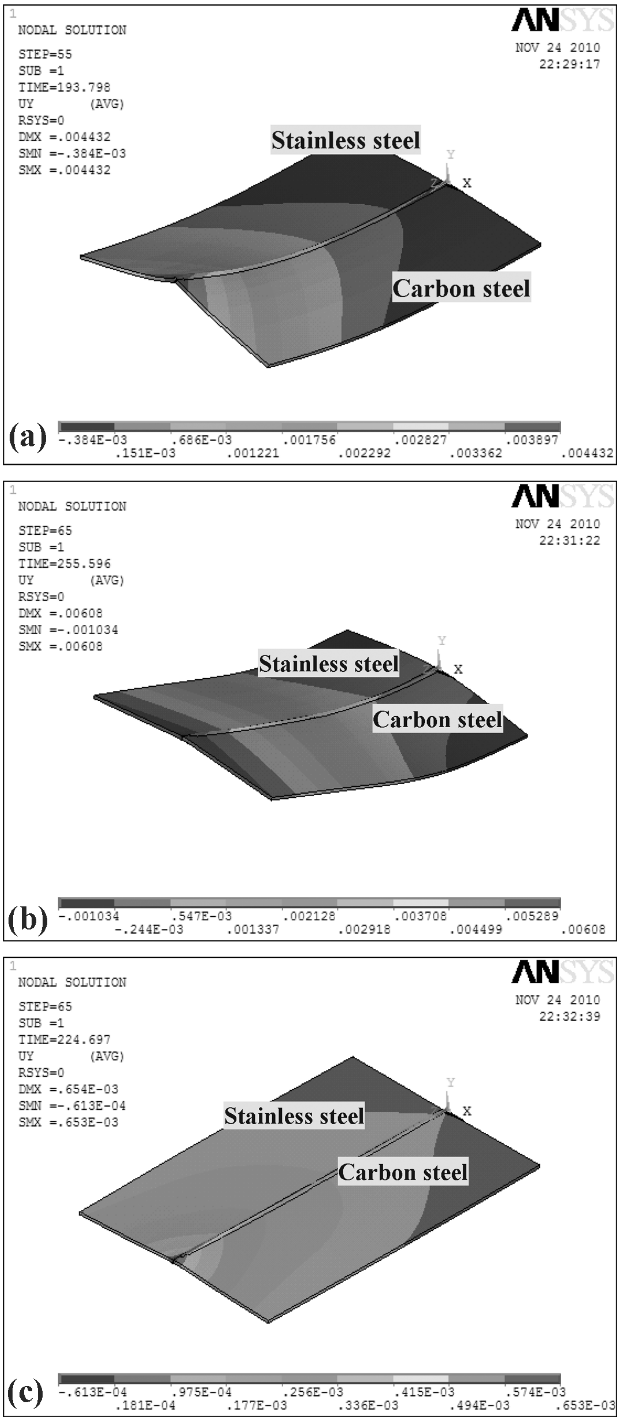

Figure 8: Effect of the welding layout on distortion: a) progressive, b) back-step and c) symmetric welding layout
Slika 8: Vpliv postavitve varjenja na popačenje oblike pri varjenju: a) progresivno, b) s koraki nazaj in c) simetrična postavitev varjenja

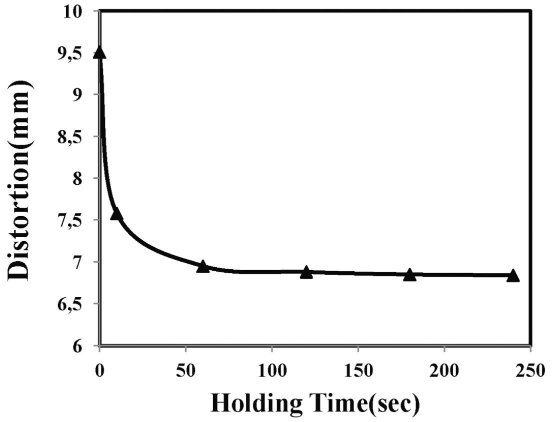

Figure 9: Effect of the holding time in the fixture on distortion
Slika 9: Vpliv časa zadržanja v držalu na popačenje oblike

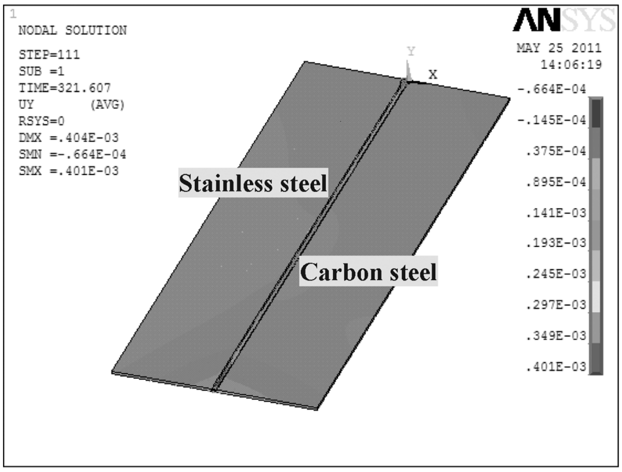

Figure 11: Distortion of sample 95LSD
Slika 11: Sprememba oblike vzorca 95LSD

fixture on the welding distortion. The question is what the effect of the holding time in a fixture on the magnitude of distortion is when a structure is welded under mechanical restraint. In order to answer this question the final distortion of sample 95LPD was determined for different holding times in the fixture and afterwards the structure was relaxed due to the removal of the applied mechanical constrains. As depicted in **Figure 9**, increasing the holding time decreases the residual welding distortion. After 120 s, the distortion-holding time curve enters a plateau region. This means that the joint in the fixture was cooled down and that, after this time, the holding time did not have a significant effect on the final magnitude of distortion. This can be due to the high yield strength of the base metal at room temperature, preventing additional distortion. **Figure 10** compares the distortions of similar and dissimilar joints. It is seen that a similar joint of stainless steel will cause a higher magnitude of distortion in comparison with a dissimilar joint. This may be attributed to the low thermal conductivity, low yield strength and the high thermal-expansion coefficient of stainless steel. Using the previous findings of this study, a simulation was done for different welding currents to reach the minimum welding distortion. The result is depicted in **Figure 11**. As can be seen, using the minimum welding current (95 A), the symmetric sequence and the 120-second holding time, the final magnitude of the welding distortion can be reduced by only about 0.4 mm which is very small in comparison with 23.7 mm for sample 135LPD.

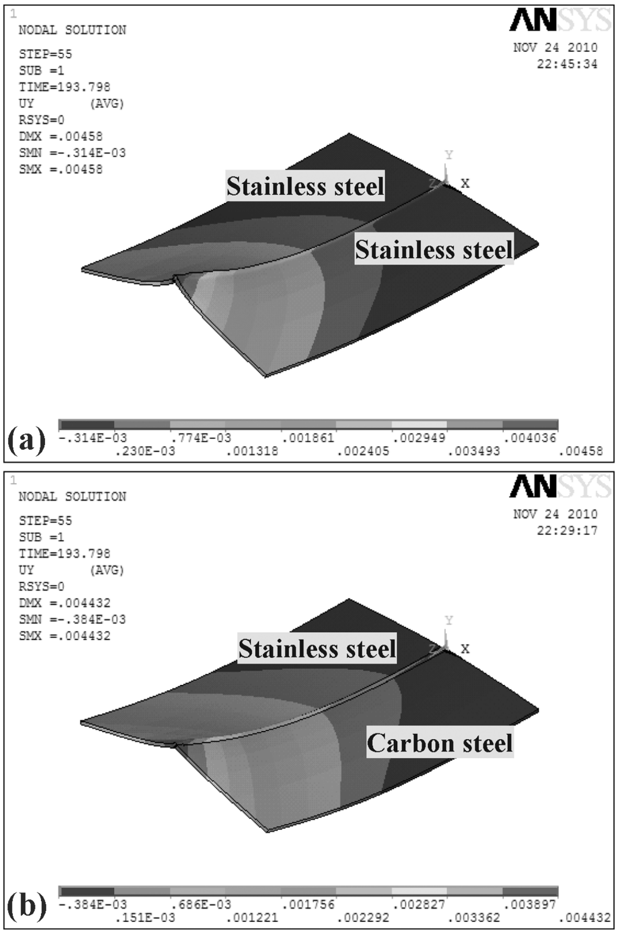

Figure 10: Comparison of the distortions of: a) similar and b) dissimilar joints
Slika 10: Primerjava popačenja oblike pri spajanju: a) enakih in b) različnih materialov

4 CONCLUSIONS

In this work, a verified 3D finite-element model[8] was utilized to evaluate the effects of the geometry, the welding current, the welding sequence, the holding time in the fixture and the similarity of the joint on the welding distortion of a dissimilar joint between carbon steel and stainless steel. Also, considering the welding current, the sequence and the fixing time, the magnitude of the welding distortion was minimized. The results showed that:

- A higher welding current, i.e., a higher heat input produces a larger distortion.
- Increasing the length and decreasing the thickness of the welded plates reduce the stiffness of the structure and, consequently, increase the welding distortion.
- Due to the low thermal conductivity and yield strength and the high thermal-expansion coefficient, the welding distortion of a similar joint of stainless steel is larger than in the case of a dissimilar joint of carbon steel and stainless steel.
- Increasing the holding time in the fixture first reduces the distortion but after 120 seconds, it no longer has a significant effect.
- The symmetric welding sequence was found to be an effective way to reduce the welding distortion of a joint compared to the other welding layouts applied in the current study.
- The minimum welding distortion in the studied joint can be obtained using the symmetric sequence, the welding current of 95 A and the holding time of 120 s.

5 REFERENCES

[1] Welding handbook, vol. 4, AWS, Miami 1997, 514–515

[2] J. A. Francis, H. J. Stone, S. Kundu, R. B. Rogge, H. K. D. H. Bhadeshia, P. J. Withers, L. Karlsson, Transformation Temperatures and Welding Residual Stresses in Ferritic Steels, Proc. of ASME Pressure Vessels and Piping Conference, San Antonio, 2007, 949–956, doi: 10.1115/PVP2007-26544

[3] D. Klobčar, J. Tušek, B. Taljat, Finite element modeling of GTA weld surfacing applied to hot-work tooling, Comput. Mater. Sci., 31 (**2004**), 368–378, doi:10.1016/j.commatsci.2004.03.022

[4] J. A. Francis, H. K. D. H. Bhadeshia, P. J. Withers, Mater. Sci. Technol., 23 (**2007**), 1009–1020, doi:10.1179/174328407X213116

[5] S. Kou, Welding Metallurgy, John Wiley & Sons, New Jersey 2003, 122

[6] S. Sahin, M. Toparli, I. Ozdemir, S. Sasaki, J. Mater. Process. Technol., 132 (**2003**), 235–241, doi:10.1016/S0924-0136(02)00932-9

[7] D. E. Katsareas, A. G. Yostous, Mater. Sci. Forum, 490–491 (**2005**), 53–61, doi:10.4028/www.scientific.net/MSF.490-491.53

[8] E. Ranjbarnodeh, S. Serajzadeh, A. H. Kokabi, A. Fisher, J. Mater. Sci., l46 (**2010**), 3225–3232, doi:10.1007/s10853-010-5207-8

[9] T. Teng, C. Lin, Int. J. Press. Vessels Pip., 75 (**1998**), 857–864, doi: 10.1016/S0308-0161(98)00084-2

[10] T. Teng, T. Chang, W. Tseng, Comput. Struct., l81 (**2003**), 273–286, doi:10.1016/S0045-7949(02)00447-9

[11] S. A. Tsirkas, P. Papanikos, T. Kermanidis, J. Mater. Process. Technol., 134 (**2003**), 59–69, doi:10.1016/S0924-0136(02)00921-4

[12] L. Gannon, Y. Liu, N. Pegg, M. Smith, Mar. Struct., 23 (**2010**), 385–404, doi:10.1016/j.marstruc.2010.05.002

UDK 669.721.5:539.511:621.73
Professional article/Strokovni članek

ISSN 1580-2949
MTAEC9, 49(2)267(2015)

MAGNESIUM-ALLOY DIE FORGINGS FOR AUTOMOTIVE APPLICATIONS

IZKOVKI IZ MAGNEZIJEVIH ZLITIN ZA AVTOMOBILSKO INDUSTRIJO

Michal Madaj[1], Miroslav Greger[1], Vlastimil Karas[2]
[1]VŠB-Technical University of Ostrava, Regional Materials Science and Technology Centre, 17. listopadu 15/2172, 708 33 Ostrava-Poruba, Czech Republic
[2]KOVOLIT, a.s., Nádražní 344, 664 42 Modřice, Czech Republic
michal.madaj@vsb.cz, vlastimil.karas@kovolit.cz

Prejem rokopisa – received: 2013-09-30; sprejem za objavo – accepted for publication: 2014-06-03

doi:10.17222/mit.2013.174

The paper presents an investigation of the effect of process variables and material condition on the forgeability of magnesium wrought alloys of the Mg-Al-Zn group. The experimental work included the studies of forging capabilities of the alloys in open-die forging at hot- and warm-working temperatures. Forging tests were performed for the material in both the as-cast and as-worked conditions, for two variants of the work-piece geometry. Different variants of the work piece indicated fracture-related problems in forging magnesium alloys in the warm-working temperature mode, which involved an interaction between the material composition and process variables, and the state of stress. By means of numerical calculations it was concluded that, in addition to the material condition, the favourable state of stress, provided by a closed die, could greatly improve the formability of magnesium alloys in the warm-working range.

Keywords: forging, magnesium alloys, automotive applications

Članek predstavlja preiskavo vplivov procesnih spremenljivk in materiala na kovnost magnezijevih zlitin iz skupine Mg-Al-Zn. Eksperimentalno delo je vključevalo študij sposobnosti za kovanje zlitin v odprtem orodju pri temperaturah vročega in toplega preoblikovanja. Preizkusi kovanja so bili izvršeni za material v litem stanju in za že predelan material za dve vrsti izkovkov z različno geometrijo. Različne variacije izkovkov so pokazale pri kovanju magnezijevih zlitin težavo z razpokami pri toplem preoblikovanju ter interakcijo med sestavo materiala, procesnimi spremenljivkami in stanjem napetosti. Z numeričnimi izračuni je bilo ugotovljeno, da dodatno k razmeram materiala lahko ugodno stanje napetosti, ki se ga doseže z zaprtim orodjem, močno izboljša preoblikovalnost magnezijevih zlitin v območju toplega preoblikovanja.

Ključne besede: kovanje, magnezijeve zlitine, uporaba v avtomobilski industriji

1 INTRODUCTION

The automotive industry, characterised by having the largest potential for development, is becoming an important user of magnesium materials. The use of magnesium in vehicles was, for decades, limited to the castings of complicated shapes for engines and wheels. Traditional die casting dominated for economic reasons. A possibility of using the components from magnesium materials including chassis and drives is now being considered. It turns out that it is suitable to replace the so-far used parts made of steel and aluminium with magnesium alloys. The use of magnesium alloys for the components of the chassis leads to high requirements for their strength, toughness and service life. Most of these properties are achieved by forging. The importance of using the forgings from magnesium alloys in passenger vehicles in comparison with the currently used die-cast castings is continuously increasing[1]. The use of magnesium alloys in cars depends on the price relation between aluminium and magnesium alloys. **Table 1** compares the current economic possibilities of replacing aluminium alloys with magnesium alloys, as well as the price relations expected in the years to come.

Figure 1 shows that the main market for forged components is the automotive industry. The forging industry

Table 1: Price relations between the forgings made of aluminium and magnesium alloys[1]
Tabela 1: Primerjava cen izkovkov iz aluminija in magnezijevih zlitin[1]

Price relation aluminium - magnesium	Aluminium		Magnesium – current price		Magnesium – target price	
	€/kg	€/dm^3	€/kg	€/dm^3	€/kg	€/dm^3
Basic metal	2.4	6.5	4.3	7.7	3.6	6.5
Initial blank	0.7	1.9	2.9 to 4.3	5.2 to 7.7	1.4 to 2.1	2.5 to 3.7
Forging and finishing	5–7	14.3–19.8	10–20	18–36	5–10	9–18
Total costs	8–10	23–28	17–29	31–51	10–16	1–28
Comparison with Al alloys	100 %	100 %	210–280 %	140–180 %	120–160 %	80–100 %

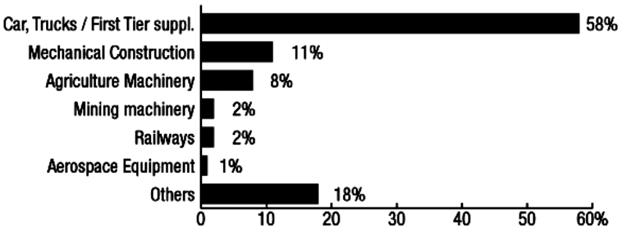

Figure 1: Customer profile of the European forging industry[2]
Slika 1: Profil porabnikov evropske industrije izkovkov[2]

is thus faced with some particular trends that relate to the developments within this sector[2].

It is increasingly recognised that aluminium (with a density of 2,700 kg/m^3) and magnesium (1,800 kg/m^3) are attractive alternatives to steel (7,800 kg/m^3). Notably magnesium is the lightest available engineering metal, being by 75 % lighter than steel and by 35 % lighter than aluminium[3]. To further specify this aspect, **Figure 2** gives an overview of the intrinsic weight-saving potential for some magnesium wrought alloys in comparison with the aluminium reference alloy which is in use for forgings.

Figure 2 distinguishes between some distinct modes of loading, taking into account the relevant material properties: modulus of elasticity E, yield stress YS and density ρ (for the other modes of loading, other design parameters apply). Although these data depend somewhat on the assumptions and the values of the specific property, this basic approach clearly demonstrates that benefits are anticipated for the strength-related and, in particular, for the bending-relevant parts, with a potential gain for magnesium of even 37 % over aluminium[3].

The mechanical properties of Mg can be substantially increased by alloying it with aluminium (up to w = 10 %), zinc (up to w = 6 %), manganese (up to w = 2.5 %) and zirconium (up to w = 1.5 %). Aluminium and zinc form a solid solution with magnesium. Intermetallic phases of types $Mg_{17}Al_{12}$ and $MgZn_2$ are formed when their amounts are higher. In both cases the quantity of the alloying element increases the basic mechanical properties. Manganese and magnesium form a solid solution, α-Mg. The solubility of manganese in magnesium decreases with the decreasing temperature and the α-Mn phase precipitates from the α-Mg solid solution. An addition of manganese does not influence the achieved strength characteristics, but it favourably influences the resistance to corrosion. An increase in the level of the resistance to corrosion can be explained with the fact that a thin layer of Mg-Mn oxides is formed on the surface. An addition of manganese decreases the effect of iron in magnesium. Manganese and iron form a compound of a high density, which settles at the bottom of the bath during the melting. Apart from the basic additions of these elements, an addition of tin is also used in magnesium alloys. Tin is soluble in magnesium at the temperature of 645 °C up to the amount of approximately w = 10 %. Its solubility decreases with the temperature, with a simultaneous precipitation of the β phase (Mg_2Sn). Complex Mg-Al-Mn alloys alloyed additionally with w = 5 % of Sn have good hot formability. Silicon is insoluble in magnesium. They form an intermetallic phase of the Mg_2Si type, which significantly strengthens the basic matrix[4]. Due to a significant increase in the brittleness, the amount of silicon in the alloys is under w = 0.3 %. As the alloying of magnesium alloys with zirconium refines the grains, the achieved level of mechanical properties increases and, at the same time, the resistance to corrosion decreases. The elements of rare-earth metals or thorium increase the refractoriness of magnesium alloys. Beryllium, in the amount of w = 0.005–0.012 %, decreases the oxidation of alloys during melting, casting and heat treatment[5].

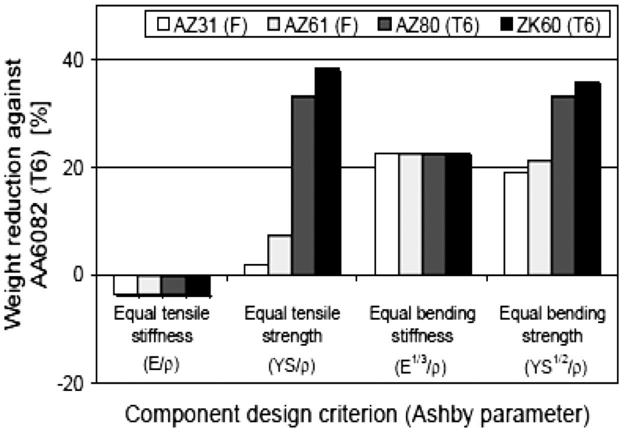

Figure 2: Mass-saving potential of magnesium over aluminium for some typical loading situations[3]
Slika 2: Možnost prihranka mase magnezija v primerjavi z aluminijem za nekatere značilne primere obremenitve[3]

One of the limitations of using the formed magnesium alloys for the production of forged parts is their low formability. For this reason, most of these materials are processed by forming at elevated temperatures, which is reflected in their strength properties. A lower forging temperature increases the precision of the forged parts, but it greatly deteriorates their formability and the material factors – the grain size, the limited number of slip systems at low temperatures and the resistance of a metal to formation of cracks, which is one of the important factors of formability.

Magnesium and the majority of its alloys crystallise in a hexagonal system. This system is characterised by a reduced formability, which is caused by a small number of slip mechanisms. Slips of dislocations take place in selected crystallographic planes and directions, and they are controlled by three known laws. Up to the temperature of 220 °C the only slip plane in magnesium is in the basal plane (0001) and direction $[11\bar{2}0]$. At higher temperatures the slip begins in plane $(11\bar{1}0)$ in direction $[11\bar{2}0]$. These are the planes and directions in HCP lattices that are most densely occupied by atoms. The formability increases significantly with an increase in the slip systems. The values of the critical slip stress (τ_{kr}) for pure magnesium are low. The value of the critical slip stress depends on the purity of the metal, the structure and thermodynamic conditions of deformation. The higher the purity of the metal, the lower is the magnitude of the critical slip stress. The impurities forming solid solutions with the basic metal increase τ_{kr} more intensely than the impurities that are insoluble in the basic metal[6]. If a metal and admixture form a solid solution, then the value of the critical stress increases in dependence of the difference between the magnitudes of atoms of both metals, and the difference between the electrochemical properties of both metals. The admixture elements in magnesium interact with the dislocations, increasing the critical slip stress. The influence of the admixture elements on τ_{kr} can be determined with the following equation:

$$\tau_{kr} = c^n \tag{1}$$

where c is the concentration of the admixture element and n is the exponent ($n \approx 0.5$–0.66).

The values of the critical slip stress decrease for the majority of metals with the increasing temperature. The influence of the temperature is not unequivocal in the case of magnesium and its alloys. Various slip planes can act at various temperatures. For example, at room temperature Mg alloys have only one system of slip planes. The number of active slip planes increases with an increase in the temperature, which is manifested with a rapid decrease in the slip stress. The yield strength of magnesium alloys can be approximately determined with the following equation:

$$\sigma_k = \frac{\tau_{kr}}{m} \tag{2}$$

where m is the Schmid factor ($m_{max} \approx 0.5$).

Table 2 presents the basic parameters of the technical procedure of forging magnesium alloys, as well as their mechanical and technological properties.

The basic properties of magnesium alloys depend on the achieved structural state, which is a function of the chemical composition, applied deformation and heat treatment. Recrystallisation annealing is performed at the temperature of around 350 °C. The recrystallisation of magnesium alloys strengthened by deformation starts in the temperature interval of 250–280 °C. This temperature interval depends on the degree of strain hardening. Most of the magnesium alloys alloyed with manganese or aluminium are used in the heat-treated conditions, i.e., after quenching and aging. The achieved higher strength is connected with the changed solubility of the admixture elements – Al, Zn and Zr – in dependence of the temperature. The heating before quenching is selected in such a way that the segregated intermetallic phases of types $MgZn_2$, $Mg_{17}Al_{12}$, $Mg_3Al_2Zn_2$ are dissolved in a solid solution. A homogenous oversaturated solid solution is obtained after the quenching. During aging the strengthening phases precipitate. A characteristic property of magnesium alloys is a low rate of diffusion processes and that is why the processes of the phase transformation run very slowly. During the heating before quenching the dwell times of 4–24 h are applied. Artificial aging in magnesium alloys runs within the interval from 16–24 h. The selected magnesium alloys can also be quenched by cooling them in air from the finish-forging temperature. The consequential aging performed directly from the finish-forging temperature is used without the inclusion of the previous solution annealing and quenching. The temperatures of the solution annealing of magnesium alloys vary from 380–420 °C. Controlled aging is performed at the temperatures from 200–300 °C. This procedure of heat treatment is marked as T1 and T4. To achieve the maximum level of strengthening, it is necessary to apply an aging temperature from 175–200 °C. The changes in the properties achieved by aging are smaller for magnesium alloys in comparison with aluminium alloys. An increase in the strength properties after aging is not higher than 20–35 %. However, the plastic properties of alloys decrease after aging. For these reasons the most frequently used heat treatment is the homogenisation annealing. The mechanical properties are enhanced as a result of a more homogeneous structure. An application of natural aging does not practically lead to more significant changes in the strength properties[6,7].

2 EXPERIMENTAL WORK

We experimentally verified the forging procedure on the piston-rod and plate forgings, the final shapes of which are illustrated in **Figure 3**. Bars with the diameter of 30 mm and the length of 178 mm were used as initial blanks for the piston-rod forgings. The flat blank for the plate forging had the following dimensions: 130 mm × 150 mm × 13 mm. The forged materials were made of magnesium alloys of types AZ31, AZ61 and AZ91. The

Table 2: Forging temperatures, mechanical and technological properties of the forgings from magnesium alloys[6]
Tabela 2: Temperature kovanja, mehanske in tehnološke lastnosti izkovkov iz magnezijevih zlitin[6]

Alloy	Forging temperatures (°C)		Mechanical properties			Technological properties	
	for forgings	for die forgings	*YS*/MPa	*UTS*/MPa	Elong. Δl/%	Weldability	Resistance to corrosion
AZ31	290–345	260–315	195	260	9.0	O	G
AZ61	315–370	290–345	180	295	12.0	G	G
AZ91	300–385	205–290	250	345	5.0	G	G

Note: O – outstanding, G – good

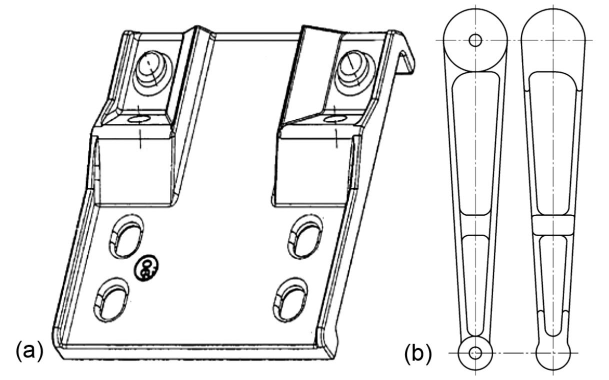

Figure 3: a) Shape of the flat-plate forging and b) shape of the piston-rod forging
Slika 3: a) Oblika izkovka plošče in b) oblika izkovka ojnice

Table 3: Chemical composition of magnesium alloys for forgings
Tabela 3: Kemijska sestava magnezijevih zlitin za kovanje

Alloy	Amounts of alloying elements in mass fractions, *w*/%						
	Al	Zn	Mn	Si	Cu	Fe	Ni
AZ31	2.50–3.50	0.20–0.80	≥ 0.200	≤ 0.100	≤ 0.05	≤ 0.005	≤ 0.005
AZ61	6.76	0.38	0.13	0.05	0.006	0.011	–
AZ91	8.76	0.73	0.22	0.05	0.010	0.011	–

Table 4: Initial parameters for forging the piston rods
Tabela 4: Začetni parametri pri kovanju ojnice

Alloy	Temperature (°C)	Mass of the blank (g)	Dimensions and shape of forgings were satisfactory (%)	Flow stress
AZ31	350	30	100	low
AZ61	320	30	97	medium
AZ91	300	30	95	high

chemical compositions of the forged alloys are presented in **Table 3**.

Forgings were used in the heat-treated as well as in the non-treated states. Before forming, the input blanks were subjected to homogenisation annealing at the temperatures of 380–420 °C. The duration of annealing was 15 h.

After the forging the samples were subjected to the heat treatment (recrystallisation annealing), which consisted of a gradual reheating of the forgings in the furnace at a rate of 20 °C per minute up to a temperature of approximately 420 °C. The forgings were left at this temperature for three hours and then cooled in water. Approximately four hours after the completion of the annealing the surfaces of the forgings were blasted with Cr-balls.

The forging of the piston-rod and plate forgings was performed in an open die on a hydraulic press MW PA 200. The samples were forged with a single strike at a temperature of 300–350 °C depending on the type of the alloy (**Table 4**). In the case of the piston-rod forging, the bleed was cut-off in the hot state, immediately after the completion of the forging.

The temperature of the die tool was approximately 150–170 °C. The Acheson Dag 554/20 lubricant diluted with water at a ratio of 1 : 20 was used as a lubricating medium. The power of the stamping machine was set to 45 % and its stroke to 220 mm (the lowest possible value on the machine for such forgings).

After the forging the test samples for a metallographic analysis of the structure were taken from the forgings. The piston-rod samples were cut along the axis of symmetry in order to examine the change in the structure at individual places of the cut. The sample preparation also included their grinding, polishing and subsequent etching.

The polishing was performed in two phases. In the first phase the samples were polished on a cloth with a soft nap using a polishing suspension based on Al_2O_3. However, after the completion of the first phase of the polishing, the sample surfaces still contained a large amount of scratches and it was, therefore, necessary to start the second phase of polishing on a very fine velvet cloth with short hair. Thus polished samples were cleaned with water, rinsed in alcohol and dried by warm air. The prepared surfaces were etched in 4 % HNO_3 (Nital) in order to remove the deformed layer for its identification.

After the heat treatment, the test specimens for the determination of Brinell hardness were taken from the forgings. The hardness test was performed 10 d after the forging, prior to the heat treatment and also after the heat treatment. The load during the hardness test was 306.5 N and the diameter of the indenting ball was 2.5 mm.

Three indents were made on each sample while keeping the distance between individual indents in accordance with the ISO 6506 standard recommending at least 5 mm in order to avoid the results to be influenced by strain hardening. The samples were subjected to a load for approximately 25 seconds.

3 RESULTS AND DISCUSSIONS

The deformation behaviour and development of the structures of six alloys and two shapes of the products were verified experimentally. All the forgings were forged without any problem and with respect to technology no problem occurred during the forging of magnesium alloys. After the forging the flow stress was assessed quantitatively (**Table 5**).

Table 5: Flow stress of the formed alloys
Tabela 5: Napetost tečenja preoblikovanih zlitin

Material – shape	Average residual energy (kN)
AZ31- piston rod	5166
AZ61- piston rod	4864
AZ91- piston rod	4858
AZ31- plate	4496
AZ61- plate	4369
AZ91- plate	4285

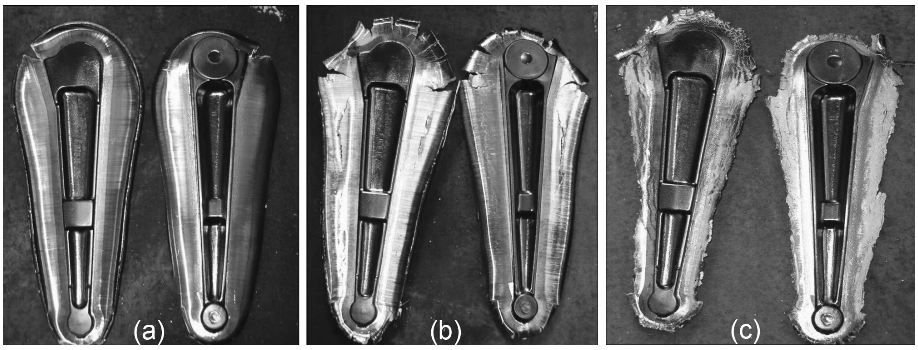

Figure 4: Shapes of the forgings from the magnesium alloys: a) AZ31, b) AZ61, c) AZ91
Slika 4: Videz izkovkov iz magnezijevih zlitin: a) AZ31, b) AZ61, c) AZ91

During the forging after a strike the energy was discharged onto the contact surfaces – it means that the forgings with the lowest residual energy had the highest flow stress. It follows from the obtained results that among the magnesium alloys the AZ91 alloy has the highest flow stress, followed progressively by AZ61 and AZ31. Some of the piston-rod forgings had a scratch on the larger diameter, which might have been related to the crack formation and such parts were investigated. The shapes of the forgings are shown in **Figure 4**.

For the preparation of the flat forging it was absolutely necessary to adapt the contact surfaces, which had to be parallel and smooth since any possible deep scratch could cause a formation of cracks. The shapes of the forgings are shown in **Figure 5**.

The metallographic investigation of the samples was performed in the initial state, after the heat treatment and, finally, after the forging and heat treatment. The analysis of the microstructure was focused on the formation of the cracks that were highlighted during the technological production of the forgings and the individual phenomena associated with the forming of magnesium alloys (dynamic recrystallisation, twinning, growth and shape of grains).

In the initial state, the microstructures of magnesium alloys AZ31, AZ61 and AZ91 contained the majority phase (a solid solution of aluminium in magnesium) and two types of the minority phase. The first type of the minority phase consisted of relatively massive particles of $Mg_{17}Al_{12}$, while the second type consisted of fine, needle-like particles of the same phase present in the vicinity of the grain boundaries (**Figure 6**).

The objective of the homogenisation annealing was to remove the segregation heterogeneities of the admixture elements. During the homogenisation annealing the

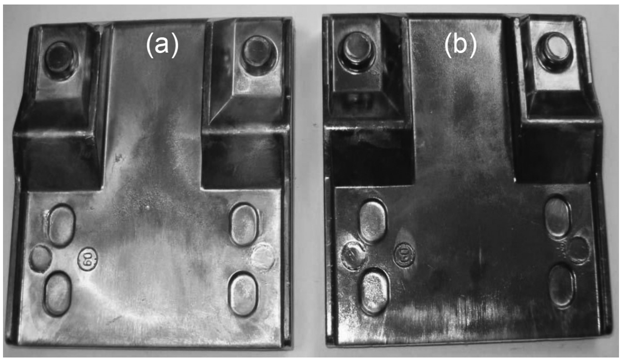

Figure 5: Shapes of the forgings from the magnesium alloys: a) AZ31, b) AZ61
Slika 5: Videz izkovkov iz magnezijevih zlitin: a) AZ31, b) AZ61

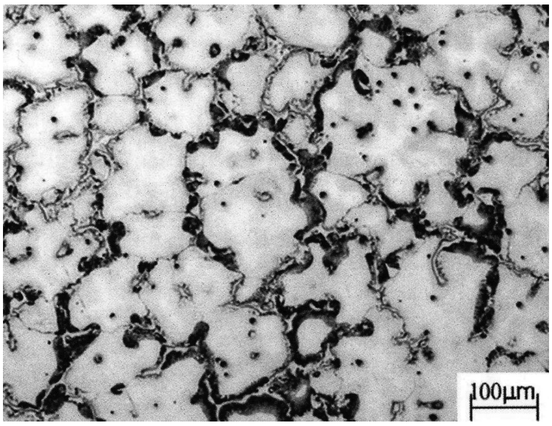

Figure 6: Microstructure of alloy AZ91 in the as-cast state, a cross-section
Slika 6: Strjevalna mikrostruktura zlitine AZ91; prečni prerez

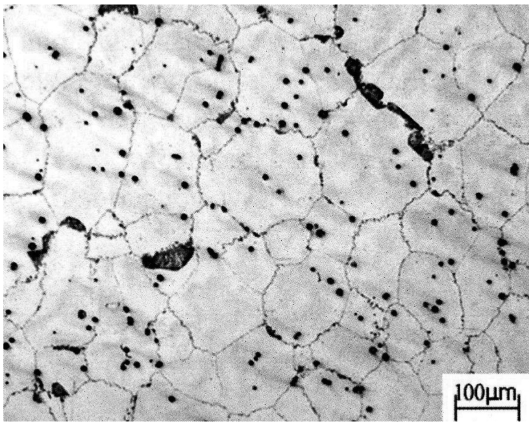

Figure 7: Microstructure of the AZ91 alloy after the homogenisation annealing, a cross-section
Slika 7: Mikrostruktura zlitine AZ91 po homogenizacijskem žarjenju; prečni prerez

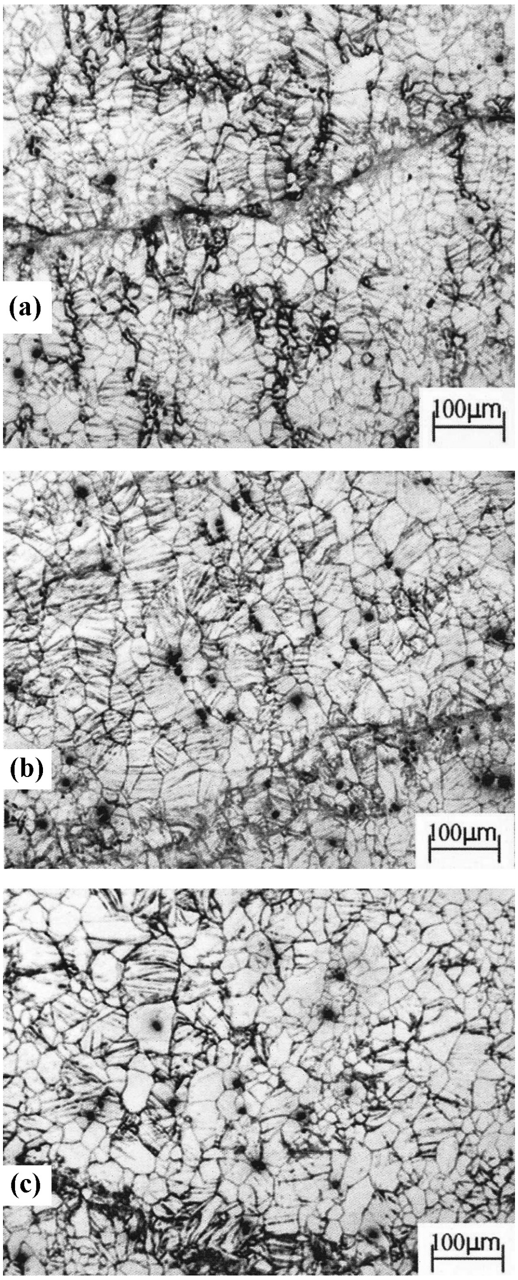

Figure 8: Microstructures of the alloys: a) AZ31, b) AZ61 and c) AZ91 after the forging, a cross-section

Slika 8: Mikrostrukture zlitin: a) AZ31, b) AZ61 in c) AZ91, po kovanju; prečni prerez

segregated phases on the grain boundaries dissolved in the basic matrix and the chemical composition of the alloy was more homogenous (**Figure 7**). This improved the formability and enhanced the level of mechanical properties.

The structures of the forged piston rods made of alloys AZ31 and AZ61 did not show any defects that could cause a subsequent failure of the components. The grains of both alloys were stretched in the direction of the intensive flow of the material, i.e., in the longitudinal direction of the forging. In alloy AZ61 a dynamic recrystallisation took place, which started at the boundaries of the original grains, being supported by a sufficiently large number of precipitates of $Mg_{17}Al_{12}$ and by the created twins. The recrystallisation gradually expanded toward the centre of the basic grains. The piston rod made of alloy AZ91 had its central part without any significant failures; however, its peripheral parts were characterised by the cracks that penetrated deeper into the sample. In this alloy a dynamic recrystallisation on the grain boundaries took place, but there was insufficient time for its propagation into the entire volume (**Figure 8**).

With respect to the flat blank for plate forging, the best forging over the entire cross-section was achieved with the AZ31 alloy that showed no cracks. The AZ61 alloy contained no cracks in the central part of the component, but under the surface some cavities were formed, which could cause a failure of the given component during the subsequent use.

The most damaged microstructure was found for alloy AZ91, where cracks were present right under the surface in all the areas, penetrating deeper into the component and, in some cases, they appeared on the surface as well. It was evident from the metallographic investigation that the cracks were preferentially formed on the grain boundaries, particularly in the presence of phase $Mg_{17}Al_{12}$ or in the places where this phase was dissolved. The grains of all the forged alloys were considerably stretched in the direction of the bleed groove and in alloy AZ91 they led to a formation of a crack over the entire component.

After the annealing, a complete recrystallisation of the grains occurred in the sample made of alloy AZ91. The grains contained acicular particles, spread over the entire grains. In alloy AZ61, the recrystallised grains were present only on the borders of the original grains, but they did not spread throughout the entire volume. The chemical composition, i.e., the amount of aluminium, had a great influence on these processes. The secondary phases, and zinc- and aluminium-based

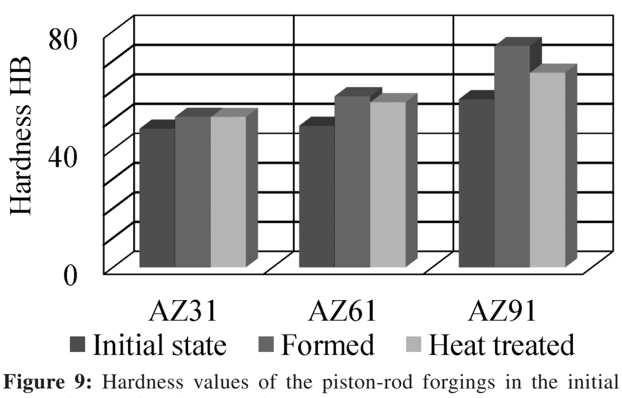

Figure 9: Hardness values of the piston-rod forgings in the initial state, after the forming and after the heat treatment

Slika 9: Trdota izkovka ojnice v začetnem stanju, po kovanju in po toplotni obdelavi

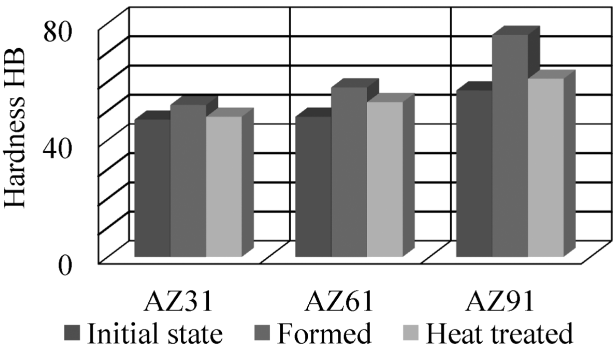

Figure 10: Hardness values of the plate forgings in the initial state, after the forming and after the heat treatment

Slika 10: Trdota izkovka plošče v začetnem stanju, po kovanju in po toplotni obdelavi

precipitates dissolved during the heat treatment in the basic matrix.

The mechanical properties of the forgings and their evolution in dependence of the heat treatment were verified with a hardness test. For all the investigated magnesium alloys in the initial state, the Brinell hardness values were measured after the forming and after the heat treatment, and they were averaged for individual alloys. The resulting hardness values are represented in **Figures 9** and **10**.

It follows from the results of the hardness tests that the heat treatment and forming had considerable influences on the hardness of magnesium alloys. The aluminium amount in the material is another factor, influencing the hardness. The material hardness decreases with the decreasing aluminium amount in the material (**Table 3, Figures 9** and **10**). During the forming the hardness of alloy AZ91 increased considerably – even by 19 HB. The hardness of alloy AZ61 increased by 10 HB. The weakest influence of the forming on the hardness value was found for alloy AZ31. After the heat treatment the hardness of alloy AZ91 dropped considerably, which was caused by the recrystallisation, taking place during the heat treatment. The heat treatment had no significant impact on the resulting hardness of alloys AZ31 and AZ61.

4 CONCLUSIONS

The deformation behaviour of alloys AZ31, AZ61 and AZ91 during die forging was experimentally verified. The influences of the forging technology and homogenisation annealing on the structures and properties of the forgings were compared. The influences of the heat treatment and the forming temperature on the final structure and mechanical properties were evaluated. It follows from the obtained results that the aluminium amount in the material as well as the heat treatment and forming had considerable influences on the hardness of the magnesium alloys. The initial structures used in the tests were in the as-cast form, which probably caused the formation of cracks in the alloys with higher aluminium amounts (AZ61, AZ91).

The results confirmed the suitability of applying heat treatment before forging. This procedure enabled us to obtain the forgings with a more homogeneous structure. After the application of forming some micro-cracks and voids were detected in the magnesium alloys of AZ61 and AZ91. The cracks were located just under the surface and they penetrated deeper into the material. In alloy AZ91 the micro-cracks were formed throughout the entire volume and the initiations of these micro-cracks were preferentially on the grain boundaries, mainly in the area of particles $Mg_{17}Al_{12}$. From the structural point of view, alloy AZ31, in which no structural defects were detected, was found satisfactory. The highest strength and hardness were obtained with alloy AZ91. It follows from the obtained results that with the increasing aluminium amount the hardness of forged magnesium alloys increases as well.

Acknowledgement

This paper was created within project No. CZ.1.05/2.1.00/01.0040 "Regional Materials Science and Technology Centre" within the frame of operational programme "Research and Development for Innovations" financed by the Structural Funds and the state budget of the Czech Republic.

5 REFERENCES

[1] R. Matsumoto, K. Osakada, Development of warm forging method for magnesium alloy, Materials Transactions, 45 (**2004**) 9, 2838–2844, doi:10.2320/matertrans.45.2838

[2] R. Asakawa, K. Hirukawa, Technology for manufacturing magnesium alloy components with excellent heat resistance, Kobelco technology review, 31 (**2013**), 76–81

[3] B. Płonka, M. L. Grega, K. Remsak et al., Die forging of high-strength magnesium alloys – the structure and mechanical properties in different heat treatment conditions, Archives of Metallurgy and Materials, 58 (**2013**) 1, 127–132, doi:10. 2478/v10172-012-0162-9

[4] M. Greger, L. Čížek, I. Juřička et al., Possibilities of mechanical properties and microstructure improvement of magnesium alloys, Archives of Materials Science and Engineering, 28 (**2007**) 2, 83–90

[5] M. Greger, M. Widomská, V. Karas, Properties of forging from magnesium alloys and their use in industry, Conference proceedings, Metal 2012, Ostrava, 2012, 440–445

[6] M. Greger, M. Widomská, Structural characteristics of magnesium alloys along the equal channel angular pressing, Advances in Engineering Plasticity and its Applications, Shanghai Jiaong University, Shanghai, 2004, 1083–1088, doi:10.4028/www.scientific.net/KEM.274-276.1083

[7] D. Kobold, T. Pepelnjak, G. Gantar et al., Analysis of deformation characteristics of magnesium AZ80 wrought alloy under hot conditions, Journal of Mechanical Engineering, 56 (**2010**) 12, 823–832

UDK 669.721.5:620.193
Professional article/Strokovni članek

ISSN 1580-2949
MTAEC9, 49(2)275(2015)

RESISTANCE TO ELECTROCHEMICAL CORROSION OF THE EXTRUDED MAGNESIUM ALLOY AZ80 IN NaCl SOLUTIONS

ODPORNOST EKSTRUDIRANE MAGNEZIJEVE ZLITINE AZ80 PROTI ELEKTROKEMIJSKI KOROZIJI V RAZTOPINI NaCl

Joanna Przondziono[1], Eugeniusz Hadasik[1], Witold Walke[2], Janusz Szala[1], Joanna Michalska[1], Jakub Wieczorek[1]

[1]Silesian University of Technology, Faculty of Materials Engineering and Metallurgy, Krasińskiego 8, 40-019 Katowice, Poland
[2]Silesian University of Technology, Faculty of Biomedical Engineering, Ch. de Gaulle'a 66, 41-800 Zabrze, Poland
joanna.przondziono@polsl.pl

Prejem rokopisa – received: 2013-10-01; sprejem za objavo – accepted for publication: 2014-04-03

doi:10.17222/mit.2013.208

The purpose of this study was to evaluate the electrochemical corrosion resistance of the extruded magnesium alloy AZ80 in NaCl solutions. The resistance to electrochemical corrosion was evaluated on the grounds of registered anodic polarisation curves. Potentiodynamic tests were performed in solution with a concentration of 0.01–2.00 M NaCl. In addition, immersion tests were performed, and they allowed us to determine the corrosion rate. Scanning electron microscopy was applied to observe the microstructure after the immersion tests (after removing the corrosion products). Phenomena that happen on the surface of the alloy were evaluated with the application of electrochemical impedance spectroscopy. The tests enabled us to determine the impedance spectra of the system and the data obtained during the measurement was matched to the equivalent system. An optical profilometer was used for the measurement of the geometrical features of the surface of the alloy. The results of the performed tests prove explicitly the deterioration of the corrosion characteristics of the alloy with an increase in the molar concentration of the NaCl solution. A decrease of the corrosion potential and the polarisation resistance was observed, as well as an increase of the corrosion current density. It was proved that irrespective of the concentration, pitting corrosion can be found on the surface of the alloy. The potential to use the extruded magnesium alloy AZ80 in the aircraft and automotive industries is connected with the necessity to apply protective layers on elements made from the tested alloy.

Keywords: extruded magnesium alloy AZ80, electrochemical corrosion, potentiodynamic and immersion tests, SEM, EIS

Namen te študije je bil oceniti odpornost ekstrudirane magnezijeve zlitine AZ80 proti elektrokemijski koroziji v raztopini NaCl. Odpornost proti elektrokemijski koroziji je bila ugotovljena na podlagi anodnih polarizacijskih krivulj. Izvršeni so bili potenciodinamski preizkusi v raztopini s koncentracijo od 0,01–2 M NaCl. Dodatno so bili izvršeni tudi preizkusi s potapljanjem, ki so omogočili določitev hitrosti korozije. Vrstična elektronska mikroskopija je bila uporabljena za slikanje mikrostrukture po potapljanju (po odstranitvi korozijskih produktov). Pojavi na površini zlitine so bili ocenjeni z elektrokemijsko impedančno spektroskopijo. Preizkusi so omogočili določitev impedančnega spektra sistema in z meritvami dobljeni podatki so se ujemali z ekvivalentnim sistemom. Optični profilometer je bil uporabljen za merjenje geometrijskih pojavov na površini zlitine. Rezultati izvršenih preizkusov so potrdili poslabšanje korozijskih lastnosti zlitine pri povečanju molske koncentracije raztopine NaCl. Opaženo je bilo zmanjšanje korozijskega potenciala in polarizacijske odpornosti, kot tudi povečanje gostote korozijskega toka. Dokazano je, da se ne glede na koncentracijo jamičasta korozija pojavi na površini zlitine. Možnosti uporabe ekstrudirane magnezijeve zlitine AZ80 v letalstvu in avtomobilski industriji je povezana z nujnostjo uporabe zaščitnih plasti na komponentah iz preizkušane zlitine.

Ključne besede: ekstrudirana magnezijeva zlitina AZ80, elektrokemijska korozija, potenciodinamski preizkus in preizkus s potapljanjem, SEM, EIS

1 INTRODUCTION

The application of magnesium alloys that can be subject to plastic strain is far less popular than for alloys obtained through casting. This results from a number of technological difficulties during plastic working (which are connected with their low formability at ambient temperature), as well as from high production costs. One of the methods of magnesium-alloy forming is extrusion, which is usually realised within the temperature range 320–450 °C at a rate of 1–25 m/min. Hot isostatic pressing (HIP) has been intensively developing for the last couple of years. Thanks to favourable thermal and mechanical conditions, hot isostatic pressing can be executed at lower temperatures and a larger grain size reduction for the magnesium alloys can be obtained. Equal channel angular pressing (ECAP) is also increasing in popularity[1–5].

The main problem when using magnesium alloys in the aircraft and automotive industries is their susceptibility to electrochemical corrosion. Magnesium as a highly electronegative element that features extreme susceptibility to passing into electrolyte solutions. The standard electrochemical potential of magnesium E_o is –2.37 V, whereas in a 3 % solution of sodium chloride it is –1.63 V (SCE). Magnesium alloys feature good corrosion resistance in weather conditions and when they are put to the reaction of alkaline, chromate and water-fluoric solutions of acids as well as to the majority of organic chemical compounds, e.g., hydrocarbons, aldehydes, alcohols (with the exception of methanol), phenols, amines, esters and most oils. Magnesium is not resistant to the influence of water containing trace elements of heavy-metals ions, sea water, inorganic and organic acids and acid salts (e.g., ammonium), anhydrous methanol, gasoline containing lead (and its compounds), and freon containing water[6–12].

It is extremely prone to electrochemical and chemical corrosion, in particular in an environment that contains chloride ions, which substantially limits the area of this alloy's application. The reason for the low corrosion resistance of magnesium is the insufficient protective properties of the layer of oxides that is formed on the surface in an oxidising atmosphere or the layer of hydroxides in water solutions. Electrochemical corrosion is most often displayed by metal defects on the surface (spots and pits) or by the deterioration of the material's strength[13–19].

The purpose of this study was to evaluate the resistance to electrochemical corrosion of the magnesium alloy AZ80 after extrusion. Corrosion tests were made in NaCl solutions featuring a concentration of chloride ions within the range of 0.01–2.00 M NaCl. Potentiodynamic tests allowed us to register anodic polarisation curves. Immersion tests in NaCl solutions were performed in the time period 1–5 d. A scanning electron microscope served to make images of the AZ80 alloy surface after the corrosion tests. Phenomena that happen on the surface of the alloy were evaluated with the application of electrochemical impedance spectroscopy. The surface morphology after the corrosion tests was evaluated by means of a surface analyser.

2 EXPERIMENTAL

Samples of AZ80 alloy after extrusion served as stock material for the tests. The chemical composition and the mechanical properties of the alloy are presented in **Tables 1** and **2**.

Table 1: Chemical composition of magnesium alloy AZ80 in mass fractions, *w*/%

Tabela 1: Kemijska sestava magnezijeve zlitine AZ80 v masnih deležih, *w*/%

Al	Zn	Si	Mn	Cu	Fe	Mg
8.2	0.34	0.02	0.13	<0.03	0.005	bal.

Table 2: Mechanical characteristics of magnesium alloy AZ80 after extrusion

Tabela 2: Mehanske lastnosti magnezijeve zlitine AZ80 po ekstruziji

R_m/MPa	$R_{p0.2}$/MPa	A/%
343	258	13.5

The resistance to electrochemical corrosion was evaluated on the grounds of registered anodic polarisation curves with the application of the VoltaLabPGP201 testing system by Radiometer. A saturated calomel electrode (NEK) of the KP-113 type served as a reference electrode. A platinum electrode of the PtP-201 type served as an auxiliary electrode. The tests were performed in solutions featuring various molar concentrations of NaCl solution (0.01–2.00 M NaCl). The temperature of the solutions during the test was (21 ± 1) °C.

The immersion tests were performed at ambient temperature with the application of the immersion method in 0.01–2.00 M NaCl solution for 1–5 d. After grinding of the surface of the samples, they were weighed and the mass m_0 was determined. After immersion of the alloy in the NaCl solution for 1–5 d, samples were taken out and the corrosion products were removed in the reagent containing 200 g/L CrO_3 and 10 g/L $AgNO_3$. Next, they were washed with distilled water, degreased with acetone, dried and weighed again with a determination of the mass m_1. The performed tests enabled us to determine the corrosion rate. Potentiodynamic tests and immersion tests were performed for three samples of AZ80 alloy for each concentration of NaCl solution.

A scanning electron microscope with field emission FE SEM S-4200 Hitachi in cooperation with a spectrometer EDS Voyager 3500 Noran Instruments was used to make qualitative and quantitative analyses of the chemical composition in micro-areas. The analysis of the morphology of the AZ80 surface was presented in diagrams and profilographs made with the application of an optical surface analyser MicroProf by FRT.

In order to obtain information about the physical and chemical properties of the surface of the samples made from the AZ61 alloy, tests with the application of electrochemical impedance spectroscopy (EIS) were performed. The measurements were made with the application of an AutoLab PGSTAT 302N measuring system equipped with a FRA2 (Frequency Response Analyser) module. The tests of electrochemical impedance spectroscopy are a linear measurement of the electrical response of the tested metallic material to stimulation with an electromagnetic signal over a wide range of frequencies. The performed tests enabled a direct comparison of the real behaviour of the object with its equivalent system, which is a model that relates to the physically realized impedance.

3 RESULTS AND DISCUSSION

The potentiodynamic tests results are presented in **Table 3**. The anodic polarisation curves are shown in **Figure 1**.

Table 3: Potentiodynamic tests results of AZ80 alloy – mean values

Tabela 3: Rezultati potenciodinamičnih preizkusov zlitine AZ80 – srednje vrednosti

Molar concentration /M*	E_{corr}/mV	I_{corr}/(A/cm^2)	R_p/(Ω cm^2)
0.01	–1434	0.010	2610
0.2	–1540	0.062	427
0.6	–1573	0.093	280
1.0	–1576	0.128	203
2.0	–1593	0.252	104

* M = mol/L (ISO 80000)

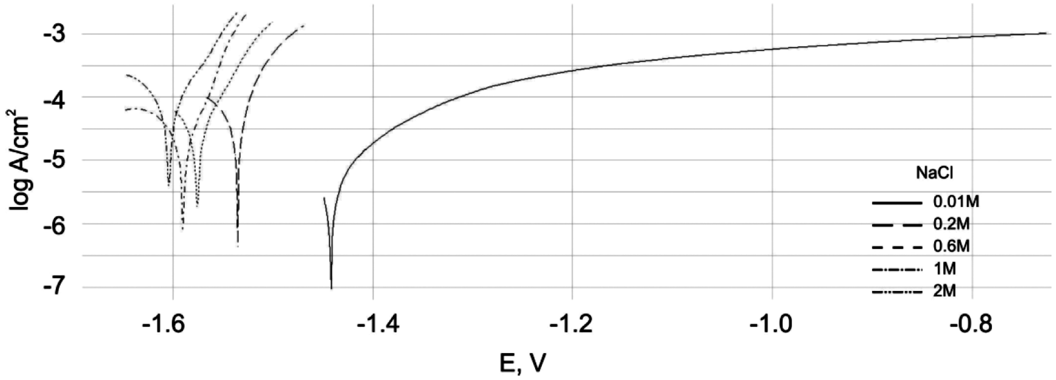

Figure 1: Anodic polarisation curves of AZ80 alloy
Slika 1: Anodna polarizacijska krivulja zlitine AZ80

The tests proved that the corrosion characteristics of the alloy decrease with the increase of the chloride ion concentration. The corrosion potential decreased from E_{corr} = –1434 mV (0.01 M NaCl) to E_{corr} = –1593 mV (2 M NaCl). It was observed that the polarisation resistance decreased from R_p = 610 Ω cm^2 (0.01 M NaCl) to R_p = 104 Ω cm^2 (2 M NaCl). The corrosion current density increased from i_{corr} = 0.01 µA/cm^2 (0.01 M NaCl) to i_{corr} = 0.252 µA/cm^2 (2 M NaCl).

Table 4 presents selected results of the immersion test. The corrosion rate V in the immersion test was determined from Equation (1):

$$V = \frac{m_0 - m_1}{St} \quad (1)$$

where V is the corrosion rate (mg/(cm^2 d)), m_0 is the initial mass of the sample (mg), m_1 is the sample mass after removal of the corrosion products (mg), S is the area (cm^2), and t is the exposure time (d).

Table 4: Immersion test results
Tabela 4: Rezultati preizkusov s potapljanjem

Concentration NaCl M	Corrosion rate, V/(mg cm^{-2} d^{-1})	
	1 d	5 d
0.01	0.256	0.343
0.6	1.103	1.295
2.0	2.332	3.850

The results of the immersion tests for the tested alloy confirmed, just as the potentiodynamic tests did, that the alloy was more prone to electrochemical corrosion when the molar concentration of the solution increased. The corrosion rate in a solution with a concentration of 0.01 M NaCl increased from 0.256 mg/(cm^2 d) after the 1st day to 0.343 mg/(cm^2 d) after 5 d. The tests performed in the time period 1 d to 5 d in the 2 M NaCl solution showed that corrosion rate increased from 2.332 mg/(cm^2 d) to 3.85 mg/(cm^2 d).

The results of the tests performed with the scanning microscope FE SEM S-4200 Hitachi are presented in **Figures 2** and **3**.

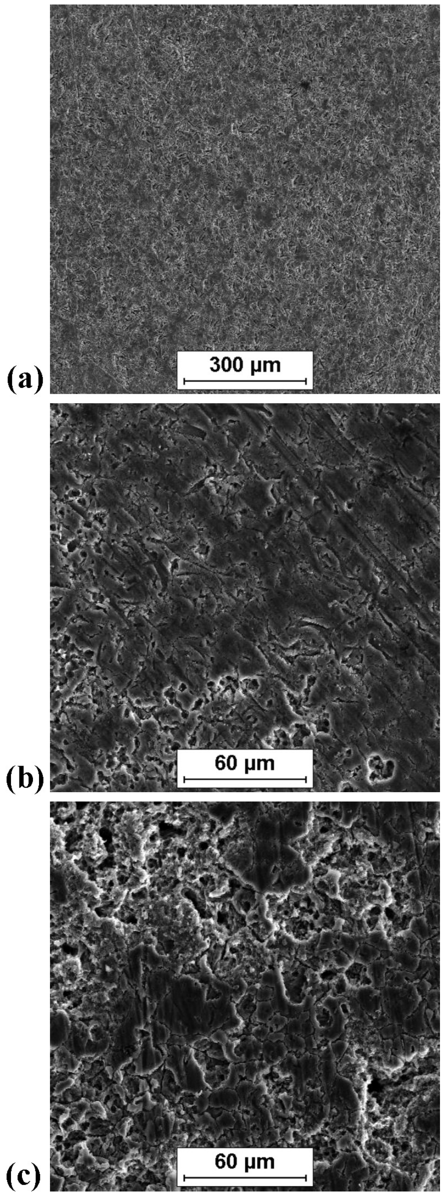

Figure 2: The surface of the alloy after 1 d exposure in the solution with a concentration of: a) 0.01 M, b) 0.6 M and c) 2 M NaCl
Slika 2: Površina zlitine po izpostavi 1 d v raztopini s koncentracijo: a) 0,01 M, b) 0,6 M in c) 2 M NaCl

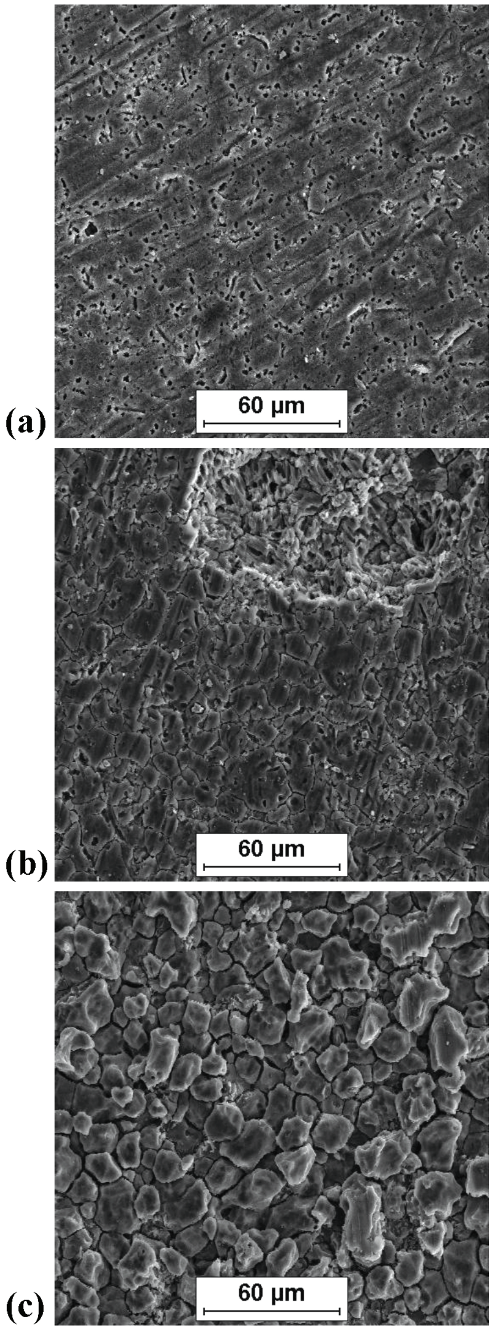

Figure 3: The surface of the alloy after 5 d exposure in the solution with a concentration of: a) 0.01 M, b) 0.6 M and c) 2 M NaCl

Slika 3: Površina zlitine po izpostavi 5 d v raztopini s koncentracijo: a) 0,01 M, b) 0,6 M in c) 2 M NaCl

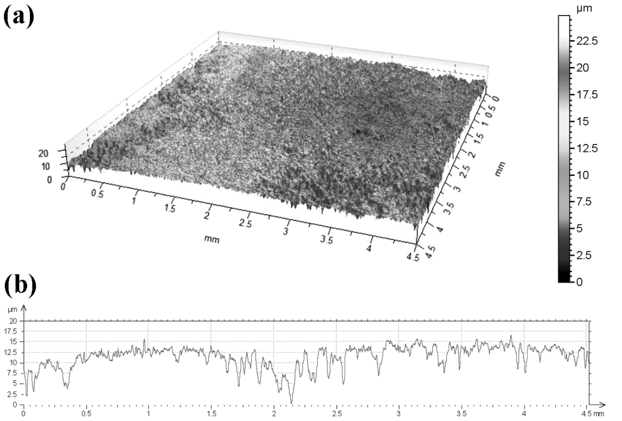

Figure 4: a) 3D image of the surface of the alloy and b) roughness distribution after 5 d exposure in 0.01 M NaCl solution

Slika 4: a) 3D posnetek površine zlitine in b) razporeditev hrapavosti po izpostavitvi 5 d v raztopini 0,01 M NaCl

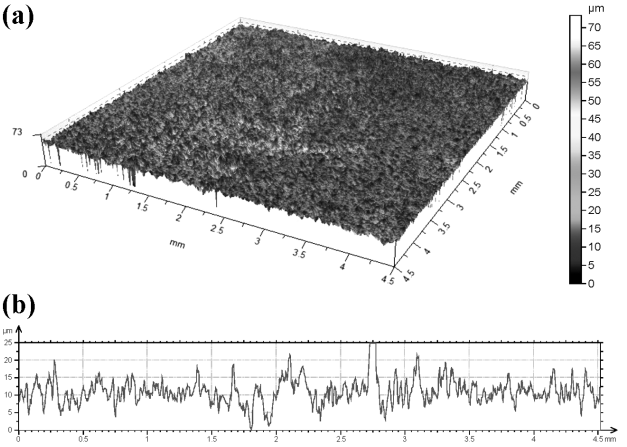

Figure 5: a) 3D image of the surface of the alloy and b) roughness distribution after 5 d exposure in 2 M NaCl solution

Slika 5: a) 3D posnetek površine zlitine in b) razporeditev hrapavosti po izpostavitvi 5 d v raztopini 2 M NaCl

Quantitative and qualitative analyses enabled us to identify the intermetallic phases present in the magnesium alloy AZ80. The presence of phases of the MgAl-, MgMnAl-, and MgAlSi-type was detected.

Figures 4 and **5** present the results of the tests performed with the optical surface analyser MicroProf by FRT, that are illustrated by selected 3D images of the AZ80 alloy and the distribution of the roughness.

Table 5: EIS analysis results

Tabela 5: Rezultati EIS-analize

NaCl concentration, M	R_s/ (kΩ cm^2)	R_f/ (kΩ cm^2)	C_f/ (µF cm^{-2})	CPE_f		C_{dl}/ (µF cm^{-2})	L/ (H cm^{-2})	R_{ct}/ (kΩ cm^2)	R_L/ (kΩ cm^2)
				Y_{01}/ (Ω^{-1} cm^{-2} s^{-n})	n_2				
0.01M	2.46	0.55	14.36	–	–	13.51	0.37e–7	0.21	0.20
0.2 M	0.49	1.10	19.03	–	–	7.99	0.14e–7	0.69	1.28
0.6 M	0.21	0.17	–	0.1572e–4	0.90	480.0	7.13	0.05	0.02
1 M	0.14	0.41	–	0.1475e–4	0.89	129.8	35.13	0.16	0.03
2 M	0.08	0.01	–	0.1652e–4	0.91	526.0	5.19	0.03	0.01

It was proved that with an increase of both the exposure time and the NaCl solution concentration the roughness parameters of the AZ80 deteriorated substantially. For instance, the average arithmetic deviation of the roughness profile R_a increases when the concentration is 0.01 M NaCl, from 0.745 µm (1 d) to 1.25 µm (5 d), and when the concentration is 2 M NaCl, from 0.944 µm (1 d) to 3.3 µm (5 d). The maximum height of the roughness profile R_z for the same concentrations 0.01 and 2 M increases from 4.89 µm (1 d) to 8.41 µm (5 d) and from 6.4 µm (1 d) even to 37 µm (5 d).

The results of the electrochemical impedance tests of the AZ80 alloy are presented in **Table 5**.

The obtained diagrams enabled us to match equivalent systems that are physical models depicting phenomena taking place in the respective object. It was proved that the best matching of the experimental impedance spectra is obtained with the application of an equivalent electrical system consisting of:

- For samples exposed to 0.01 M and 0.2 M NaCl solution from two consecutive parallel systems: within the range of low frequencies from the parallel capacitance system connected with the resistance of ion transition through phase boundary: metal – solution R_{ct}, resistance R_L together with coil (metallic conductor with electromagnetic induction) L representing the corrosion processes; within the range of medium frequencies from the parallel capacitance system C_f connected with the resistance of transition of the R_f ions placed on the surface of the alloy in the result of corrosion (the layer consisting of corrosion products) and resistance at high frequencies, which may be attributed to the resistance of the electrolyte R_s (**Table 5**).

In **Figure 6** R_f and C_f designate, respectively, the resistance and capacitance of the layer created as the result of corrosion (corrosion product layer). R_{ct} indicates the resistance of the charge transition and C_{dl} the capacitance of the double (porous) layer, then R_L and L – induction loop, implicating the initiation and development of the pitting corrosion process.

The mathematical model of the impedance for the system: AZ80 alloy – double layer –NaCl solution (0.01 M and 0.2 M) is presented by Equation (2):

$$Z = R_S + \frac{1}{1/R_f + (j\varpi)C_f} + \frac{1}{1/R_{ct} + (j\varpi)C_{dl} + 1/R_L - (j\varpi)L} \tag{2}$$

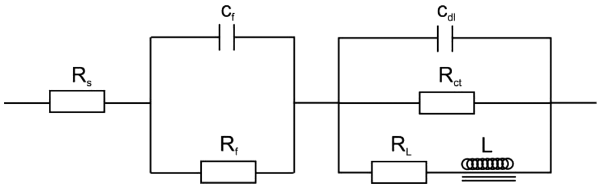

Figure 6: Physical model of equivalent electrical system
Slika 6: Fizikalni model enakovrednega električnega sistema

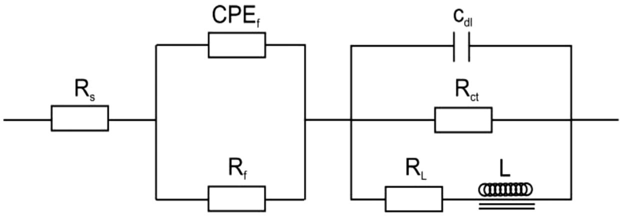

Figure 7: Physical model of equivalent electrical system of corrosion system metal – solution
Slika 7: Fizikalni model električnega sistema, enakovrednega korozijskemu sistemu kovina – raztopina

- For samples exposed to a solution from 0.6 M to 2 M NaCl within the range of low frequencies from a parallel capacitance system connected with the resistance of ion transition through the phase-boundary metal – solution R_{ct}, resistance R_L with the coil (metallic conductor with electromagnetic induction) L representing corrosion processes; within the range of medium frequencies from the parallel system of CPE_f connected with the resistance of transition of the R_f ions placed on the surface of the alloy as the result of corrosion (corrosion product layer) and the resistance at high frequencies that may be attributed to the resistance of electrolyte R_s (**Table 5**).

In **Figure 7** CPE_f indicates CPE depicting the character of the layer created as the result of the corrosion (corrosion product layer), R_f indicates, respectively, the resistance of that layer, whereas R_{ct} resistance of ion transition, and C_{dl} capacitance of double (porous) layer, when R_L and L – induction loop, implicating the initiation and development of the pitting corrosion process.

The mathematical model of the impedance for the system: AZ80 alloy – double layer –NaCl solution (0.6 M, 1 M and 2 M) is presented by Equation (3):

$$Z = R_S + \frac{1}{1/R_f + Y_0(j\varpi)^n} + \frac{1}{1/R_{ct} + (j\varpi)C_{dl} + 1/R_L - (j\varpi)L} \tag{3}$$

4 CONCLUSIONS

It is anticipated that the application of magnesium alloys in future years will be systematically increasing and more and more machine parts and units will be made from that group of materials. Their advantage is the fact that they can be formed with the application of casting as well as plastic working.

The application of the magnesium alloy AZ80 after plastic working is dependent to a large extent on its resistance to electrochemical corrosion. The results of the performed tests prove explicitly the deterioration of the corrosion characteristics of the alloy with an increase of the molar concentration of the NaCl solution. Potentiodynamic tests performed in solutions with concentrations of 0.01–2.00 M NaCl showed that with an increase in the chloride ions concentration, a decrease of the corrosion potential and polarisation resistance, as well as an increase of the corrosion current density of the alloy can be observed. The deterioration of the corrosion characteristics with an increase of the NaCl solution concentration was also confirmed by immersion tests and during the metallographic tests.

Microscopic tests of the samples made of the AZ80 alloy enable us to observe corrosion pits at each stage of the test. Within the early stage of pitting, pits were selectively located in the areas where non-metallic precipitates or inclusions were present (**Figures 2a** and **3a**). The effect of the internal galvanic corrosion was evidenced. The secondary-phase particles were preferentially and uniformly corroded, while the α phase was being obviously unattacked. During the development of corrosion, galvanic corrosion should thus have been less important and the increased corrosion attack of the whole structure was noticed. Significant degradation of the grain boundaries (**Figure 3c**) and the existence of crevices (**Figures 2c** and **3b**) were observed.

Deep anodic etching of the micrstructure and corresponding roughness of the samples were observed with an increase of the exposure time.

The performed EIS tests enabled a direct comparison of the behaviour of the real object with its equivalent system, i.e., an electrical model related to physically realised impedance.

To sum up, it must be highlighted that pitting corrosion is present in the tested magnesium alloy. This proves that the extruded magnesium alloy AZ80 is not resistant to that type of corrosion. The prospects for its application in the aircraft industry trigger the need for covering elements made of the tested alloy with protective coatings.

Acknowledgements

Financial support of Structural Funds in the Operational Programme–Innovative Economy (IE OP) financed from the European Regional Development Fund – Project "Modern material technologies in aerospace industry", No POIG.0101.02-00-015/08 is gratefully acknowledged.

5 REFERENCES

[1] A. Kiełbus, D. Kuc, T. Rzychoń, Magnesium alloys – microstructure, properties and application, Modern metallic materials – presence and future, Department of Materials Engineering and Metallurgy, Katowice, 2009 (in Polish)

[2] K. Bryła, J. Dutkiewicz, L. Lityńska-Dobrzyńska, L. L. Rokhlin, P. Kurtyka, Influence of number of ECAP passes on microstructure and mechanical properties of AZ31 magnesium alloy, Archives of Metallurgy and Materials, 57 (**2012**) 3, 711–717, doi:10.2478/v10172-012-0077-5

[3] Z. Cyganek, M. Tkocz, The effect of AZ31 alloy flow stress description on the accuracy of forward extrusion FE simulation results, Archives of Metallurgy and Materials, 57 (**2012**) 1, 199–204, doi:10.2478/v10172-012-0010-y

[4] R. Kawalla, G. Lehmann, M. Ullmann, H. P. Vogt, Magnesium semi-finished products for vehicle construction, Archives of Civil and Mechanical Engineering, 8 (**2008**) 2, 93–101, doi:10.1016/S1644-9665(12)60196-4

[5] M. Gandara, Recent growing demand for magnesium in the automotive industry, Mater. Tehnol., 45 (**2011**) 6, 633–637

[6] G. L. Makar, J. Kruger, Corrosion of magnesium, International Materials Reviews, 38 (**1993**) 3, 138–153, doi:10.1179/095066093790326320

[7] G. Song, A. Atrens, X. Wu, B. Zhang, Corrosion behaviour of AZ21, AZ501 and AZ91 in sodium chloride, Corrosion Science, 40 (**1998**) 10, 1769–1791, doi:10.1016/S0010-938X(98)00078-X

[8] G. Song, A. Atrens, Corrosion mechanisms of magnesium alloys, Advanced Engineering Materials, 1 (**1999**) 1, 11–33, doi:10.1002/(SICI)1527-2648(199909)1:1 11::AID-ADEM11 3.0.CO;2-N

[9] J. Przondziono, W. Walke, E. Hadasik, Galvanic corrosion test of magnesium alloys after plastic forming, Solid State Phenomena, 191 (**2012**), 169–176, doi:10.4028/www.scientific.net/SSP.191.169

[10] H. Altun, S. Sen, Studies on the influence of chloride ion concentration and pH on the corrosion and electrochemical behaviour of AZ63 magnesium alloy, Materials and Design, 25 (**2004**) 7, 637–643, doi:10.1016/j.matdes.2004.02.002

[11] R. Ambat, N. N. Aung, W. Zhou, Evaluation of microstructural effects on corrosion behaviour of AZ91D magnesium alloy, Corrosion Science, 42 (**2000**) 8, 1433–1455, doi:10.1016/S0010-938X(99)00143-2

[12] J. Przondziono, W. Walke, E. Hadasik, J. Szala, J. Wieczorek, Corrosion resistance tests of magnesium alloy WE43 after extrusion, Metalurgija, 52 (**2013**) 2, 242–246

[13] S. Amira, D. Dubé, R. Tremblay, E. Ghali, Influence of the microstructure on the corrosion behavior of AXJ530 magnesium alloy in 3.5 % NaCl solution, Materials Characterization, 59 (**2008**) 10, 1508–1517, doi:10.1016/j.matchar.2008.01.018

[14] Z. Yu, D. Ju, H. Zhao, Effect of Stress on the Electrochemical Corrosion Behavior of Mg-Zn-In-Sn Alloy, International Journal of Electrochemical Science, 7 (**2012**) 8, 7098–7110

[15] T. Zhang, G. Meng, Y. Shao, Z. Cui, F. Wang, Corrosion of hot extrusion AZ91 magnesium alloy, Corrosion Science, 53 (**2011**) 9, 2934–2942, doi:10.1016/j.corsci.2011/05.035

[16] Z. Yu, D. Ju, N. Takashi, Effect of Stresses for Electrochemical Calculations of Mg-Zn-In-Sn Alloy, International Journal of Electrochemical Science, 7 (**2012**) 10, 10164–10174

[17] P. Lichy, J. Beňo, M. Cagala, J. Hampl, Thermophysical and thermomechanical properties of selected alloys based on magnesium, Metalurgija, 52 (**2013**) 4, 473–476

[18] P. Palček, M. Chalupová, I. Hlaváčová, Efect of microstructure on the development of plastic deformation around the propagating cracks, Acta Metallurgica Slovaca – Conference, 3 (**2013**), 202–208, doi:10.12776/amsc.v3.128

[19] M. Kappes, M. Iannuzzi, R. M. Carranza, Pre-exposure embrittlement and stress corrosion cracking of magnesium alloy AZ31B in chloride solutions, Corrosion, 70 (**2014**) 7, 667–677, doi:10.5006/1172

UDK 54.057:542.9
Professional article/Strokovni članek

ISSN 1580-2949
MTAEC9, 49(2)281(2015)

MICROWAVE-ASSISTED HYDROTHERMAL SYNTHESIS OF Ag/ZnO SUB-MICROPARTICLES

HIDROTERMIČNA SINTEZA PODMIKROMETRSKIH DELCEV Ag/ZnO Z MIKROVALOVI

Lukáš Münster[1,2], Pavel Bažant[1,2], Michal Machovský[2], Ivo Kuřitka[1,2]

[1]Polymer Centre, Faculty of Technology, Tomas Bata University in Zlin, Nam. T. G. Masaryka 275, 762 72 Zlin, Czech Republic
[2]Centre of Polymer Systems, University Institute, Tomas Bata University in Zlin, Nad Ovcirnou 3685, 760 01 Zlin, Czech Republic
l_munster@ft.utb.cz

Prejem rokopisa – received: 2013-10-02; sprejem za objavo – accepted for publication: 2014-04-03

doi:10.17222/mit.2013.223

A fast and environmentally friendly, microwave-assisted, hydrothermal synthesis was utilized for the preparation of a Ag/ZnO hybrid system by using zinc acetate dihydrate and silver nitrate as the sources of Zn^{2+} and Ag^+, and hexamethylentetramine as the reducing and precipitating agent. The influence of the concentration was investigated by X-ray diffraction analysis, scanning electron microscopy and energy-dispersive analysis. It was found that the concentration has a strong effect on the morphology and proportion between the Ag and ZnO components of the prepared particulate materials. With a decreasing concentration, the morphology of the ZnO changed from twinned or single frustums to rod-like microparticles, whereas the silver morphology changed from large polygon-shaped microparticles to very small, spherical nanoparticles.

Keywords: zinc oxide, silver, nanoparticle, hydrothermal, microwave synthesis

Uporabljena je bila hitra in okolju prijazna mikrovalovna hidrotermična sinteza hibridnega sistema Ag/ZnO z uporabo cink-acetat dihidrata in srebrovega nitrata kot vira Zn^{2+} in Ag^+ ter heksametilentetramina kot reducenta in sredstva za izločanje. Z rentgensko difrakcijo, vrstično elektronsko mikroskopijo in energijsko disperzijsko analizo je bil preučevan vpliv koncentracije. Ugotovljeno je bilo, da ima koncentracija močan vpliv na morfologijo in razmerje med komponentama Ag in ZnO pripravljenega zrnatega materiala. Z zmanjšanjem koncentracije se je morfologija ZnO spremenila iz dvojčičnih ali stožčastih mikrodelcev v paličaste, medtem ko se je morfologija srebra iz velikih poligonalnih mikrodelcev spremenila v majhne sferične nanodelce.

Ključne besede: cinkov oksid, srebro, nanodelec, hidrotermičen, sinteza z mikrovalovi

1 INTRODUCTION

Various metals (Au, Ag) and metal oxides (ZnO, TiO_2, SnO_2, CuO) have been the subjects of investigation for a long time because of their unique optical, electrical, and mechanical properties that can be modulated by varying the size and the morphology of the particles on the nano- and sub-micro scales[1,2]. Recently, hybrid metal-semiconductor materials have attracted great attention because their metal and semiconductor interface possesses a unique electronic band structure resulting in a specific chemical activity[3]. Therefore, great efforts have been devoted to the synthesis of hybrid materials by combining various metals and semiconductors such as Ag/TiO_2, Ag/SiO_2, Pt/SnO_2 and Ag/ZnO.[4–7] Among them, Ag/ZnO is of great interest because of potential applications in many fields, such as catalysis and medicine.[7,8] This particulate material has been successfully demonstrated as a suitable filler for an inorganic antibacterial polymer system[9]. ZnO is an important semiconducting material because of its unique optoelectronic and piezoelectric properties.[10,11] Moreover, it possesses strong antibacterial activity towards gram-negative bacteria and it is both non-toxic and biocompatible[10]. Metallic silver, its salts and complexes have been exploited for their antibacterial properties for millennia before the realization that bacteria are the agents of the infection[2]. Silver nanoparticles are commercially available on the antibacterial-additives market, exhibiting a broad spectrum of antibacterial activity against gram-positive, gram-negative bacteria, fungi, certain viruses, including antibacterial-resistant strains.[12–14] Therefore, with the combination of Ag and ZnO in a hybrid material on the nano- or sub-micro scales could achieve a synergic effect of antibacterial and photocatalytic activity, biosensing, electrochemical properties, etc.[15–17]

Hence, we developed a simple, fast and efficient preparation of a Ag/ZnO hybrid via a microwave (MW) assisted hydrothermal synthesis using a modified open-vessel laboratory microwave-oven system[18]. Introducing microwaves instead of the conventional heating allowed us to shorten the reaction time to 12 min, compared to hours reported in references for conventional heating[17]. The concentration of reactants is one of the key factors affecting the properties of the prepared hybrid material. Therefore, a study of the influence of the reactants' concentrations on the morphology and particles size was performed.

Table 1: Sets of samples and amounts of precursors and reducing/precipitating agent used in MW synthesis and yields of the powder product
Tabela 1: Sklopi vzorcev in količina predhodnikov in reducirnega/izločevalnega sredstva, uporabljenih v MW-sintezi, in izkoristki proizvodov v obliki prahu

Set	Sample	$Zn(Ac)_2·2H_2O$ mol	$AgNO_3$ mol	HMTA mol	Yield g	Theoretical Yield g
I	I-ZnO	0.0500	–	0.0500	0.740	4.070
	I-Ag	–	0.0050	0.0500	0.501	0.539
	I-AgZnO	0.0500	0.0050	0.0500	1.160	4.609
II	II-ZnO	0.0050	–	0.0050	0.190	0.407
	II-Ag	–	0.0005	0.0050	0.048	0.054
	II-AgZnO	0.0050	0.0005	0.0050	0.182	0.461
III	III-ZnO	0.0010	–	0.0010	0.025	0.041
	III-Ag	–	0.0001	0.0010	0.003	0.005
	III-AgZnO	0.0010	0.0001	0.0010	0.026	0.046

2 EXPERIMENTAL WORK

2.1 Sample preparation

Zinc acetate dihydrate $Zn(Ac)_2 \cdot 2H_2O$ (PENTA) and silver nitrate $AgNO_3$ (PENTA) were used as the sources of Zn^{2+} and Ag^+, respectively. Hexamethylentetramine (HMTA), $(CH_2)_6N_4$ (LACHNER) was used as the source of OH^-, acting as a precipitating agent and CH_2O as a reducing agent. All the chemicals were of analytical grade and used as received without any further purification. Demineralised water with a conductivity 0.1 µS cm^{-1} was used throughout the experiment.

The synthesis was carried out using an open-vessel microwave-oven laboratory system MWG1K-10 operated at 800 W and 2.45 GHz (RADAN) with an external reflux cooler. In a typical experimental procedure a given amount of precursor (Zn^{2+}, Ag^+ or both) and reducing/precipitating agent were dissolved in 100 mL and 50 mL of demineralised water, respectively. The precursor solutions were first preheated in the microwave oven for 2 min, then the solution of HMTA was added via a dropping funnel, and then microwave heating continued for another 10 min. Hence, the total time of the microwave synthesis was 12 min for each prepared sample. The reaction mixture was always left to cool to approximately 50 °C and then the material was collected and washed by microfiltration. Samples were dried at 40 °C in a laboratory oven until a constant weight was achieved. In all the experiments, the molar ratio of Zn^{2+}/Ag^+ was set to 10/1. In order to investigate the influence of concentration, the initial solution mixture concentration, which is close to the saturation limit for zinc acetate (set I), was lowered ten (set II) and fifty times (set III), giving rise to three sets of samples. The concentration of HMTA was kept at a constant ratio to the precursors as well. For the reaction-mixture compositions (**Table 1**).

2.2 Characterization methods

Crystal-phase structure identification was conducted using the multifunctional X-ray diffractometer PANalytical X'Pert Pro MPD (PANalytical) and Cu-K_α X-ray source (λ = 0.15418 nm), at 40 kV and 30 mA and the 2θ diffraction angle range 10–90 °. The morphology was observed in a scanning electron microscope (SEM) Vega II LMU (TECSAN) at an acceleration voltage of 10 kV. Semi-quantitative elemental analysis was performed with the energy-dispersive X-ray (EDX) analyzer (Oxford Instruments, INCA, UK) mounted on the microscope.

3 RESULTS AND DISCUSSION

All the samples were examined by powder X-ray diffraction (XRD) analyses. As an example of the crystal-phase structure investigation, X-ray patterns of the samples prepared at the lowest concentration, i.e., pure ZnO, Ag and hybrid Ag-ZnO (set III) are shown in **Figure 1**. Other sets of the experiment with higher concentrations of precursors and reducing/precipitating agents (set I and II) showed similar XRD patterns. Specific diffraction lines (labeled by #) were observed at approximately 2θ = (31.7, 34.4, 36.2, 47.5, 56.5, 62.8, 66.2, 67.8, 72.5, 76.8, 81.3 and 89.7) °. According to the

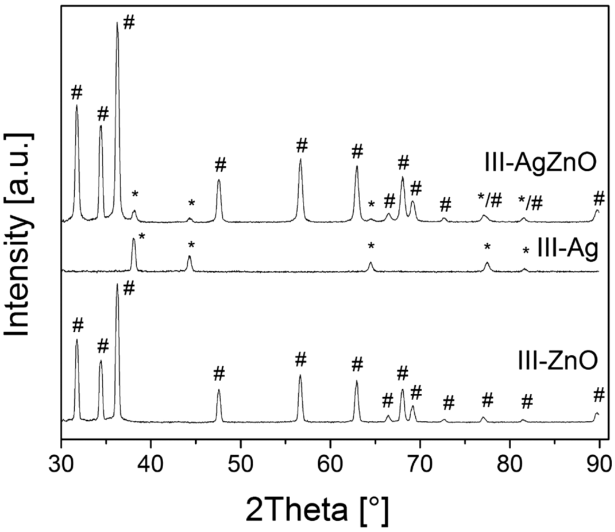

Figure 1: X-ray diffractogram of samples from set III, the 2θ range is cropped at lower values in the graph as no peaks were detected between 10 ° and 30 °
Slika 1: Rentgenski difraktogram vzorcev iz sklopa III, področje 2θ je odrezano pri nižjih vrednostih, ker v območju 10–30 ° ni bilo vrhov

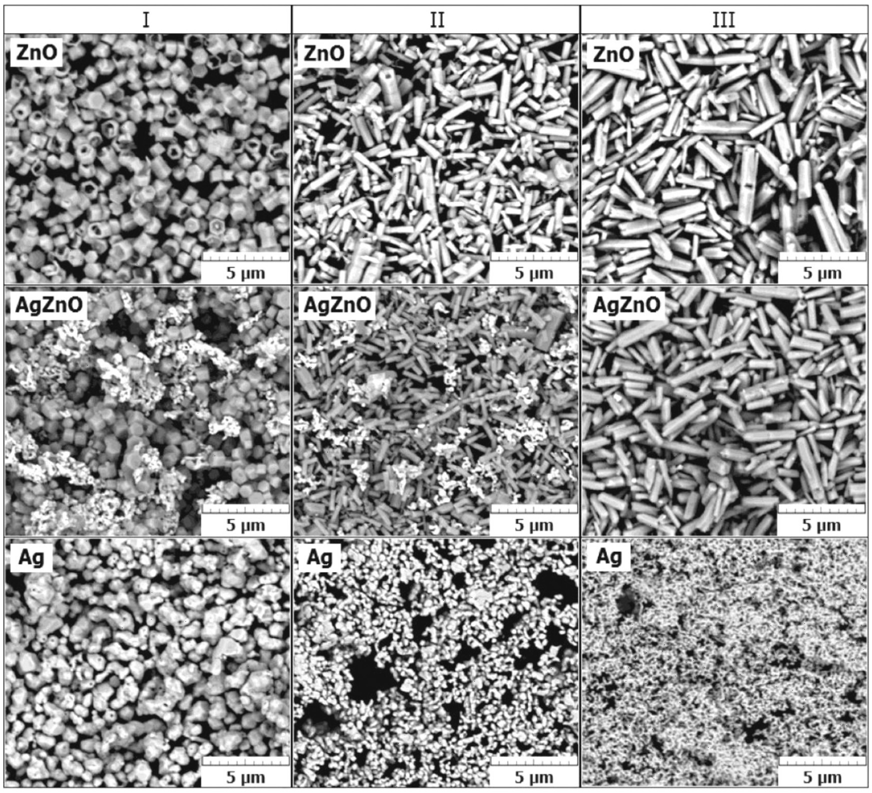

Figure 2: SEM micrographs of prepared samples of ZnO, Ag and AgZnO particles arranged in dependence of the concentration of precursors and HMTA in the reaction mixture

Slika 2: SEM-posnetki pripravljenih vzorcev ZnO, Ag in AgZnO delcev, razvrščenih v odvisnosti od koncentracije predhodnikov in HMTA v reakcijski zmesi

JCDD PDF-2 entry 01-079-0207, these peaks can be unambiguously assigned to the ZnO wurtzite hexagonal crystal phase. Other observed diffraction peaks (labeled by *) at approximately 2θ = (38.2, 44.4, 64.6, 77.6 and 81.8) ° were assigned to a metallic silver cubic crystal phase according to JCDD PDF-2 entry 01-087-0720. Moreover, the sharpness and the narrowness of the diffraction peaks imply well-developed crystalline structures for both the Ag and ZnO, with no level traces of crystalline impurities.

The morphology of the prepared particles is shown in **Figure 2**. A back-scattered electron (BSE) detector was utilized to enhance the contrast between the Ag and ZnO particles. It is clear that the concentration strongly influenced the particles size and the morphology. For pure ZnO synthesized at the highest concentration (set I), the particles form typical twinned frustums joined by their apical bases, in many cases hollow if single frustums. The dimensions of these particles are diameter up to 1.5 μm and in length up to 2 μm. The particles with a hollow core have a wall thickness starting from tens of nanometers. Lowering the concentration to one tenth of the ZnO precursor (set II) resulted in an increased aspect ratio from approximately 1 : 1 observed for pure ZnO at the highest concentration (set I) to 6 : 1. The approximate diameter and length were 500 nm and 3 μm. At the lowest concentration (set III), rod-shaped ZnO particles have the same aspect ratio; however, there is observable a slight increase of the particles' length and diameter. The morphology of the Ag particles prepared by using the highest concentration of the precursor (set I), displayed polygon-shaped particles with a diameter up to 1.5 μm. The lowering of the concentration of the Ag precursor (set II) results in spherically shaped Ag particles with an approximate diameter of 250 nm. The lowest concentration of Ag (set III) displayed the smallest particles with a size in the range of tens of

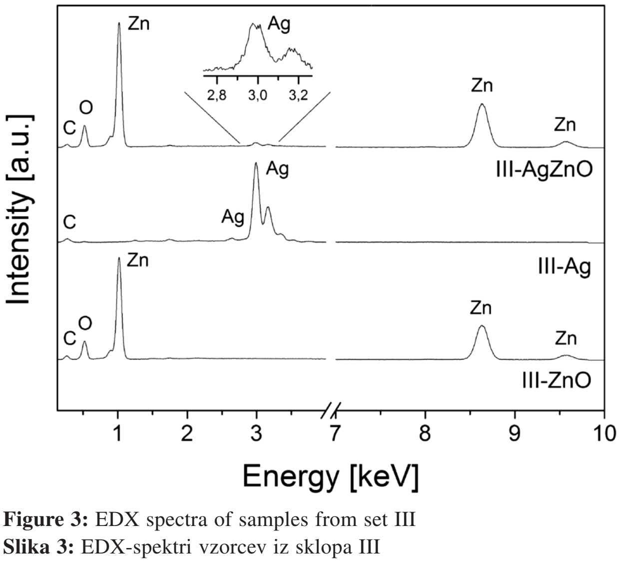

Figure 3: EDX spectra of samples from set III

Slika 3: EDX-spektri vzorcev iz sklopa III nanometers. For the hybrid AgZnO system, the trend is very similar as that observed for the pure Ag and ZnO components in the prepared material.

Figure 3 shows typical spectra obtained from the EDX analyses. For the sake of brevity, only spectra for the lowest concentration (set III) are presented. The presence of elemental zinc (peaks at (1.0, 8.6 and 9.5) keV) and oxygen (peak at 0.5 keV) from the ZnO particles was confirmed in the samples ZnO, Ag/ZnO. Elemental silver (peaks at 2.6 keV and 3.0 keV) was confirmed even within the lowest concentration used in the samples Ag and Ag/ZnO. Elemental carbon with a peak at 0.3 keV can be assigned to the carbon tape used for fixation of the sample to the holder inside the microscope chamber or to other organic impurities. The semi-quantitative results from the EDX in the weight percentage of Ag, Zn and O content are listed in **Table 2**. It is clear that the weight percentage of Zn increases with lowering of the concentration, whereas the content of Ag decreases with lowering the concentration, which is in accordance with observations based on the SEM micrographs. The large observed content of O points towards the presence of water adsorbed at the surface or in the pores of the particles.

Table 2: EDX results of prepared samples, content of Zn, Ag and O in mass fractions, *w*/%

Tabela 2: EDX-rezultati pripravljenih vzorcev, vsebnost Zn, Ag in O v masnih deležih, *w*/%

	EDX (*w*/%)		
Set	ZnO	Ag	AgZnO
I	Zn: 59.1; O: 40.9	Ag: 100	Ag: 39.5; Zn: 31.7; O: 28.8
II	Zn: 60.9; O: 39.1	Ag: 100	Ag: 28.2; Zn: 36.4; O: 35.5
III	Zn: 65.2; O: 34.8	Ag: 100	Ag: 3.3; Zn: 62.2; O: 34.4

4 CONCLUSION

A simple one-pot open-vessel microwave-assisted hydrothermal synthesis of a ZnO, Ag and Ag/ZnO hybrid combination of both types of particles was introduced. The influence of the concentration of precursors and the precipitating/reducing agent on the properties and on the morphology was investigated. Powder XRD analysis showed wurtzite crystalline phases of zinc oxide in all the samples prepared using $Zn(Ac)_2 \cdot 2H_2O$ as a precursor and cubic crystalline phases of silver prepared using the precursor $AgNO_3$, even at the lowest concentrations. The alternation of the concentration has a marked effect on the particle morphology: (i) the decrease of the concentration of the zinc precursor results in prolongation and an increased size of the ZnO particles, whereas (ii) the size of the silver particles decreases directly with the concentration decrease, from micrometer down to tens of nanometers, and the highest percentage yield was almost 93 % of pure silver particles.

Acknowledgment

The authors wish to thank the internal grant of TBU in Zlin No. IGA/FT/2013/014 funded from the resources of specific university research for financial support.

This article was written with the support of the Operational Program "Research and Development for Innovations" co-funded by the European Regional Development Fund (ERDF) and the national budget of the Czech Republic, within the Centre of Polymer Systems project (reg. number: CZ.1.05/2.1.00/03.0111).

This article was written with the support of the Operational Program "Education for Competitiveness" co-funded by the European Social Fund (ESF) and the national budget of the Czech Republic, within the "Advanced Theoretical and Experimental Studies of Polymer Systems" project (reg. number: CZ.1.07/2.3.00/20.0104).

5 REFERENCES

[1] D. C. Look, Materials Science and Engineering: B, 80 (**2001**), 383–387, doi:10.1016/S0921-5107(00)00604-8

[2] C. Marambio-Jones, E. M. V. Hoek, Journal of Nanoparticle Research, 12 (**2010**), 1531–1551, doi:10.1007/s11051-010-9900-y

[3] Y. H. Zheng, L. R. Zheng, Y. Y. Zhan, X. Y. Lin, Q. Zheng, K. M. Wei, Inorganic Chemistry, 46 (**2007**), 6980–6986, doi:10.1021/ic700688f

[4] W. Su, S. S. Wei, S. Q. Hu, J. X. Tang, Journal of Hazardous Materials, 172 (**2009**), 716–720, doi:10.1016/j.jhazmat.2009.07.056

[5] G. Gu, J. Xu, Y. Wu, M. Chen, L. Wu, Journal of Colloid and Interface Science, 359 (**2011**), 327–33, doi:10.1016/j.jcis.2011.04.002

[6] M. H. Madhusudhana Reddy, A. N. Chandorkar, Thin Solid Films, 349 (**1999**), 260–265, doi:10.1016/S0040-6090(99)00194-7

[7] C. Ren, B. Yang, M. Wu, J. Xu, Z. Fu, Y. lv, T. Guo, Y. Zhao, C. Zhu, Journal of Hazardous Materials, 182 (**2010**), 123–129, doi:10.1016/j.jhazmat.2010.05.141

[8] A. Meng, S. Sun, Z. Li, J. Han, Advanced Powder Technology, 24 (**2013**), 224–228, doi:10.1016/j.apt.2012.06.006

[9] P. Bazant, I. Kuritka, O. Hudecek, M. Machovsky, M. Mrlik, T. Sedlacek, Polymer Composites, 35 (**2014**), 19–26, doi:10.1002/pc.22629

[10] C. Jagadish, S. Pearton, Zinc Oxide Bulk, Thin Films and Nanostructures, Elsevier, Amsterdam 2006

[11] A. Corso, M. Posternak, R. Resta, Physical Review: B, 50 (**1994**), 10715–10721, doi:10.1103/PhysRevB.50.10715

[12] R. M. Slawson, M. I. Van Dyke, H. Lee, J. T. Trevors, Plasmid, 27 (**1992**), 72–79, doi:10.1016/0147-619X(92)90008-X

[13] D. J. Balazs, K. Triandafillu, P. Wood, Y. Chevolot, C. Van Delden, H. Harms, C. Hollestein, H. J. Mathieu, Biomaterials, 25 (**2004**), 2139–2151, doi:10.1016/j.biomaterials.2003.08.053

[14] N. Stobie, B. Duffy, D. E. McCormack, J. Colreavy, M. Hildalgo, P. Mchale, S. J. Hinder, Biomaterials, 29 (**2008**), 963–969, doi:10.1016/j.biomaterials.2007.10.057

[15] W. Lu, G. Liu, S. Gao, S. Xing, J. Wang, Nanotechnology, 19 (**2008**), 1–10, doi:10.1088/0957-4484/19/44/445711

[16] C. Tian, Q. Zhang, B. Jiang, G. Tian, H. Fu, Journal of Alloys and Compounds, 509 (**2011**), 6935–6941, doi:10.1016/j.jallcom.2011.04.005

[17] X. Feng, Y. Cheng, C. Ye, J. Ye, J. Peng, J. Hu, Materials Letters, 79 (**2012**), 205–208, doi:10.1016/j.matlet.2012.03.098

[18] M. Machovsky, P. Bazant, Z. Kozakova, M. Pastorek, P. Zlebek, I. Kuritka, Open Vessel Microwave-Assisted Synthesis of Ag/Zno Hybrid Fillers with Antibacterial Activity, Proc. of the Nanocon, Brno, 2011, 628–634

UDK 621.74.047:620.192.46
Professional article/Strokovni članek

ISSN 1580-2949
MTAEC9, 49(2)285(2015)

DETERMINATION OF THE CAUSE OF THE FORMATION OF TRANSVERSE INTERNAL CRACKS ON A CONTINUOUSLY CAST SLAB

UGOTAVLJANJE VZROKOV ZA NASTANEK NOTRANJIH PREČNIH RAZPOK V KONTINUIRNO ULITEM SLABU

Zdeněk Franěk[1], Miloš Masarik[2], Jaromír Šmíd[3]
[1]Silesian University in Opava, School of Business Administration in Karvina, Univerzitní nám. 1934/3, 733 40 Karviná, Czech Republic
[2]VITKOVICE STEEL, a.s., Českobratrská 3321/46, 702 00 Ostrava, Czech Republic
[3]TaM, Technologie a Metalurgie, Areál VÚHŽ, a.s., 739 51 Dobrá 120, Czech Republic
franek@opf.slu.cz

Prejem rokopisa – received: 2013-10-03; sprejem za objavo – accepted for publication: 2014-06-09

doi:10.17222/mit.2013.224

The paper describes a determination of the cause of transverse internal cracks on a continuously cast slab using an analytical software tool, called LITIOS. It is a complex system based on long-term monitoring of the casting parameters and their impact on the quality of the slabs. Transverse internal cracks are characterised by identifying the possible causes of their origin. Using the LITIOS system, selected constant (invariable) and variable parameters of the casting were assigned to specific cracks and on their basis the causes of the cracks were determined.

Keywords: continuous casting of steel, slab, casting parameters, quality prediction, crack, software tool

Članek opisuje ugotavljanje vzrokov notranjih prečnih razpok v kontinuirno litem slabu z uporabo analitskega programskega orodja LITIOS. To je kompleksen sistem, ki temelji na dolgotrajnem nadzoru parametrov pri litju in njihovem vplivu na kvaliteto slabov. Ocenjene so prečne notranje razpoke s prikazom mogočih vzrokov za njihov nastanek. Z uporabo sistema LITIOS so bile dodeljene izbrane konstante (nespremenljivke) in spremenljivi parametri litja določeni razpoki in na tej osnovi so bili določeni vzroki za nastanek razpok.

Ključne besede: kontinuirno litje jekla, slab, parametri litja, napovedovanje kakovosti, razpoka, programsko orodje

1 INTRODUCTION

Continuous casting is a complex process, characterised by a considerable instability, i.e., by the so-called fluctuations. The fluctuations have a negative influence on the quality of slabs. To a large extent, they make it difficult to determine the causes of defects and, hence, also the optimum technological parameters for the casting process or their control during the events caused by the technology.

The whole process of casting steel is thoroughly mapped by measuring and reading the monitored data, including the chemical-analysis results. Quality ratings are assigned to the produced continuously cast slabs and to the products rolled from them. In this way, a timeline of very extensive data, mapping the production process is created. It can be, however, concluded that the potential of these data has not yet been sufficiently used. The reason this is, among other things, the fact that it is very difficult to handle these data and that assigning the data to the appropriate place on a slab and a possible defect is not easy. In spite of that, the operation of continuous casting, especially the casting of slabs, is nowadays practically impossible without the use of the systems for monitoring the casting parameters and the software systems for optimising the casting parameters.

An example of an artificial-intelligence technique for optimising the process parameters used for the continuous casting of steel is given in[1]. The mathematical modelling and optimisation strategy, genetic algorithm and knowledge base, applied to the continuous casting of steel are given in[2]. A description of a properly developed algorithm solving an essential component of the above mentioned systems, including the assigning of the data to a specific place on the slab, is described in several works, e.g., in[3]. A multi-dimensional, statistical, model-based system for monitoring continuous casting and detecting the risk of impending breakouts is also the subject of the U.S. patent.[4]

Today, specialised companies offer different solutions for meeting the requirements for an ever increasing quality of steel, with simultaneous reductions in the manufacturing costs. For example, the company Siemens Metals Technologies provides the basic automation solutions for all the types of continuous-casting machines, i.e., for casting slabs, blooms, billets, the blanks for dog-bone sections (beam-blank casters) as well as for the equipment for producing endless strips. Sets of automation programs meet the requirements for the performance of production units, dimensional flexibility, the quality of semi-products and final products, and the maximum yield. Reference[5] states that the described solutions were installed on hundreds of casting machines worldwide, in both the new and the existing plants.

An extensive and comprehensive range of optimisation processes, optimisation models, technology-management functions and services is crucial for meeting the production and quality goals. On-line data links for a continuous support provide a rapid system for modernisation, maintenance and metallurgical assistance. Reference[5] also states that with the support of a vast experience the described packages combine excellent technology and automation solutions that perfectly control the process of continuous casting and its complex parameters.

2 USE OF THE SYSTEMS FOR MONITORING THE PARAMETERS AND QUALITY PREDICTION

The data obtained from the above-mentioned systems for monitoring the casting parameters and the software systems for optimising the casting parameters call for the use of advanced statistical methods for monitoring and evaluating the quality of continuously cast blanks[6–8] and for the subsequent prediction of defects.

At present, it can be said that the basic technical development of the classical machines for continuous casting of steel has mostly reached such a level that a further development is often not necessary. Minor metallurgical, technical and technological improvements are naturally still ongoing in these areas, but, in general, it can be said that other possibilities for making the production more efficient through major changes are already limited by very narrow barriers.

One of the areas where some reserves still exist is increasing and control of the quality of continuously cast blanks and, particularly, the final products of a metallurgical plant. This can be achieved by introducing prediction systems, in the first stage, for predicting the quality of continuously cast blanks and then of the final products. According to the design of these systems their primary objective is to predict the quality of the products at the moment when they leave the production line, or even before it.

There is a possibility of a transition from a discontinuous production in the segment of liquid-steel rolled products to a continuous production, with evidenced savings, by eliminating the energy-intensive reheating before the next forming of the slabs. The prediction of quality allows another direct processing of the slabs without a significant risk that the absence of their control in the cold state, with the subsequent removal of the detected defects, will lead to a rejection or a quality degradation of the final products due to their defects. Even in the case of non-removable defects of the slabs, their rejection before the useless further processing is economically advantageous.

The second benefit of the prediction systems, which probably has not yet been sufficiently appreciated, is the use of the feedback between the quality of a slab and a final product, and the technological parameters for casting steel on a CCM, or the parameters for processing a continuously cast slab at a rolling mill. Archiving and statistical processing of the data describing these relations (the parameters versus the quality level) can provide, with a surprising success, the optimum technological parameters for casting and for further processing.

The methods for acquiring data and explaining their use in the metallurgical-industry operating conditions as a tool for improving the steelmaking processes, description of the basic processes and various approaches to the implementation of the necessary software tools, as well as data acquisition, creation of knowledge databases and their storing, displaying of the results and diagnostics – all of these represent the essential activities and the segments of the developed software systems aimed at achieving the basic objective, i.e., an increase in the quality and in the yield of the production of steel products.[9]

3 LITIOS SOFTWARE SYSTEM

Within the research, under the support of various projects, in cooperation with technologists and metallurgists, numerous statistical analyses were made on the concrete CCM. The procedure and the obtained result for the specific defect are described below. This article describes the possibility to monitor dozens of the parameters that are assigned to any section of a cast slab. In the event that the Baumann sulphur print made on a transverse sample taken from a cast slab in the standard manner shows any defects, it is possible to assign certain casting parameters to this sample and compare them with the documented reality.

This procedure is then also the basic prerequisite for predicting the quality of cast slabs and, subsequently, of the sheets rolled from these slabs. If we assume, already at the general level, the knowledge about the qualitative relation between a casting parameter and a slab defect, this procedure is then used for confirming their relation. And, in the case of the limit values that differ between different CCMs, this procedure allows their exact determination. This makes it possible to express the basic result of a prediction with a YES-NO verdict about the presence of a defect.

Another necessary prerequisite for analysing the causes of defects in a slab is also the selection and assignment of the casting parameters to the place where these defects are formed. In the case of Baumann sulphur prints the above refers to the data assigned to the place, from which they were taken.

The company EVRAZ VÍTKOVICE STEEL, a. s., implemented an original complex system of long-term monitoring of the casting parameters and of their impact on the quality of the slabs, called LITIOS.[3] This software system is organically linked with an on-line temperature

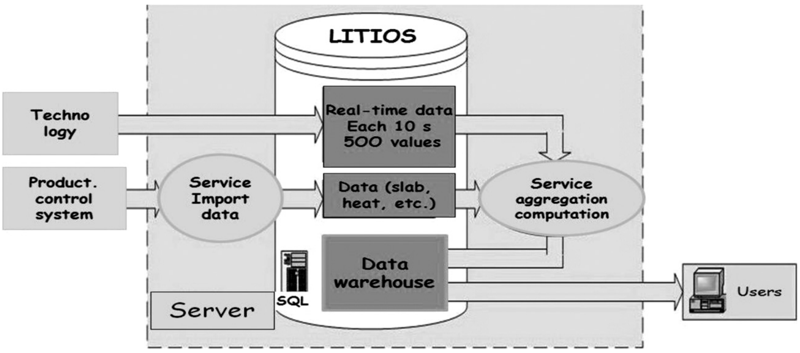

Figure 1: Architecture of the LITIOS monitoring system
Slika 1: Shema nadzornega sistema LITIOS

model, as well as with an on-line module of data acquisition. The system deals with all the data available from the CCM process. The system comprises the recording and filtering of the data, their sorting, entering into the relational database system, as well as the data aggregation and their graphical interpretation. Technological data, measured every 10 seconds, are entered from the temperature model. The software of the temperature model directly enters the data into the database of the LITIOS system. The LITIOS software system also records all the necessary data about each sequence of the superior system for the automatic control of the steel shop, called FLS, and it enters them into the database system. It enables a filtration of the data and performs the necessary data aggregation. This aggregation is necessary in order to simplify the work and handle large amounts of data. It turns out that it is appropriate and sufficient to aggregate the data per meter of the length of a casting strand. The developed software is modular, using the latest knowledge on the database technology and data-analysis methods. The system architecture is shown in **Figure 1**.

Data storage is performed according to the hierarchy of their formation: the data about the sequence, heat, slab, measured value (the so-called channels) of the continuous casting machine, the data about the quality of the slabs and the products rolled from them. The files are divided into items with their attributes. The whole system (**Figure 1**) thus contains approximately 500 items, and if we take into account that the technological parameters, the so-called channels, are measured every 10 seconds, we see that a very large amount of data is created.

The system provides reports and it is possible to view the data for individual sequences, heats and slabs. The selected data are represented graphically. Various selections of the data are available for the analytical methods. A user can transform the data into a matrix of the causes – the measured values and the consequences – i.e., the quality indicators. The employees of a steel shop use these narrowed data analyses of the evolution of casting. The system allows an export of the selected data to the other statistical programs for more detailed analyses. The data from the LITIOS system were used for the analyses of the crack formation presented below.

4 TRANSVERSE INTERNAL CRACKS

These cracks, also called the half-way cracks because of their position on a slab cross-section, which are caused by straightening or bending, are situated between the surface and the centre of a slab, in the plane perpendicular to the direction of casting. They mostly occur in the top half of a slab cross-section. They are schematically illustrated in **Figure 2**.

In some cases transverse internal cracks in continuously cast slabs may cause a deterioration of the utility properties of the heavy plates rolled from them, or possibly even their rejection from the production as a result of an ultrasonic inspection. The best prevention against these undesirable phenomena during the production of heavy plates is an elimination of these cracks already during the continuous casting of slabs on a CCM.

The basic causes of the formation of these cracks are high tensile deformations in the high-temperature zone of low strength and ductility. The formation of these deformations is explained with three different facts[10]:

- intensive secondary cooling, which causes high-temperature reheating of the surface of a continuously cast slab

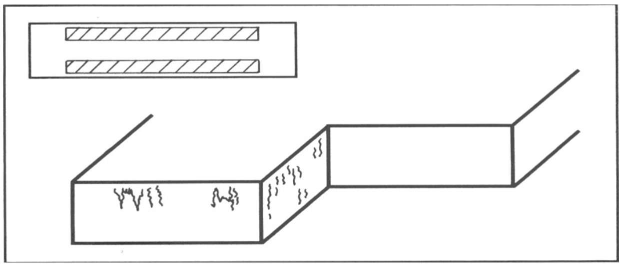

Figure 2: Schematic illustration of transverse cracks and localisation of their occurrence in the transverse and longitudinal sections of a continuously cast slab
Slika 2: Shematski prikaz prečnih razpok in mesto njihove pojave na prečnem in vzdolžnem prerezu kontinuirno litega slaba

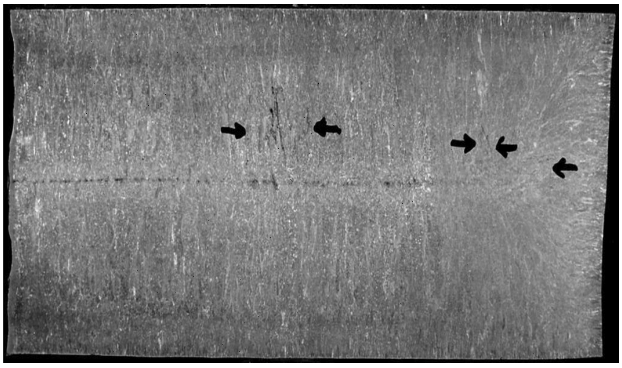

Figure 3: Transverse internal cracks in the top half of a macro-etched slab sample; example from the catalogue of defects

Slika 3: Notranje prečne razpoke v gornji polovici makro jedkanega vzorca slaba; primer iz kataloga napak

- a depression of the wide side of a slab
- slab bending and straightening, particularly in the temperature interval of the reduced strength and ductility of steel, i.e., within the temperature interval from 950 °C to 700 °C

In addition to the usual sensitivity of some steel grades to the formation of these cracks, there are also some other technological parameters that contribute to the formation of transverse cracks:

- a high casting temperature, causing a wide zone of a columnar casting structure, sometimes taking place even after the transcrystallisation
- a low casting rate, causing a reduction in the slab temperature in the area of its straightening
- a high casting rate
- a drastic increase in the cooling intensity after the exit of a slab from the mould
- a chemical composition of steel; micro-alloyed steels are particularly susceptible to the formation of these cracks since micro-alloying elements, namely, vanadium, titanium, niobium, etc., reduce the ductility of steel exactly at the critical temperatures of the slab straightening.

When inspecting the causes of the formation of transverse intermediate cracks we see an obvious antagonism of the influence of the secondary cooling on the formation of these defects. The so-called soft cooling is required, which causes a hotter and thinner strand shell leading to a lower resistance to depression. The compromise must be, therefore, the optimum intensity of the cooling.

In the case of a formation of the cracks caused by slab bending and straightening, it is probable that a more important role is played by the straightening, indicated by the fact that the cracks are almost always situated in the top part of a slab, i.e., in the half of the cross-section belonging to the smaller radius of bending. This defect cannot be removed. If it is situated at a sufficient depth under the slab surface and if further processing of the slab is not too demanding, this defect need not present a cause of difficulties during such processing or a cause of a lower quality of the plate.

A determination of the presence and form of transverse cracks as well as their quantification according to the methodology used in the given case are performed in the standard manner on macro-etches and/or on Baumann sulphur prints. **Figure 3** shows an example of such manifestations of transverse cracks.

5 DETERMINATION OF THE CAUSES OF CRACK FORMATION

For a determination of the cause, or causes, of the formation of internal transverse cracks on the concrete slab we first chose the parameters that might have caused the defect. With the LITIOS analytical software tool we then assigned the values of the selected casting parameters to the evaluated sample and compared these values with the values defined, in the standard manner, for the given CCM as satisfactory, i.e., with the limits specified by the supplier of the equipment or by the CCM operator on the basis of long-term experience.

For an exploration of the causes of the internal transverse cracks in the specific slab we chose the heat and the sample that was subjected to a metallographic evaluation.

A transverse sample was taken, i.e., a sample from the plane perpendicular to the direction of casting. The sample was cut with oxygen-acetylene flame at the end of the cooling bed. For a determination of the possible degree of defects the sample was then polished in a metallographic laboratory, etched in order to see the nature of the macrostructure and then Baumann sulphur prints were made. The evaluation presented in the table below was carried out according to the commonly used standard methodology for evaluating cast slabs.

Table 1 below presents the degrees of defects determined on the Baumann print in the metallographic testing laboratory.

Transverse internal cracks were visible on the sample. Using a 6-degree scale, from degree 0 denoting no defect to degree 5 denoting the largest defect, we determined the cracks of the 3rd degree, which already exceeded the limit of the harmlessness of the defect, see the Baumann sulphur print in **Figure 4**.

Table 1: Evaluation of defects on the sulphur print

Tabela 1: Stopnje napak, določene na Baumannovem odtisu v metalografskem laboratoriju

Defect	Point inclusions	Cluster inclusions	Central segregation	Lateral cracks	Corner cracks	Transverse internal cracks	Longitudinal internal cracks
Degree	2	0	2	2	0	3	NA

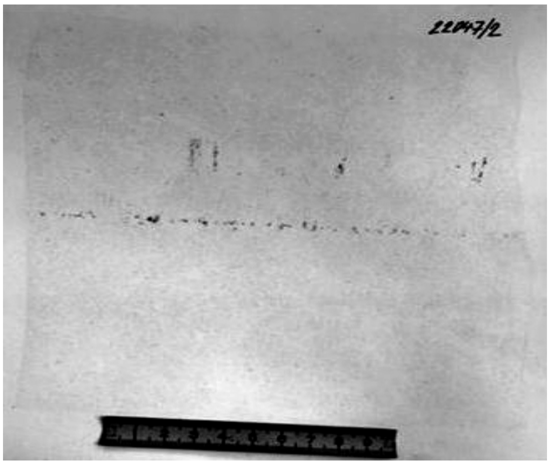

Figure 4: Transverse internal cracks on the sulphur print of the investigated sample

Slika 4: Prečne notranje razpoke na Baumannovem odtisu preiskovanega vzorca

The investigated heat and slab were produced using the following "fix" technical parameters that did not change during the casting of the given heat:

- Steel grade – low-carbon, micro-alloyed with vanadium, titanium and niobium
- Chemical composition – 0.06 % C, 1.66 % Mn, 0.30 % Si, 0.016 % P, 0.005 % S, 0.02 % V, 0.03 % Nb, 0.005 % Ti
- Liquidus temperature – 1516 °C
- Slab dimensions – 180 mm × 1580 mm

The values of the variable casting parameters presented in **Table 2** and assigned to the exactly defined section of the slab, from which the sample was taken for a metallographic investigation, were the following:

Only one parameter, which directly specifies the degree of failure of its stipulated value, is contained in the values presented in this table. It is the non-achievement of the minimum casting rate specified by the technological standard. In the investigated heat it was necessary to reduce the casting rate on the upstream units due to technological causes. For a possible comparison with the state before the slowdown of the casting rate and for an evaluation of a possible influence of the deviations of the values of individual parameters, we give, in the last row of the table, the average values of the monitored parameters, acquired from approximately 250 heats of the same slab format and the same steel grade.

6 RESULTS AND DISCUSSION

On the basis of the presented values of the selected casting parameters and the occurrence of the internal transverse cracks on the slab it is possible to draw rather unequivocal conclusions:

- The cause of the internal transverse cracks in the specific slab represented by a sample of the Baumann sulphur print and macro-etching, was a reduction in the casting rate. The value of the casting rate specified by the technological standard for the given steel grade of 1.20 m/min was reduced down to 0.74 m/min, indicating the overall drop in the casting rate by 38 %.
- The reduction in the casting rate is also documented in the system of prediction by the monitored parameter of the non-achievement of the minimum casting rate – the value recorded in our case was minus 470 mm.
- The reduced casting rate entailed a reduction in the surface temperature of the measured planes of the secondary cooling and, consequently, also a reduction in the density of the heat flux from the slab into the cooling media. Particularly the reduction in the surface temperature of the slab in the area of its straightening might have been the primary cause of the transverse cracks.
- The steel grade also played its unfavourable role during the formation of the investigated cracks. Namely, the micro-alloying elements – vanadium, niobium and titanium – reduce the steel ductility already at approximately 950 °C. They form the so-called "trough" of the ductility reduced below this temperature value, which means that micro-alloyed steels are here more susceptible to a crack formation in continuously cast products.

The paper describes one of the possible approaches of using the prediction system, or using the values of the casting parameters selected for this system, for an exact determination of the causes of the transverse internal cracks on a concrete slab. In the professional literature, we did not find any solutions or results for exactly this, or a similar, problem. On the other hand, it is possible to find studies or articles dealing with a prediction system and the use of this software as an analytical tool for an assessment of the continuous casting process and the quality of cast blanks.

Table 2: Values of the parameters for the investigated sample and the average values for 250 heats

Tabela 2: Vrednosti parametrov preiskovanih vzorcev in povprečne vrednosti iz 250 šarž

Parameter	Casting rate (V_g)/(m min^{-1})	V_g below the minimum limit V_g/(mm min^{-1})	Overheating of steel above Tl in the tundish (°C)	Type Seg 6 (°C)	Type Seg 11 (°C)	Heat-flux density (W m^{-2})
Value	0.74	–470	35	915	842	989705
Average for 250	1.19	3	33	965	876	1086773

Their results are generally comparable with the use of the LITIOS analytical software tool, presented here. They are presented, for example, in[11], which describes the strategies and methods for monitoring and controlling the quality during the production of flat steel. It gives a complete description of the quality, technological parameters and information technology. The data are archived and used in an appropriate manner for intervening at a specified place in order to improve the quality. The percentage of success is said to be 85 %. Reference[12] gives an example of a complex system integrated in CSP at the ACB company, including the modules that collect and process the data, search and visualise them, draw up statistics and analyse the phenomena. Individual, special cases can be quickly solved with the use of this software.

7 CONCLUSIONS

The cause of the transverse internal cracks in a continuously cast slab was determined with a complex system of a long-term monitoring of the casting parameters using the LITIOS analytical software tool:

- In a metallographic laboratory a cross-section sample taken from a continuously cast slab was evaluated. Some transverse internal cracks were found on it at a degree exceeding the harmlessness of such a defect.
- The technologist determined the possible technological parameters of the casting that might have caused these cracks.
- Subsequently, using the LITIOS analytical software tools, we assigned concrete variable casting values, corresponding exactly to the taken sample, to these parameters.
- Only one technological parameter was found to be beyond the standard limits set for casting the relevant steel grade.

This analysis clearly revealed the cause of the examined cracks. It was the forced reduction in the casting rate to approximately 62 % of the value specified by the standard technological procedure.

By using a similar procedure it is possible to determine the technological cause of any defect found on the Baumann sulphur print or on a macro-etched sample taken from a continuously cast slab, and to perform interventions aiming at controlling the casting technology, leading to a minimisation or complete elimination of the causes of the defect during the subsequent casting.

By using the LITIOS software tool, together with examining the samples and determining their exact evaluation in the metallographic laboratory, we can efficiently contribute to improving the quality of cast slabs and, ultimately, to increasing the efficiency of the final products made from them.

8 REFERENCES

[1] C. A. Santos, J. A. Spim, M. C. Flerardi, A. Garcia, The use of artificial intelligence technique for the optimisation of process parameters used in the continuous casting of steel, Applied Mathematical Modelling, 26 (**2002**) 11, 1077–1092, doi:10.1016/s0307-904x(02)00062-8

[2] C. A. Santos, J. A. Spim, A. Garcia, Mathematical modelling and optimization strategies (genetic algorithm and knowledge base) applied to the continuous casting of steel, Engineering Applications of Artificial Intelligence, 16 (**2003**) 5–6, 511–527, doi:10.1016/S0952-1976(03)00072-1

[3] F. Kavička, Z. Franěk, J. Štětina, Software Analytical Instrument for Assessment of the Process of Casting Slabs, Proceedings of the 10th International Conference on Numerical Methods in Industrial Forming Processes NUMIFORM 2010, Pohang, Republic of Korea, 2010, 586–592, doi:10.1063/1.3457607

[4] V. Vaculik, R. B. MacCuish, R. K. Mutha, Multivariate statistical model-based system for monitoring the operation of a continuous caster and detecting the onset of impending breakouts, US Patent 6564119, 2003

[5] Electrics and Automation for Continuous Casting – SIMETAL CC Control, Basic automation, Metals magazine, 1 (**2014**)

[6] J. Štětina, Z. Franěk, F. Kavička, M. Masarik, V. Krol, Quality Optimization of Casting Slab via Mathematical and Statistical Method, DVD Proceedings of the 7th European Continuous Casting Conference METEC InSteelCon, Düsseldorf, Germany, 2011, 193–200

[7] T. Mauder, C. Sandera, J. Stetina, M. Seda, Optimization of The Quality of Continuously Cast Steel Slab Using the Firefly Algorithm, Mater. Tehnol., 45 (**2011**) 4, 347–350

[8] T. Mauder, Z. Franek, F. Kavicka, M. Masarik, J. Stetina, A Mathematical & Stochastic Modelling of the Concasting of Steel Slabs, Proceedings of the 18th International Conference on Metallurgy and Materials, Hradec nad Moravici, 2009, 41–48

[9] A. Ebel, J. Hackmann, N. Holzknecht, N. Link, H. Peters, Industrielles data mining in der stahlindustrie, Stahl und Eisen, 132 (**2012**) C.2, 29–37

[10] J. Šmíd, Catalogue of defects of continuously cast slabs, Technologie und Metallurgie, Ltd., Business Studies, 2011, 125 p.

[11] H. Peters, T. Heckenthaler, N. Holzknecht, Strategies and methods for quality monitoring and quality control in flat steel production, Stahl und Eisen, 126 (**2005**) C.7, 29–36

[12] M. Reifferscheid, J. Kempken, M. Bruns, J. I. L. Garcia-Echave, J. M. Ovejero, Integrated Product Improvement by Quality Analysis and Modelling, Stahl und Eisen, 125 (**2005**) 12, 29–34

UDK 519.61/.64:621.9
Professional article/Strokovni članek

ISSN 1580-2949
MTAEC9, 49(2)291(2015)

EFFECTIVE PREPARATION OF NON-LINEAR MATERIAL MODELS USING A PROGRAMMED OPTIMIZATION SCRIPT FOR A NURIMERICAL SIMULATION OF SHEET-METAL PROCESSING

UČINKOVITA PRIPRAVA NELINEARNIH MODELOV MATERIALA S PROGRAMIRANIM OPTIMIZACIJSKIM ZAPISOM ZA NUMERIČNO SIMULACIJO OBDELAVE PLOČEVINE

Miroslav Urbánek, Filip Tikal
COMTES FHT a.s., Prumyslova 995, Dobrany, Czech Republic
miroslav.urbanek@comtesfht.cz

Prejem rokopisa – received: 2013-10-14; sprejem za objavo – accepted for publication: 2014-05-23

doi:10.17222/mit.2013.248

Progressive methods and technologies are the key to the dynamic development of the automotive and electrical-engineering industries. The processes in sheet-metal processing have changed fundamentally since the end of the 1990s. Previously, the operations such as cutting, punching holes, etc., were carried out separately on different press machines. These operations can now be integrated into a single tool on one press machine due to the development of progressive tools and, especially, the fine-blanking technology. The result is an already completed component that can be used for the assembly. The development of progressive tools must be supported with the FEM simulations of sheet-metal processing that are dependent on their inputs. Therefore, only a correct material model can be expected to provide the right results.

For the reasons described above, an experimental program dealing with measuring and fitting the data to the models with orthotropic material properties such as rolled sheets was designed and implemented. The aim is to obtain the material models of rolled sheets made of selected aluminum, copper and steel alloys. One of the objectives of the solution is to provide more efficient and more accurate data fitting because the more accurate the input material data are, the more accurate are the simulation results for sheet-metal processing.

The optimization script using the simplex method was made for fitting. The main function of the optimization script is to specify the parameters of the material model iteratively and to compare the simulation results and the mechanical-test results. The script was programmed in the Python environment for the MSC.MARC/MENTAT software using the Johnson-Cook plasticity model. Fitting the data from the pressure tests by Rastegaev at different loading speeds is presented. The difference between the measured and simulated curves is less than 1 %.

Keywords: FEM simulation, measurement, compression test, fitting, MSC.MARC, Python

Napredne metode in tehnologije so ključne za dinamičen razvoj avtomobilske in elektro- industrije. Procesi preoblikovanja pločevin so se bistveno spremenili od devetdesetih let zadnjega stoletja. Prej so se operacije, kot so rezanje, prebijanje lukenj in podobno, izvajale ločeno na različnih strojih. Zaradi razvoja naprednih orodij in še posebej tehnologije precizijskega štancanja se te operacije lahko združi v enem orodju na enem stroju. Rezultat je kompletna komponenta, ki je primerna za vgradnjo. Razvoj naprednih orodij mora biti podprt s FEM-simulacijami obdelave pločevine, kar je odvisno od vhodnih veličin. Zato samo pravilen model materiala lahko zagotavlja prave rezultate.

Iz navedenih razlogov je bil postavljen in uporabljen eksperimentalni program, ki obravnava merjenje in ujemanje podatkov za modele z ortotropnimi lastnostmi materiala, kot je valjana pločevina. Namen je dobiti modele materiala valjane pločevine za izbrane aluminijeve in bakrove zlitine ter jekla. Eden od ciljev je zagotoviti bolj učinkovito in bolj zanesljivo pridobivanje podatkov, kajti čim bolj zanesljivi so vhodni podatki materiala, bolj natančni so rezultati simulacije pri obdelovanju pločevine.

Za prilagajanje je bila uporabljena optimizacija zapisa z uporabo simpleksne metode. Glavna vloga optimizacijskega zapisa je iterativna opredelitev parametrov modela materiala in primerjava rezultatov simulacije z rezultati mehanskih preizkusov. Zapis je bil programiran v okolju Python za programsko opremo MSC.MARC/MENTAT z uporabo Johnson-Cookovega modela plastičnosti. Predstavljeno je ujemanje podatkov iz Rastegaevega tlačnega preizkusa pri različnih hitrostih obremenjevanja. Razlika med izmerjenimi in simuliranimi krivuljami je manj kot 1 %.

Ključne besede: FEM-simulacija, merjenje, tlačni preizkus, ujemanje, MSC.MARC, Python

1 INTRODUCTION

The economic crisis dragging on since 2007 exerts an increasing pressure on the suppliers of the components for the automotive and electrotechnical industries. In general, the aim is to maintain a high quality of the components while reducing the inputs. The aim can only be achieved by deploying more advanced and less costly technologies that offer a higher efficiency. Such were also the reasons leading to the creation of the international EUREKA project aimed primarily at replacing the costly machining processes with lower-cost and more advanced manufacturing processes for making flat products. The existing fine-blanking process delivers precision sheet products with the tolerances of IT8-IT9. Fine-blanking combined with bulk forming (chamfering, stepping down and other operations) of metal-sheet components represents an advanced manufacturing approach. The production time for a part made with this technique is reduced to seconds, while the required accuracy and quality of the functional surfaces are maintained. A typical example of a flat product with

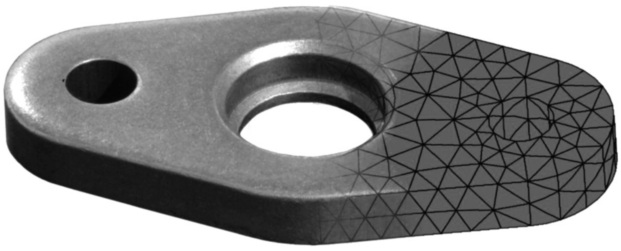

Figure 1: Example of a flat product with spatial features
Slika 1: Primer ploščatega izdelka s prostorsko mrežo

spatial features, such as a cylindrical recess, is shown in **Figure 1**.[1–3]

Today's professional literature around the world describes various approaches to measuring material characteristics. They concern not only elastic-plastic materials, such as metal alloys, but also viscoelastic materials, such as rubber. Elastic-plastic models typically rely on a suitable form of the Johnson-Cook flow-stress model, defined with Equation (1) representing the stress-strain curve. This model can provide a comprehensive description of a material at various strain rates and temperatures.[4,5]

Previously, we performed fitting by hand when individual states were fitted, which provided us with more accurate results for a single load condition (a single temperature or strain rate), but for a comprehensive assessment of material properties this method is insufficient and also time-consuming. In addition, the dependence of the material behavior on the states was not respected. Specifically, a material stiffens more during faster loading and it is more pliable at a higher temperature.

2 PREPARATION OF THE MATERIAL MODELS

Material characteristics are measured using standardized and other physical methods with the test machines that record the force and time or displacement (the plunger displacement). The force-versus-displacement plots are evaluated and transformed by means of formulas to obtain the required quantities, such as stress, strain, elongation and others.

In order to obtain the correct values of material characteristics, it is advisable to perform a test simulating the actual manufacturing process in a simplified form: on a smaller scale, for instance. There are various factors having an impact on the quality of the measurement record, such as the measurement method, the test configuration, the quality of the sensors, the machine stiffness, the loading velocity and others.[1–3]

In the present project, a rapid and effective data-fitting procedure for various physical measurements was developed and implemented. Data fitting is in essence a fine tuning of the material-property data obtained with the mechanical tests. Data fitting comprises four main steps. The first one involves a physical measurement and an evaluation. The next step is smoothing where a smooth continuous polynomial curve is fitted to the jagged test plot. In the third step, parameters are estimated with an approximation. The last step consists of a numerical analysis under the conditions identical to those of the physical measurement. Using a pre-programmed optimization script, the constants for the material model are sought.

In the following sections, these steps for an effective material-data preparation will be described in greater detail. For most of the steps, the scripts were developed in the user-friendly Python environment. Most scripts were written with the aid of open source libraries facilitating the preparation.

The term physical measurement can denote a standard compression or tension test. The COMTES FHT a. s. company generally deals with standard and non-standard measurements of specimens and functional items. For this reason, the optimization script used for finding the parameters of a material model should be versatile enough to apply to most of the measurements.

The measurement data is evaluated and corrected for further processing, if required. In general, smooth curves are easier to work with, especially when using mathematical algorithms. The smoothing can be modified with a user-defined parameter, which alters the shape of the resulting curve. The time required is very short: at the order of seconds.

Using the corrected curve obtained from the physical measurement under the quasi-static conditions at room temperature, some parameters can be estimated with the aid of the generally known formulas based on the volume conservation, the yield strength and the engineering strain.[2,3,5]

In addition, these estimated parameters are used as the input parameters for the optimization script controlling the numerical simulation. The optimization script is iterative (**Figure 2**) seeking the constants for a general material model according to Johnson-Cook. The model is defined with an equation comprising five constants derived from the material properties. Other terms of the

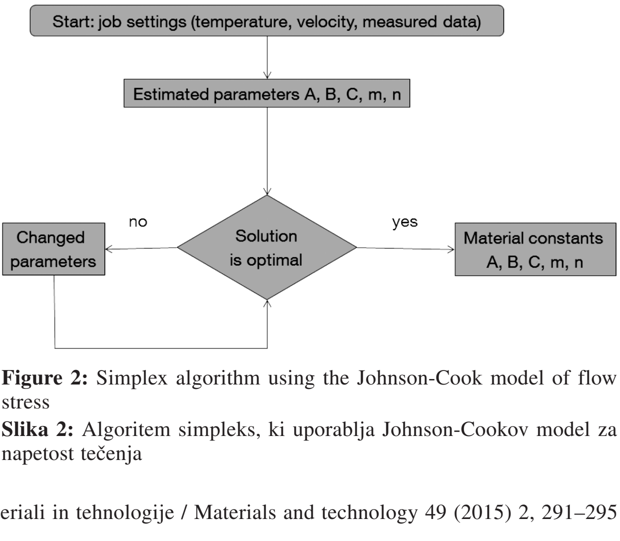

Figure 2: Simplex algorithm using the Johnson-Cook model of flow stress
Slika 2: Algoritem simpleks, ki uporablja Johnson-Cookov model za napetost tečenja

equation (Equation (1)) depend on the boundary and initial conditions of the process (temperatures, strain rates) and their meanings are described below. In the previous step, constants *A*, *B* and *n* of the Johnson-Cook equation, which depend on the strain hardening and yield strength, were estimated. Generally, the equations of the Johnson-Cook model describe the material in all the states. The state change is defined with the value of the relevant constant. The *A*, *B*, *C*, *m* and *n* constants determine the material state at all the temperatures and rates:

$$\sigma_v = (A + B\cdot\varepsilon_{\mathrm{p}}^{n})\cdot\left(1 + C\cdot\ln\left(\frac{\dot{\varepsilon}}{\dot{\varepsilon}_0}\right)\right)\cdot\left(1 - \left(\frac{T - T_{\mathrm{room}}}{T_{\mathrm{melt}} - T_{\mathrm{room}}}\right)^{m}\right) \quad (1)$$

The Johnson-Cook model represents the flow-stress values describing the material behaviour under deformation. Equation (1) consists of a product of the terms governed by the plastic strain, the strain rate and the temperature. The first term $(A+B\cdot\varepsilon_{\mathrm{p}}^{n})$ describes the beginning of the plastic-flow segment of the stress-strain curve where *A* is the yield strength (MPa). The plastic-flow segment depends on the *B* strain-hardening modulus (MPa), the plastic strain ε_{p} and the strain exponent *n*. The second term $(1+C\cdot\ln(\dot{\varepsilon}/\dot{\varepsilon}_0))$ consists of a dimensionless coefficient of sensitivity to strain rate *C*, the strain-rate ration logarithm $\dot{\varepsilon}$ (s^{-1}) and the reference strain rate ε_0 (s^{-1}), which is normally taken as $\varepsilon_0 = 1\ \mathrm{s}^{-1}$. The last term of the equation $\left(1-\left(\frac{T-T_{\mathrm{room}}}{T_{\mathrm{melt}}-T_{\mathrm{room}}}\right)^{m}\right)$ which describes the effect of the temperature consists of a ratio of two temperature differences where individual terms denote the current temperature *T* (°C), the room temperature T_{room} (°C) and the melting temperature T_{melt} (°C).[6,7]

The optimization script relies on the simplex algorithm, which is a linear iterative method. The outcome of the simplex algorithm is the value of the objective function. The values of the previous and the current steps are compared. The objective function is the evaluation criterion for the optimization method that seeks the minimum value of the function. With the single-digit values (e.g., 5), the curves are virtually identical. By contrast, at higher values (such as 120), there are differences between them, leading to inaccurate results.

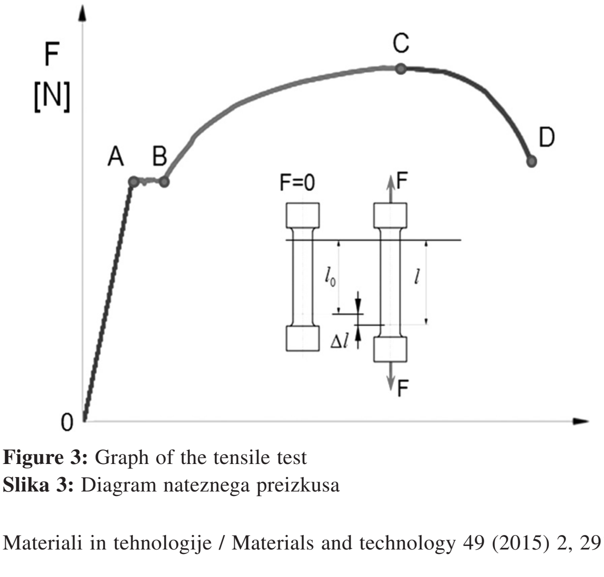

Figure 3: Graph of the tensile test
Slika 3: Diagram nateznega preizkusa

The optimization involves comparing the measured data (or smoothed data) with the results of the numerical simulation (**Figure 2**). COMTES FHT a. s. uses the software solutions provided by MSC Software, which has been developing the finite-element-method-based software for numerical simulations for 50 years. The script relies on MSC.MENTAT as the pre- and post-processor and on MSC.MARC as the solver. The latter was developed for strongly non-linear analyses.[6–8]

It is important to bear in mind that errors occur in both the physical measurement and the numerical simulation. In addition, when the material-model constants are corrected with regard to multiple measurements under varying conditions, the results cannot be identical for all the states.

3 DESCRIPTION OF THE MATERIAL

The complex behaviour of the materials can be described in a simplified manner with a tension-test curve (**Figure 3**) which, generally, comprises three segments. The first linear segment of the tension-test plot is described with Hooke's law (from 0 to A) given by the Poisson's ratio and Young's modulus. In the second segment of the plot (from A to C), the plastic deformation begins to occur at the yield stress. Beyond that point, the plastic flow continues and the material strain hardens up to the ultimate tensile strength. This red segment is described with plasticity models. In this case, it is the Johnson-Cook model. Once the ultimate strength is exceeded, the plasticity of the material is used up and cracks develop, leading to a destruction of the test specimen (from C to D). The last segment of the curve is modelled using damage criteria which describe the condition of the material through the widely known Cockroft-Latham model:

$$\int \frac{\sigma_{\max}}{\bar{\sigma}}\dot{\varepsilon}\,\mathrm{d}t \geq C \quad (2)$$

4 COMPRESSION TEST

In a demonstration of the application, the Rastegaev compression test (**Figure 4**) is described as a test suitable from multiple standpoints. First, the test configuration allows the data to be measured correctly without any friction effects. Furthermore, the test can be simplified for the numerical simulation to a 2D axially symmetric problem (**Figure 5**), due to the axially symmetric test specimen. This type of analysis provides an excellent description of the specimen throughout the process using a relatively small number of elements. Thanks to the small number of elements, short computation times are

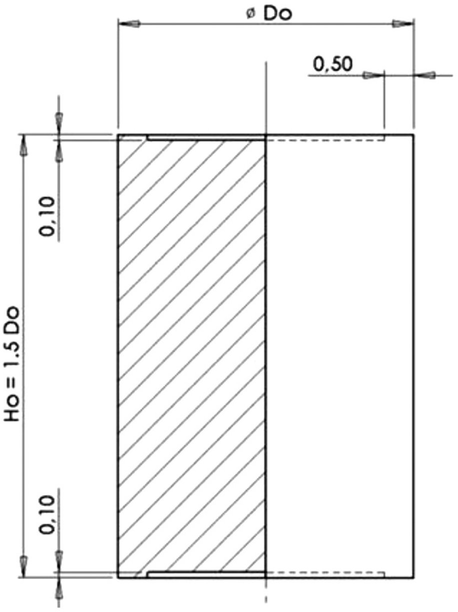

Figure 4: Specimen for the Rastegaev compression test
Slika 4: Vzorec za Rastegaevov tlačni preizkus

achieved. With the optimization of the material parameters for the compression test, a single iteration step of the optimization script takes approximately 10 s, of which the calculation itself takes about 6 s. The remaining time is used for setting up and evaluating the calculation. These times are, understandably, dependent on the computer-workstation hardware. With the above steps, this short data fitting becomes a comparatively rapid procedure. The optimization iteration takes place involving multiple measurement-data sets in order to find the correct material constants. Naturally, the more measurement-data sets are available for various temperatures and speeds, the easier it is to find the material-model constants.

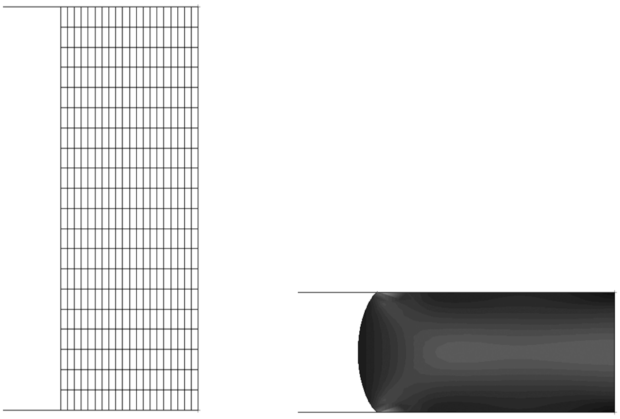

Figure 5: Axisymmetric model of the compression test in MSC.MARC/MENTAT in the initial and deformed states
Slika 5: Osnosimetrični model tlačnega preizkusa v MSC.MARC/MENTAT začetnem in deformiranem stanju

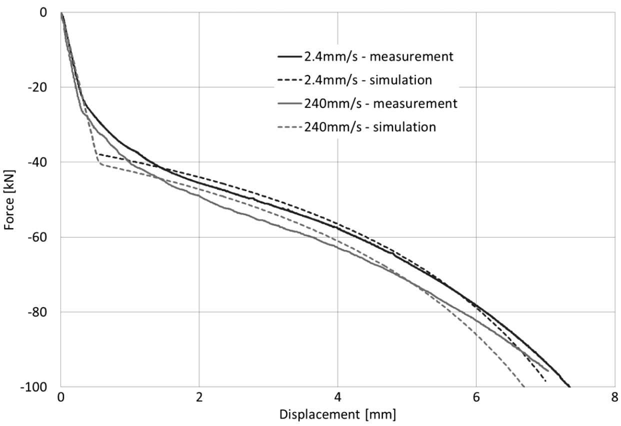

Figure 6: Comparison of the numerical simulation and physical measurements
Slika 6: Primerjava numerične simulacije in fizikalnih meritev

The method was applied to fitting the measurement data for the 16MnCr5 manganese steel. The specimens of this material were taken along the forming direction and loaded at the rates of 2.4 m/s and 240 mm/s at room temperature. The plot (**Figure 6**) contains solid lines representing the measured curves and dash-and-dot lines showing the simulation curves for identical boundary conditions. Upon fine tuning, the Johnson-Cook model parameters were as follows: A = 554 MPa, B = 198 MPa, n = 0.00035, C = 0.0215 and m = 0.0335. Although the specimens were kept at room temperature, the effect of the temperature on the specimens this small (D_0 = 8 mm and height H_0 = 11.5 mm) and loaded at high strain rates is not negligible.

5 CONCLUSION

Using the above-demonstrated data-fitting procedure for obtaining the material constants, the material models can be fine-tuned quickly and effectively. A smart choice of the test specimens simplifies the numerical simulation and allows the entire data-fitting process to be automated. Thanks to the MSC.MARC/MENTAT environment, the optimization script was developed in the PYTHON language and the curve-smoothing tools, so that the material data of the Johnson-Cook flow-stress model can be used in other FEM-based programs as well.

The objective of the solution developed herein was to obtain as accurate the material data as possible for constructing a numerical model of shearing and forming flat products with spatial features for orthotropic materials.

The comparison graph (**Figure 6**) suggests that the material model is suitable for characterizing the spatial features in forming a flat product.

The main result is the working optimization script for fitting, which efficiently searches for the material-model constants that will subsequently be used for the simulations of cold forming. With precise results, it is possible to better describe the process of forming and to optimize it not only in terms of the material flow, but also in terms of the tools stress. The next step will be the preparation of a script for fitting for various mechanical tests and material-seeking models using other measurement types, such as tensile, compressive or shear tests.

Acknowledgement

The authors of this paper gratefully acknowledge the support from the EUREKA LF12009 project: Research and Development of a New Technology of Cold Precision Forming as a Replacement for the Cutting Operations.

6 REFERENCES

[1] M. Urbánek, F. Tikal, Určení koeficientů materiálových modelů pro tvářecí procesy, Hutnické listy, LXVI (**2013**) 4, 71

[2] M. Španiel, A. Prantl, J. Džugan, J. Růžička, M. Moravec, J. Kuželka, Calibration of fracture locus in scope of uncoupled elastic–plastic-ductile fracture material models, Advances in Engineering Software, 72 (**2014**), 95–108, doi:10.1016/j.advengsoft.2013.05.007

[3] P. Kubík, F. Šebek, J. Petruška, J. Hůlka, J. Růžička, M. Španiel, J. Džugan, A. Prantl, Calibration of Selected Ductile Fracture Criteria Using Two Types of Specimens, Key Engineering Materials, 592–593 (**2013**), 258–261, doi:10.4028/www.scientific.net/KEM.592-593.258

[4] R. A. Smidt, F. Bitzer, P. Höfer, M. Hellmann, B. Reh, P. Rademacher, H. Hoffman, Cold Forming and Fineblanking, Druckhaus Thomas Mützen, Germany 2007

[5] J. Dzugan, M. Spaniel, P. Konopík, J. Ruzicka, J. Kuzelka, Identification of Ductile Damage Parameters for Austenitic Steel, World Academy of Science, Engineering and Technology, 6 (**2012**) 5, 1291–1296

[6] J. Džugan, M. Zemko, Input data influence on FEM simulation of steam turbine blades materials hot forming, Materials Science Forum, 773–774 (**2013**), 79–88, doi:10.4028/www.scientific.net/msf.773-774.79

[7] Marc® 2012, Volume A, Theory and User Information

[8] Simplexová metoda, website, www.algoritmy.net/article/1416/Simplexova-metoda, accessed 14 Oct. 2013

UDK 658.567.5
Professional article/Strokovni članek

ISSN 1580-2949
MTAEC9, 49(2)297(2015)

NEUTRALIZATION OF WASTE FILTER DUST WITH CO_2

NEVTRALIZACIJA ODPADNEGA FILTRSKEGA PRAHU S CO_2

Ana Kračun[1,2], Ivan Anžel[1], Lidija Fras Zemljič[1], Andrej Stergaršek[3]

[1]University of Maribor, Faculty of Mechanical Engineering, Smetanova 17, 2000 Maribor, Slovenia
[2]Institute of Metals and Technology, Lepi pot 11, 1000 Ljubljana, Slovenia
[3]Kemek, d. o. o., Cimpermanova ulica 3, 1000 Ljubljana, Slovenia
ana.kracun@imt.si

Prejem rokopisa – received: 2014-09-29; sprejem za objavo – accepted for publication: 2014-12-12

doi:10.17222/mit.2014.247

In this paper we report on the possibility of neutralizing filter dust from Talum Livarna d.o.o. The filter dust that remains after cleaning flue gas with the classification number of waste 10 10 09* is alkaline and contains heavy metals, non-metals, organic pollutants, and, therefore, has the properties of hazardous waste. The possibility of neutralizing this dust with CO_2 was studied. The results showed that the treatment successfully lowered the pH value between the limits 6 and 9, which is within the legal constraints of pollution for strong acidic or alkaline waste. The contents of the hazardous substances were lowered, i.e., As, Cu, Ba, Zn, Cd, Cr, Ni, Pb, Sn, Mn and V, with percolation values that are below the level of the prescribed threshold-limit values for substances that allows their disposal in non-hazardous waste landfills. Only the percolation values of Sb, Cd, Mo and Se exceed the prescribed threshold limit values of substances that allow their disposal in inert waste landfills. The XRD analysis after the neutralization of the filter dust using CO_2 showed no presence of CaO. The neutralized filter dust can be land filled as a stabilized and unreactive waste in landfills for nonhazardous wastes. Their properties also offer the possibility for incorporating them into some other material or product, such as the production of new composite materials, their use in construction products and perhaps cements or usage in backfills.

Keywords: hazardous waste, filter dust, neutralization, stabilization, chemical properties

Raziskali smo možnost nevtralizacije filtrskega prahu iz podjetja Talum Livarna, d. o. o. Filtrski prah po čiščenju dimnih plinov s klasifikacijsko številko odpadka 10 10 09* je alkalen, vsebuje težke kovine, nekovine, organska onesnaževala, zato ima lastnosti nevarnega odpadka. Filtrski prah smo nevtralizirali s CO_2, da je nastal pretežno amorfen produkt. Po obdelavi smo uspešno znižali pH-vrednost v meje med 6 in 9, kar je v dovoljenem območju za odpadke, onesnažene z močno kislino ali bazo. Prav tako je bila zmanjšana vsebnost nevarnih snovi, in sicer As, Cu, Ba, Zn, Cd, Cr, Ni, Pb, Sn, Mn in V, tako da so izluževalne vrednosti pod mejo predpisanih parametrov izlužka in je tako dovoljeno odlaganje na odlagališčih za nenevarne odpadke. Samo izluževalne vrednosti Sb, Cd, Mo in Se še prekoračujejo predpisane mejne vrednosti, ki so dovoljene za odlaganje na odlagališčih za inertne odpadke. XRD-analiza po nevtralizaciji filtrskega prahu s CO_2 ni pokazala prisotnosti CaO. Nevtraliziran filtrski prah se lahko odloži kot stabiliziran in nereaktiven odpadek na odlagališčih nenevarnih odpadkov. Glede na lastnosti obstaja možnost predelave in uporabe v koristne namene, npr. za proizvodnjo novih kompozitnih materialov, gradbenih izdelkov, morda cementa ali za zasipavanje.

Ključne besede: nevarni odpadki, filtrski prah, nevtralizacija, stabilizacija, kemijske lastnosti

1 INTRODUCTION

Hazardous wastes are a problem of modern civilization and therefore need to be handled in a prudent manner. A rapid increase in their amount, negative effects on the environment and a growing environmental awareness have led to changes in the field of waste management in recent decades. These factors have contributed to stricter regulations and the development of new technical and operational solutions.[1,2] The strategy of waste management in Slovenia is directed towards actions that enable the overseeing, removal and reduction of the harmful effects of these wastes on the environment and humans, as well as their preparation for reuse, recycle and use as an energy source.[2]

The metallurgical industry is a major source of potentially hazardous waste materials, those by-products of the production of metals and alloys. These metallurgical wastes consist mainly of slags and dust sludges that result from flue-gas filtering. These so-called waste materials can be potentially utilized as resources, for example, dust from the EAF process can be used as a source of Zn,[3,4] metallurgical slags can be used in the production of building materials.[5] A special aspect of the steel industry that requires particular attention is the production of stainless steel. During stainless-steel production, chromium oxidation occurs, which leads to the formation of CrO_x phases. They not only represent a loss from the production point of view,[6–8] but also represent an environmental risk, because they can oxidize to dangerous hexavalent chromium (Cr^{6+}).[9] During the melting of secondary aluminium contaminated with oil, paint or plastic flue gases that contain dust contaminated with heavy metals, nonmetals, dioxins, furans and fluorides.[10]

Waste filter dust is formed inside the exhaust gas treatment apparatus of foundry furnaces during operation with help of an additive DESOMIX HK. The additive DESOMIX HK is a mixture of calcium hydroxide [$Ca(OH)_2$] and active chalk. Filter dust is classified as a hazardous waste with a classification number 10 10 09*, which puts it as far as regulation is concerned[1] amongst the group of dusts that contain dangerous substances.

The filter dusts are homogenous, alkaline, contain heavy metals, nonmetals, dioxins, furans and fluorides. Because the limit values of these toxic substances are exceeded during leeching, it is determined that these dusts have the properties of hazardous waste. Therefore, it has to be deposited in accordance with the relevant regulations.[2] Industrial wastes are deposited in subterranean depots, usually prepared in closed coal and ore mines.[11]

There are many waste substances that react with carbon dioxide, for example, metallurgic slags, dusts from industrial thermical processes, combustion remains in which calcium oxide is a key component. The reaction between calcium hydroxide [$Ca(OH)_2$] and carbon dioxide (CO_2) is called carbonization. It is a natural reaction between an oxide or a base and CO_2.[12,13] Direct binding between CO_2 and calcium hydroxide is slow. However, it can be accelerated with the addition of water. In such cases the CO_2 dissolves in water and dissociates and reacts with the dissolved and dissociated calcium hydroxide, therefore forming carbonate materials.[12,13] During the formation of these carbonate materials the pH of the waste dust decreases, which results in the minimal solubility of the metals present in the waste dust.[12–14] Complete carbonization can decrease the leaching of metals by 80 %.[14–16] Previous research[14–28] has shown that metal stabilization processes are more efficient if the treatment of the waste dust is conducted over an extended period of time and at high CO_2 concentrations.

The main goal of this research was to determine whether it is possible to obtain a chemically stable product from waste filter dust with the process of neutralization using CO_2. This would also enable this material to be reused in some other useful application or at least to process it enough so that long-term monitored deposition would be possible according to Slovenian regulations.[2] Should the treated waste powder leaching values be inside the legal constraints for nonhazardous waste there would be a possibility that this waste could be deposited as a cost-reducing measure in dumps for nonhazardous waste. If it could achieve the constraints for inert waste it could be reused for practical purposes, for example, the production of new composite materials, use in construction materials, perhaps in cements or use in landfills.

2 EXPERIMENTAL

Filter dust, a by-product of the treatment of exhaust gases, is classified as a hazardous waste with the classification number 10 10 09*. The analyzed sample comes from the release of a exhaust-gas treatment apparatus filter L9 in the company Talum Livarna, d. o. o.

The granulometric composition of the filter dust and the average particle size was determined with a device for laser-diffraction particle size analysis Cilas 1064. A qualitative analysis of the sample microstructure was facilitated using a high-resolution Scanning Electron Microscope SIRION NC 400, equipped with NICA brand EDS detector. The X-ray analysis was conducted using a Philips XRD-analyzer W1800 hardware and X'pert High Score software.

2.1 Neutralization of the filter dust with CO_2

The first step in this research was the determination of the initial pH of the leachate of the filter dust sample originating from Talum Livarna, d. o. o. Three samples with different moisture contents were prepared:

- 11 % moisture content (sample label NFP1).
- 8 % moisture content (sample label NFP2)
- 14 % moisture content (sample label NFP3).

The moisturized samples were stirred using a glass rod, which helped to achieve a uniform water consistency of the sample. A Rushton mixer and a supply tube for the CO_2 were placed inside a glass beaker. The samples were exposed to a flow of 10 L/min of CO_2 for a period of 1 h.

The leaching and neutralization of the waste filter dust were carried out in accordance with the standard SIST EN 12457 – 4 (24 h leaching with water; ratio water/solid was 10/1). This was followed by a measurement of the pH and the leached inorganic parameters (metals) with help of the ICP-MS method. The ICP-MS device ionizes the sample with an inductively coupled plasma of argon gas. The ionized particles of the sample are then directed into a mass spectrometer. With the help of the ICP the presence of the following elements could be determined: Ag, Al, As, Ba, Ca, Cd, Co, Cr, Cu, Fe, Mn, Ni, Pb, Sb, Se, Sn, Sr, Zn, B, Be, Mo, Tl, V.

3 RESULTS AND DISCUSSION

3.1 Analysis of waste filter dust

With the aid of laser diffraction we determined that the sizes of the filter particles range from 0.47 µm to 47.30 µm. Some 20 % of the particles are in the size range between 0.47 µm and 10 µm, while the remaining

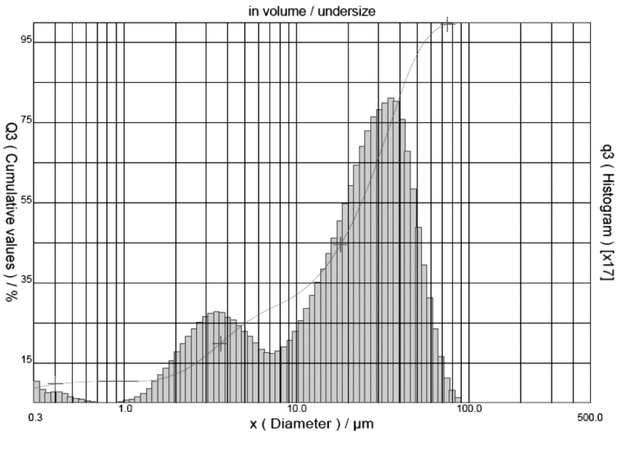

Figure 1: Size of the filter particulates
Slika 1: Velikost delcev filtrskega prahu

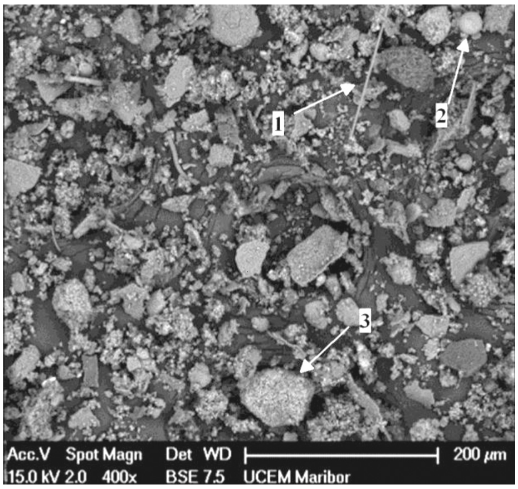

Figure 2: SEM analysis of filter dust: 1-rod-shaped particle, 2-spherical particle, 3-asymmetrical particle
Slika 2: SEM-analiza filtrskega prahu: 1-paličast delec, 2-sferičen delec, 3-asimetričen delec

80 % fall between 10 μm and 47.30 μm. **Figure 1** shows the size of filter particulates.

The SEM analysis of the sample dust showed that the morphology of the sample is not uniform. The particles were of different shapes, i.e., rod-shaped, spherical and asymmetrical (**Figure 2**). The particles also differed according to the chemical composition. The EDS analysis of the sample dust showed asymmetrical particles that had peaks for the elements: O, Al, Ca and Zn. The rod-shaped particles had peaks for the elements: O, Na, Mg, Al, Si, K and Ca. The spherical shaped had peaks for the elements: O, Si, Ti, Mg, Zn, Al, Si, Ca in K. Recurring elements with in all shapes were elements: O, Al and Ca.

The results of the chemical analysis of the waste filter dust are presented in **Table 1**.

Table 1: Levels of measured parameters in the filter dust
Tabela 1: Vsebnost izmerjenih parametrov v filtrskem prahu

Parameter	Amount in the s. s. sample, mg/kg
Al	2.1
Sb	45.1
As	10.0
Cu	540.2
Ba	3225.3
Zn	2501.6
Cd	24.7
Cr	154.7
Mo	15.4
Ni	128.0
Pb	282.3
Se	20.2
Co	2.1
Sn	130.9
Mn	130.3
Tl	0.6
V	15.4

The chemical analysis also revealed that the samples contained 3.5 % of moisture.

3.2 Filter-dust leachate analysis

The filter dust leachate contains high levels of heavy metals, such as: Sb, Cu, Ba, Cd, Mo, Ni, Se. It contains chlorides and fluorides. Present are also As, Zn, Cr, Pb, Co, Sn, Mn, Tl and V (**Table 2**). In the presence of water these chemical elements could leach into the soil and damage the environment, if the waste dust were to be deposited freely. It can be seen by observing **Table 2** that some quantities of leached heavy metals exceed the limiting values for dumping on sites equipped to handle inert waste. The leachate of filter dust has a highly alkaline pH value of 12.71. The data shows that the waste filter dust is of a heterogeneous composition and that it presents a hazard to the environment and it could have a great impact on the chemical and ecological balance, if not deposited correctly.

3.3 Analysis of filter-dust leachate neutralized with CO_2

The aim of the neutralization experiment with CO_2 was to evaluate the reduction of the pH values and the inorganic parameters and to attain, if it is possible, a chemically stable product that could be safely and harmlessly stored or deposited. The results show that the pH values could be reduced with this process, as shown in **Figure 3**.

The leachate pH values for the samples NFP1, NFP2 and NFP3 were monitored for a period of 32 d. The chemical stability of the neutralized samples was satisfactory and the pH values were between 6 and 9. The attained pH values confirm that the waste is not contaminated with a strong acid or base. Because of the leachate exposure to CO_2 found in the surrounding air, metal

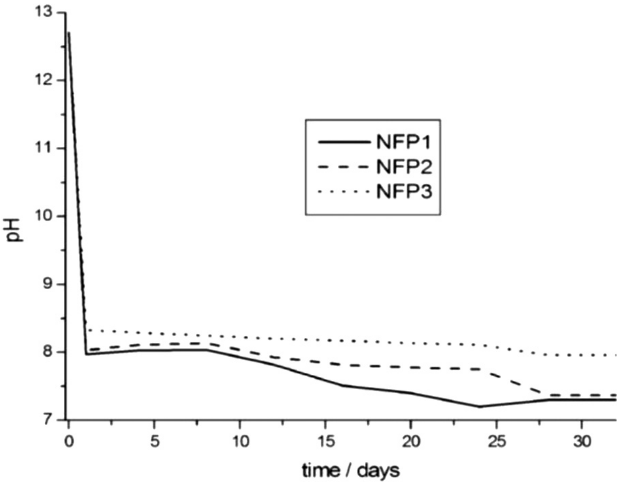

Figure 3: Filter dust leachate pH values of samples NFP1, NFP2, NFP3
Slika 3: pH-vrednosti izlužkov vzorcev NFP1, NFP2 in NFP3

Table 2: Leachate results for chosen parameters in the samples NFP1, NFP2, NFP3 and filter dust – compared to limiting legal constraints
Tabela 2: Vrednosti izluževanja nevarnih snovi vzorca NFP1, NFP2, NFP3 in filtrskega prahu - primerjava z zakonodajnimi vrednostmi

Parameter	Filter dust leachate result mg/kg	CO_2 NFP1 neutralized filter dust leachate result mg/kg	CO_2 NFP2 neutralized filter dust leachate result mg/kg	CO_2 NFP3 neutralized filter dust leachate result mg/kg	Limiting legal constraint of a parameter *L/S* = 10 L/kg (mg/kg)		
					Inert waste	Hazardous waste	Non-hazardous waste
Sb	0.26	0.34	0.26	0.31	0.06	5	0.7
As	0.01	0.01	0.01	0.01	0.5	25	2
Cu	2.63	12.99	1.95	0.38	2	100	50
Ba	73.17	5.19	4.71	4.86	20	300	100
Zn	3.41	0.77	0.38	0.37	4	200	50
Cd	0.18	0.21	0.11	0.11	0.04	5	1
Cr	0.01	0	0	0	0.5	70	10
Mo	0.49	0.77	0.73	0.65	0.5	30	10
Ni	0.44	0.20	0.15	0.11	0.4	40	10
Pb	0	0.05	0.01	0.04	0.5	50	10
Se	0.19	0.36	0.28	0.28	0.1	7	0.5
Co	0	0.01	0	0			
Sn	0.05	0.01	0.01	0.01			
Mn	3.73	1.92	1.57	1.51			
Tl	0	0.04	0.03	0.02			
V	1.00	0.31	0.23	0.10			

oxides bound to CO_2 and there was an additional drop in the pH over a period of 32 d. In sample NFP1 the initial pH was 12.71, while after neutralization it dropped to 7.97, and after a period of 32 days it was measured at 7.30.

Table 2 presents the leaching results for the chosen leachate parameters of the samples NFP1, NFP2, NFP3 and the waste filter dust, compared to environmental legal constraints. The neutralization reduced the leachate values of the As, Cu, Ba, Zn, Cr, Ni, Pb, Sn, Mn and V to a level that could enable this waste to be deposited as non-hazardous waste. The leachate values for the Sb, Cd, Mo and Se remained too high for this waste to be deposited as inert waste. The highest heavy-metal reduction occurred in sample NFP3 with 14 % moisture. This proves that the reaction of the carbonization is the fastest and most successful when the moisture is high and there is a lot of water present. During the neutralization waste filter dust in samples NFP1, NFP2 and NFP3 CO_2 underwent a chemical reaction and bound to calcium hydroxide [$Ca(OH)_2$] in the presence of moisture. The carbonate $CaCO_3$ was formed. An XRD analysis showed no presence of CaO in any of the samples, which indicates that the carbonization was complete. The formed carbonates are less soluble and less alkaline than the oxides and hydroxides found in the filter dust.

4 CONCLUSIONS

Neutralization helped to transform a hazardous waste into a non-hazardous waste, which could be deposited on sites for non-hazardous waste. CO_2 neutralization presents a viable technological solution for the stabilization of waste filter dust. The neutralized dust could be used as a bulk material.

Acknowledgment

The authors would like to thank dr. Marko Homšak and Talum Inštitut d.o.o. for their technical support.

5 REFERENCES

[1] Uredba o odlaganju odpadkov na odlagališčih, Uradni list RS, št. 61/2011, str. 8857, Available from World Wide Web: http://www.uradni-list.si/1/content?id=104808 [7. 4. 2014] (in Slovene)

[2] Uredba o odpadkih, Uradni list RS, št. 103/2011, str. 13935, Available from World Wide Web: http://www.uradni-list.si/1/content?id=106484 [27. 4. 2014] (in Slovene)

[3] P. Drissen, A. Ehrenberg, M. Kuhn, D. Mudersbach, Recent Development in Slag Treatment and Dust Recycling, Steel Research International, 80 (**2009**) 10, 737–745, doi:10.2374/SRI09SP055

[4] C. Scharf, A. Ditze, Processing of Agglomerated Red Filter Dust in the Converter Operation from Metallurgical Point of View, Steel Research International, 84 (**2013**) 9, 917–925, doi:10.1002/srin.201300126

[5] V. Zalar Serjun, B. Mirtič, A. Mladenovič, Evaluation of ladle slag as a potential material for building and civil engineering, Mater. Tehnol., 47 (**2013**) 5, 543–550

[6] B. Arh, F. Vode, F. Tehovnik, J. Burja, Reduction of chromium oxides with calcium carbide during the stainless steelmaking process, Metalurgija, 54 (**2015**) 2, 368–370

[7] J. Burja, F. Tehovnik, F. Vode, B. Arh, Microstructural characterization of chromium slags, Metalurgija, 54 (**2015**) 2, 379–382

[8] J. Burja, F. Tehovnik, J. Medved, M. Godec, M. Knap, Chromite spinel formation in steelmaking slags, Mater. Tehnol., 48 (**2014**) 5, 753–756

[9] G. Albertsson, L. Teng, B. Bjorkman, S. Seetharaman, F. Engstrom, Effect of Low Oxygen Partition in CaO-MgO-SiO2-Cr2O3-Al2O3 Synthetic Slag at Elevates Temperatures, Steel Research International, 84 (**2013**) 7, 670–679, doi:10.1002/srin.201200214

[10] A. Grochowalski, C. Lassen, M. Holtzer, M. Sadowski, T. Hudyma, Determination of PCDDs, PCDFs, PCBs and HCB Emissions from the Metallurgical Sector in Poland, Env Sci Pollut Res., 14 (**2007**) 5, 326–332, doi:10.1065/espr2006.05.303

[11] J. A. Roether, D. J. Daniel, D. Amutha Rani, D. E. Deegan, C. R. Cheeseman, A. R. Boccaccini, Properties of sintered glass-ceramics prepared from plasma vitrified air pollution control residues, Journal of Hazardous Materials, 173 (**2010**) 1/3, 563–569, doi:10.1016/j.jhazmat.2009.08.123

[12] G. Montes-Hernandez, R. Perez-Lopez, F. Renard, J. M. Nieto, L. Charlet, Mineral sequestration of CO2 by aqueous carbonation of coal combustion fly-ash, Journal of Hazardous Materials, 161 (**2009**), 1347–1354, doi:10.1016/j.jhazmat.2008.04.104

[13] J. Jianguo, C. Maozhe, Z. Yan, X. Xin, Pb stabilization in fresh fly ash from municipal solid waste incinerator using accelerated carbonation technology, Journal of Hazardous Materials, 161 (**2009**), 1046–1051, doi:10.1016/j.jhazmat.2008.04.051

[14] H. Ecke, H. Sakanakura, T. Matsuto, N. Tanaka, A. Lagerkvist, State-of-the-art treatment processes for municipal solid waste incineration residues in Japan, Waste Management & Research, 18 (**2000**) 1, 41–51, doi:10.1177/0734242X0001800106

[15] H. Ecke, N. Menad, A. Lagerkvist, Carbonation of municipal solid waste incineration fly ash and the impact on metal mobility, J. Environ. Eng. ASCE, 129 (**2003**) 5, 435–440, doi:10.1061/(ASCE)0733-9372(2003)129:5(435)

[16] H. Ecke, N. Menad, A. Lagerkvist, Treatment-oriented characterization of metal-bearing dry scrubber residue from municipal solid waste incineration (MSWI), Journal of Material Cycles and Waste Management, 4 (**2002**) 2, 117–126

[17] H. Ecke, H. Sakanakura, T. Matsuto, N. Tanaka, A. Lagerkvist, Effect of electric arc vitrification of bottom ash on the mobility and fate of metals, Environmental Science & Technology, 35 (**2001**) 7, 1531–1536, doi:10.1021/es0001759

[18] T. T. Eighmy, B. S. Crannell, L. G. Butler, F. K. Cartledge, E. F. Emery, D. Oblas, J. E. Krzanowski, J. D. J. Eusden, E. L. Shaw, C. A. Francis, Heavy metal stabilization in municipal solid waste combustion dry scrubber residue using soluble phosphate, Environmental Science & Technology, 31 (**1997**) 11, 3330–3338, doi:10.1021/es970407c

[19] E. Rendek, G. Ducom, P. Germain, Carbon dioxide sequestration in municipal solid waste incinerator (MSWI) bottom ash, J. Hazard. Mater., 128 (**2006**) 1, 73–79, doi:10.1016/j.jhazmat.2005.07.033

[20] T. Van Gerven, E. Van Keer, S. Arickx, M. Jaspers, G. Wauters, C. Vandecasteele, Carbonation of MSWI-bottom ash to decrease heavy metal leaching, in view of recycling, Waste Management, 25 (**2005**) 3, 291–300, doi:10.1016/j.wasman.2004.07.008

[21] M. Fernandez Bertos, X. Li, S. J. R. Simons, C. D. Hills, P. J. Carey, Investigation of accelerated carbonation for the stabilisation of MSW incinerator ashes and the sequestration of CO_2, Green Chem., 6 (**2004**) 8, 428–436, doi:10.1039/B401872A

[22] X. Li, M. Fernandez Bertos, C. D. Hills, P. J. Carey, S. Simon, Accelerated carbonation of municipal solid waste incineration fly ashes, Waste Management, 27 (**2007**), 1200–1206, doi:10.1016/j.wasman.2006.06.011

[23] G. Cappai, S. Carab, A. Muntoni, M. Piredda, Application of accelerated carbonation on MSW combustion APC residues for metal immobilization and CO_2 sequestration, Journal of Hazardous Materials, 207–208 (**2012**), 159–164, doi:10.1016/j.jhazmat.2011.04.013

[24] T. Sicong, J. Jianguo, Z. Chang, Influence of flue gas SO_2 on the toxicity of heavy metals in municipal solid waste incinerator fly ash after accelerated carbonation stabilization, Journal of Hazardous Materials, 192 (**2011**), 1609–1615, doi:10.1016/j.jhazmat.2011.06.085

[25] L. Wang, Y. Jin, Y. Niea, Investigation of accelerated and natural carbonation of MSWI fly ash with a high content of Ca, Journal of Hazardous Materials, 174 (**2010**), 334–343, doi:10.1016/j.jhazmat.2009.09.055

[26] P. Gunning, C. Hills, A. Antemir, P. Carey, Novel approaches to the valorisation of ashes using aggregation by carbonation, Proc. of the 2nd International Slag Valorisation Symposium, Leuven, 2011, 103–116

[27] H. Katsuura, T. Inoue, M. Hiraoka, S. Sakai, Full-scale plant study on fly ash treatment by the acid extraction process, Waste Management, 16 (**1996**) 5/6, 491–499, doi:10.1016/S0956-053X(96)00091-8

[28] A. J. Chandler, T. T. Eighmy, J. Hartlén, O. Hjelmar, D. S. Kosson, S. E. Sawell, H. A. van der Sloot, J. Vehlow, Municipal Solid Waste Incinerator Residue, Studies in Environmental Science 67, Elsevier Science B. V., Netherlands 1997

UDK 621.762:621.77 ISSN 1580-2949
Professional article/Strokovni članek MTAEC9, 49(2)303(2015)

THE INFLUENCE OF THE MORPHOLOGY OF IRON POWDER PARTICLES ON THEIR COMPACTION IN AN AUTOMATIC DIE

VPLIV MORFOLOGIJE DELCEV ŽELEZOVEGA PRAHU NA NJEGOVO SPOSOBNOST ZA AVTOMATSKO ENOOSNO STISKANJE

Borivoj Šuštaršič[1], Matjaž Godec[1], Črtomir Donik[1], Irena Paulin[1], Srečko Glodež[2], Marko Šori[2], Milan Ratej[3], Nada Javornik[3]

[1]Institute of Metals and Technology, Lepi pot 11, 1000 Ljubljana, Slovenia
[2]University of Maribor, FNM, Koroška cesta 160, 2000 Maribor, Slovenia
[3]UNIOR, Forging Industry, Kovaška cesta 10, 3214 Zreče, Slovenia
borivoj.sustarsic@imt.si

Prejem rokopisa – received: 2014-10-24; sprejem za objavo – accepted for publication: 2014-12-16

doi:10.17222/mit.2014.273

Fe- and steel-based powder metallurgy (P/M) products, such as steel gears, spurs, locking mechanisms, porous filters, sliding bearings and bushes, as well as other machine parts and structural elements, are mainly produced with the so-called conventional sintering technology. It is the most efficient technology for the mass production of small, complex, functional and structural parts. Therefore, it is the most convenient and popular among all of the P/M technologies. The most important end-user of sintered parts is the automotive industry. However, small, complex, sintered parts can also be frequently used in the furniture and household industries, precise mechanics, articles for recreation and sports. A fine, iron-based powder mixture or prealloyed powder is first automatically uniaxial-die compacted (ADC) into the final shape of the product with a mechanical or hydraulic press and then sintered in a protective atmosphere at approximately 1100 °C. The metal powder mixture must have the appropriate engineering properties given by the chemistry and particle morphology, enabling a fast and reliable die-compaction process. The most important are a high tap density, a good powder flowability and a low compressibility. All this gives the green compacts an appropriate final shape with a smooth surface, a relatively high and uniform green density, as well as a green strength without internal flaws and cracks. In the case of very small two-or-more-heights products, for example, spur gears with a low module, it is very difficult to obtain a uniform green density at acceptable compaction pressures. Often small cracks are formed at height crossings and big differences in the green density appear in smaller or thinner regions. In the frame of our investigation we analysed the influence of the selected prealloyed commercial iron powder's morphology and its technological properties on automatic die compaction, as well as the sintering process in the case of small two-level sintered gear dimensions of 5/40–7/10 × 7 mm with module $m = 0.5$. The original iron powder was sieved and the finest powder particle fraction (< 45 µm) was compared with the original powder mixture considering ADC and sintering process. It was found that the selection of the finer powder mixture could not contribute to the improvement in the overall ADC process, as well as a better green compact. In the present paper the results of our investigations are presented and the reasons why a finer powder mixture cannot contribute much to an improvement of the conventional sintering process.

Keywords: Fe-based alloy powders, morphology and microstructure of particles, influence on automatic die compaction, sintering

Jekleni izdelki, izdelani po P/M-postopkih, kot so npr. zobniki, mehanizmi za zaklepanje, porozni filtri, drsni ležaji in puše, kakor tudi drugi strojni elementi ali strukturni deli, se v glavnem izdelujejo po konvencionalni tehnologiji sintranja. To je najbolj učinkovita in zato najpopularnejša tehnologija za masovno proizvodnjo majhnih kompliciranih funkcionalnih in strukturnih izdelkov. Avtomobilska industrija je najbolj pomemben končni uporabnik sintranih delov, vendar se le-ti pogosto uporabljajo tudi v pohištveni industriji, beli tehniki, precizni mehaniki, v izdelkih za šport in rekreacijo itd. Fina prašna mešanica na osnovi Fe ali predlegiranih jeklenih delcev se najprej avtomatsko enoosno stiska v končno obliko na mehanskih ali hidravličnih stiskalnicah in nato sintra v zaščitni atmosferi pri pribl. 1100 °C. Kovinska prašna mešanica mora imeti primerne tehnološke lastnosti, ki omogočajo hiter in zanesljiv proces zgoščevanja v surovce želene oblike in velikosti. Te so definirane s fizikalno-kemijskimi lastnostmi in predvsem morfologijo (obliko in velikostjo) delcev. Najbolj pomembne so visoka nasipna gostota, dobra tekočnost in nizka stisljivost prašne mešanice. Vse to daje surovemu izdelku želeno končno obliko z gladko površino, relativno visoko in enakomerno zeleno gostoto in trdnostjo brez lokalnih napak in razpok. Pri zelo majhnih dvo- ali večvišinskih izdelkih, kot so npr. dvojni zobniki z majhnim zobniškim modulom, je zelo težko dobiti surovce (zelence) brez napak in z enakomerno gostoto pri sprejemljivih tlakih stiskanja. Pogosto na surovcih nastajajo razpoke na prehodu iz tanjšega v debelejši del zobnika zaradi velikih razlik v zeleni gostoti. V okviru naših raziskav smo analizirali vpliv morfologije izbranega predlegiranega komercialnega Fe-prahu in njegovih tehnoloških lastnosti na razmere pri avtomatskem enoosnem stiskanju in sintranju majhnega dvovišinskega sintranega zobnika dimenzij 5/40–7/10 × 7 mm z modulom $m = 0,5$. Originalni Fe-prah smo presejali in najfinejšo frakcijo prahu (< 45 µm) uporabili za stiskanje in sintranje ter jo primerjali z originalno prašno mešanico. Ugotovili smo, da finejši prah ne prispeva k izboljšanju postopka avtomatskega enoosnega stiskanja oz. k boljšim surovcem iz več razlogov. V tem prispevku predstavljamo rezultate naših raziskav in razloge, zakaj izbira finejše prašne mešanice ne prispeva celovito k izboljšanju konvencionalnega sintrnega postopka.

Ključne besede: legirani prahovi na osnovi železa, vpliv morfologije in mikrostrukture na avtomatsko enoosno stiskanje, sintranje

1 INTRODUCTION

The conventional sintering technology is the most popular among the all P/M technologies. It enables the large-scale production of small complex parts (**Figure 1**) with the lowest raw-material and energy consumption.[1–3] This technology is used in the Unior forging industry, Sinter workshop, Zreče, Slovenia, mainly for the production of sintered steel parts for the automotive industry.[4]

Sinter technology consists of three main production phases: powder manufacture and the preparation of the mixture, automatic (uniaxial cold) die compaction (ADC) and sintering (**Figure 2**). The improvement of the dimensional tolerances and the mechanical properties can be obtained with te additional post-sintering operations, i.e., sizing, surface and heat treatment and machining.

Figure 1: Some typical sintered steel parts
Slika 1: Nekaj tipičnih oblik sintranih jeklenih izdelkov

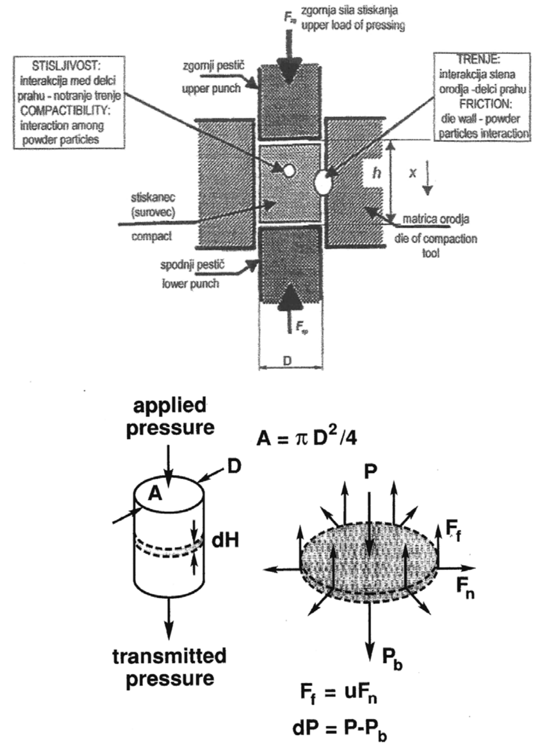

Figure 3: Schematic presentation and analysis of the uniaxial cold die compaction of metal powder in a cylindrical die[6]
Slika 3: Shematični prikaz in analiza hladnega enoosnega stiskanja prahu v cilindričnem orodju[6]

Some geometrical limitations exist in the phase of product design and later in the phase of tool manufacture when considering uniaxial automatic die compaction. These limitations have their origin in the nature of uniaxial ADC. Namely, the forces (pressures) of compaction are not uniformly transferred over the height and cross-section of the formed green compact because of the internal friction among the powder particles and the friction on the die walls (**Figure 3**). This has already been shown by the classic analysis[1] introducing an equation where one can see that the transferred compaction force depends not only on the internal friction and the die-wall friction, but also on the ratio between the height and the diameter of the green compact (*h*/*D*):

$$F_x = F_0 \cdot e^{-4\mu z x/D} \tag{1}$$

In Equation (1) F_x is the resulting force at a distance x from the upper punch, F_0 is the acting (compaction) force on the upper punch, μ is the die-wall friction coefficient and the factor z describes the ratio between

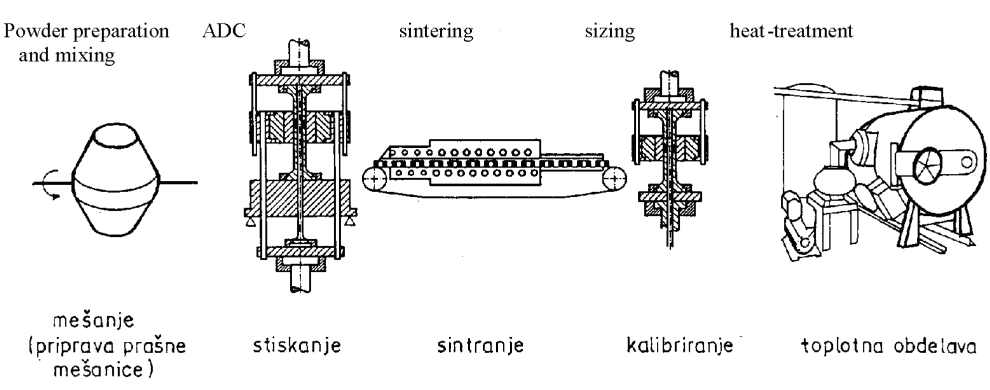

Figure 2: Schematic presentation of the phases of the conventional sintering process for the production of steel parts
Slika 2: Shematični prikaz postopka izdelave sintranih jeklenih izdelkov

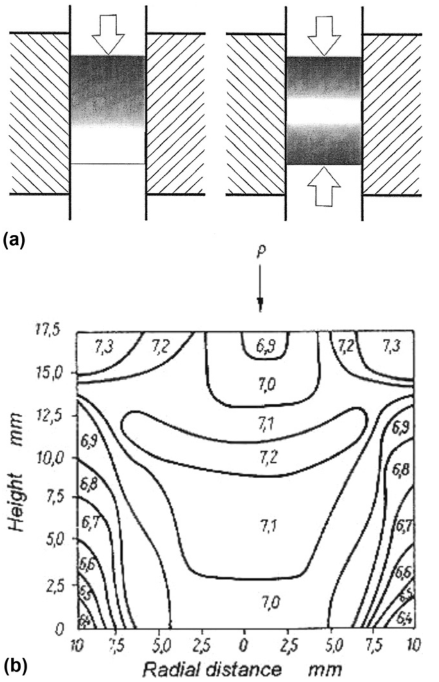

Figure 4: a) Schematic and b) practical presentation of the green-density distribution in a cylindrical specimen after the uniaxial cold compaction of steel powder[5]

Slika 4: a) Shematični in b) praktični prikaz porazdelitve zelene gostote v cilindričnem surovcu po enoosnem stiskanju jeklenega prahu v orodju[5]

the normal and the powder-transferred radial stresses, which depends on the internal friction among the powder particles.

From Equation (1) we can calculate the transferred force at any distance *x* in the formed green powder compact, as well as the lowest transferred force on the bottom punch (at $x = h$) if the die and powder characteristics μ and z are known. The higher is the ratio h/D, the larger are the local differences in the green density and the formed green compact has an unequal green density over its volume (**Figure 4**). The higher is the compaction pressure, the higher is the local and overall (average) green density of the compact.

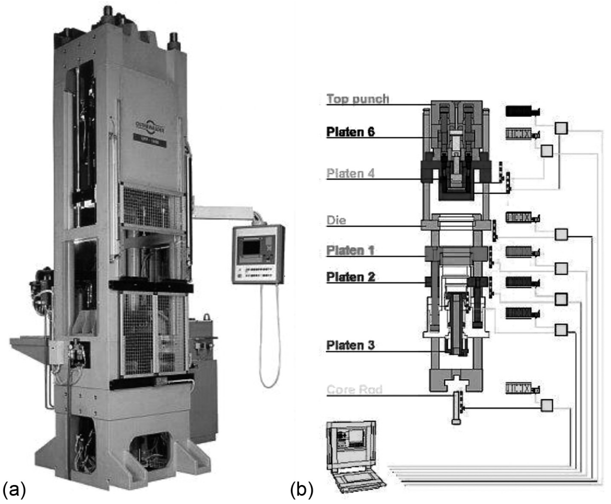

(a) (b)

Figure 5: a) Modern hydraulic computer-controlled press for the automatic die compaction of steel powders and b) a schematic presentation of a multi-platen adapter system for the fixation of the tool into the press[5]

Slika 5: a) Moderna hidravlična računalniško vodena stiskalnica za avtomatsko enoosno stiskanje jeklenih surovcev in b) shematični prikaz adapterja z večploščnim sistemom vpetja orodja v stiskalnico[5]

The green density distribution can be mitigated if the compaction force acts from both sides (top and bottom) when forming the green part. Therefore, modern tools for ADC consist of a large number of parts; their movement is programmed and controlled by a computer on hydraulic or mechanical presses (**Figure 5**) in order to avoid too large differences in the green density of the compact and its uniform ejection out of the die.

In spite of this, it is not possible to ensure that a green compact has a completely uniform green density over the whole volume (**Figure 4**), especially, if in the product design phase, it is not possible to avoid larger height differences, sharp crossings and chamfers, because of other functional limitations of the final sintered product.[5] The results of an unsuitable geometry of the product are: non-uniform powder filling of the die, large local compaction pressures, forming large local green-density differences, and finally cracking of the green compact during ejection. However, these also lead to wear/fracture of the most loaded tool parts and overall shorten the life of the tool. Tools (dies) for the compaction of metal powders are very precise, made of advanced tool steels and cemented carbides, and therefore, their manufacture is very complex and expensive. Tool life depends not only on its complexity but also on powder engineering (technological) properties. Metal powders have to have a large tap density, good flowability and compressibility for the appropriate ADC.

One such sintered steel product that has a difficult ADC geometry is the two-height small gear produced in the Unior factory (**Figure 6**). It also has a very small gear module ($m = 0.5$) as well as large height and diameter differences.

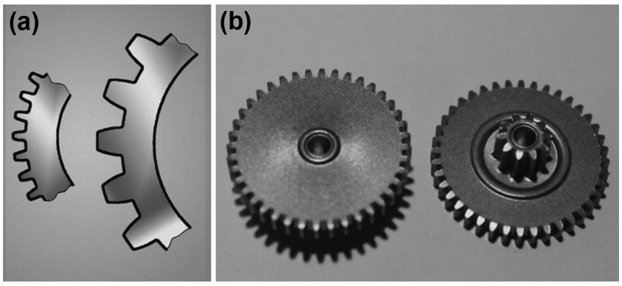

Figure 6: a) Schematic presentation of small and large gear module and b) a photograph of the discussed small complex double spur gear with the dimensions 5/40-7/10 × 7 mm, produced in the Sinter Workshop, Unior factory, Zreče, Slovenia

Slika 6: a) Shematični prikaz ozobljenja z majhnim in velikim modulom in b) posnetek obravnavanega majhnega dvojnega sintranega zobnika 5/40–7/10 × 7 mm, ki ga izdelujejo v obratu Sinter, Unior, Zreče

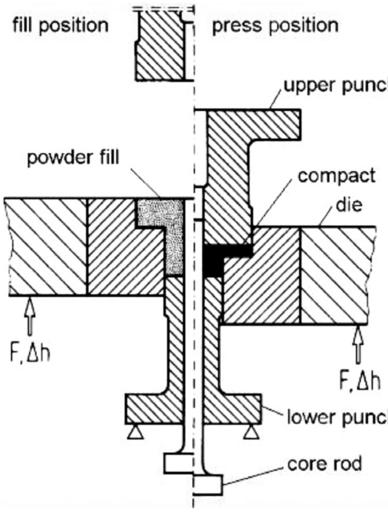

Figure 7: Schematic presentation of the cross-section of the tool for the uniaxial ADC of the double-height product[5]

Slika 7: Shematični prikaz prereza sestave orodja za stiskanje dvovišinskega izdelka[5]

This small gear is compacted with very high compacting pressures in order to decrease the differences in the green density in the gear teeth because of poor filling of the engraving, as well as to decrease the differences in the green density between the gear parts with a large height difference to avoid cracking at the height crossing. This demands high compaction pressures over 700 MPa. The result is a too short tool-life because of frequent fracture of the most loaded tool parts (punches and core rods, **Figure 7**).

Different solutions (better tool materials, more precise tooling, optimization of the die and press set up) have been researched to solve this problem. But no one has found a complete result and a final solution. Therefore, we also tried with a change of the existing powder granulometry. The hypothesis was that the selection of a finer powder could offer better compressibility and filling of the die. Unfortunately, as it follows, the change of the granulometry to a finer powder also did not give an improvement of the ADC process but gave us a lot of useful and interesting information.

2 EXPERIMENTAL WORK

For the production of the investigated two-height gear a standard commercial diffusion prealloyed Fe-based powder Distaloy AB, Höganäs, Sweden was used. Its average nominal bulk chemical composition in mass fractions (w/%) is: 1.7 Ni, 1.5 Cu, 0.5 Mo, and the rest is Fe. The addition of carbon (generally 0.4–0.6 % graphite) changes it during the sintering into a steel with the required chemical composition. The 5 kg of original Distaloy AB powder was sieved on a set of vibrating sieves in the frame of our experimental work. The finest powder fraction (< 45 μm) was selected for our subsequent experiments and investigations.

The compressibility of the selected fine (< 45 μm) and rough (> 45 μm) mixtures was determined by instrumented apparatus[6] in standardized die dimensions of ϕ 24 mm × 16 mm. The experiment for the compressibility determination is performed at a ram speed of 10 mm/min. It is a much slower speed than the actual industrial ADC process. Therefore, the densification and deformation rate of the green compact in industrial conditions are different and higher (a larger number of structural defects affecting the sintering), respectively. The flowability and tap density of the selected powder mixtures were determined with a Hall flowmeter[1]. The prescribed amount of graphite (w = 0.5 %) and Kenolube lubricant (w = 0.9 %) were added to the original Distaloy AB and the fine sieved powder and both were then homogenized in a double-cone mixer. The experimental compaction of the gears was performed on an industrial 60 kN Dorst, Germany, mechanical press. Approximately 100 gear pieces were compacted from both powder mixtures followed by the sintering of green compacts in an industrial continuous-belt Mahler furnace under standard sintering conditions (1120 °C/30 min) in a protective atmosphere (N_2 + 5/10 % H_2). The sintered gears were additionally heat treated after sintering (oil quench-

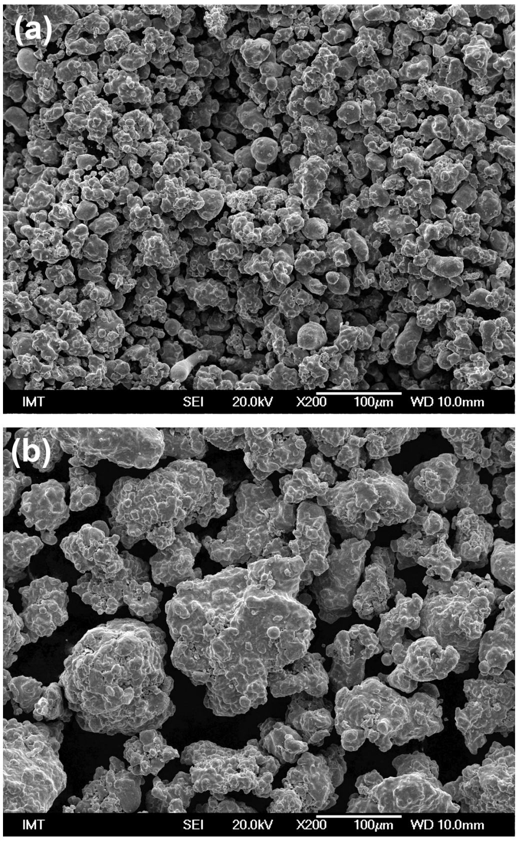

Figure 8: SEM micrograph of: a) fine (sieved < 45 μm) and b) large (> 45 μm sieve residual) powder mixture Distaloy AB; magnification 200-times

Slika 8: SEM-posnetka: a) fine (presejane na < 45 μm) in b) grobe (ostanek po sejanju > 45 μm) frakcije kovinskega prahu Distaloy AB; povečava 200-kratna ing from 890 °C and tempering at 200 °C/30 min) The Vickers hardness HV5 of the sintered and heat-treated gears and the mechanical moment (teeth strength) were determined. The local bulk and micro-chemical compositions of the powders, green compacts and sintered gears were determined with an SEM/EDS (Jeol – JSM6500F/Oxford INCA ENERGY 450, INCA X-SIGHT LN2) and an XRF analyzer (Thermo Scientific, Niton XL3t Goldd+).

3 RESULTS AND DISCUSSION

Figure 8 shows scanning electron micrographs of the fine and rough fractions of the investigated powders. The powders do not have large differences in morphology (shape and surface state), with the exception of the particle size. However, micro-chemical SEM/EDS analyses have shown that the local chemical composition of the fine fraction is significantly different compared to the original mixture. The most probable reason is the method of powder alloying. The used Distaloy AB powder is diffusion prealloyed (**Figure 9b**) and segregation of the alloying elements occurred during sieving and finer powder particles have a different chemical composition than the larger ones. **Figure 10** shows EDS micro-chemical mapping analyses of the fine and large powder particles. It is clear that their local compositions are quite different. This was also confirmed by the XRF analyses, which included a much larger volume of analyzed sample. In spite of this, the local chemical compositions of all the samples differ significantly from the nominal chemical composition of the Distaloy AB powder. **Table 1** shows the average chemical compositions of all the analyzed samples. It is clear that the fine powder mixtures have a much higher content of alloying elements than the original powder mixture. As will be shown later, this over-alloying also has a significant influence on the mechanical properties of the sintered and heat-treated gears.

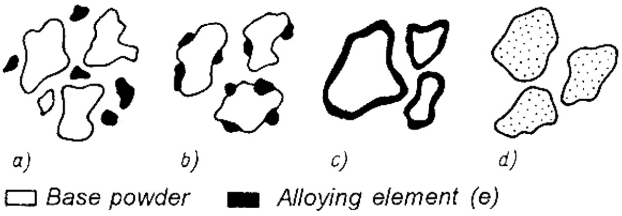

Figure 9: Standard ways of alloying techniques in powder metallurgy[5]
Slika 9: Standardni načini legiranja v metalurgiji prahov[5]

Table 1: Average XRF bulk chemical compositions of analyzed samples in mass fractions, *w*/%
Tabela 1: Povprečne XRF kemijske sestave analiziranih vzorcev v masnih deležih, *w*/%

No.	Sample	Fe	Ni	Cu	Mo	Mn	Cr	Si
1	Fine powder	74.14	14.38	9.99	0.84	0.09	0.05	0.13
2	Green compact fine powder	83.03	9.73	5.91	0.78	0.09	0.04	0.12
3	Sintered gear fine powder	88.92	5.47	4.42	0.80	0.20	0.05	0.08
4	Green compact original powder	90.57	4.72	3.53	0.60	0.10	0.06	0.17
5	Sintered compact original powder	93.65	3.10	2.11	0.65	0.13	0.06	0.12

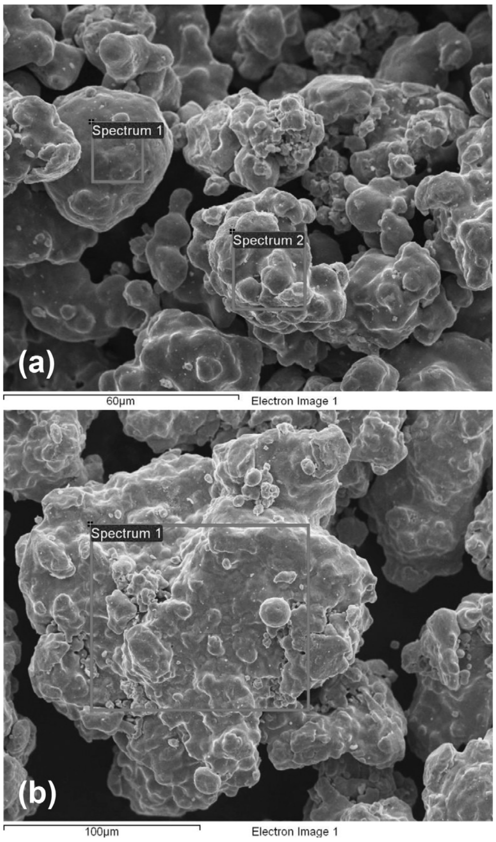

(a)	Fe	Ni	Cu	Mo
Spectrum 1	92.54	4.01	1.71	1.74
Spectrum 2	98.96	0.41	0.63	0.00

(b)	Fe	Ni	Cu	Mo
Spectrum 1	97.51	0.81	0.71	0.97
Spectrum 2*	87.27	0.76	9.94	2.03

* not designated in the micrograph

Figure 10: Mapping SEM/EDS microanalyses of: a) fine and b) large powder particles in mass fractions, *w*/%
Slika 10: Primer ploskovne SEM/EDS-mikroanalize: a) finega in b) grobega delca v masnih deležih, *w*/%

Table 2 shows the results of the technological properties of the original, fine and rough powder mixture. We can see from this table that the fine fraction mixture has a poorer flowability, a lower tap density (ρ_n) and a negligibly better compressibility (ρ_z at p_{sr}). Our hypothesis was that the finer powder mixture has a better ability to fill the die cavity, but obviously the experiments disprove this.

In this way the original powder mixture has a significantly better flowability, a higher tap density and a negligibly lower compressibility, and is therefore more suitable for ADC. This was also confirmed by our indu-

Table 2: Technological properties of the steel powder Distaloy AB, Höganäs
Tabela 2: Tehnološke lastnosti kovinskega prahu Distaloy AB, Höganäs

Powder type	ρ_n/(g/cm^3)	Flowability s/50 g	p_{max}/ MPa	p_{sr}/MPa	ρ_z/(g/cm^3)	Remarks
Original powder*	3.06	26	7.10 g/cm^3 at 600 MPa			lubricant Kenolube
Fine fraction (< 45 μm)	2.75	30	722.6	595.4	7.15	lubricant stearic acid
Rough fraction (> 45 μm)	2.99	26	738.5	512.4	6.94	

* manufacturer's data

strial experiments of the gear compaction. The powder mixture better filled the die cavity and a higher average green density (approx. 7.0–7.1 g/cm^3) of the gears at lower compaction pressures (approx. 180 kN) are obtained. The fine powder mixture did not fill the die cavity so well and a lower average green density (approx. 6.9–7.0 g/cm^3) of the gears at higher compaction pressures (approx. 210 kN) were obtained. Besides this, the gears made of the fine powder mixture have poorer mechanical properties after sintering and heat-treatment (**Table 3**). **Figures 11** and **12** show the microstructures of the sintered and heat-treated gears. **Figures 11a** and **11b** show a typical microstructure of a polished sample in the region of the tooth-root of the sintered gear visible under a light microscope (LM). It is clear that the sintered gear made of the original mixture has a larger fraction of large pores, but it is better densified in the gear core. This could be a problem of gear resistance to wear and fatigue. On the other hand, the gear made of the finer powder mixture has well-distributed, finer pores, but it is much less densified.

Figures 12a and **12b** show typical microstructures of polished and etched samples of the gears after sintering

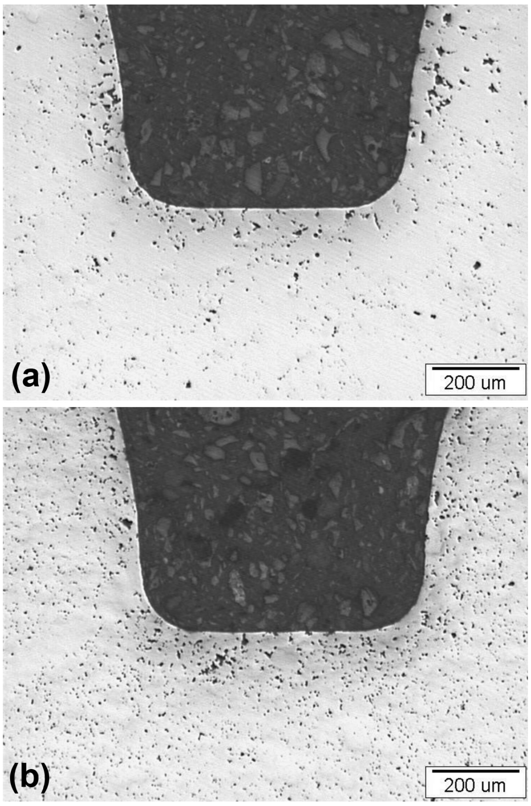

Figure 11: Microstructure of sintered gear: a) produced from original powder mixture and b) produced from fine sieved powder mixture; polished sample, light microscope; magnification 50-times
Slika 11: Mikrostruktura sintranega zobnika: a) izdelanega iz originalne mešanice in b) iz fine mešanice; poliran vzorec, svetlobni mikroskop; povečava 50-kratna

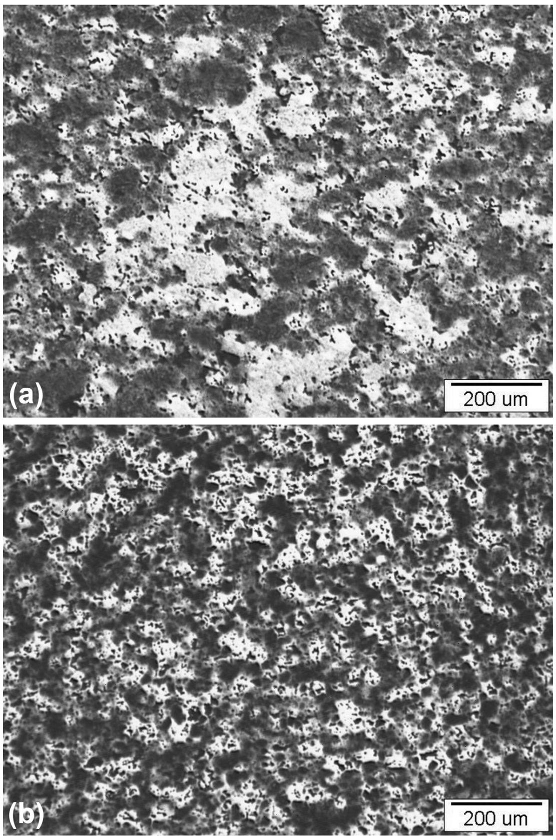

Figure 12: Microstructure of sintered and heat-treated gear: a) produced from original powder mixture and b) produced from fine sieved powder mixture; polished and nital-etched sample, light microscope, magnification 100-times
Slika 12: Mikrostruktura sintranega in poboljšanega zobnika: a) izdelanega iz originalne mešanice in b) iz fine mešanice; poliran in v nitalu jedkan vzorec, svetlobni mikroskop; povečava 100-kratna

Table 3: Vickers hardness of sintered and tempered gears
Tabela 3: Trdote sintranih in poboljšanih zobničkov

	Original powder	Fine sieved powder
Sintered gears	212	298
Tempered gears	318	293

and heat treatment, visible under a LM. The gear made of the original powder mixture has a typical and correct, but heterogeneous, martensitic/bainitic microstructure. However, the gear made of the fine powder mixture has a microstructure in accordance with the inappropriate (over-alloyed) chemical composition.

4 CONCLUSIONS

The original prealloyed Fe-based powder Distaloy AB was sieved and the technological properties of the fine and rough powder fractions important for ADC were determined. The fine powder fraction has a lower tap density, worse flowability and a negligibly better compressibility. It was expected that the selection of the fine powder fraction can contribute to an improvement in the ADC process of a small, two-height gear, especially to better filling of the teeth engraving, as well as a more uniform green-density distribution at a lower compaction pressure. This hypothesis has been disapproved based on experimental and semi-industrial work. It has been found that the selection of the finer powder mixture also has other traps. The sieved finer fraction has a different chemical composition than the original powder mixture. This has an important influence on the sintering and heat-treatment response of the material. Therefore, the poorer mechanical properties of the gears made of the fine fraction were obtained. The open question is also the price of manufacture of the fine powder mixture with the correct chemical composition. For now, the existent ADC procedure for the selected small gears is indicated as optimal. In the future, it will be necessary to find other ways to improve the ADC of small spur gears.

5 REFERENCES

[1] R. M. German, Powder Metallurgy Science, Metal Powder Industries Federation (MPIF), Second Edition, Princeton, New Jersey 1994

[2] F. Thümmler, R. Oberacker, Introduction to Powder Metallurgy, The Institute of Materials, The University Press, Cambridge 1993

[3] Powder Metallurgies and Application, ASM Handbook, Volume 7, 1993

[4] Unior, d. d., Forging Industry, Zreče, program Sinter, web page address: http://unior-schmiede.com/cgi-bin/cms.cgi?doc=20454

[5] Powder Metallurgy, materials, processes and application, CD product of the European Commission's Leonardo Da Vinci Program, EPMA (European Powder Metallurgy Association), 2000

[6] B. Šuštaršič et al., An instrumented cell to analyse the behaviour of metal powders during cold uniaxial die compaction, Mater. Tehnol., 35 (**2001**) 6, 351–360